1-1-2015

Commercial-Scale Conversion of Algae to Biofuel

Cory Stephen Silva
University of Pennsylvania, silvacor@seas.upenn.edu

Commercial-Scale Conversion of Algae to Biofuel

Abstract
Biodiesel, derived from renewable feedstocks like algae, has the potential to replace traditional, petroleum-based fuels — providing a carbon-neutral, sustainable transportation fuel. However, with plummeting oil prices, alternative fuels have become less competitive. Thus, process modeling and optimization are needed to reduce costs. Extensive modeling has been done for the conversion of algae and plant lipids to biofuels, but the upstream operations remain poorly understood. We partnered with other organizations to create an overall techno-economic model for a commercial-scale algae-to-biodiesel venture, using software packages like ASPEN PLUS, the ASPEN Process Economic Analyzer, gPROMS, and AIMMS. The two most important findings from this model were that: (1) cultivation represented 90% of the total capital expense because of the massive fields required to grow the algae, and (2) extraction of the oil from algae had highly variable cost estimates, which spanned three orders of magnitude. The low photosynthetic efficiency of the algae was the major limiting factor in terms of algae growth. Therefore an exergy analysis was undertaken to rigorously calculate the efficiency (3.9%) and determine what could be done to improve it. Overall, the algae cell's absorption of sunlight was the largest loss of exergy, and therefore the most crucial factor in decreasing capital expenditures for this venture. Regarding the extraction of the oils, supercritical carbon dioxide is a green, non-toxic solvent that can be used to extract and convert algae-oils to biodiesel in a single step, eliminating the need for pre- or post-processing of the oil or biodiesel product. The statistical associating fluid theory equations-of-state in ASPEN PLUS (PC-SAFT) and gProms (SAFT-γ Mie) were used to perform the fluid-phase equilibria calculations because of their improved robustness and higher accuracy for long-chain hydrocarbons when compared with cubic equations-of-state. A multi-phase reactor model was formulated to account for the effects of changing phase equilibria on reaction conversions. While further research is required to obtain cost estimates, preliminary results for this system show that it is possible to achieve high oil-to-biodiesel conversions at much lower pressures than previous anticipated.

Degree Type
Dissertation

Degree Name
Doctor of Philosophy (PhD)

Graduate Group
Chemical and Biomolecular Engineering

First Advisor
Warren D. Seider

Keywords
Algae, Biodiesel, Exergy, Life-cycle, Process, Supercritical

Subject Categories
Chemical Engineering

COMMERCIAL-SCALE CONVERSION OF ALGAE TO BIOFUEL

Cory Silva

A DISSERTATION

in

Chemical and Biomolecular Engineering

Presented to the Faculties of the University of Pennsylvania

in

Partial Fulfillment of the Requirements for the

Degree of Doctor of Philosophy

2015

Supervisor of Dissertation

Warren D. Seider, Professor, Chemical and Biomolecular Engineering

Graduate Group Chairperson

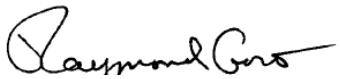

Raymond J. Gorte, Professor, Chemical and Biomolecular Engineering

Dissertation Committee

Leonard Fabiano, Adjunct Professor, Chemical and Biomolecular Engineering

Robert Riggleman, Associate Professor, Chemical and Biomolecular Engineering

John Vohs, Professor, Chemical and Biomolecular Engineering

Andrew Jackson, Adjunct Professor, Mechanical Engineering and Applied Mathematics

Eric Dunlop, Industrial Consultant, Pan Pacific Technologies

COMMERCIAL-SCALE CONVERSION OF ALGAE TO BIOFUEL

DEDICATION

To Jill Silva, my mother,

who always pushes me to be my best, and whose loving support brought me through the best and worst of times

ACKNOWLEDGMENT

It was an incredibly rewarding experience to work with Warren Seider, who is such a giant in our field. Warren's decades of experience and knowledge of not only core chemical engineering concepts but also the research community was crucial in defining the goals and scope of this very difficult thesis. I learned a lot from Warren, both inside and outside the lab. I've definitely become a more competent chemical engineer after working with him, but he also mentored me in inter-personal interactions, presentations, teaching, and of course writing/editing. As I prepare to graduate, I feel like I have not only gained more specialized technical aptitudes, but also greatly refined personal and professionals skills thanks to Warren's guidance.

The perfect offset to Warren's theoretical knowledge was Len Fabiano's practical experience. After Warren, he was the person that had the largest impact on me during this thesis. Early on, the sessions we had together were what set me on the road to completing my first, first-author paper (Chapter 3). I learned more about the software tools from him than from everyone else combined. I also learned quite a bit about the industry from our talks together, and his influence played a large part in shaping my overall career goals.

I was grateful for the opportunity to work with both Eric Dunlop and Kim Ogden in the National Alliance for the Advancement of Biofuels and Bioproducts (NAABB). Kim Ogden was crucial in initiating our involvement in the NAABB project and providing us with material to help us begin our research. Similarly, Eric helped shape

our research during the intermediate stages. He shared his wealth of knowledge with us concerning biological processes, and allowed us to cooperate with him in investigating many of his novel ideas. Without Eric's help, my first paper would not have existed (Chapter 2), my first, first-author paper (Chapter 3) would have been much poorer in quality, and it would have been much more difficult to find meaningful areas to explore for the latter half of this thesis.

It was an honor to meet and work with Lindsay Soh and Julie Zimmerman. Without them, Chapter 5 of this thesis could not have existed. Julie shared her knowledge of supercritical processes with us, as well as her reaction data that gave us a system to model and explore during the second half of my thesis. Lindsay went outside her typical research area to take vapor-liquid equilibria and liquid-liquid equilibria data for us, despite being busy with her duties as a first-year professor. Without her dedication, our analyses in Chapter 5 would not have been meaningful or practical.

Prof. Noam Lior was crucial in defining Chapter 4 of this thesis. He provided the topic, and was a continual source of knowledge to draw upon while I worked. He also imparted the fundamentals of this topic, as well as many others, when I took his class.

Esteban Brignole first made Warren and I aware of the SAFT equations of state and the supercritical method of converting algae-oils to biodiesel. In addition, he continued to provide helpful advice and crucial data while we worked on this problem. I was fortunate to meet him at AIChE 2014 in Atlanta, where he gave me some final insights that helped me complete my phase equilibrium work (Chapter 5).

Ian Moskowitz was my only real lab-mate during my time at UPenn. He was an excellent sounding-boarding for many of my more theoretical ideas. He was also my ride to and from Princeton, as well as PSE's U.S. headquarters. I learned a lot from him during my last year about gPROMS and numerical methods in general, which helped me complete Chapter 5. He was also a good friend, who propped me back up during some of the more difficult periods of graduate school. In addition, I had the help of three excellent undergraduate students during my tenure: Greg Cameron, Eiman Soliman, and Tony Barberio. All three contributed unique research ideas and a lot of hard work, without which, much of this thesis would not have been possible.

Finally, I would like to thank Rob Riggleman for being on my committee and helping me define some key long-term objective for this thesis. I would like to thank John Vohs for helping me several times with reactor modeling and for being one of my committee members. And I would like to thank Andy Jackson for serving on my committee, providing me with some industrial contacts, and helping to properly frame my thesis in a larger scope.

Cory Silva

Philadelphia

July 7th, 2015

ABSTRACT

COMMERCIAL-SCALE CONVERSION OF ALGAE TO BIOFUEL

Cory Silva

Warren D. Seider

Biodiesel, derived from renewable feedstocks like algae, has the potential to replace traditional, petroleum-based fuels — providing a carbon-neutral, sustainable transportation fuel. However, with plummeting oil prices, alternative fuels have become less competitive. Thus, process modeling and optimization are needed to reduce costs. Extensive modeling has been done for the conversion of algae and plant lipids to biofuels, but the upstream operations remain poorly understood. We partnered with other organizations to create an overall techno-economic model for a commercial-scale algae-to-biodiesel venture, using software packages like ASPEN PLUS, the ASPEN Process Economic Analyzer, gPROMS, and AIMMS. The two most important findings from this model were that: (1) cultivation represented 90% of the total capital expense because of the massive fields required to grow the algae, and (2) extraction of the oil from algae had highly variable cost estimates, which spanned three orders of magnitude. The low photosynthetic efficiency of the algae was the major limiting factor in terms of algae growth. Therefore an exergy analysis was undertaken to rigorously calculate the efficiency (3.9%) and determine what could be done to improve it. Overall, the algae cell's absorption of sunlight was the largest loss of exergy, and therefore the most crucial

factor in decreasing capital expenditures for this venture. Regarding the extraction of the oils, supercritical carbon dioxide is a green, non-toxic solvent that can be used to extract and convert algae-oils to biodiesel in a single step, eliminating the need for pre- or post-processing of the oil or biodiesel product. The statistical associating fluid theory equations-of-state in ASPEN PLUS (PC-SAFT) and gProms (SAFT-γ Mie) were used to perform the fluid-phase equilibria calculations because of their improved robustness and higher accuracy for long-chain hydrocarbons when compared with cubic equations-of-state. A multi-phase reactor model was formulated to account for the effects of changing phase equilibria on reaction conversions. While further research is required to obtain cost estimates, preliminary results for this system show that it is possible to achieve high oil-to-biodiesel conversions at much lower pressures than previous anticipated.

TABLE OF CONTENTS

LIST OF TABLES

LIST OF FIGURES

CHAPTER 1

Introduction

Every year, the United States consumes approximately 7 billion barrels of oil (about 300 billion gallons), accounting for 22% of world-wide demand (Webpage: How much oil does the United States consume per year?); 25-45% is imported, of which 35-40% comes from OPEC countries (Webpage: How Much Petroleum is Imported?). This consumption of fossil fuels, which began during the industrial revolution, has increased atmospheric CO_2 concentrations (Figure 1.1) to the highest levels in at least the last 400,000 years (Webpage: Atmospheric CO_2 Concentrations over Thousands of Years), and they continue to rise at an exponential pace (Webpage: Atmospheric Concentration of CO_2 with Time). The high concentration of CO_2 in the atmosphere is associated with a rise in global temperatures and an increased occurrence of extreme weather events (Intergovernmental Panel on Climate Change, 2007), which will only worsen unless greenhouse gas emissions (GHGE) are eliminated.

While the discovery of hydraulic fracturing for natural gas mining will cause a net CO_2 emissions decrease (because natural gas is more hydrogen-rich than petroleum or coal), it will only delay the problems caused by GHGE. In addition, in the transportation sector, fuel prices are often unstable (Figure 1.2) because of fluctuating technological progress, instability in oil-rich regions, and policy decisions by OPEC (Webpage: EIA: Real Prices Viewer). For instance, Figure 1.2 displays the oil prices for the past 47 years; the maximum price per barrel (averaged by year) is 616% higher than the lowest value.

Even in the last five years, the highest value is 220% higher than the lowest value. For the reasons of both price stability and environmental concern, attention has turned to biofuels several times in the past several decades.

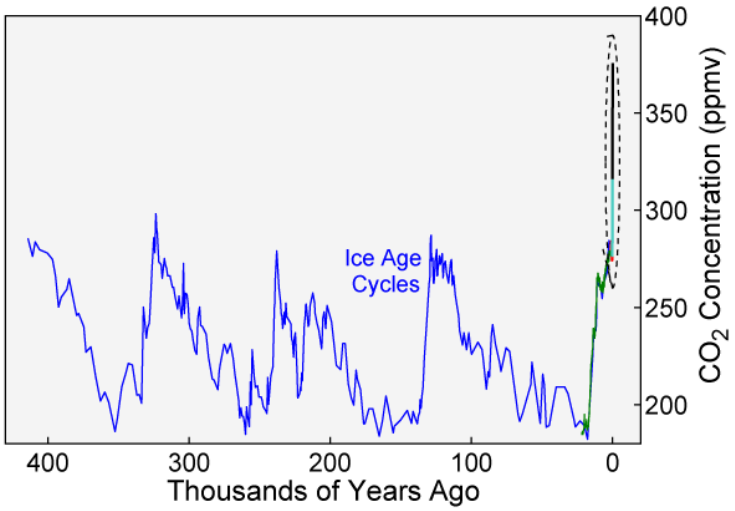

(a) Prehistoric times (Webpage: Atmospheric CO2 Concentrations over Thousands of Years)

Figure 1.1. CO2 concentration in the air with time.

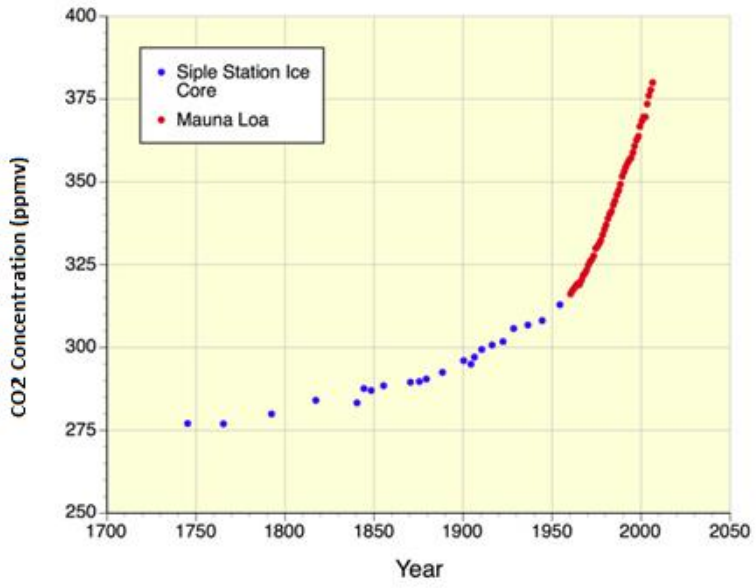

(b) Since the industrial revolution (Webpage: Atmospheric Concentration of CO2 with Time)

Figure 1.1. CO2 concentration in the air with time (Cont'd).

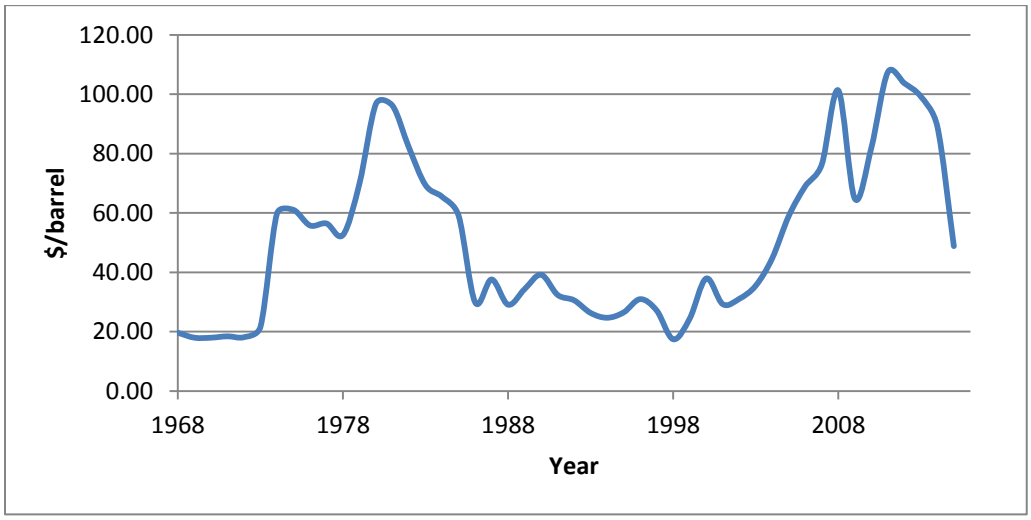

Figure 1.2. Crude oil prices with time (Webpage: EIA: Real Prices Viewer)

The flow of solar radiation into the earth's upper-atmosphere is approximately 174,000 TW, of which, 114,000 TW reaches the Earth's surface (Szargut, 2005). That radiation can be converted directly to electricity using photovoltaic devices or converted to biofuels using autotrophic organisms. Solar radiation is absorbed by autotrophs and transformed into biomass (chemical exergy) at a rate of 37 TW, a large amount relative to the total exergy used by humans, which is estimated to be 13-14 TW (Barber, 2009; Szargut, 2005). If methods of harnessing this exergy could be improved, biofuels could potentially replace all non-renewable fuels (coal, petroleum, natural gas, peat, nuclear).

Therefore, biofuels, derived from renewable resources, can provide a domestic, carbon-neutral fuel that can eliminate CO_2 emissions and major fluctuations in cost. First generation biofuels, such as ethanol, were produced from cellulosic feedstocks, like corn; however, this led to an increase in food prices while producing a low quality fuel. Second generation biofuels were derived from waste products, such as tallow, soapstock, and used cooking oils. While these feedstocks are cheap and don't negatively impact other markets, they don't exist in sufficient quantities to satisfy a significant portion of U.S. demand (Heredia-Arroyo et al., 2010). Used cooking oils, for example, can satisfy only 1% of US oil demands (Webpage: Learn about Biodiesel). Third generation biofuels are derived from crops specifically cultivated for the sake of producing biofuels. Examples are the jatropha plant and strains of microalgae; both of which can be cultivated using land and water that is unfit for food-bearing crops. Of the two, microalgae are the more promising crop because they are the fastest growing autotrophic organism (Webpage: Algae Biofuels: An Introduction; Demirbas and Demirbas, 2011),

they can be cultivated autotrophically or heterotrophically (Heredia-Arroyo et al., 2010), and they store oil in much higher density (around 50 wt% in the most promising studies) (Tornabene et al., 1983).

The use of algae as a biofuel dates back to the Second World War. In 1941, Japan instituted an algal process for the production of diesel fuel to compensate for the major fuel shortages of the period (Morimura et al., 1955; Tamiya, 1957; Tamiya et al., 1953). Germany did likewise, but with an additional emphasis on fats (Witsch and Harder, 1953). The U.S. briefly studied using algae as a fuel source in the 1950s (Burlew, 1953), but concluded that biofuels could not compete with the low oil prices at the time. During the period of oil shocks in the 1970s and early 1980s (Figure 1.2), attention seriously turned towards investigating algae's fuel production potential, which began the Aquatic Species Program at the Solar Energy Research Institute (now National Renewable Energy Laboratory (NREL)) funded by the U.S. Department of Energy (Benneman and Oswald, 1996; Sheehan et al., 1998). The program continued for roughly two decades before the low oil prices in the late 1990's led to its discontinuation in 1996, with the final report being released in 1998 (Sheehan et al., 1998). Ten years later, elevated petroleum prices led to the revival of algae-to-biofuel research, under the umbrella of the National Alliance for the Advancement of Biofuels and Bioproducts (NAABB) (Webpage: NAABB Final Report). The framework for NAABB was set in 2010 by the National Algal Biofuels Technology Roadmap. It noted that there was a need for an integrated systems model that included detailed engineering design and process modeling. The National Academy of Sciences also issued a report outlining the challenges that lie ahead for algal oil

production in the U.S (Webpage: Sustainable Development of Algal Biofuels in the United States).

The NAABB was divided into six groups designed to study different aspects of the feasibility of an algae-to-biofuels venture within the United States, as outlined in Figure 1.3. The arrows show some examples of information flows between the different groups. For example, the harvesting group provided the extraction group with information pertaining to the concentration of the algae slurry (the input to extraction). However, the extraction group would also convey information back to the harvesting group on how well the solvents performed with different amounts of water in the slurry. To use a different example, the oil extraction groups would produce oils of varying quality, and then the upgrading group would analyze the pre-processing costs for each oil quality and report back to the extraction groups. In this way, the input and output parameters of each group were optimized. Note that the sustainability group took information from all other groups to synthesize and optimize the entire venture.

The genetic modification of algae is beyond the scope of this thesis, although some brief mention of it will be made in Chapter 4. Of the remaining five groups, four correspond to the major algae-to-biodiesel processing steps (cultivation, harvesting, lipid extraction, and lipid upgrading). It should be noted that the boundaries between these processing steps are flexible. Certain processing technologies, like supercritical transesterification (Levine et al., 2010; Patil et al., 2012; Vyas et al., 2009) and hydrothermal liquefaction (Duan and Savage, 2010), can combine the extraction

technologies into a single processing step. Supercritical extraction and transesterification (Soh et al., 2013) will be explored in Chapter 5.

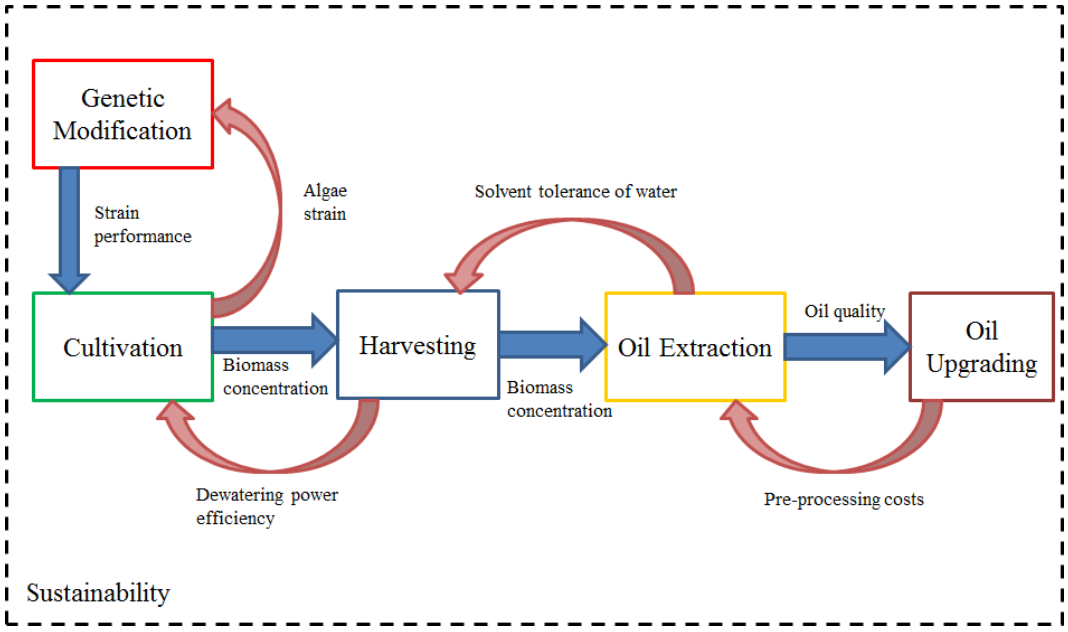

Figure 1.3. NAABB framework for studying algae-to-biofuels

A number of software packages are used throughout this thesis, predominantly among them is ASPEN PLUS because it provides good estimates of thermophysical properties, phase equilibria, chemical process vessels, and is useful for converging mass and energy balances. MS Excel was also used to handle exergy balances in Chapter 4, mass and energy balances in Chapters 3 and 5, as well as to provide initial guesses for kinetic parameters in Chapters 3 and 5. gPROMS was used as a comparison for thermophysical properties and phase equilibria in Chapter 5. COMSOL was used to determine pond depth in Chapter 2, and AIMMS was used to regress kinetic parameters

in Chapter 3. Finally, the ASPEN Process Economic Analyzer was used to generate cost estimates in Chapter 3.

Most of these software packages have been employed in previous studies. For example, numerous studies have examined the economic feasibility of algae-to-biofuels (Davis et al., 2011; Gebreslassie et al., 2013; Martin and Grossmann, 2012; Richardson et al., 2012; Sun et al., 2011), but the previous studies have all used an assumed algae growth rate and based their modeling on older processing methods that existed before NAABB.

To obtain improved designs, this thesis begins with a calculation of the algae growth area using a rigorous thermodynamic energy balance in Chapter 2, which assumes that sunlight is the major limiting factor to algae growth and oil generation (Dunlop et al., 2013), yielding an upper-bound on algae growth potential. Pond depth is also briefly analyzed in this study to fully specify the algae ponds. However, Chapter 2 is limited by assumed values for several key parameters, with the most important being the photosynthetic efficiency. Chapter 3 takes the information from Chapter 2 and combines it with newly developed NAABB technologies for harvesting and extraction (Webpage: NAABB Final Report) as well as kinetic information for algae-oil transesterification reactions and information from a functioning industrial pilot-plant to create a techno-economic model for the entire venture. Chapter 4 examines the previously established definitions of photosynthetic efficiency (Bisio and Bisio, 1998; Bolton and Hall, 1991; Lems et al., 2010; Petela, 2008) and synthesizes them into a transparent definition that can be easily adjusted to account for various cultivation factors. Finally, Chapter 5

explores the use of supercritical CO_2 to extract and convert the algae oil. This is a novel process for the most poorly understood step in the algae-to-biodiesel venture. This method has been studied for use with vegetable oils (Glisic and Orlovic, 2014; Macaira et al., 2014), but previous studies used overly-simplistic equations-of-state that do not accurately capture much of the phase behavior of this complex system. Overall, this thesis aims to examine key areas in the algae-to-biodiesel process and create higher fidelity models that address the most pressing issues using a systems methodology.

Next, brief introductions to these areas are presented, with new models introduced in this research described in the chapters that follow.

1.1 Thermophysical Properties of Algal Cultivation

The lack of an exhaustive properties database for biological materials has severely hampered attempts to develop models of algal growth and oil production. Similarly, the absence of reliable thermodynamics and kinetic rate constants has been problematic (Anitescu and Bruno, 2012; Cheng and Ogden, 2011; Wooley and Putsche, 1996). Furthermore, the absence of a generally accepted flowsheet for biofuel production means that detailed simulation of the wrong approach is a real possibility. Thus, any model of algal biofuels using computer-aided process design must overcome these limitations.

Chapter 1 introduces an energy-limited model of algal biofuel production using the aspenONE® V7.3 software suite, with emphasis on Aspen Plus® 7.3 (Dunlop et al., 2013). This model was developed initially by Dunlop (Dunlop et al., 2013) and further clarified in this thesis research. The model uses an integrated systems approach that

offers solutions to some of the intractable problems in simulating light-driven biological processes in chemical engineering process design. Thermodynamic properties, particularly enthalpy and free energy, are identified. The construction of the flowsheet is discussed in terms of key issues for modeling an algae-to-biofuels process. The concept of energy-limited algal growth and its implications for reactor design are then considered, and it was found that this concept obviates the need for detailed chemical kinetics schemes. Most importantly, it sets the upper limit for conversion efficiency and energetics. Selected results relating to the mass and energy balances obtained from the modeling are examined with respect to water use, carbon flow, and lost work, demonstrating how the energy-limited model offers significant advantages, not only in terms of process design, but also for meeting the criteria for the commercial-scale production of advanced algal biofuels.

1.2. An Overall Systems Analysis of Biodiesel Production Processes

Over the previous decade, numerous studies have been published attempting to provide models (Davis et al., 2011; Sun et al., 2011) and cost estimates (Richardson et al., 2012) for algae-to-biodiesel ventures. In addition, there have been a number of alternatives for the four major processing steps (Webpage: Algae Industry Magazine – NAABB Chooses Harvesting and Extraction Technologies; Webpage: Green Car Congress – NAABB selects Los Alamos ultrasonic algae harvester for Phase II development; Webpage: NAABB Final Report; Webpage: SRS Energy, Algae Fractionation). However, all studies are either bench-scale, focusing exclusively upon

their own processing technology with no consideration for how it relates to the overall framework (Iqbal and Theegala, 2013; Patil et al., 2012), or they focus upon some interesting modeling aspect, but neglect rigor and fail to consider promising alternatives (Gebreslassie et al., 2013; Martin and Grossmann, 2012; Richardson et al., 2012).

In contrast, this chapter rigorously evaluates alternative pathways to cost-effective production of biofuels at a commercial scale. The thermodynamic cultivation model from Chapter 2 is used to predict the area required for algae growth. This ASPEN PLUS model was combined with the most promising commercial-scale methods to harvest algae and extract the oil. Conversion experiments were conducted using oil extracted from *Nannochloropsis salina* algae, which was grown in salt water by Solix Biofuels. Glycerolysis was performed to reduce the free fatty-acid content of the oils. Transesterification was then carried out using a solid catalyst. Rate constants were regressed to adapt kinetic models to the rate data, which allowed the glycerolysis/transesterification process to be simulated using ASPEN PLUS V7.3.1.

Cost estimates from the Aspen Process Economic Analyzer (APEA) were combined with industrial quotes and literature data. A cash flow analysis was performed for the entire carbon sequestration-to-biodiesel production train, yielding a biodiesel selling price of $4.34/gal. Finally, a sensitivity analysis was performed to examine the impact of various costing parameters on the viability of the process. These analyses show that the current bottlenecks for the large-scale production of biodiesel are cultivation techniques and extraction operations.

1.3. Exergy Analysis of Photosynthesis

Chapter 2 identified photosynthetic efficiency as one of the key variables that defined the algae cultivation area (Dunlop et al., 2013), which in turn determines the economic feasibility of the process (Silva et al., 2014). The relationship between photosynthetic efficiency and feasibility is crucial for all biosynthetic processes since almost all exergy contained in biomass originates from solar radiation. Therefore, a high photosynthetic efficiency is the gateway to sustainable bioprocess development. The literature shows a wide range of efficiency predictions, 2.6% to 41%, due to different definitions and methods of analysis. Consequently, the objective of Chapter 4 is to dissect the complex bio-processes involved in photosynthesis and study the exergy flows through the system, portraying photosynthesis in a way that is easily understood by researchers analyzing sunlight driven bioprocesses.

Exergy balances were formulated for a number of photosynthetic subprocesses that convert sunlight, carbon dioxide, and water into glucose – glucose was chosen over triglycerides as the standard product for the sake of comparison with previous studies. Note that the major inefficiency in organic carbon synthesis is the sequestration and initial transformation of CO_2 using sunlight (Silva et al., 2015). Lipid and sugar biosynthesis (Webpage: Glyceraldehyde Dehydration; Webpage: Lipid Biosynthesis; Webpage: Triglyceride Synthesis) have high efficiencies (Silva et al., 2015), implying that triglycerides could have been synthesized without a substantial drop in efficiency.

The bioprocesses for which the exergy balances were formulated include the initial absorption of light, the flow of excited, high-energy electrons through

photosystems II and I, and the dark reactions. In addition, exergy losses to transpiration, cellular metabolism, sunlight reflection, and photorespiration are taken into account, although their effects are relatively small. The overall exergy efficiency of photosynthesis is calculated to be 3.9 percent, which is comparable to the assumed efficiency in Chapter 2.

Note that the photosynthetic mechanism in Chapter 4 justifies the key specification of 3.9 percent photosynthesis efficiency, but for readers concerned principally with the design of large-scale algae to biodiesel processes, these details can be bypassed before studying phase equilibria of the transesterification reactions in Chapter 5.

1.4. Phase Equilibria of Transesterification Reactions

This chapter is concerned with the phase equilibria and conversion of algal-oils to biodiesel at supercritical conditions. The use of supercritical CO_2 is explored because it allows the extraction and conversion to be carried out in a single step (Glisic and Orlovic, 2014; Macaira et al., 2014; Soh et al., 2013; Soh and Zimmerman, 2011, 2015), reactions occur at mild temperatures (Soh and Zimmerman, 2011), and it eliminates the need for preprocessing and purifying the algae-oil or biodiesel product (Silva et al., 2014).

Previous studies that modeled the phase behavior of algae-oil systems used crude models (Redlich-Kwong in ASPEN PLUS without binary interaction parameters (Anikeev et al., 2012; Glisic and Orlovic, 2014; Macaira et al., 2014)), which are not suitable in the critical region or with large, asymmetric molecules.

Although there is still more work needed on this subject (discussed in Chapter 6), Chapter 5 sets a solid thermodynamic foundation that can be used in future studies to obtain better estimates for the reactor conversion rates, separation efficiencies, and vessel sizes, which will all lead to more accurate profitability analyses. In addition, Chapter 5 explores the phase interactions of CO_2, water, and triglyceride, which are crucial to understanding the extraction of algae-oil from wet biomass, which was identified as a key area of research in Chapter 3.

PC-SAFT in ASPEN PLUS and SAFT-γ Mie in gPROMS were used to provide higher-accuracy estimates for the phase equilibria of these systems. Pure-component density and liquid vapor-pressure data were used to regress the necessary pure-component parameters for both variants of the SAFT equations. Experimental vapor-liquid and liquid-liquid equilibrium data were taken to supplement the data available in the literature for the regression of binary interaction parameters. Finally, a thermo-kinetic reactor model was developed to analyze the system's phase equilibria under reacting conditions, and give preliminary estimates for reactor conversions.

1.5. Nomenclature

Acronym	Term
APEA	ASPEN Process Economic Analyzer
GHGE	Green House Gas Emissions
NAABB	National Alliance for the Advance of Biofuels and Bioproducts
NREL	National Renewable Energy Laboratory

CHAPTER 2

An Energy-limited Model of Algal Biofuel Production

2.1. Introduction

This chapter is based upon a novel simulation method developed by Eric Dunlop of Pan Pacific Technologies (Dunlop et al., 2013). In addition to the biochemical model developed by Dunlop, more specifics to clarify and refine this approach, especially the ASPEN convergence algorithm (Section 2.3.2), were developed and are provided herein. Besides this initial paragraph, the text in this chapter was taken from a previously published study (Dunlop et al., 2013) and modified to fit the format of this thesis.

This chapter concentrates on the light driven synthesis of triglycerides, which are converted to biodiesel through transesterification. The source of carbon dioxide is not important in this analysis, although a cement works source was used, as the model was originally designed to study a case in Queensland, Australia. Likewise, while the details of the transesterification process are important, and are the subject of numerous other studies (Chang and Liu, 2009; Pokoo-Aikins et al., 2010; Vyas et al., 2009; Zhang et al., 2003a, b), an elementary model (not using detailed chemical kinetics) is sufficient for this analysis. Note that other lipid conversion processes (e.g., hydro-treating to produce green diesel) could have been substituted for the biodiesel process in this model without major changes to the results.

The overall envelope for this chapter has inputs: sea water, flue gas containing carbon dioxide, urea as a nitrogen source, and sodium hydroxide as a carbon dioxide absorber and outputs: biodiesel (methyl-oleate), evaporated water, and blowdown from

the reactors. The model takes as fixed 10^5 tonne/yr of carbon dioxide, an average solar input of 5.7 kWh/(m^2day), an average evaporation rate of 3.5 m^3/(hc-hr), and a photosynthetic efficiency of 4%. Variables not fixed, but which arise in the model, include pond size, cell concentration in the ponds, cell growth rate, oil content of the cells, and the number of times the cells divide (generation number). After running Aspen Plus to solve the model equations, it remains to select the endogenous metabolism extent and pond depth. Stated differently, the model is limited in that it focuses on the energetics of the reaction ponds and a hypothetical steady-state using annual averages.

It should be noted that the process, reactions, pseudo-species (including their thermodynamic properties), were developed by Eric Dunlop of Pan Pacific Technologies — with the main technical contribution herein being the elucidation of the solution mechanisms used by Aspen Plus (Section 2.3.2) to determine the pond area and accompanying quantities.

2.2. Development of the Key Modeling Components

Initial work began with the simplest model to enable key components to be established and the basic design concept to be constructed. For example, biodiesel was characterized as methyl-oleate ($C_{19}H_{26}O_2$) and the algae empirical formulae set as $C_{50}H_{50}O_{30}N_7$ with no sulfur or phosphorous. During the second phase of development, greater complexity in inputs was introduced. Biodiesel, for example, was now formed by reacting nine TAG to produce nine methyl esters, while the algae empirical formulae for *Nannochloropsis salina*, a common species used in algae biofuel studies, became $CH_{1.80}O_{0.40}N_{0.083}S_{0.0017}P_{0.002}$.

2.2.1. Identifying the Key Components

Many databases for engineering design simulation have been primarily developed for the petroleum and heavy chemical processing industries. Consequently, many physical properties of the compounds needed for process design involving algae are not in conventional databases, are obscure bioproducts which have been poorly characterized, or do not exist. The compounds needed for this simulation fell into five categories. First, compounds already in a database, such as methanol, CO_2, O_2, N_2, urea, NH_3, water, and methyl-oleate (biodiesel). Second, compounds that can be substituted; in particular, "Soluble Carbon/Organics" (SOLC), which can be substituted with glucose. Third, compounds that do not exist and thus need to be "invented". Algae itself falls into this category, as does algal debris, and the range of oil-bearing cells of variable composition. In this context, the term "debris" refers to spent cells that are recycled or sent for conversion into animal feed. For the purposes of this simulation, debris is assumed to have the same chemical formula as algae and the same energy if used for animal feed. If debris is recycled, the debris degradation needs to be acknowledged in some way, but no figures are currently available. As an assumption, debris is considered to have only 80 percent of the heat of combustion of algae and heats of formation are calculated on this basis.

The fourth category involves defining the Algal Oil (triacyl-glyceride or TAG). Algae naturally produce a range of TAGs; they are too numerous and unpredictable to be useful in models of this type. It is, however, necessary to have physical properties that are as accurate as can realistically be obtained. It was therefore decided to use C_{18} carbon

chains as the standard, and to use triolein as the reference TAG, as it is a component in the Aspen database. The choice of triolein as the TAG automatically leads to methyl-oleate as the biodiesel produced.

Finally, compounds of convenience are required. They are identical to the base algae to which they are always subsequently converted in an energy-less reaction. Examples are the sub-species AlgNew (algae newly synthesized in the reaction operation; i.e., not recycled or otherwise re-used), AlgDeb (algae regenerated from recycled debris or smashed/lysed cells) and AlgGly (algae synthesized from glycerol). These subspecies are identical to "Algae" in every respect and have the same formulae, enthalpy of formation, and physical properties. The distinction is purely for internal "book-keeping" purposes to track where parts of the total biomass came from and to where they disappeared. A final reaction operation converts all these subspecies into "Algae". This is referred to as "normalization". It can be ignored if desired, but is internally useful during the early stages of model development.

2.2.2. Development of Assumptions

One of the early difficulties in the modeling of algal biofuel production is deciding how to deal with the range of triglycerides made by algae. While more than 100 triglycerides are known, their physical properties are not usually available. In model development, this was approached in two stages. First, in Stage One, a single representative triglyceride, triolein, was chosen due to its properties being readily available. It forms methyl-oleate to be used as biodiesel and its properties were also readily available. This greatly simplified the development of the model and allowed

attention to be focused on key issues. Consequently, this model is used in subsequent discussions when focusing on broad principles rather than detailed engineering. For example, an algae empirical form was chosen that did not contain sulfur or phosphorous. While sulfur and phosphorous are very important biologically, they contribute only in a minor way to the mass and energy balances. Table 2.1 contains a summary of the properties assumed. Note the components OC5, OC35, and OC70 are defined shortly.

Table 2.1. Components and Their Properties for Stage One Analysis

	Formula	ΔH_f (kJ/mol)	ΔS_f (kJ/mol-K)	ΔG_f (kJ/mol)	MW
Algae	$C_{50}H_{50}O_{30}N_7$	−2,949	−7.30	−773	1228.98
OC5	$C_{68}H_{71}O_{39}N_9$	−3,939	−9.80	−1,016	1638.35
OC35	$C_{58}H_{76}O_{24}N_5$	−2,982	−7.66	−697	1227.26
OC70	$C_{55}H_{88}O_{13}N_2$	−2,424	−6.45	−500	985.31
TAG	$C_{57}H_{104}O_6$	−2,202	−6.03	−404	885.45

In Stage Two, these simplifications were removed and a real algae, *Nannochloropsis salina*, which has an empirical formula of $CH_{1.80}O_{0.40}N_{0.083}S_{0.0017}P_{0.002}$, was selected. A range of nine triglycerides were then established as important, because not all algae processing is directed to biofuels (Table 2.2). Some is geared towards pharmaceuticals, and higher numbered triglycerides in the C_{63} to C_{69} range are known to have medicinal applications (Barclay et al., 2005). They exist in smaller quantities but merit inclusion for the non-fuel applications of the model. The single triacyl-glyceride (TAG), triolein, is now replaced by the composite triglyceride TAG9, which refers to a weight-average composite of the nine triglycerides used. Once nine triglycerides are incorporated into the model, nine methyl esters automatically follow.

Table 2.2. Components and Their Properties for Stage Two Analysis

Algae Empirical Formula: *Nannochloropsis salina* $CH_{1.90}O_{0.40}N_{0.083}S_{0.0017}P_{0.002}$				
Triglycerides (TAG)				
$C_{45}H_{86}O_6$		Trimyristin		
$C_{51}H_{98}O_6$		Tripalmitin		
$C_{51}H_{92}O_6$		Tripalmitolein		
$C_{57}H_{110}O_6$		Tristearin		
$C_{57}H_{104}O_6$		Triolein		
$C_{57}H_{98}O_6$		Trilinolein		
$C_{63}H_{122}O_6$		Triarachine		
$C_{63}H_{92}O_6$		Trieicosapentanate		
$C_{69}H_{128}O_6$		Trierucin		
$C_{63.830}H_{116.2086}O_{7.263}$		TAG9		
Methyl Esters				
$C_{15}H_{30}O_2$	C14:0	Methyl myristate	2%	wt%
$C_{17}H_{34}O_2$	C16:0	Methyl palmitate	36.5%	wt%
$C_{17}H_{32}O_2$	C16:1	Methyl palmitoleate	37.5%	wt%
$C_{19}H_{38}O_2$	C18:0	Methyl stearate	2%	wt%
$C_{19}H_{36}O_2$	C18:1n9	Methyl oleate	9%	wt%
$C_{19}H_{34}O_2$	C18:2n6	Methyl linoleate	3%	wt%
$C_{21}H_{34}O_2$	C20:4n6	Methyl arachidonate	2%	wt%
$C_{21}H_{32}O_2$	C20:5n3	Methyl eicosapentanate	7%	wt%
$C_{23}H_{44}O_2$	C22:1	Methyl erucinatem	1%	wt%
Oil Bearing Cells				
OC5	$C_{47.1619}H_{89.3726}O_{17.9517}N_{3.6496}S_{0.0748}P_{0.0879}$			
OC35	$C_{52.4180}H_{97.9490}O_{14.5756}N_{2.4971}S_{0.0511}P_{0.0602}$			
OC70	$C_{58.5501}H_{107.9549}O_{10.6368}N_{1.1525}S_{0.02368}P_{0.0278}$			

Another difficulty in developing an algal biofuels process model is the terminology, "algae", with or without oils. All species of cells, including algae, need a baseline quantity of triglyceride oils for structure and function. Algae over-accumulate these oils, which is the basis for this process. Because it was not possible to obtain data that dealt reliably with this issue, an explicit objective of the model has been to remove as much ambiguity as possible. Thus, "algae" refers to cells that contain only the base level of oil with no extra accumulation, while "oil-bearing cells" are defined as OC5, OC35 and OC70 containing, respectively, 5, 35 and 70 wt% of triglyceride oil. OC70, for example, was defined to have the arithmetic sum of 30 wt% of the heats of combustion of

algae (19.44 MJ/kg) and 70 wt% of the triacyl-glyceride (39.66 MJ/kg). Cells of any arbitrary composition can be similarly defined by mixing molar quantities.

To reduce confusion and permit analysis of the process, the model is explicitly developed in two separate stages: the first reaction operation, in which cells grow without making oil, and the second reaction operation, in which there is no new cell growth, but oil accumulates. In actual operation these two stages may occur in one reactor, but the benefits of two reaction operation models are becoming apparent (Sánchez et al., 2011).

2.2.3. Defining the Thermodynamic Properties of the Key Components

The heats of formation are fundamental to calculate the heats of reaction and are rarely known for biological substances. The latter can be used as a starting point to arrive at reasonable approximations for the enthalpy of combustion, but even these are often ambiguous. The best available data appears to be that of Larsson on Baker's yeast (*Saccharomyces cerevisiae*) (1999), who also provides entropy data. These were used to estimate the thermodynamic properties in Figure 2.1. Larsson's data give 19.44 MJ/kg for the enthalpy of combustion, and -150 J/mol/K for the entropy, based on a molecular weight of 25.229. Our molecular weight is larger, at 1,208.976. This allows a conversion of the Larsson data to -23,900 MJ/kmol for the enthalpy of combustion and -7.036 MJ/kmol/K for the entropy. It is clear that this area requires further, careful work for the future development of biofuels.

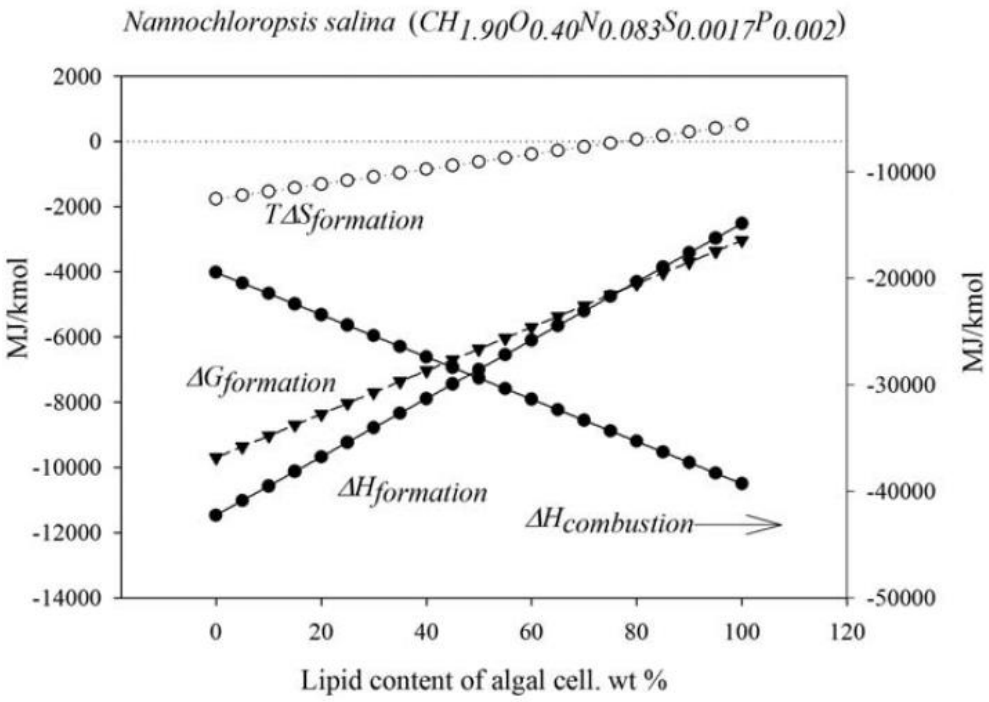

Figure 2.1. Thermodynamics of algal cells with oil at 25°C.

The enthalpy and free energy of formation of the required compounds were then calculated from the reverse of the combustion reaction with the equations for the formation of water, carbon dioxide, SO_2, and P_3O_4, summed according to the first law of thermodynamics. They are reported in later sections.

2.2.4. Main Reactions and their Enthalpy Changes

Having obtained the required thermodynamic properties, some non-integer reaction stoichiometry is needed to provide the remaining information. To calculate the heats of reaction, the heats of formation of each compound are required from within the simulation database or the NIST database. Documenting the source of the data is helpful as conflicting data occur occasionally. Thermodynamic data for some compounds are not

available in these databases, either because the compounds are contrived in the modeling process, as in the case of algae or OC5 discussed above, or because their importance has only so recently been recognized that they have not yet been incorporated, as with, for example, some of the higher triglycerides.

In view of non-integer stoichiometric coefficients, balancing the equations can be difficult. To facilitate this process, a small matrix-based stoichiometry generator was developed. In the early stages of model development, when only carbon, hydrogen, oxygen and nitrogen were used, a 4 × 4 matrix was developed which, after inversion, yielded stoichiometric coefficients. When sulfur and phosphorous were added, a 6 × 6 matrix was created, but the matrix can be adjusted for any degree of complexity, as shown in Table 2.3. In this table, *A* is the atom matrix, with the rows and columns representing the atoms and the chemical components. The weight percents of C, H, and O are shown in the desired product, TAG9, vector. Then, the stoichiometric coefficients, *a*, *b*, ..., *f*, in the reaction are in the *X* vector, which is computed by mass balance, $X = A^{-1}B$. The resulting reaction, in which negative stoichiometric coefficients denote reactants and positive ones denote products, is shown at the bottom of Table 2.3.

Table 2.3. Calculations using the Matrix Stoichiometry Generator

Example:
a OC70 +b Debris +c O_2 +d H_20 +e SO_4^{2-}+f HPO_4^{2-} → TAG9

INPUT MATRIX [*A*]
Raw materials

	OC70	Debris	O_2	H_2O	SO_4^{2-}	HPO_4^{2-}
C	58.5501	1	0	0	0	0
H	107.955	1.9	0	2	0	1
O	10.6368	0.4	2	1	4	4
N	1.1525	0.083	0	0	0	0
S	0.02368	0.0017	0	0	1	0
P	0.02780	0.002	0	0	0	1
	a	b	c	d	e	f

RESULT VECTOR [*B*]
Desired product

TAG9
63.83
116.21
7.263
0
0
0

INVERSE MATRIX $[A]^{-1}$

0.022389	1.51E-21	0	-0.269	0	3.5-17
-0.31089	1.01E-17	0	15.793	0	-2.1E-15
0.399691	-0.25	0.5	-1.420	-2	-1.75
-0.91317	0.5	0	-0.432	0	-0.50
-1.7E-06	-3.8E-19	0	-0.020	1	4.3E-19
-6.5E-07	-1.6E-19	0	-0.024	0	1

SOLUTION VECTOR [*X*]
Stoichiometric coefficients

1.429097	a OC70
-19.84379	b Debris
0.091596	c O_2
-0.183107	d H_2O
-0.00011	e SO_4^{--}
-4.13E-05	f HPO_4^{--}

$[A][X]=[B]$ or $[X]=[A]^{-1}[B]$

A positive coefficient in the solution vector denotes a reactant, while a negative coefficient denotes a product.

Thus the balanced equation for this example is :-

1.429097 OC70 +0.091596 O_2 → TAG9 + 19.84379 Debris +0.183107 H_2O+0.00011 SO_4^{2-}+4.13E-05 HPO_4^{2-}

Clearly, it is impractical, and likely impossible, to analyze a reaction system having large numbers of chemical reactions involving thousands of chemical components. Instead, a set of overall (or lumped) reactions, which represent the conversion of CO_2 to algae and algae to triglycerides, are defined The enthalpies and free energies of reaction are estimated as shown in Table 2.4 and tabulated for all reactions in Table 2.5. As mentioned previously, it is convenient to group reactions (1-3) that involve cell growth without oil generation into reaction operation 1; and reactions (6-11) that accumulate oil without new cell growth in reaction operation 2. Reactions 4 and 5

(equivalent to 12 and 13) represent the cell's "endogenous metabolism." In reaction 4 (12), algae break down to CO_2, releasing energy for metabolism, while in reaction 5 (13), algae yield non-useful "soluble carbon," which is modelled as glucose herein. Finally, the lysis reactions (14-16) break down the oil cells, releasing TAG and algae debris. These assumptions should be reasonable to estimate the energy requirements of the cultivation system.

Table 2.4. Example of Calculating Heats of Reaction for Each Reaction Operation

	Reactants						Products					
	n	H_f (kJ/mol)	nH_f (kJ/mol)	S_f (kJ/mol-K)	TS_f (kJ/mol)	nG_f (kJ/mol)	n	H_f (kJ/mol)	nH_f (kJ/mol)	S_f (kJ/mol-K)	TS_f (kJ/mol)	nG_f (kJ/mol)
Reaction 1						46.5 HCO_3^- + 18 H_2O + 3.5 Urea → AlgNew + 42.25 O_2 + 46.5 OH^-						
CO_2	46.5	−393.80	−18,312	0.003	1	−18,352	AlgNew	1.00	−2,949	−7.30	−2,175	−774
Water	18	−286.01	−5,148	−0.163	−489	−4,273	O_2	42.25	0	0.21	61.13	−2,583
Urea	3.5	−333.00	−1,165	−0.522	−156	−621						
Sum Reactants			−24,626			−23,245	Sum Products		−2,949			−3,357
Heat of Reaction = ΣProducts − ΣReactants				ΔH	21,677	kJ/mol overall reaction			Endothermic			
				ΔG	19,889	kJ/mol overall reaction			Unfavorable			
Reaction 6						Algae + 31.2 HCO_3^- + 28.2 H_2O → 1.4 OC35 + 43.5 O_2 + 31.2 OH^-						
CO_2	31.2	−394	−12,287	0.003	1	−12,313	OC35	1.4	−2,982	−4,175	−7.664	−2,284	−978
Algae	1	−2,949	−2,949	−8.758	−2610	−339	O_2	43.5	0	0	61.135	18,218	−2,659
Water	28.2	−2,861	−8,065	−0.613	−49	−6,694							
Sum Reactants			−23,301			−19,347	Sum Products				−4.175		−3,637
Heat of Reaction = ΣProducts − ΣReactants				ΔH	19,126	kJ/mol overall reaction			Endothermic			
				ΔG	15,710	kJ/mol overall reaction			Unfavorable			

Table 2.5. Reactions with Corresponding Heats of Reaction

Reaction Number		ΔH kJ/mol of reaction	ΔG kJ/mol of reaction
Reaction Operation 1			
1	$46.5\,HCO_3^- + 18\,H_2O + 3.5\,Urea \rightarrow AlgNew + 42.25\,O_2 + 46.5\,OH^-$	21,676	19,889
2	$3.5Urea + 15.5\ Glycerol + 12\,O_2 \rightarrow AlgGly + 44\ H_2O$	−3,888	−6,682
3	$Debris \rightarrow AlgDeb$	4,778	4,344
4	$AlgNew + 42.25\,O_2 \rightarrow 46.5\,CO_2 + 3.5\,Urea + 18\,H_2O$	−21,676	−21,264
5	$3AlgNew + 75\,H_2O \rightarrow 10.5\,N_2 + 7.5\,O_2 + 5\,SOLC$	−1,148	−3,600
Reaction Operation 2			
6	$Algae + 31.2\,HCO_3^- + 28.2\,H_2O \rightarrow 1.4\,OC35 + 43.5\,O_2 + 31.2\,OH-$	19,126	15,710
7	$142.5\,HCO_3^- + Algae + 129\,H_2O \rightarrow 3.5\,OC70 + 199.25\,O_2 + 142.5\,OH-$	24,993	19,042
8	$Algae + 10.4\,Glycerol \rightarrow 1.4\,OC35 + 7.1\,O_2 + 13.4\,H_2O$	1,973	1,209
9	$Algae + 47.5\,Glycerol \rightarrow 3.5\,OC70 + 33\,O_2 + 61\,H_2O$	9,132	5,487
10	$1.2857142857\,Algae + 3.7142857143\,HCO_3^- + 3.3571428571\,H_2O \rightarrow 1\,OC5 + 5.1785714286\,O_2 + 3.7142857143\,OH^-$	2,276	1,740
11	$1.2857142857\ Algae + 1.238095238\ Glycerol \rightarrow 1\ OC5 + 0.845238095\ O_2 + 1.595238095\ H_2O$	234	146
12	$Algnew + 42.25\,O_2 \rightarrow 46.5\,CO_2 + 3.5\,Urea + 18\ H_2O$ (duplicate of Reaction 4)	−21,676	−21,264
13	$3\,Algnew + 75\ H_2O \rightarrow 10.5\,N_2 + 7.5\,O_2 + 25\ SOLC$ (duplicate of Reaction 5)	−1,148	−3,600
Lysis Operation			
14	$OC35 + 0.187970\,H_2O \rightarrow 0.714286\,Debris + 0.206767\,O_2 + 0.390977\,TAG$	−3,344	−3,083
15	$1.4\,OC70 + 0.4\,H_2O \rightarrow 0.4\,Debris + 0.3\,O_2 + TAG$	−1,899	−1,768
16	$OC5 + 0.031328\,H_2O \rightarrow 1.285714\,Debris + 0.31328\,O_2 + 0.065163\,TAG$	−6,131	−4,963

Returning to the stoichiometric matrix in Table 2.3, for each reaction in Table 2.5, just two compounds are needed: (1) the reactant, usually HCO_3^- or algae; and (2) the desired product, typically algae (reactions 1 and 2) or an oil-containing cell (reactions 6-11). The remaining compounds are those that appear in each reaction: CO_2, H_2O, O_2, N_2, and urea. The signs of the stoichiometric coefficients in the solution vector identify reactants (negative) and products (positive).

2.3. Modeling the Process of Algal Biofuel Production

The use of process simulators, and aspenOne in particular, for bioprocesses has been proposed in the past, but has met with difficulties (Bhattacharya et al., 1986; Evans, 1988). Since then, a number of Aspen Plus models have appeared for cellulosic ethanol (Evans, 1988; Galbe and Zacchi, 1992; Wooley et al., 2008) and, more recently, for algal biofuels building on these and similar models,(Davis et al., 2011; O'Grady and Morgan, 2011) but each presupposes a process flowsheet.

This section presents a strategy for creating models when designing processes to cultivate algae, extract TAG, and convert TAG to biodiesel. Three levels of modeling are introduced briefly in the subsections below. The first, a heuristic model, has been used for techno-economic analyses in the early stages of process design and is demonstrated here.

i. Heuristic model (to be used in the *Discovery* mode): This is intended to permit the examination of process alternatives (real and imaginary) to discover the necessary components for a process to conform to the strict limitations of experimentally measured photosynthetic efficiencies, subject to conventional mass and energy balances. It is intended to provide maximum flexibility in design, permitting streams to be introduced as needed, recycled if necessary or desired, and generally used to identify the areas in which effective operation may occur. Overall reactions are modeled to provide sound estimates of the energy requirements, while yielding key estimates for capital cost estimation – especially the cultivation pond area, pipe lengths, and pump sizes. Note that equipment items, such as pipes and pumps, are included only when energy and installation costs are estimated to be significant.

ii. Steady-state process model: Here, separate reaction operations in the discovery stage, principally for stoichiometric calculations of heats and free energies of reaction, are combined to model tubular or stirred-tank reactors using chemical kinetics equations with rate constants and rates of conversion. Also, missing unit operations are added to provide better estimates of operating and capital costs.

iii. Time-dependent reactor model: To accurately represent the light intensity to grow algae, dynamic modeling of the sunlight intensity over 365 days of the year is

needed, as sunlight is obviously not at steady-state, either throughout the day or throughout the year. A dynamic model is under construction using Aspen Dynamics®. It is also possible to address the non-steady-state nature of sunlight using the steady-state model over separate, discrete time intervals, an approach which, so far, has proven to be adequate to modeling needs.

2.3.1. Process Block Diagram

The process model was initiated with a generalized process block flow diagram (Figure 2.2), followed by a process simulation flowsheet. The construction of the simulation flowsheet involved setting up the Calculator Blocks in Aspen Plus that are required to solve for the unknowns, and to collect and analyze data. The unknowns include the physical construction of the reactor (i.e., surface area), and the modeling of solar energy and light limitation, evaporation, and CO_2 absorption. Including these variables in the simulation provides a more accurate picture of the expected algal growth.

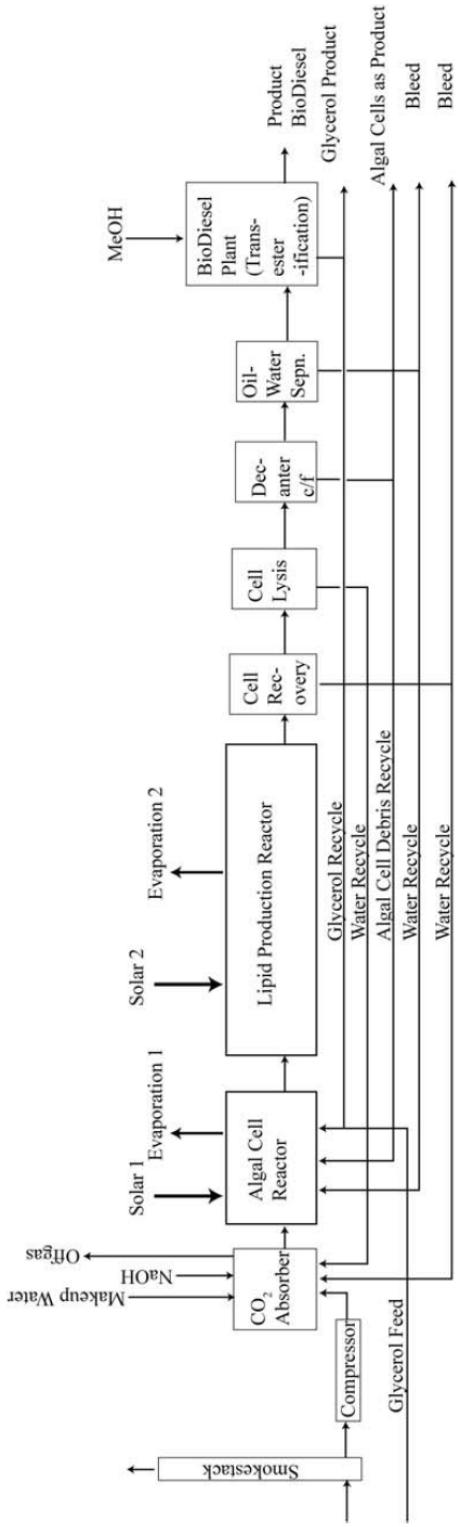

Figure 2.2. Generalized process block flow diagram.

There are several key process operations in Figure 2.2. First, a smokestack is modeled as a source of CO_2, and the CO_2 is absorbed in water, and not bubbled into the following two reaction operations. The first reaction operation models just algae growth, and a separate reaction operation models lipid production. Note that it was helpful to have these last three operations totally independent, although all three operations could be carried out in a single equipment item. At this stage of process development, the type of reactor is not specified; i.e., raceways or glass tubes (e.g., photo-bioreactors). It was also deemed advisable to retain maximum flexibility in the modeling process by having recycle streams available to suit different design concepts. Water, biomass, and glycerol may or may not be recycled, according to different needs (O'Grady and Morgan, 2011). An additional possibility was created to bring in glycerol that has originated outside of the defined flowsheet, as the additional glycerol can be viewed as a supplemental carbon source. This may be helpful when there is an excess availability of glycerol from other processes. Also, bleed streams are provided to purge inert species; e.g., buildup of salt as evaporation occurs.

2.3.2. Construction of the Process Simulation Flowsheet

The main technical contribution in this thesis to this work is contained in this section; specifically the development of Figure 2.4 and its accompanying explanation.

When constructing the process simulation flowsheet, the following considerations are important. The absorber is modeled as rate-based, which is more accurate than equilibrium-staged, and allows the absorption rate constants to be adjusted to reflect

mass-transfer performance. Also, accurate species diagrams are needed, as shown in Figure 2.3, not just for CO_2 and water, but also for phosphate. These include the ionic species, especially the bicarbonate ion, as the industry returns to the higher pHs (9-10) used in food processing to control contamination (Cornet et al., 1998).

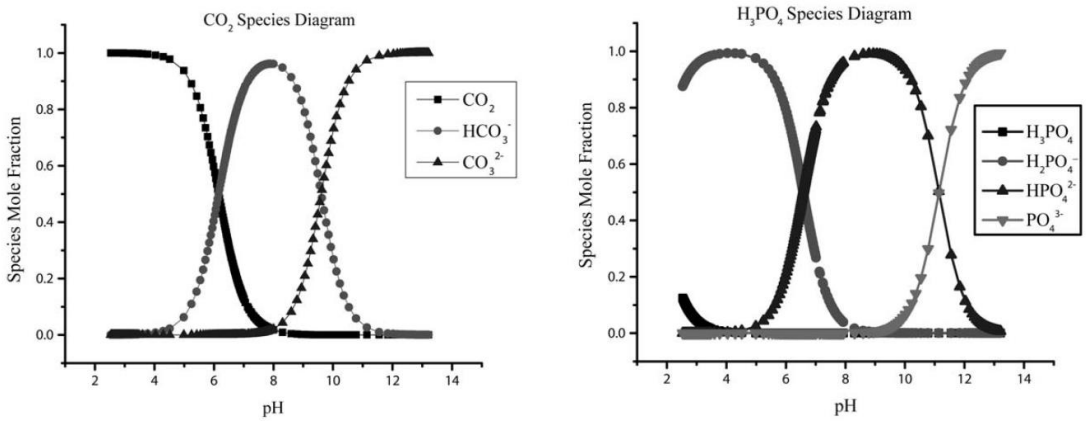

Figure 2.3. Species diagrams for the carbon dioxide and phosphate systems.

Next, as mentioned above, the cultivation section is simulated using two reaction operations, one for algal cell generation and the other for lipid production. Both use information recycle loops, as illustrated in Figure 2.4, with blocks that account for solar energy input, that estimate the conversion of the limiting reactant, the extents of reactions, and the heats of the reactions, and that account for energy losses due to the evaporation of water.

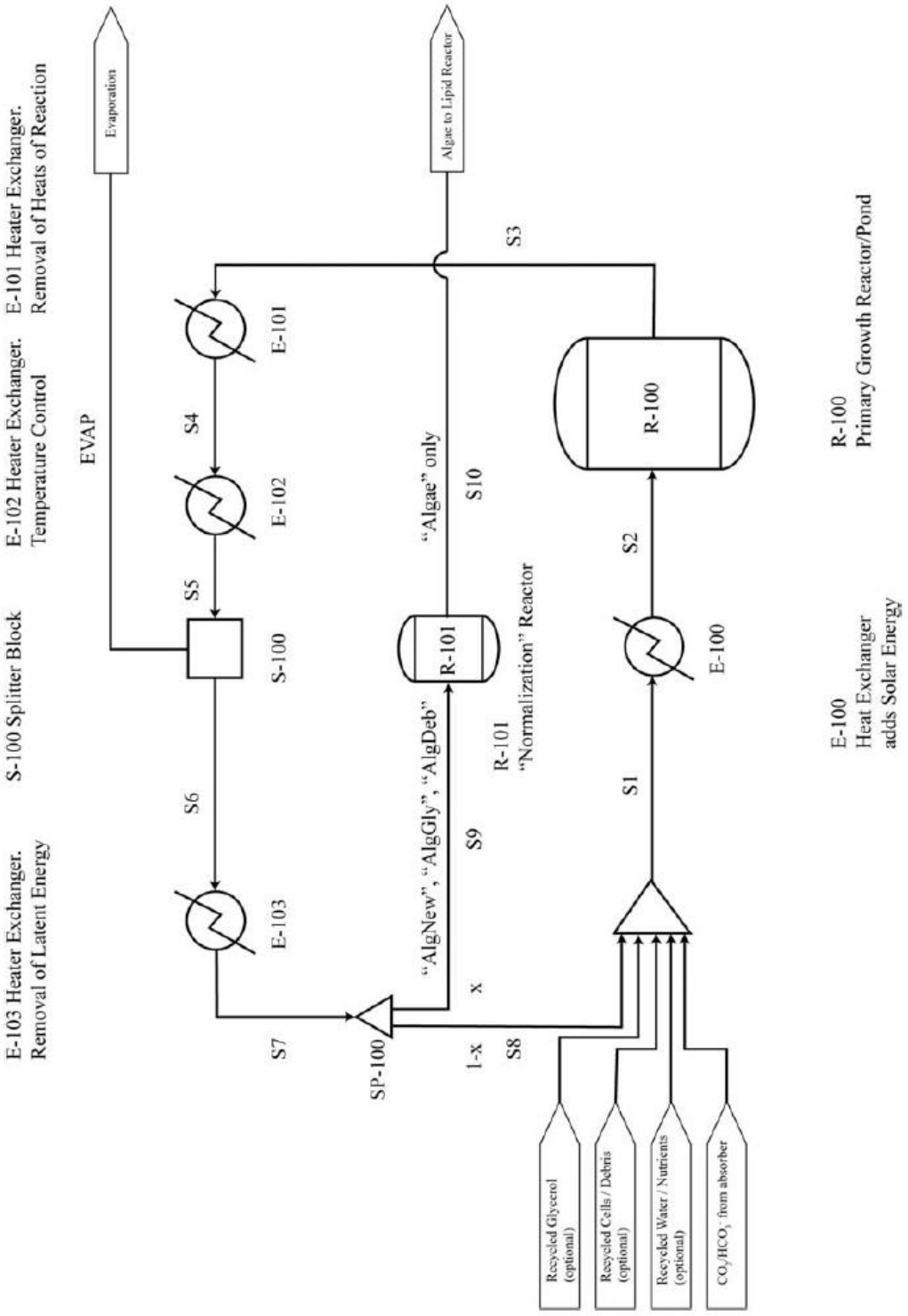

Figure 2.4. Information recycle loop for algal cell generation.

Specifications for the model are measured local rates of evaporation, local solar inputs, pond depth, and photosynthetic efficiency (typically 4 percent). Incident light, in kW, is one of the most fundamental variables in this process, and setting up the simulation flowsheet to run in light limitation is critical. Pond depth is typically ignored, yet it is of fundamental importance. Both of these factors are discussed in Section 2.3.4.

Returning to Figure 2.2, the block diagram shows the key information flows in the heuristic model for the entire process to grow and convert algae to biodiesel. As mentioned above, for the first reaction operation (algal cell generation), the information recycle loop in Figure 2.4 is used. Here, the material inputs are mixed with recycle stream, S8. The combined stream, S1, is sent to a single-stream heat exchanger (implemented using the HEATER block), E-100, where 100% of the solar energy flux (KW/m^2) multiplied by a guess for the cultivation area, A_1^*, is the heat duty added to S1. The effluent, S2, is sent to a RSTOIC block, R-100, that models reactions 1-5 in Table 2.5, and algae biomass is produced until the limiting reagent (urea in this case) is entirely consumed. Meanwhile, the extents of the other reactions are estimated and stored in the Calculator block.

In the E-101 single-stream heat exchanger block, the extents of reaction are combined with the heats of reaction to determine the amount of energy consumed in biomass production. Also, the area for the next iteration is determined:

$$A_1 = \frac{\sum_{i=1}^{5} \xi_i \Delta H_{R_i}}{\Phi_s \phi} \qquad (2.1)$$

where A_1 is the area for biomass generation, ξ_i is the extent of reaction i, ΔH_{R_i} is heat of reaction i, Φ_s is solar energy flux, and ϕ is the photosynthetic efficiency.

The effluent, S4, with the heats of reaction removed, is sent to a single-stream heat exchanger block, E-102, which cools/heats it to a specified temperature – maintained using utilities. A Calculator block multiplies the specified evaporation flux (Kg/s-m^2) by the pond area to give the isothermal evaporation rate. Then, Separator S-100, removes water in the EVAP stream using a SEP block. A Calculator block computes the heat lost to evaporation and a single-stream heat exchanger block, E-103, adjusts the enthalpy of stream, S6. Finally, the splitter block, SP-100, sends 100x percent of S7 to R-101, a so-called normalization operation to form the Algae species which is sent to the second reaction operation loop. The remaining 100(1 – x) percent is recycled to the beginning of the "reaction operation 1 loop." For the results presented herein, x = 0.25. Note that SP-100 simulates the action of a raceway in which the bulk of the algae slurry is recycled. Iterations about this information recycle loop are repeated until convergence is achieved; that is, until the relative change of the pond area, $\frac{\left|A_1 - A_1^*\right|}{A_1^*}$ is negligible.

The lipid-production reaction operation is similar to that in Figure 2.4. While not shown herein, its units are comparable, E-200, R-200, E-201, E 202, S-200, E-203, SP-200, and R-201. Note that the lipid production reaction operation, modeled with the RSTOIC block in R-200, requires a cultivation area:

$$A_2 = \frac{\sum_{i=6}^{13} \xi_i \Delta H_{R_i}}{\Phi_s \phi} \tag{2.2}$$

It is also important to recognize that both reaction operation models are implemented as small nested iteration loops inside a larger system of recycle loops. While the entire process simulation flowsheet is not shown herein, its recycle loops correspond closely to the recycle streams in Figure 2.2. Furthermore, the overall material and energy flows through the system are discussed in the section 2.4.

2.3.3. Algal Oil Content

In Section 2.2., the lipid content of the algal cells was discussed. OC5 was identified as one species created for modeling purposes. While it is not used directly in the case presented herein, it plays a role in the process simulation. For example, if a cell containing 37 wt% oil is desired, it can be modeled either as a mixture of OC35 and OC70 or, alternatively, as a mixture of OC5 and OC70. It was found useful to retain this flexibility as cells containing above or below 35 wt% oil were frequently encountered. Desired oil blends result from formation reactions that occur in parallel and are useful when a specific oil composition is required (Figure 2.5). It was initially expected that the model would produce cells of a given oil percentage, for example, 45 wt%. The formation of OC35 and OC70 would therefore occur in the proportions shown in Figure 2.5. It was, however, found in practice that the simulator exhausted mass and/or energy before this goal was reached. For clarity in the heuristic model, the reactions were then set to run in series such that OC35 was produced first. Any remaining mass/energy went to the formation of OC70 depending on the simulator's calculations towards a converged mass and energy balance. It took many hundreds of iterations to achieve a converged outcome.

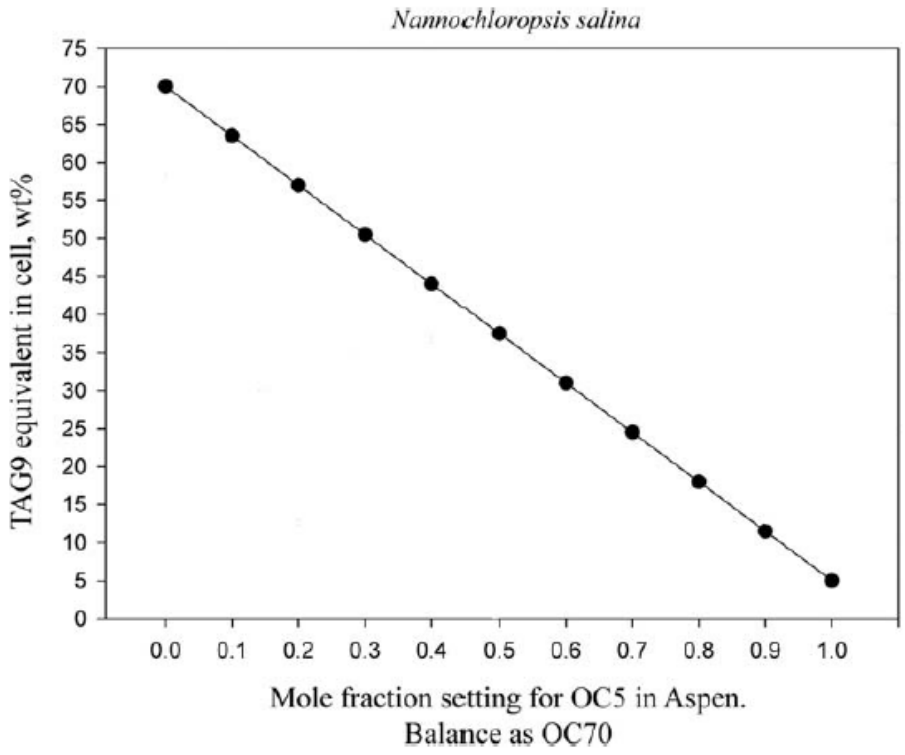

Figure 2.5. Setting up the simulator to generate oil cells.

2.3.4. Energy-limited Algal Growth

This model starts with the assumption that 100,000 tonnes per annum of carbon dioxide is available from an industrial source such as a chemical process, cement works, or similar. For the purposes of the model, the source is not important. Based on the previous thermodynamics discussion, the energy required to convert the carbon to algae and algae oil is known. The only source of energy is sunlight, which is determined by location and, therefore, is known. The evaporation rate, which removes substantial quantities of latent energy from the systems, is also known. Thus, the incoming carbon dioxide gives a carbon limitation, while the sunlight and evaporation give an energy limitation. This energy logic is displayed in Table 2.6. It shows that the average

evaporation rate at a confidential site is 3.5 m^3/(hc-hr) and that the average incident solar flux is 5.7 kWh/(m^2day) at the same location.

Table 2.6. Energy Logic for the Model

INPUT	CO_2 supplied	100,000	tonne/year
INPUT	Evaporation rate	3.5	m^3/hc/h
INPUT	Incoming solar	5.7	kWh/m^2/day
		8.5	GJ/h/hc
INPUT	Useable @ 4% Photosynthetic Efficiency	0.34	GJ/h/hc
	Separate cell growth from oil accumulation. Assign to separate ponds (real or imaginary).		
	Establish thermodynamics of each macro-reaction		
CALCULATE	Needed by Algae	17.2	GJ/h
CALCULATE	Thus, area required	40.22	hc
CALCULATE	Thus, evaporation required	140.77	m^3/h
CALCULATE	Latent Heat	2.26	GJ/tonne
CALCULATE	Enthalpy used	317.72	GJ/h
CALCULATE	Incoming energy	343.39	GJ/h
CALCULATE	Heat exchanger E-100 adds solar energy	8.48	GJ/h
	Repeat for Oil accumulation		
	Loop until converged		
OUTPUT	Area of Pond 1		
OUTPUT	Area of Pond 2		
OUTPUT	Evaporation from each pond		
OUTPUT	Full mass and energy balances		
OUTPUT	Flow in each reactant stream		
OUTPUT	Size of each unit operation		
OUTPUT	Cost of each unit operation		
OUTPUT	Capex & Opex for process		

Note that the calculations above yield the total area of the cultivation pond required. The need for detailed rate constants which are rarely, if ever, available, has been bypassed. Nevertheless, the surface area and all the important energetics and yields are calculated. These results, therefore, correspond to the best achievable case for oil production by solar means for an advanced biofuel from algae.

There is considerable information on the rates of sunlight across the earth, and therefore the local insolation levels can be fed into the model. In translating the local data into the model (Muneer, 2004) was used for rates of daily insolation and its variation over the year for almost any location on earth. It is, therefore, possible to calculate the maximum theoretical yield of either algae or algal oil from a given level of sunlight, as all the energy input comes from the sun. A typical energy input from the sun would be around $20MJ/m^2/day$. The calorific value (heat of combustion) of algae is approximately 20MJ/kg. The maximum output from any algal growth system would be around 1kg of algae per square meter per day. Algal oil has approximately twice the calorific value of algae (about 37MJ/kg). Therefore, for the same amount of incident sunlight, the maximum yield would be about 0.5kg of algal oil per square meter per day, the upper bound given by the first law of thermodynamics. However, this ideal yield cannot be achieved as it assumes a photosynthetic efficiency of 100 percent, much higher than typical photosynthetic efficiencies for algae, which is usually between 2 and 5 percent. To summarize, there are only three factors involved: (1) the solar input, which depends on time and geography; (2) photosynthetic efficiency, which depends on the algal species

and conditions; and (2) the calorific value (heat of combustion) of the algae (or the oil), which is not variable.

One missing piece of information remains: pond depth. The required surface area of the bioreactors arises naturally from the energy balance. Depth does not. The model gives the surface area and total biomass by weight. The missing design variable, pond depth, then gives the reactor volume, which in turn determines the cell concentration (g/l) and dilution rate, which at steady state equals the growth rate. It is, therefore, intuitively obvious that depth, cell concentration (dry weight), and growth rate are interlinked. Clearly, the attenuation of light penetration is a key concern. Applying the Lambert-Beer law for the absorption of light through an algal suspension, using a typical molar absorption coefficient ($\varepsilon = 7$ m^2/mol for an apparent molecular weight of 30), the light intensity is attenuated by two orders of magnitude in 0.01m. Note that pond depths of 0.25 m are typical and were used in this chapter.

2.4. Analyzing the Model Output

The heuristic mode permits analysis of the generalized process block diagram in Figure 2.2. In this case, Aspen Plus was set to link directly into an Excel spreadsheet to facilitate analysis. Most notably, it permits the identification of problems and possible solutions that can be used to make the system viable at different stages of development — for example, the addition of Calculator Blocks that give results requiring closer monitoring. Similarly, costing and financial modeling which is critical for techno-economic analysis and central to an integrated systems approach to algal biofuel production can be undertaken from the model outputs to ascertain the key drivers for

optimizing commercial-scale production. In the development of the model under discussion, sixteen areas were analyzed including mass balances, energy balances, effluent streams, bioreactor salinity, energy flows, evaporation, photosynthetic efficiency, glycerol use, carbon flow, water flow, and lost work. They are representative of the types of analysis that are possible using the simulator in a heuristic mode, but are not exhaustive. Next, representative results and conclusions derived from the energy-limited algal biofuels model are discussed.

2.4.1. Results

Table 2.7 summarizes the results after heuristic mode analysis as described herein. The model assumes 90 percent operation throughout the year (330 day/year), consuming 100,000 tonnes of carbon dioxide from flue gas. For Stage One analysis (biodiesel is methyl-oleate), carbon conversion to biodiesel is found to be 94.6 wt%, which is 4.5 tonne/hour or 253,400 barrels of oil (equivalent). The total surface area is 666.6 hectares, of which 90.5 hectares are associated with the algae-generating reaction operation and 576 hectares are associated with the second, oil-generating reaction operation. This corresponds to a productivity of oil based on the total active surface area of 16.2 $g/m^2/day$ and equivalent to 36.5 percent w/w oil in the cell. Only small differences have been observed in the preliminary Stage Two analysis using the same approach and this is the subject of ongoing work. Nevertheless, while most actual figures from research and development work are confidential, this is known to be close to observed practice.

Table 2.7. Simulation Results

Process operation	7,884	h/year (90%)
CO_2 removal	100,000	ton/year CO_2
Carbon conversion to biodiesel (Methyl Oleate)	94.6	wt%
Biodiesel produced (as Methyl Oleate)	4.5	ton/h
	253,400	barrel oil equivalent/year
Total Area	666.6	hc
Reaction Operation 1 Area for algae generation	90.5	hc
Reaction Operation 2 Area for oil generation	576.0	hc
Oil productivity (based on total area)	16.2	$g/m^2/day$
Effective oil content	36.5	wt%
Genetic stability requirements		
−Number of generations/year (binary fision)	41.4	

In a typical chemical process simulator, a chemical compound is only described by state variables, temperature, pressure, molar composition, and the like. When biological cells are introduced, another variable, the population doubling level (Davis, 2002), is added. It is well known in vaccine production that there are optimal cell generation numbers and these are meticulously recorded in every laboratory experiment or production batch. As genetic engineering is carried out on algal species, this will also become an issue for biofuels production. In the heuristic model, the cell generation number is calculated at the end of the expected operating period – 330 days. It gives the number as the genetic stability requirement the cell must possess, $N(t)/N(0) = 2^n$, where n is the number of generations, assuming binary fission. For the calculations herein, a 10 liter inoculum containing 2g/l of algae is present at $t = 0$. This is equivalent to 0.000002 tonnes of algal cells and is $N(0)$. The simulator shows that 57 million tonnes of algal

cells are produced in 330 days, during which the inoculum has doubled by binary fission (Blackburn and Parker, 2005) or other methods. This corresponds to 40 plus cell generations and gives the benchmark against which genetic stability programs (including algae from natural sources), are evaluated. In terms of genetic stability, this is a high number and the issue of genetic drift must be considered, even for naturally occurring algae cells. Therefore introducing this biological consideration into the earliest stages of development of a simulation may be helpful and draws attention to this simple, but often overlooked, yet biologically significant calculation.

2.4.2. Energy Flows

In the heuristic model, it was useful to turn off the heats of individual reactions to view their effects on the results. This allows the energy flows to be examined more clearly, as shown in Figure 2.6, which also displays the extents and heats of reaction. These energy flows can be used to assess the relative importance of key factors such as evaporation. There are five flows shown for each reactor in Figure 2.6. The first is the solar energy influx (E-100/E-200). This gives rise to the evaporation of water (S-100/S-200). The third flow shows the latent heat of evaporation required to make this happen (E-103/E-203). As the heats of reaction have been switched off in the Aspen block, they need to be explicitly removed (E-101/E-201). Finally, there is an energy flow which may be either cooling or heating of the stream to ensure the desired temperature, usually $30^{o}C$, is attained in the reactor for evaporation to occur (E-102/E-202).

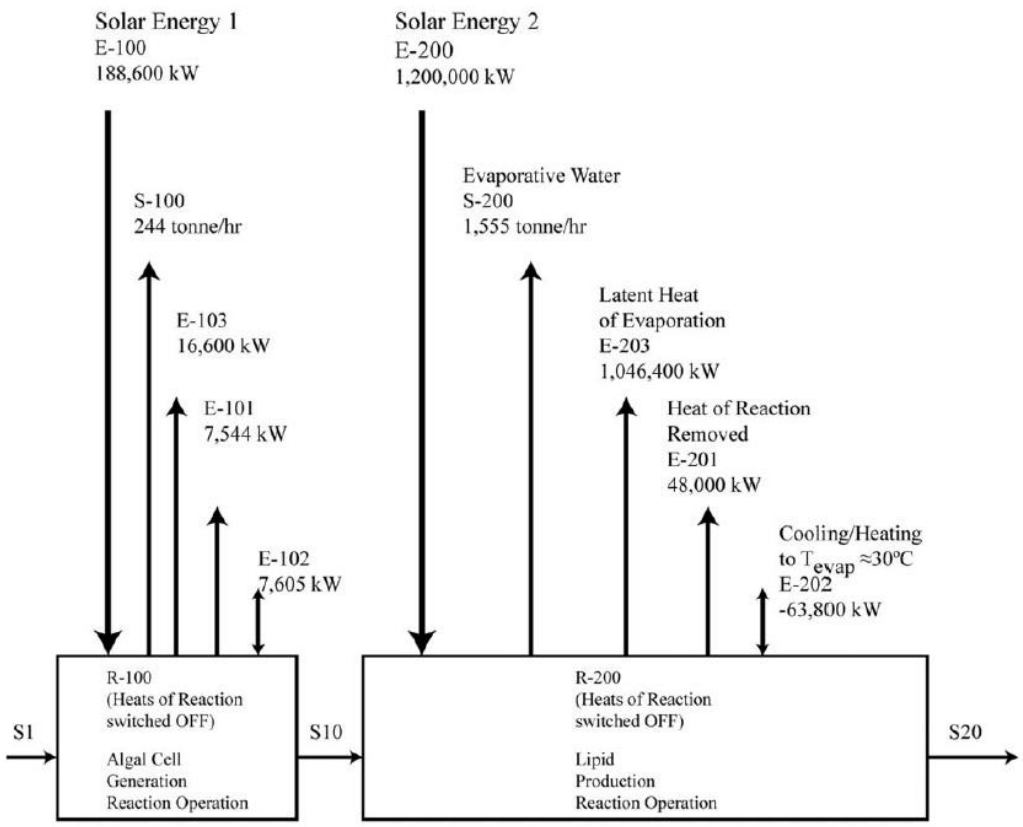

Figure 2.6. Mass and energy flows in reaction operations*.

*calculated using Aspen blocks in Figure 2.4.

2.4.3. Evaporation

In the absence of this integrated systems model, it can be difficult to appreciate the role of evaporation. The undesirable role of evaporation is that it removes water, which is often a scarce resource. A wide range of evaporation rates occur in regions where algal processes are likely to be implemented. It is usually in the range 1 to 5 m/year which forms the basis of Table 2.8. Data, of variable quality, is typically available as it is vital to the farming community. The usual unit for reporting is m /year of water equivalent to $m^3/m^2/day$ – with the range of 1 to 5 examined in line a. Likewise solar insolation is either available or can be calculated with the usual units of reporting

kWh/m^2/day with a range of 2-7 being typical. This is held constant here at 5.7 kWh/m^2/day or 8.5 GJ/hr/hc for ease of calculation and seen in line b. A very small fraction of the solar power is available for photosynthesis, typically 4% (line c). Aspen, using the iterative information recycle loop in Figure 2.4, computes 17.2 GJ/hr required in the reaction operations to grow algal cells – with the reactor area estimated as line d divided by line c. After subtraction of the latent heat of evaporation and the chemical energy requirements of the algae, the residual enthalpy content of the pond is left (line j). Under typical reactor conditions the temperature rise, ΔT, that corresponds to this enthalpy content, can readily be calculated (line m). It can be seen that it takes a local evaporation rate of between 3 and 4 m/year to be thermally neutral. Without additional cooling, the temperature can build to levels that affect the biology.

Table 2.8. Evaporation Rates and their Effect on Temperature

Line		1	2	3	4	5	Note
a	Local evaporation rate, (m^3/m^2/year)	8.5	8.5	8.5	8.5	8.5	Determined by location
b	Incoming Solar (GJ/h/hc)	0.34	0.34	0.34	0.34	0.34	Determined by location
c	Useable solar@ 4% Photosynthetic efficiency (GJ/h/hc)	17.2	17.2	17.2	17.2	17.2	4% is around current best case
d	Energy required by algae GJ/h	50.4	50.4	50.4	50.4	50.4	See Figure 4
e	Area required (hc)	57.5	115.0	172.4	229.9	287.4	d/c
f	Pond evaporation rate (m^3/s)	2.3	2.3	2.3	2.3	2.3	a*e
g	Latent heat of evaporation (GJ/tonne)	129.9	259.8	389.7	519.6	649.5	f*g
h	Heat removed by evaporation (GJ/h)	429.5	429.5	429.5	429.5	429.5	b*e
i	Total Incoming solar (GJ/h)	282.4	152.5	22.6	−107.3	−237.2	i-h-d
j	Solar energy remaining in pond (GJ/h)	0.2	0.2	0.2	0.2	0.2	
k	Liquid velocity (m/s)	4.0	4.0	4.0	4.0	4.0	
l	Volumetric flowrate (m^3/s)	4.7	2.5	0.4	−1.8	−3.9	
m	Net temperature rise in pond, ΔT (°C)						

2.4.4. Glycerol

Glycerol represents an interesting dilemma in terms of the current state of the biofuels market and its place in future developments in commercial-scale production. Glycerol is an inevitable and major by-product in the manufacture of biodiesel by transesterification. At present, there is a market for glycerol and the process economics benefit from its sale. This market is, at best, limited and would be rapidly overwhelmed if this by-product came from even a modest-sized biodiesel plant. Given an inexpensive source of glycerol, the simulator was used to investigate adding extra glycerol from external sources into the process. Figure 2.7 shows that while the overall area of the plant clearly increases, glycerol being of lower energy content than biodiesel, the area (hectares) required to produce one unit of biodiesel falls dramatically. This is believed to be an important model output that permits assessment of market shifts over time.

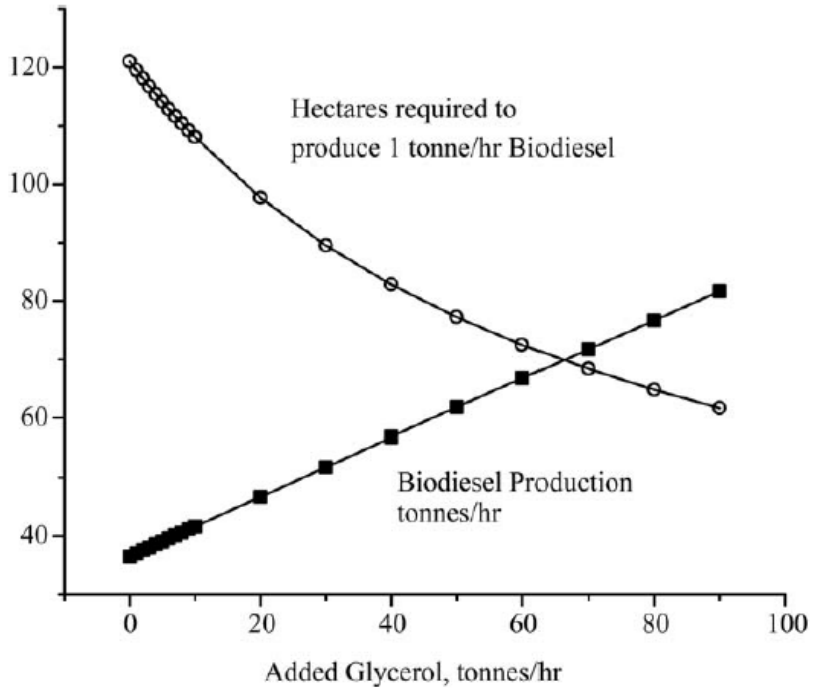

Figure 2.7. The effect of adding extra glycerol to the process.

2.4.5. Carbon and Water Flow

Carbon and water flows are shown in Figures 2.8 and 2.9. It is instructive to note the scale of carbon is in kg/hr and water flow is in tonne/hr, that is, a 1,000-fold change in scale. This draws attention to the massive quantities of water that are circulated, which is due to the low concentration of algae in the process (typically in the range of 0.5-1.0 g/l). Until this is addressed, commercial-scale production will be challenging. The optically-dense algal solution means that only the top few centimeters of the pond or bioreactor receive light and, therefore, are biochemically active.

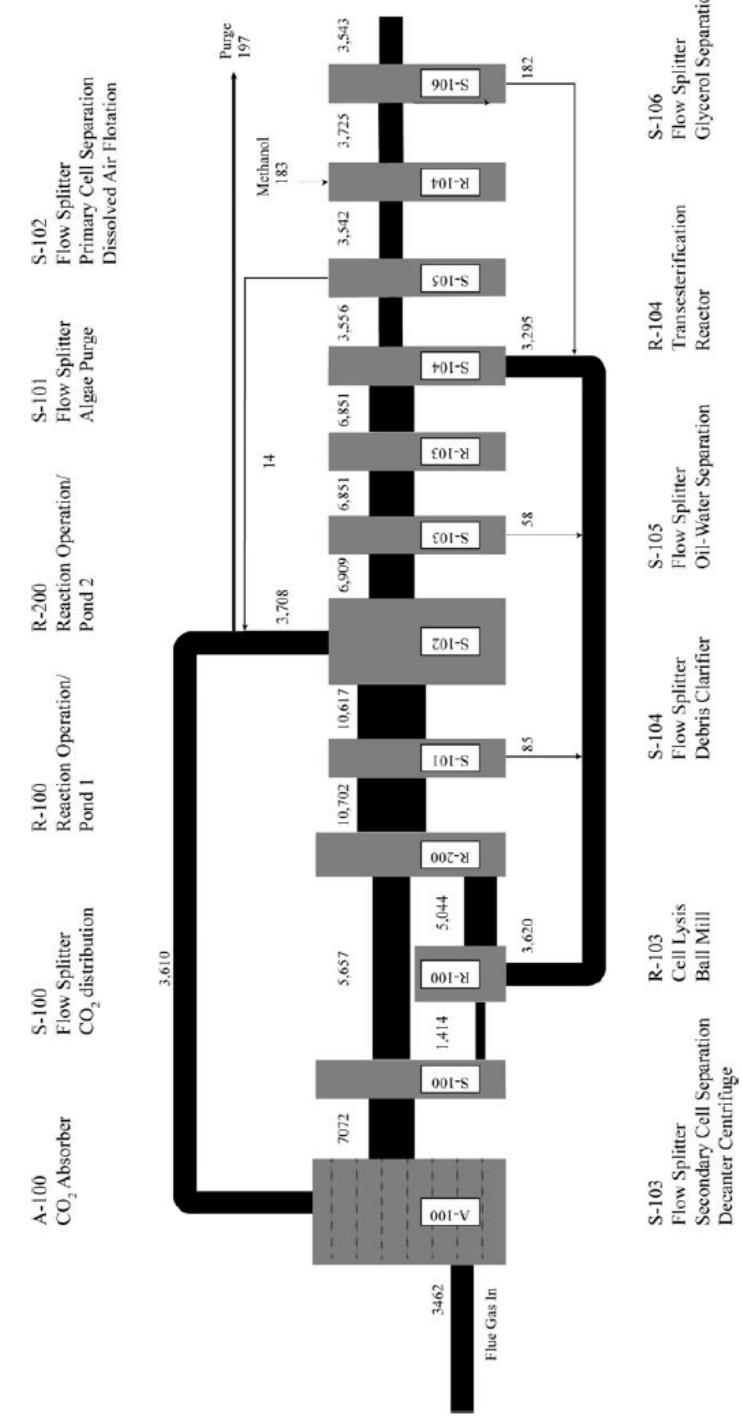

Figure 2.8. Carbon flowrate (kg/hr).

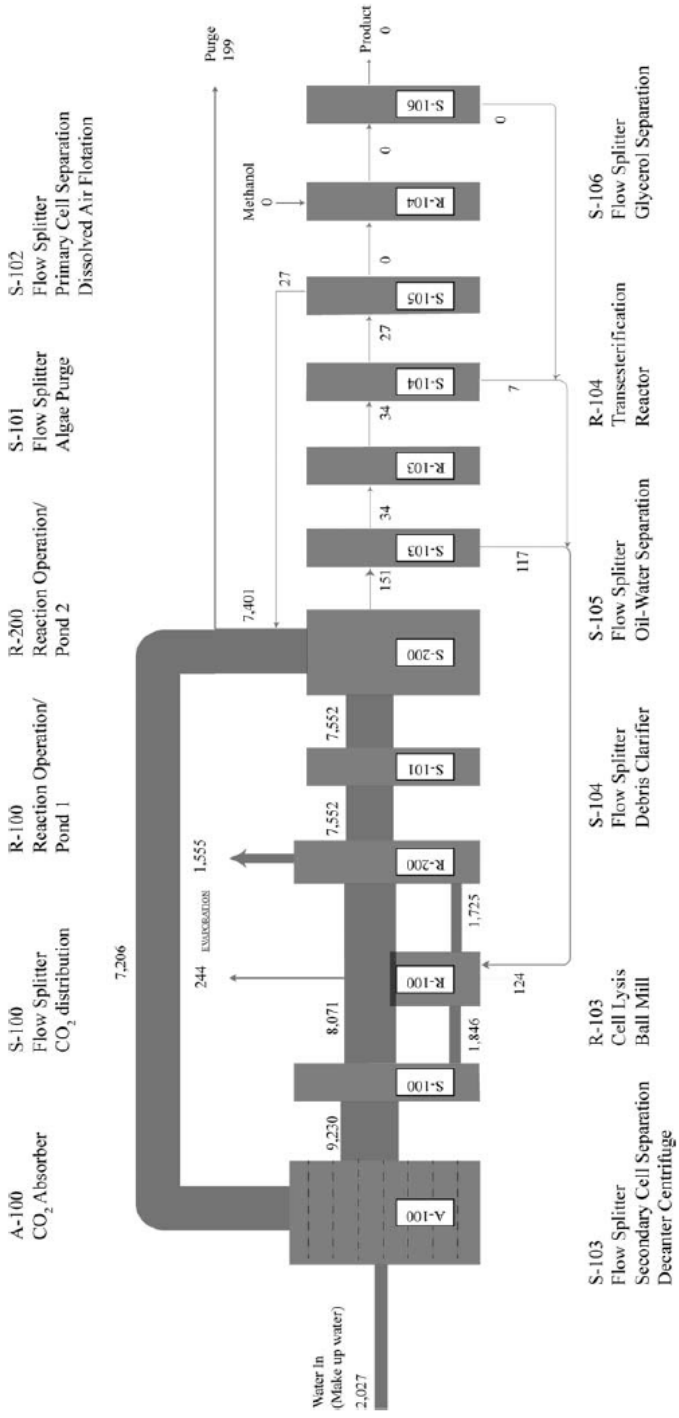

Figure 2.9. Water flow (tonne/hr).

2.4.6. Lost Work

Lost work/exergy calculations are well-established (Keenan, 1951; Seider et al., 2004; Sussman, 1980). The thermodynamic availability, or exergy, defined as $B = H - T_0S$, where T_0 is a reference temperature taken here at 298.15K, is calculated for each stream entering and leaving. H and S are estimated by Aspen Plus for each stream. In this case the sum of inlet stream availabilities is -7,614,300 kW and the sum of outlet stream availabilities is -7,558,600 kW, giving an availability increase of 55,700kW. The solar work done on the system in Reaction Operation 1 (187,600 kW) and in Reaction Operation 2 (1,204,000 kW), minus the shaft work needed for compressors and pumps (3,100 kW) yields a net increase of 1,395,000 kW; giving 1,339,000 kW of lost work and a thermodynamic efficiency of just under 4%. Perhaps the most instructive outcome of this analysis is the exergy diagram in Figure 2.10. Clearly, most of the work is lost in evaporation, and consequently, a very small proportion of sunlight is carried forward in a thermodynamically useful form in the biodiesel. Nevertheless, Figure 2.10 highlights exciting opportunities for chemical engineers to contribute innovative solutions that reduce lost work, improving sustainability through the development of advanced biofuel production from algae.

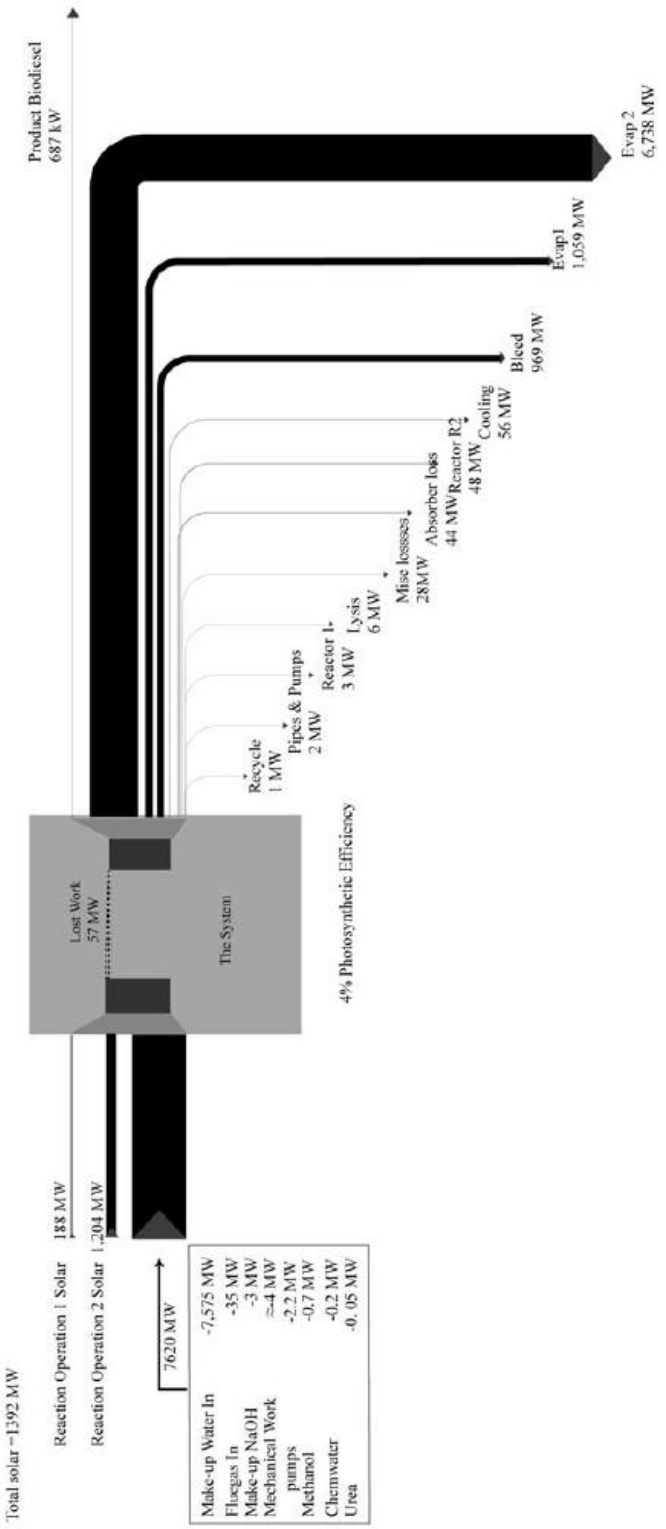

Figure 2.10. Exergy diagram for lost work analysis.

2.5. Conclusions

The energy-limited model of biofuels production highlights that an integrated systems approach, using computer-aided simulation, can be used to find solutions to some of the most intractable problems in the commercial-scale production of algal biofuels (Chapter 3). Reasonable approximations of the key thermodynamic properties (photosynthetic efficiency, light flux, and heats and entropies of formation) have been made and the energetics of the process are thus established.

The concept of energy (light) limitation is sufficient to bypass the intractable problem of obtaining kinetic data for the multitude of algae-growth reactions. It has also been shown that the simulator can be made to run in discovery (heuristic) mode to predict the missing design information: including the required cultivation areas, evaporation rate, and oil content of algal cells. Reactor depth remains unspecified and is the subject of a separate study by Pan Pacific Technologies.

The results demonstrate that land area requirements are great. A lower bound on the required land area can be predicted from the first law of thermodynamics and photosynthetic efficiency. Photosynthetic efficiency is the key variable in defining the land area. A photosynthetic efficiency of 4% was assumed herein. The validity of this assumption and the details that affect the photosynthetic efficiency will be discussed in more detail in Chapter 4.

The impact of recycle cannot be overestimated. While fundamental in optimizing conventional chemical processes, recycle costs and energy savings have not been fully understood in the algal industry to date. The importance of recycling water, carbon, and debris has been stressed in this model, and the corresponding energetics achieved has

been shown. However, it cannot be assumed that the biology will support these recycles (Section 6.2.1).

Finally, this chapter laid the framework for a commercial-scale algae-to-biofuel venture and explored what might be possible through the use of the Discovery Mode. However, as such it did not provide specifics on process models and did not generate costs for the processing steps. Chapter 3 will take the background information presented in this chapter and expand it to create a techno-economic model for biodiesel production from algae.

CHAPTER 3

Commercial-scale Biodiesel Production

3.1. Introduction

The production of biofuels from algae consists of four major processing steps: cultivation, harvesting, lipid extraction, and lipid upgrading. A block diagram of the process superstructure is shown in Figure 3.1. Note that this figure includes only a small fraction of the processing alternatives, each of which is discussed in the following sections within the context of cost-effective production of biofuels at a commercial scale. A cost analysis is then performed for each of the sections individually, by analyzing the various alternatives. A cash-flow analysis is completed for the entire process, and a production cost of biodiesel is computed for the base-case scenario. Finally, the effect of using different processing steps is analyzed in a sensitivity analysis, and this work is compared with other studies in the literature.

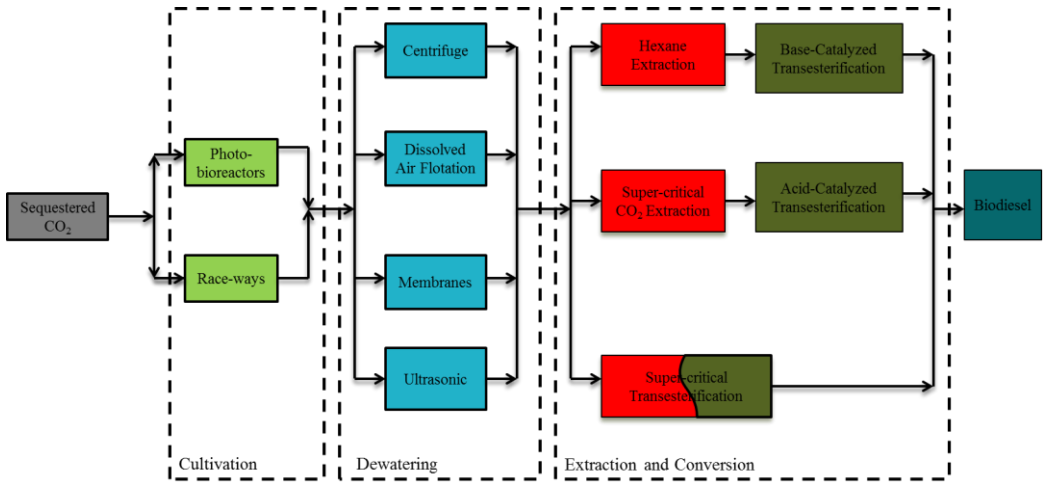

Figure 3.1. Block-flow superstructure.

3.1.1. Cultivation

During the cultivation stage, a purified source of carbon dioxide is either bubbled into or dissolved in water containing an algae inoculant and other nutrients, such as nitrates and phosphates (Handler et al., 2012). Salt water is significantly cheaper and more plentiful than fresh water; therefore, the *Nannochloropsis salina* algae, which is cultivated in salt water, is an excellent candidate for the production of biofuels. Under photosynthetic conditions, the *Nannochloropsis salina* algae consume the carbon dioxide, water, and other nutrients and use light to build biomass. Because CO_2 and other nutrients are plentiful within the solution, it has been postulated that the limiting factor for this stage is light absorption into the chloroplasts (Chapter 2, Chapter 4) (Dunlop et al., 2013). The *Nannochloropsis salina* can also be grown using organic sources of carbon, like glucose, cell debris, or glycerol, which has been shown to yield oil levels in excess of 50% (on a dry basis (Boussiba et al., 1987)). Combining these two cultivation techniques together is referred to as mixotrophic conditions (Heredia-Arroyo et al., 2010), and it allows for carbon-neutral oil production while still maintaining high lipid accumulation. Therefore, mixotrophic growth conditions are used herein.

Previous studies (Davis et al., 2011; Richardson et al., 2012; Sun et al., 2011) have shown that cultivation represents the largest costs in profitability analyses – with considerable disagreement concerning the best cultivation equipment and techniques (Bretner et al., 2011). The two main alternatives are raceways and photo-bioreactors (PBR). Numerous PBR designs have been postulated and tested. PBRs offer a more controlled environment, lowering the threat of contamination by foreign species and

predators. PBRs also decrease impurities, which can harm the algae cells or cause them to accumulate worthless material, like ash. However, thus far, the advantages of PBRs have been insufficient to offset the increased capital costs, establishing raceways as the industry standard because of their simplicity (Li et al., 2008). Other studies have considered both PBRs and raceways (Davis et al., 2011; Sun et al., 2011); however, PBR production costs of algae-oil are roughly $10/gal higher (Sun et al., 2011).

For this chapter, the ASPEN PLUS thermodynamic cultivation model developed in Chapter 2 (Dunlop et al., 2013) has been selected. It uses heats of formation for the algae and algae-derived compounds to perform rigorous energy balance calculations. The rate of energy input to the system (by solar radiation) is calculated by the energy balance, and then an area of cultivation is back-calculated using a fixed solar flux (average at a local site). The calculated area is used to determine other important quantities, like water losses to evaporation. As it is purely thermodynamic, for a given photosynthetic efficiency and oil concentration (4% and 37%, respectively), the Chapter 2 cultivation model estimates the minimum pond area and utilities (water make-up, pumping electricity, etc.) for a given algae production rate. As sunlight-limitation is the only constraint on growth rate, the calculated areas for the PBR and raceway are identical. Since the PBR is more expensive per unit area, it is the less favorable choice – and was rejected from the analyses herein.

3.1.2. Harvesting

Algae emerge from the cultivation section at a concentration of approximately 1 g (dry weight) per liter of water. Since oil-extraction methods often rely on solvents, a

more concentrated feedstock (about 60-100 g of algae per L of water) is required. The most common methods of harvesting involve flocculation (Smith and Davis, 2012; Weissman and Goebel, 1987), which causes the algae to aggregate and thereby increases the efficiency of settling, clarification, filtration, and centrifugation operations (Webpage: Flocculants Info). Alternatives to flocculation exist, such as membranes (Zhang et al., 2010) and ultrasonic harvesting (Webpage: Algae Industry Magazine – NAABB Chooses Harvesting and Extraction Technologies; Webpage: Green Car Congress – NAABB selects Los Alamos ultrasonic algae harvester for Phase II development). Thus far, ultrasonic harvesting has not been demonstrated on an industrial scale, and membrane-based processes suffer from high capital costs.

A wide variety of algae-flocculants have been studied over the years (Bilanovic and Shelef, 1988; Harith et al., 2009; Tenney et al., 1969). The flocculant used usually depends on the algae strain selected, as each algae species has specific chemistry that needs to be taken into account (Webpage: Algae Industry Magazine – Natural vs. Synthetic Flocculents). Flocculants can either be minerals (Smith and Davis, 2012), natural polymers (polysaccharides) (Webpage: Algae Industry Magazine – Natural vs. Synthetic Flocculents), or synthetic polymers. Mineral flocculants leave residual metal ions in the biomass when the dosing rates are not optimized, which can cause problems with downstream processing. Likewise, synthetic polymer flocculants can leave residual carcinogens in the biomass, rendering it worthless (Webpage: Algae Industry Magazine – Natural vs. Synthetic Flocculents). Synthetic flocculants also require a fixed pH and salinity to operate effectively. After algae have been flocculated (using one of the three options), they can be harvested using centrifuges, dissolved air flotation, and/or

electrolytic dewatering (Webpage: Algae Industry Magazine – NAABB Chooses Harvesting and Extraction Technologies; Shelef et al., 1984).

3.1.3. Extraction

Vegetable oil extraction is a mature process that has been used for food-grade consumables for over one hundred years, and was considered for fuel production as early as the 1880s (Knothe and Gerpen, 2010). Most commonly, oil is extracted from plant seeds using a mechanical press or hexane leaching (Webpage: SRS Energy, Solvent Extraction), although, newer methods, which employ supercritical carbon dioxide, are being developed (Döker et al., 2009; Zarinabadi et al., 2010). The seeds, on average, have a high oil content (Webpage: Fat content and fatty-acid composition of seed oils; Erasmus, 1993), and the extraction technology is mature.

Algae are single-cell organisms, which contain polysaccharides, proteins, trace metals, and nucleic acids, in addition to the desired lipids. Thus far, mechanical disruption techniques and hexane extraction have been used to extract algae oil (Geciova et al., 2002; Lee et al., 2010a). However, the extracted oils often contain a large percentage of the residual cell mass, including salts and metal ions, sugars, aromatics, and free-fatty-acids, which make the oil difficult to process or analyze. They also cause an increase in the density and viscosity of both the oil and fatty-acid methyl-esters (FAME). As a result, algae-oils need preprocessing before they can be converted to useable fuels.

New extraction techniques are in the development stage. Some processes use electric fields (Eckelberry et al., 2010), ultrasonic waves (Lee et al., 2010a), or

microwaves (Iqbal and Theegala, 2013; Terigar et al., 2011) to disrupt their cell walls. Another option is to use a nonpolar solvent (n-hexane) and pH conditioning to adjust cell permeability and to partition the wet biomass into a nonpolar solvent solution (containing the oil), an aqueous biomass solution, and an insoluble fraction (Webpage: SRS Energy, Algae Fractionation; Czartoski et al., 2011). Alternatively, supercritical CO_2 ($scCO_2$) can be used to disrupt cell walls and fractionate triglycerides (or other nonpolar species) as desired from cellular debris by adjusting the density of the $scCO_2$ (Bretner et al., 2011; Soh and Zimmerman, 2011) – see Chapter 5. It should be noted, however, that none of these processes have been demonstrated at a large scale, and that traditional mechanical disruption and hexane extraction is still the industry standard.

3.1.4. Transesterification and Catalyst Selection

Algae-extracted oil has a high viscosity, which is incompatible with automotive-transportation engines. In addition, the oils (primarily triglycerides) congeal in frigid weather, leading to blockages in fuel lines and engine damage. Algal lipids must therefore be modified to match certain desirable characteristics of petroleum diesel.

The most common method of preparing lipid for automotive consumption is cell extraction and transesterification at relatively mild conditions (about 1 bar and 100^{o}C), using an acidic or basic catalyst (Vyas et al., 2009). Herein, processes involving hydro-treating are not considered, due to their high cost of equipment relative to transesterification processes. Enzyme-catalyzed conversion was also discarded because of the high cost and fragility of the enzymes involved. Rather, it was decided to focus on

the chemical catalyst-based conversion of triglycerides to fatty-acid methyl-esters (FAME).

For the transesterification reactions, the four most common catalyst types are homogeneous acid, homogeneous base, heterogeneous acid, and heterogeneous base. While acidic catalysts handle a much higher degree of impurities, they yield much slower reaction rates and less favorable yields (Vyas et al., 2009); therefore, a basic catalyst has been selected. The most common homogeneous catalyst for transesterification is sodium methylate dissolved in methanol (Webpage: Biodiesel Magazine – Standard-For Good Reason). This catalyst is readily available from a number of providers, and it gives high yields and fast reaction rates. Its high solubility in methanol keeps it from forming precipitates, which can foul the process and slow the reaction. It is, however, highly flammable (with an auto-ignition temperature at 88^{o}C), carcinogenic, and has undesirable side reactions with water (Webpage: Sodium Methoxide MSDS).

The other options for homogeneous catalysis are alkali, such as sodium hydroxide or potassium hydroxide. While they are non-flammable and have comparatively few safety risks, they have low solubility in methanol. Also, as with sodium methylate, after the products are separated from the residual methanol, the alkali must be washed out of the FAME and glycerol product phases.

In contrast to homogeneous catalysis, a solid catalyst can be removed from the product phases easily using mature and inexpensive separation equipment, like centrifuges or candle-filters – circumventing the water washing operations and allowing the catalyst to be re-circulated. A proprietary solid catalyst was chosen for this research,

due to the comparability of its cost and product yield to that of sodium methylate, and its non-toxic and non-flammable nature.

3.2. Experimental Methods

After receiving 5 L of algae-extracted oil from Solix Biofuels, two small samples were subjected to alkaline titrations, using phenolphthalein, to determine the acid number (AN) – which was 22. In addition, a small vial of oil was sent to determine the moisture and trace metal contents, with the results in Table 3.1. From this analysis, it is believed that Solix used traditional hexane extraction. Degumming (Webpage: Degumming – Introduction) is the recommended process for producing a cleaner feedstock; however, in the interest of minimizing the amount of pre-processing, no degumming was performed. A high AN will poison basic catalysts, like the one used herein; therefore, to achieve a lower AN, glycerolysis was performed (more information about glycerolysis is provided in Section 3.3.1).

Table 3.1. Initial Algal Oil Analysis

Appearance	Calcium (PPM)	Other metals (PPM)	Moisture (wt%)	Acid Number	FFA (%)
Very thick, black liquid (partially solid at R.T.)	25	K=486 Mg=143 Na=426 P=401	0.043	22	11

The glycerolysis experiments used 1,380 g of algal oil and 249 g of glycerol in a stirred 2 L reactor at 100 torr. For the first experiment, a temperature of 193^{o}C was used.

Two other glycerolysis experiments were conducted at 204^{o}C (400^{o}F). In all experiments, samples were taken every hour and analyzed by titration and GC. After six hours, the oil was allowed to cool before being placed in a dehydrator overnight. The final AN was approximately 5 for the second and third batches and 7 for the first batch, which is too high for reliable use with a basic catalyst. However, due to the impurities in the algae oil, greater reductions were not achievable.

The transesterification reactions were carried out with 1.8 L of the treated algae oil in a 2 L reactor. For the first experiment, the contents were heated to 66^{o}C. A slurry, containing the catalyst and methanol, was added, and the temperature was maintained at 66 ± 2^{o}C, at 40 psig. For the second experiment, the reactor was heated to 73.9^{o}C, the catalyst and methanol were added, and the temperature was maintained at 73.9 ± 2^{o}C, at 40 psig. A third experiment was performed at 82^{o}C, but too few data points were obtained for use in the regression analysis.

All three experiments continued for two hours, with samples taken at 15 minute intervals for the first hour and 30 minute intervals for the second hour. The samples were immediately filtered and evaporated to quench the reactions. The samples separated into two phases; the top (oil) was analyzed, and the bottom (aqueous) phase was discarded. The compositions of triglyceride (TG), diglyceride (DG), monoglyceride (MG), and free fatty-acid (FFA) were analyzed for each sample taken during the glycerolysis experiments. Likewise, the composition of TG, DG, MG, and fatty-acid methyl-ester (FAME) were analyzed for transesterification experiments. A gas chromatograph was used – following the procedure outlined in ASTM D-6584. Note that this procedure was not designed to measure the quantities of TG, DG, MG, or FFA; however, it is useful for

obtaining relative concentrations. Because glycerol was in excess, the concentrations of TG, DG, MG, and FAME were normalized for both sets of experiments by assuming a constant wt% of all fatty-acid groups; i.e., assuming that no fatty-acid groups were degraded.

3.3. Kinetics Regression

In this section, activation energies and pre-exponential factors for two semi-empirical Arrhenius kinetic models are regressed from experimental data. Two sets of reactions are analysed: the glycerolysis and transesterification reactions. All regressions were formulated as weighted, relative least-squares difference problems. The CONOPT 3.14V solver, provided by AIMMS^{TM}, was used to perform the regressions.

3.3.1. Glycerolysis

Kinetic reactions to describe glycerolysis were located (Kumoro and Soedarto, 2012; Moquin et al., 2005), leading to the postulated kinetic model in Figure 3.2 – with potential degradation during glycerolysis neglected due to measurement limitations (as mentioned above). Note that this model is semi-empirical and is not intended to be mechanistic; therefore the regressed constants do not have physical significance. Also, the glycerol used in the experiments (and the process model presented herein) was effluent from the transesterification process.

The GC measurements were unable to distinguish between molecules of the same type (triglycerides, for example). Therefore, the scheme is expressed in terms of molecule types, which are assumed to follow the distribution in Table 3.2 – taken from an

internal report by the National Alliance for Advanced Biofuels and Bioproducts (NAABB) based on experimental measurements at the University of Arizona.

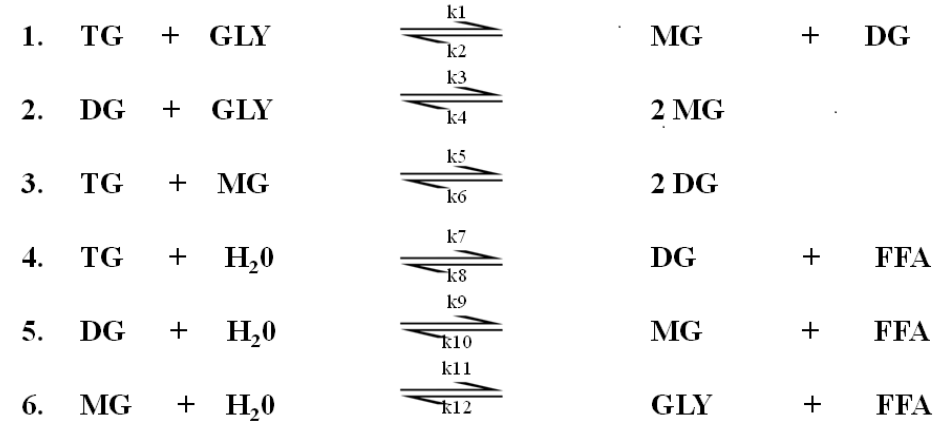

Figure 3.2. Glycerolysis kinetic scheme.

Table 3.2. Triglycerides from Nannochloropsis Salina Algae

Number	Triglyceride	Fatty-Acid Group*	Chemical Formula	Percentage
1	Trimyristin	C14:0	$C_{45}H_{86}O_6$	4.63%
2	Tripalmitin	C16:0	$C_{51}H_{98}O_6$	81.79%
3	Tristearin	C18:0	$C_{57}H_{110}O_6$	2.53%
4	Trioleate	C18:1	$C_{57}H_{104}O_6$	10.34%
5	Trilinoleate	C18:2	$C_{57}H_{98}O_6$	0.70%

*The first number after C is the number of carbon atoms. The second is the number of double bonds

Kinetic constants were regressed from the composition data obtained in the experiments. The hydrolysis reactions (4-6 in Figure 3.2) were assumed to involve only the back-reactions because the high temperature and vacuum pressure ensure that water will not be present in significant quantities in the liquid phase. For the six reversible

reactions, nine kinetic constants ($k_7 = k_9 = k_{11} = 0$) were determined using the CONOPT 3.14V solver, provided by AIMMS^{TM}. The objective function and constraints were:

$$Min \quad \sum_t \sum_i \frac{w_t * \left([X]_{exp,i,t} - [X]_{calc,i,t}\right)^2}{([X]_{exp,i,t})^2}$$

s. t. (3.1)

$$[FFA]_{calc,(t-1)} \geq [FFA]_{calc,t} \quad for\ t > 1$$

$$k_j \geq 10^{-6} \quad for\ all\ j$$

$$k_j(T = 204^oC) \geq k_j(T = 193^oC) \quad for\ all\ j$$

where t is the sampling-time index, w_t is the weighting factor for sampling time t, i is the species counter, j is the reaction counter, $[X]_i$ is the concentration of species i, and k_j is the rate constant for reaction j.

The first inequality constraint was implemented to force the system to approach the final concentrations; otherwise, the solver found parameters that drove the system to a premature equilibrium point. Weighting factors were also used for this purpose. The kinetic parameters at different temperatures were related using the Arrhenius expression:

$$k = A * e^{-\frac{E_a}{R*T}} \tag{3.2}$$

where A is the pre-exponential factor, E_a is the activation energy, R is the ideal-gas constant, and T is the absolute temperature. The resulting parameters are shown in Table 3.3. Figure 3.3 shows good agreement between the model and the experimental data points at 400^{o}F.

Table 3.3. Glycerolysis Arrhenius Constants

Constant	E_a kcal/mol	A $m^3/(kmol*s)$
k_1	2.29E+01	3.83E+05
k_2	0.00E+00	2.83E-05
k_3	2.21E+02	3.88E+95
k_4	2.78E+02	3.67E+122
k_5	5.98E+00	9.41E-02
k_6	9.75E+00	1.94E+01
k_7	0.00E+00	1.67E-08
k_8	1.42E-13	1.67E-08
k_9	0.00E+00	1.67E-08
k_{10}	0.00E+00	1.67E-08
k_{11}	2.04E+02	4.38E+87
k_{12}	2.17E+01	5.23E+05

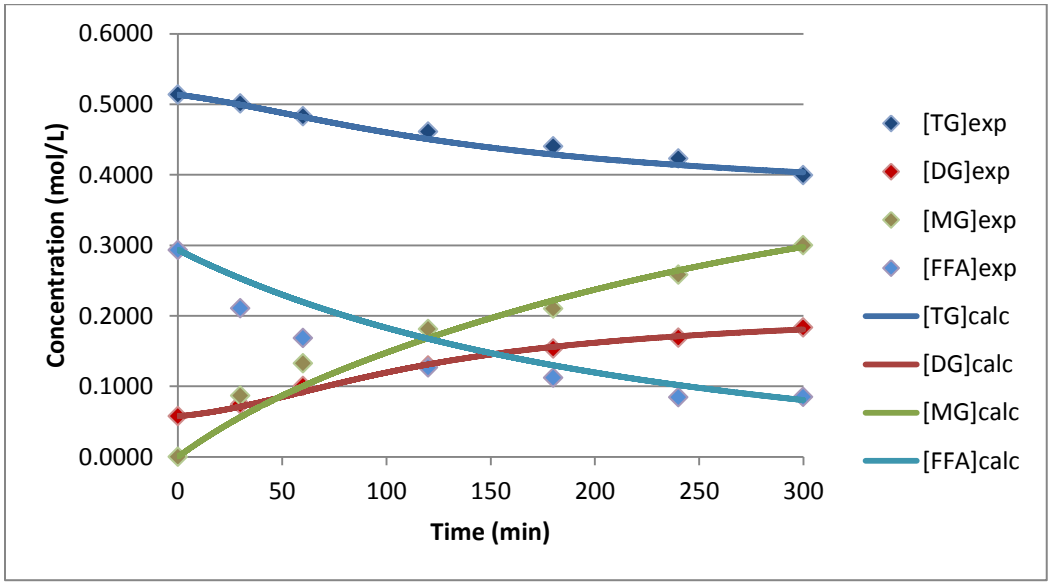

Figure 3.3. Glycerolysis at 400°F.

3.3.2. Transesterification

The postulated kinetic model for converting triglycerides to biodiesel is the three-reaction scheme (Chang and Liu, 2009) in Figure 3.4. Note that this model is semi-empirical and is not intended to be mechanistic; therefore the regressed constants do not

have physical significance. In each step, a fatty-acid group, attached to the glycerol backbone, is reacted with methanol to form a FAME molecule. First, the triglycerides are converted to diglycerides, which become monoglycerides, finally yielding glycerol.

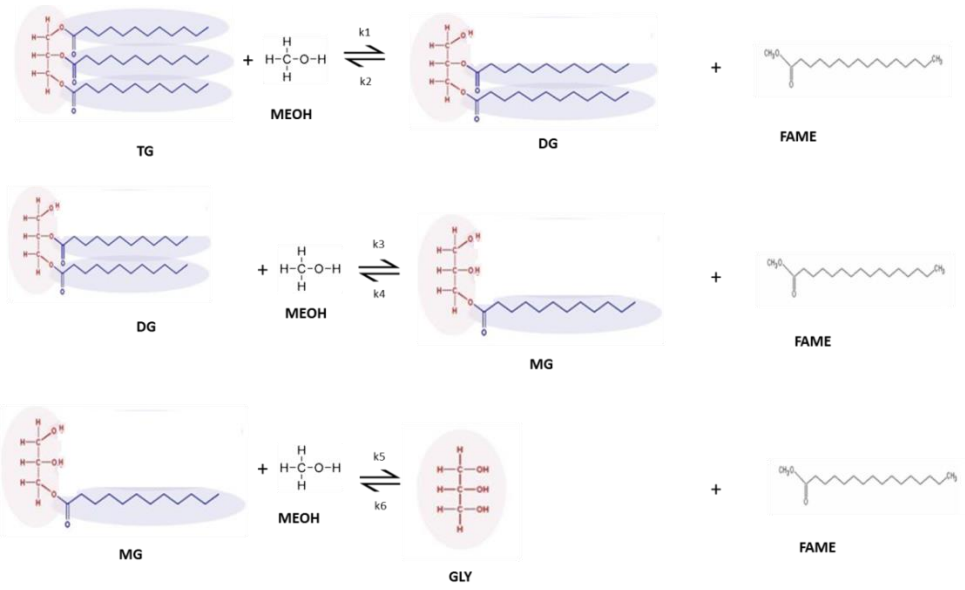

Figure 3.4. Transesterification kinetic scheme.

Arrhenius constants were regressed from the composition data obtained in the experiments. For the three reversible reactions, six kinetic constants were determined at each temperature. The objective function and constraints were:

$$Min \quad \sum_t \sum_i \frac{w_t * \left([X]_{exp,i,t} - [X]_{calc,i,t}\right)^2}{([X]_{exp,i,t})^2}$$

s. t. (3.3)

$$[TG]_{calc,final} \leq 1.10 * [TG]_{exp,final}$$

$$[FAME]_{calc,final} \geq 0.95 * [FAME]_{exp,final}$$

$$[FAME]_{calc,t} \geq [FAME]_{calc,(t-1)} \quad for\ t > 1$$

$$k_j \geq 10^{-6} \quad for\ all\ j$$

where t is the sampling-time index, w_t is the weighting factor for sampling time t, i is the species counter, j is the reaction counter, $[X]_i$ is the concentration of species i, and k_j is the rate constant for reaction j.

The constraints were implemented to force the slower reactions (at lower temperatures) to approach the final concentrations gradually; otherwise, the solver found parameters that drove the system to a premature equilibrium point. Weighting factors were selected to penalize errors in the later data points. The regressed Arrhenius constants are listed in Table 3.4. Figure 3.5 shows good agreement between the model and the experimental data points at 165°F.

Table 3.4. Transesterification Arrhenius Constants

Constant	E_a **kcal/mol**	A **m^3/(kmol*s)**
k_1	5.26E+01	9.62E+28
k_2	0.00E+00	1.67E-08
k_3	5.81E+01	8.42E+32
k_4	2.93E+02	5.51E+180
k_5	8.08E+01	2.04E+47
k_6	2.26E+02	6.40E+137

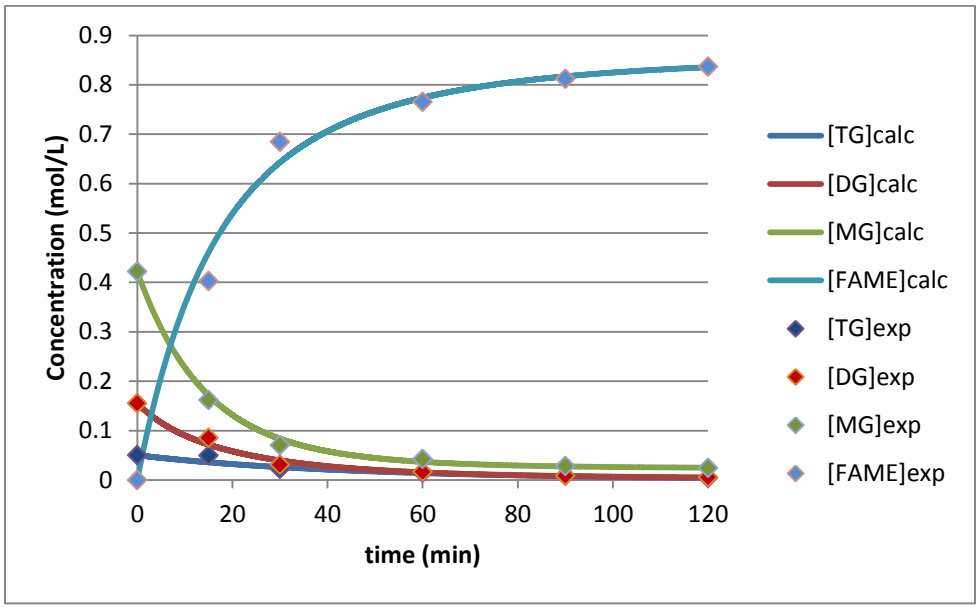

Figure 3.5. Transesterification at 165°F.

3.4. Chemical Species Data

The thermophysical property data for triglycerides and their derivatives within ASPEN PLUS are limited. The Aspen Tech databanks were supplemented with information from NIST, which is interfaced to ASPEN PLUS for easy data-sharing; however, many important properties for key chemical species were not present in the databanks. Therefore, an extensive literature search was performed to obtain the missing properties.

Three sources were used for the Antoine-equation parameters for the triglyceride and FAME molecules (Goodrum and Geller, 2002; Perry et al., 1949; Yuan et al., 2005); such data do not exist for the monoglycerides and diglycerides. When necessary, unsaturated bonds were assumed not to affect the Antoine constants or boiling points. When Antoine constants could not be found or regressed, boiling-point data were used

(Webpage: CRC Handbook of Chemistry and Physics, section 3; Perry and Green, 1999). When there was a disparity between two sources, the most recent was used. A similar search was conducted for density data, with five sources identified (Perry and Green, 1999; Phillips and Mattamal, 1978; Su et al., 2011; Sum et al., 2003).

When pure-component data were unavailable, they were estimated by ASPEN PLUS, using the Joback group-contribution method (Poling et al., 2001), which is assumed to be sufficient for species that are present in small quantities, such as diglycerides and monoglycerides. Liquid-phase activity coefficients were calculated for liquid-liquid equilibria using the UNIFAC-LL group-contribution method, and for vapor-liquid equilibria using the traditional UNIFAC group-contribution method.

3.5. Conversion Process Description

In this section, a fuel conversion process is presented, which begins with a glycerolysis pre-processing section to remove free fatty-acids. The glycerolysis process flow diagram is shown in Figure 3.6.

The extracted triglyceride feed is combined with glycerol from the transesterification process and sent to a heater, where the temperature is raised to 205^{o}C. The preheated feed is then combined with recycled glycerol and sent to the glycerolysis stirred-tank reactor, which is under vacuum (0.464 bar). Herein, the fatty-acids are reacted with glycerol until they comprise less than 3 wt%. Vapor wastes, including decomposed organics, water from the reactions, and air that has leaked into the vessel, are removed by a vacuum system. The liquid effluent is sent to a decanter, where the purified oil is separated from glycerol in the aqueous phase. The glycerol is recycled

using a 5% purge to prevent the build-up of impurities, such as metals and undesirable organics. The oil (light phase from the decanter) is sent to the transesterification process shown in Figure 3.7.

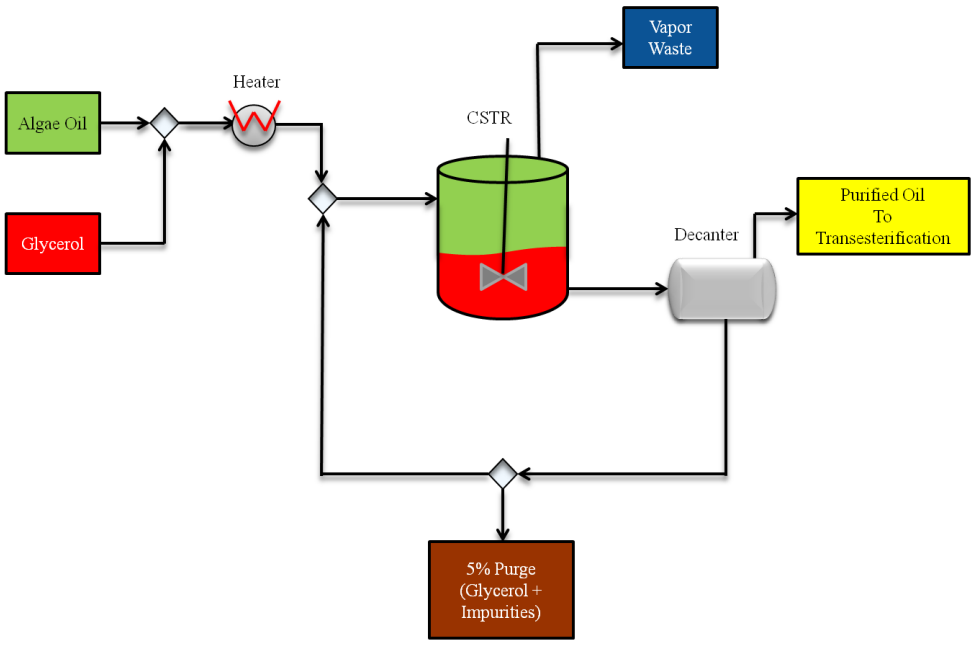

Figure 3.6. Glycerolysis process.

The glycerol process effluent is mixed with excess methanol (6 mol methanol/mol oil – containing catalyst). The catalyst can vary from 1-10 wt% of the methanol and oil mixture. The mixture is heated, and sent to a CSTR, where the triglycerides are converted to the FAME product and glycerol byproduct. The effluent is filtered to remove the catalyst (which is recycled to the reactor) before being sent to a decanter.

The decanter separates the FAME (light phase) and glycerol (heavy phase) by gravity; methanol distributes itself between the two phases.

The light phase is sent to a second CSTR for further conversion. Its effluent is subjected to the same separation techniques and sent to a distillation column, where the FAME (biodiesel) is recovered from methanol. The glycerol effluents from the decanters are combined and sent to the glycerol distillation column, where methanol is recovered from nearly-pure glycerol. The methanol effluents are combined and recycled while the glycerol is recycled to the glycerolysis and cultivation sections. Note that to purify further the glycerol or FAME, other distillation columns or washing operations may be required, but these are not accounted for herein.

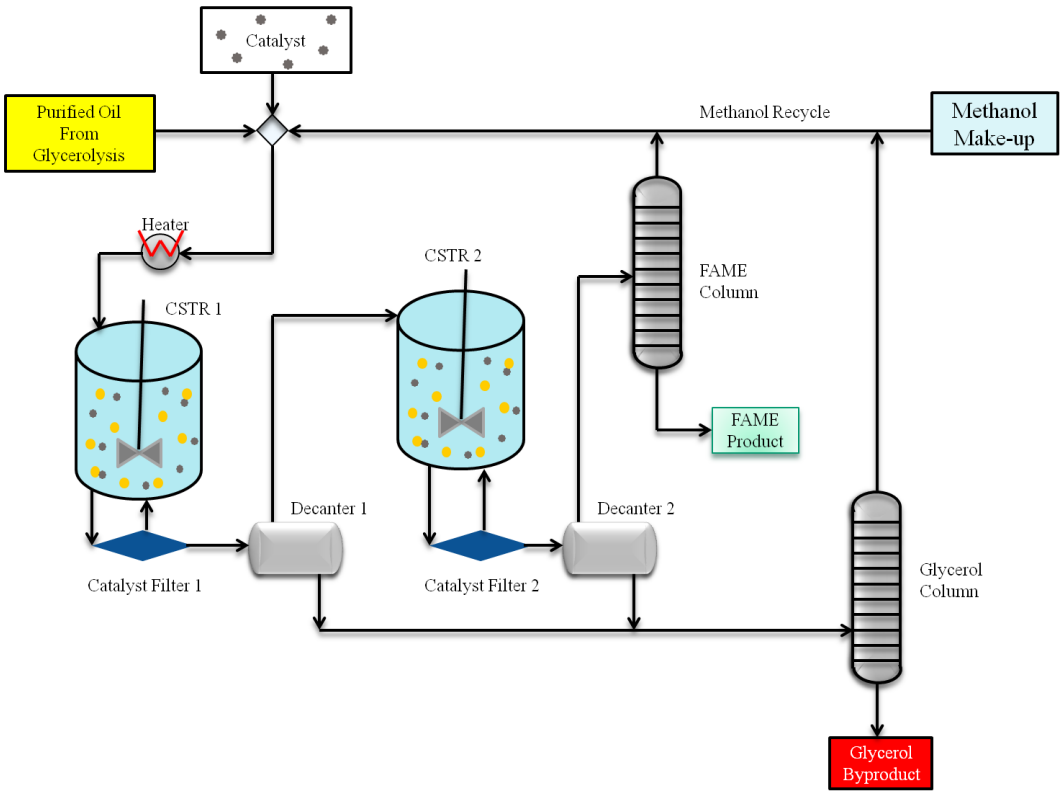

Figure 3.7. Transesterification process.

3.6. Economics

In this section, economic estimates are provided for the cultivation, harvesting, extraction, and conversion sections of a process that grows algae and converts it to biodiesel — at a scale of approximately 175 million gallons of biodiesel produced per year. The estimates for cultivation, harvesting, and extraction are derived from industrial quotes, NAABB estimates, and literature studies. The price of the proprietary solid catalyst is estimated based on the price of the competitive homogeneous catalyst. The economics of glycerolysis and transesterification processes are based upon rigorous engineering design and cost estimation calculations, using the Aspen Software Suite. The overall analysis is compared with economic analyses by others.

3.6.1. Cultivation Economics

The cultivation model from Chapter 2 (Dunlop et al., 2013) estimates the heats of formation for the key components, including algae cells (containing a base level of oil), oil-bearing cells (containing larger amounts of oil), and algae debris (after oil is removed). Then, heats of reaction are estimated for the formation of algae cells, algae oils, and algae debris. Given the incoming solar flux and the photosynthetic efficiency (4%), these are combined in an energy balance to yield a thermodynamic lower bound on the area required for cultivation. The oil concentration in the algae was calculated from the mass balances in ASPEN PLUS as 37 dry wt%.

Note that water is recycled through the raceway ponds to decrease pumping from the ocean. While this increases pump investment costs, it drastically reduces electricity

required to supply fresh sea water. Also, when nutrients are supplied in excess (e.g., phosphorus), they are recycled. In addition, all spent algae debris and much of the glycerol is recycled as a source of organic carbon for the algae, lowering the pond area requirements.

The costing analysis uses scaled results of those calculations, sequestering 1.5 MM tonne/yr of carbon dioxide to produce 1.35 MM tonne algae/yr by dry weight. The outputs from these simulations were evaluated by confidential industrial sources and combined with projections from within the NAABB. Raceways were selected for cultivation due to their reduced cost, with the ponds defined by the NAABB at $50,600 per hectare. The sensitivity of this costing parameter is discussed in section 3.6.6. Tables 3.5, 3.6, and 3.7 display the major capital expenditures (CAPEX) for carbon sequestration and cultivation, as well as their combined operating expenditures (OPEX).

Table 3.5. Carbon Sequestration CAPEX*

Equipment	**Number of Units**	**Total Installed Cost (MM $)**
Compressor	1	20
Fluegas Pipeline	10 K meters	79
Absorption Tower	1	30
Storage Tanks	3	9.3
Total		138.3

*All estimates are from confidential industrial sources

Table 3.6. Cultivation CAPEX

Investment	Quantity	Cost (MM $)	Source
Land (without ponds)	10 K hectares	77.5	Industrial Quote
Pond installation	10 K hectares	508.9	NAABB Estimate*
Pipelines	18 K meters	44.7	Industrial Quote
Pumps	26	46.6	Industrial Quote
Total		677.7	

*This is the estimate used in the AISIM (now called FARM) model from 2012.

Table 3.7. Sequestration and Cultivation OPEX*

Investment	Quantity	Units	Cost	Units	Cost (MM $/yr)
CO_2	192	tonne/hr	0	$/tonne	0.0
NaOH	8	tonne/hr	300	$/tonne	19.0
Urea	0.7	tonne/hr	285	$/tonne	1.6
Sea Water	32,000	tonne/hr	0	$/tonne	0.0
Power	483,000	MWh/yr	0.08	$/kWh	38.6
Labor					0.4
Trace Metal Addition					0.1
Effluent Treatment					5.9
Maintenance					11.9
Total					77.5

Clearly, the pond installation represents the most significant capital investment in the carbon sequestration and cultivation sections – and the entire algae-to-biodiesel process (see the section 3.6.6.).

3.6.2. Harvesting Economics

The costs of mineral flocculants were reported in a 1987 source (Weissman and Goebel, 1987). After adjusting these to 2012 dollars using the Consumer Price Index

(CPI) (Webpage: Consumer Price Index), the cost for a mineral flocculant is $0.12/(kg dry algae). Because some algae can auto-flocculate, or flocculate using species already present in brackish or waste water (Smith and Davis, 2012), the cost of flocculation can be negligible. For the base case, an intermediate value of $0.06/(kg dry algae) is used, which is in good agreement with estimates provided within the NAABB for both mineral and natural (chitosan) flocculants.

Centrifuges are traditionally used to separate solids. However, because of algae's small diameter (5-20μm) (Smith and Davis, 2012) and low concentration, centrifuges are energy intensive. Also, centrifuge forces might disrupt the flocculated algal clusters. Dissolved air flotation (DAF) is a gentler alternative, and it is easily coupled with flocculation. Other techniques include membrane (Webpage: NAABB Final Report; Zhang et al., 2010), ultrasonic (Webpage: Green Car Congress – NAABB selects Los Alamos ultrasonic algae harvester for Phase II development; Webpage: NAABB Final Report), and electrolytic harvesting (Webpage: Algae Industry Magazine – NAABB Chooses Harvesting and Extraction Technologies; Webpage: NAABB Final Report). A summary of the capital and operating cost estimates for these techniques is displayed in Table 3.8. The flow rate of wet algae into these operations is 150 MM kg/hr with 1.15 kg algae/1,000 L, yielding a dry algae flow rate of approximately 172,000 kg/hr.

Table 3.8. Cost Comparison for Harvesting

Equipment	Total CAPEX (MM $)	Operating Cost ($/kg dry algae)	Total OPEX (MM $)
Flocculant (Weissman and Goebel, 1987)	-	0.06	82
Decanter Centrifuge*	70	0.076 - 0.264	104 - 360
Dissolved Air Flotation*	67	0.028	38
Membrane (Webpage: NAABB Final Report)	113	0.004	5
Electrolytic (Webpage: NAABB Final Report)	336	0.007	10
Ultrasonic (Webpage: NAABB Final Report)	66	0.006	8

* From confidential industrial sources.

All technologies are coupled with a flocculent to assist in the separation. Of the three new technologies (membrane, electrolytic, and ultrasonic), ultrasonic harvesting is the only technology with a low capital cost. The CAPEX for membrane separations is likely even higher than the projected cost, due to their fragility and the need to replace them frequently. When estimating the CAPEX in Table 3.8, a 2-year lifetime for the membranes was assumed. Because the DAF/chitosan combination is the most reliable cost estimate, it is taken as the baseline for this analysis. The effect of the other technologies is examined in Section 3.6.6.

3.6.3. Extraction Economics

The basis of these costing estimates is derived from the existing literature and NAABB estimates. In most cases, equipment costs were either not present or unreliable. Therefore, only operating costs are presented, and capital costs are assumed to be

negligible. This is a good assumption for the overall process, because cultivation capital costs are dominant. Additionally, this analysis assumes that all solvents used in the extraction are recycled entirely (without losses) and that electricity is supplied at 0.08$/kWh. The results are presented in Table 3.9. The flow rate into all of these operations is 172,000 kg dry algae/hr with a concentration of 65 g dry algae/L, yielding a total flow rate of 2.8 MM kg/hr.

Table 3.9. Operating Cost Comparison for Extraction

Equipment	**Operating Cost ($/kg dry algae)**	**Total OPEX (MM $)**
Bead Mill + Hexane Extraction (Bretner et al., 2011)	2.135	2,908
Ultrasound (Webpage: NAABB Final Report; Lee et al., 2010a)	0.031	42
Microwave (Terigar et al., 2011)	0.008	11
Hexane Leaching (Webpage: NAABB Final Report; Webpage: SRS Energy, Algae Fractionation; Czartoski et al., 2011)	0.010	14
Pulsed Electric Field (Eckelberry et al., 2010)	0.045 – 0.922	61 - 1256
scCO2 (Bretner et al., 2011)	0.225	307

The traditional "Bead Mill + Hexane" extraction has the largest cost, due to the energy intensive drying step required to extract the majority of the oil (Bretner et al., 2011). The microwave extraction process appears to be the cheapest; however, this process was evaluated in a "pilot-scale" study (Terigar et al., 2011), and might not work reliably at biodiesel manufacturing scales. This is true of all estimates in Table 3.9, except for the "bead mill + hexane" extraction. A wide range of prices were provided for the pulsed electric field method — with upper and lower bounds reported. Note that

although $scCO_2$ appears unfavorable, it is predicted to have the greatest selectivity, which would yield the cleanest triglyceride feedstock (Soh and Zimmerman, 2011). For the "base case" analysis herein, the microwave OPEX cost is used because it is most cost-effective. The range of costs and its effect on the overall economics is examined in Section 3.6.6.

3.6.4. Catalyst Pricing

The proprietary catalyst was assumed to be priced competitively with the most common alkaline catalyst, sodium methoxide. Estimates were obtained for the bulk-price of sodium methoxide from three major suppliers: BASF, Zouping Runzi, and Shandong Xinruida. All three costs were comparable, yielding an estimate of $2.03/kg for sodium methoxide (excluding methanol).

The lifetime of the catalyst was estimated, and the catalyst cost per year was calculated for three different replacement schedules. An intermediate case of $11.62MM/yr was used for the techno-economic analysis herein. Note that the intermediate case was biased towards the maximum replacement schedule because of the dirty feedstock.

3.6.5. Glycerolysis and Transesterification Economics

The major material inputs and outputs for the combined glycerolysis/transesterification process are shown in Table 3.10. Note that the FAME outlet flow of 67,000 kg/hr represents approximately 16.4% of the biodiesel consumed daily in the United States in 2011 (Webpage: Soystats – Biodiesel Consumption).

Table 3.10. Major Process Inlet and Outlet Flow Rates

Stream	Triglyceride Inlet	Methanol Inlet	FAME Outlet	Net Glycerol Outlet
Flow Rate (kg/hr)	67,220	10,533	67,104	5,346

Heat integration of the glycerolysis/transesterification process was performed to minimize utility costs. Average heat capacities (of source and target temperatures) of each stream were used. A pinch-analysis spreadsheet, produced by the Institution of Chemical Engineers (ICHEME), was used to determine the minimum utility targets. Stream matching was done using methods in the literature (Seider et al., 2009b). Although the FAME product stream and glycerol byproduct stream were sources of heat for the "cold" streams, they were cooled only by the cold streams, without using the cooling water utility. The resulting heat-integrated process has 11 heat exchangers, including the condensers and reboilers for the two distillation columns. The heat integration decreased the hot utility requirements from 25,444 KW to 9,149 KW and the cold utility requirements from 24,995 to 8,700 KW. The heat exchanger areas were estimated using heuristics (Seider et al., 2009a).

The hourly labor costs for operators and supervisors were estimated at $20/hr and $35/hr, respectively, with 330 operating days per year. The price of methanol ($1.45/gal) was taken from industrial sources (Webpage: METHANEX – US methanol Price). Cooling water [at 32.2°C (90°F), heated to 48.9°C (120°F)] and high-pressure steam were provided by a nearby utilities plant. Costs for these utilities were obtained from the literature (Seider et al., 2009c) and compared with APEA values.

Using the APEA in 2012, cost estimates for the glycerolysis and transesterification process equipment were computed. The total depreciable capital was estimated to be approximately 20 million USD, with the key results in Tables 3.11, 3.12, and 3.13. Clearly, the transesterification plant has a relatively small effect on the overall economics.

Table 3.11. Transesterification and Glycerolysis CAPEX Costs

Equipment	**No. of items**	**Purchase Cost (K$)**	**Total Cost (K$)**
Pumps	15	94	536
Decanters	3	134	551
Distillation Towers	2	206	579
Heat Exchangers	11	1,831	3,267
Chemical Reactors	12	10,609	14,429
Misc. Vessels	3	134	551
Total	58	12,959	19,710

Table 3.12. Annual Labor Costs

Operating Costs	**Costs (K$/yr)**
Operating Labor	$640
Maintenance	$1,190
Supervision	$280
Total Labor Cost	$2,110

Table 3.13. Annual Utilities Costs

Utilities	**Cost (K$/yr)**
Chilled Water	$ 992
Steam	$1,076
Electricity	$ 434
Catalyst Replacement Cost	$11,616
Methanol	$31,955
Total	$46,073

3.6.6. Overall Economics and Sensitivity Analysis

The cost information from the previous sections is compiled in Table 3.14. Auxiliary costs, such as for contracting, general and administrative (G&A), and a contingency were added, with percentages recommended by the APEA. The total CAPEX is 1.2 billion dollars, with a yearly OPEX of 257 million dollars. A block-flow diagram summarizing the major material and energy flows is shown in Figure 3.8. Information on the flow rates in Figure 3.8 is in Table 3.15. The price of chitosan was taken as $20/kg (Webpage: Price of Industrial-grade Chitosan). Note that streams 20-22 are purges (roughly 3%).

Table 3.14. Overall Economic Analysis

Processing Step	**Method**	**CAPEX (MM$)**	**OPEX (MM$/yr)**
Sequestration and Cultivation	Pan Pacific Thermodynamic Model	739	78
Harvesting	Chitosan Flocculant + Dissolved Air Flotation	67	120
Extraction	Microwave Extraction*	0	11
FFA Reduction and Tranesterification	Glycerolysis Pre-treatment and Solid-Base Catalyst Transesterification	20	48
SUBTOTAL	**-**	**825**	**257**
Contract	10%	83	-
G & A	8%	66	-
Contingency	30%	248	-
GRAND TOTAL	**-**	**1,221**	**-**

*CAPEX unavailable, but low relative to the cost of sequestration and cultivation.

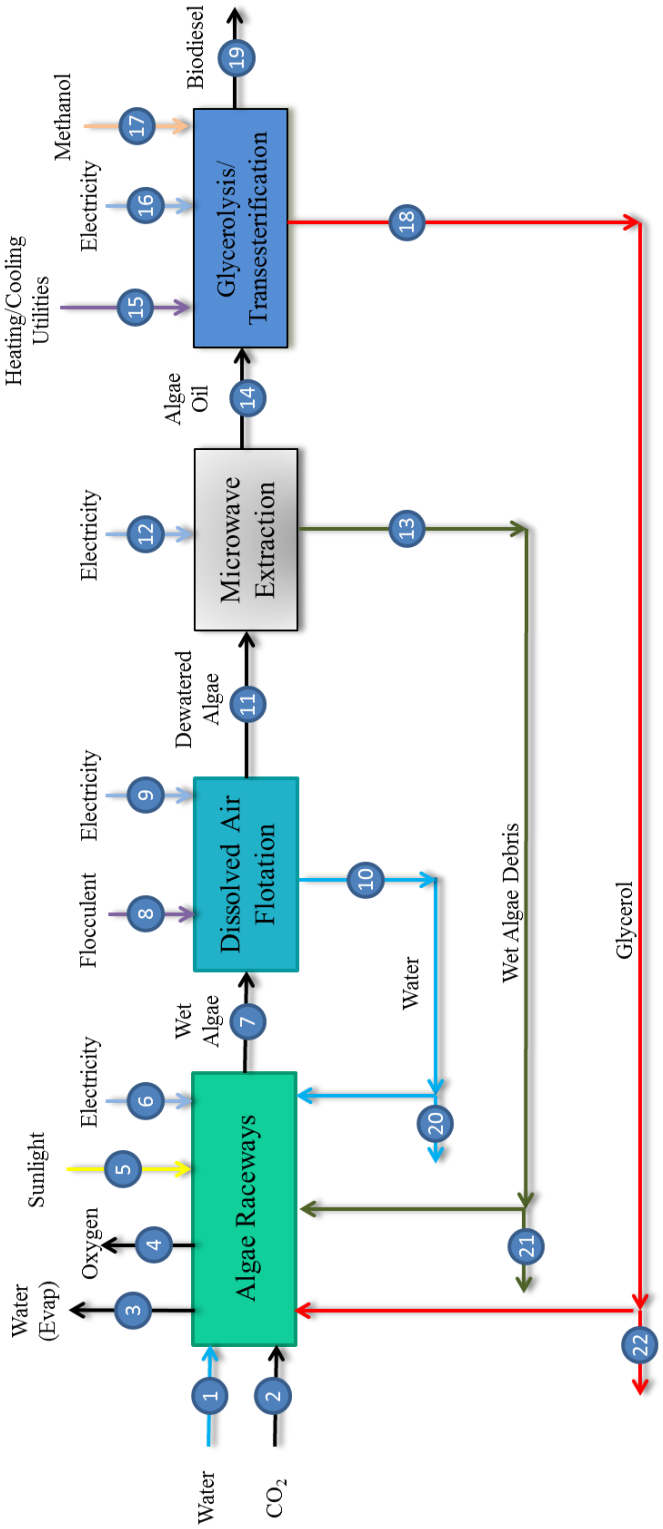

Figure 3.8. Overall block diagram.

Table 3.15. Major Stream Flow Rates

Stream #	Material	Flowrate	Units
1	Water	253	MM tonne/yr
2	CO_2	1.5	MM tonne/yr
3	Water	214.64	MM tonne/yr
4	O_2	1.49	MM tonne/yr
5	Sunlight	1.88E+08	MWh/yr
6	Electricity	483,000	MWh/yr
7	Algae + Water	1,188	MM tonne/yr
8	Flocculant	0.0041	MM tonne/yr
9	Electricity	475,000	MWh/yr
10	Water	1,166	MM tonne/yr
11	Water + Algae	22.18	MM tonne/yr
12	Electricity	137,500	MWh/yr
13	Water + Algae Debris	21.646	MM tonne/yr
14	Algae Oil	0.530	MM tonne/yr
15	Cooling Water + Heating Oil	141,364	MWh/yr
16	Electricity	5425	MWh/yr
17	Methanol	0.083	MM tonne/yr
18	Glycerol	0.042	MM tonne/yr
19	Biodiesel	0.530	MM tonne/yr
20	Water	37.231	MM tonne/yr
21	Water + Algae Debris	0.691	MM tonne/yr
22	Glycerol	0.001	MM tonne/yr

A profitability analysis was performed, using an investor's rate of return (IRR) of 10%, a project life at 15 years, a tax rate at 35%, and 2012 dollars. The back-calculated selling price of the biodiesel fuel was $4.34/gal, which is within 10% of the highest diesel price in 2012 ($4.12/gal) (Webpage: U.S. Retail Diesel Price). Note that like other studies, a tax rate of 35% was used for comparison with their diesel price estimates (to be shown in Table 3.17); the current U.S. Federal Income Tax rate is 40%.

The most crucial costing parameters from each section (raceway liner cost, harvesting cost, extraction cost, and the impact of degradation) were varied in a sensitivity analysis, by examining the resulting selling price of biodiesel. The results are shown in Table 3.16.

Table 3.16. Summary of Sensitivity Analyses

Scenario	Raceway Install Cost ($ per hectare)	Harvesting Technology*	Extraction Technology*	Percent of Oil Degraded	Selling Price of Biodiesel ($/gal)
Base Case	50,500	Flocculant/DAF	Microwaves	0	4.34
Cheap Raceways	10,000	Flocculant/DAF	Microwaves	0	3.2
Expensive Raceways	200,000	Flocculant/DAF	Microwaves	0	8.55
Cheap Harvesting	50,500	Ultrasonic Harvesting	Microwaves	0	3.51
Expensive Harvesting	50,500	Flocculant/Centrifuge	Microwaves	0	6.73
Expensive Extraction**	50,500	Flocculant/DAF	scCO2	0	6.53
Worst-case Extraction**	50,500	Flocculant/DAF	Beadmill Extraction	0	25.79
Oil Degradation	50,500	Flocculant/DAF	Microwaves	0.25	5.79

*See Table 3.8 and Table 3.9 for Harvesting and Extraction costs respectively.
**Note that the base case for extraction (microwaves) is the cheapest option.

Clearly, the two most crucial factors are the cost of the pond liners and the operating cost of the extraction technology. As mentioned in previous sections, the transesterification process has a relatively small effect on the economics. The cost of harvesting, while substantial, is not subject to as much variability among projections as either the costs of cultivation or extraction. Also, it is theorized that improvements in cultivation, which allow a denser concentration of algae culture, will provide the most

substantial decrease in the cost of harvesting. Therefore, efforts in the algae-to-biodiesel industry should focus primarily on improving cultivation techniques and scaling up extraction technologies.

3.6.7. Comparison with Economic Analyses by Others

The selling prices of biodiesel from algae-based studies were taken from five other sources (Davis et al., 2011; Gebreslassie et al., 2013; Martin and Grossmann, 2012; Richardson et al., 2012; Sun et al., 2011), which are shown in Table 3.17.

Table 3.17. Cost of Algal Oils and Biodiesel

Source	Cost of FAME ($/gal)
This Chapter	4.34
Sun et al. (2011)	14.39 - 17.53
Davis et al. (2011)	11.37
Richardson et al. (2012)	16.79
Martin et al. (2012)	0.42
Gebresiassie et al. (2013)	6.34

The Sun et al. results are based upon NREL, Sandia, NMSU, and Seambiotic estimates. They involve a mixture of processes; however, no specifics are provided. Davis et al. use ASPEN PLUS for simulation of their flowsheet. They compare open-pond raceways and photo-bioreactors for cultivation, and use flocculation with chitosan, centrifugation for harvesting, and high-pressure homogenizers for extraction. Richardson et al. examined the Davis et al. best-case scenario and coupled it with a risk analysis, accounting for events often ignored in other models (e.g., pond crashes).

Martin et al. created a process superstructure, which yielded a substantially lower selling price than other studies. Their optimization model used second-order surface-response methodologies, with parameters regressed from literature data. Martin et al. primarily focused their attention on the transesterification process options, which all other recent models (including this chapter) show to be a small fraction of the overall cost. As a result, they used crude approximations for cultivation, harvesting, and extraction operations, which drastically underestimated the production costs.

Gebreslassie et al. also created a process superstructure, which drew upon a wide array of literature data for parameter estimations, giving them more reliable values for process costs than Martin et al. However, Gebreslassie et al. used linear equations for all of their mass and energy balance constraints, and used a power-law scaling rule for their equipment sizing, making the accuracy of their calculations questionable.

Both the Sun and Davis articles focus heavily on technologies and processing methods available before the NAABB project, in contrast with this chapter, which presents an optimistic case based on emerging discoveries. The Richardson et al. model presents the worst-case scenario using pre-NAABB technologies. Martin et al. focused too heavily upon the transesterification process, which only accounts for a small fraction of the cost. While the Gebreslassie et al. model provides a good review of the available processes, it suffers from a lack of rigor.

In contrast with the other models, the Chapter 2 cultivation model is rigorous, but purely thermodynamic. Consequently, it represents the best achievable cultivation cost for a photosynthetic efficiency of 4% and a cell oil-concentration of approximately 37 wt%. As these two parameters are increased through research (improved cultivation

techniques and genetic modifications), the costs estimated herein will decrease. In addition, all lipid-extracted algae (LEA) is recycled to the cultivation section as feed to grow algae, which lowers the area required to produce a barrel of oil. While reductions are possible, the $4.34/gal selling price of FAME calculated herein is a low estimate compared with other studies of this type; it is meant to show what may be possible, rather than what is immediately practical.

3.7. Conclusions

This chapter created a rigorous techno-economic model of a complete algae-to-biodiesel process. The algae were grown using raceways, sequestered CO_2, and other nutrients. A harvesting step was used to dewater the algae, creating a concentrated algae slurry. During the extraction step, the algal lipids are separated from cellular debris and residual water. The acid content of the lipids is reduced using glycerolysis, before they are converted to biodiesel in a transesterification process. Meanwhile, the cellular debris and residual water are recycled to the cultivation stage. Recycling water lowers the amount of sea water pumped from a lake or ocean, and therefore, lowers pumping operating costs. The LEA recycle, on the other hand, reduces the land area required for algae cultivation, and thereby, lowers raceway and land capital expenditures.

A best-case ASPEN PLUS cultivation model (developed in Chapter 2), which computes a thermodynamic lower limit for the pond area, was used. Raceways were selected for cultivation due to their reduced costs relative to photo-bioreactors. Even so, pond construction represents the bulk of the cultivation CAPEX costs – a significant deterrent to an algae-to-biodiesel venture. As such, the cost and location of the land used

for cultivation drastically alters the process economics. Similarly, the algae species and its photosynthetic efficiency plays a key role in determining the cultivation cost, and therefore the viability of the process. The photosynthetic efficiency is examined in Chapter 4.

Dissolved-air flotation, coupled with a chitosan flocculent, was used for harvesting because it is both inexpensive and mature. Consequently, future research efforts should focus elsewhere for methods of drastically lowering the production cost of biodiesel. A microwave method was used for extraction. In the base case, extraction cost was not significant, but it had the largest variability. Therefore, the extraction was determined to be a crucial area of research for this thesis. A new method of algae-oil extraction, using supercritical CO_2, is discussed in Chapter 5.

Glycerolysis was needed to remove free fatty-acids. Afterward, many impurities were still present in the algae-oil. A rigorous ASPEN PLUS model was used to simulate the glycerolysis/transesterification process. It should be noted that glycerolysis and other pre-processing steps are often ignored in studies of this type; however, they are required to avoid catalyst denaturation and to meet transportation-grade quality specifications. The transesterification process has an almost insignificant cost; however, the glycerolysis process almost doubled the capital and operating costs of the conversion process. Further pre-processing steps could cause major unexpected expenditures that could make the cost of lipid upgrading prohibitive. The alternative is to use a more selective extraction processes to yield a cleaner oil feedstock, one of which is discussed in Chapter 5.

Finally, the selling price of biodiesel was calculated as $4.34/gal using a project life of 15 years, a tax rate of 35%, and an IRR of 10%. This cost is lower than most other

recent literature studies, due to the thermodynamic nature of our cultivation model. However, it is important to establish a lower-bound for the production cost of biodiesel to determine if the venture is worthy of further examination.

3.8. Nomenclature

Acronym	Term
AN	Acid number
APEA	Aspen Process Economic Analyzer
CAPEX	Capital expenditure
DG	Diglyceride
FAME	Fatty-acid methyl-ester
FFA	Free fatty-acid
GLY	Glycerol
HTL	Hydrothermal liquefaction
ICHEME	Institution of Chemical Engineers
IRR	Investor's rate of return
MG	Monoglyceride
NAABB	National Alliance for Advanced Biofuels and Bioproducts
OPEX	Operating expenditure
RT	Room temperature
TG	Triglyceride

CHAPTER 4

Exergy Efficiency of Photosynthesis

4.1. Introduction

Chapter 2 identifies the major process variables, which define the cultivation area as the extents of reaction, the heats of reaction, the influx of solar light, and the photosynthetic efficiency (Eq. 2.1). Chapter 3 identifies cultivation cost as the largest impediment to an algae-to-biodiesel venture, and therefore it becomes crucial to examine these variables. The extents of reaction are determined by the nutrients added to the pond; for example, in Chapter 2, urea is listed as the limiting resource or limiting reagent in the biomass production reactions. The heats of reaction are fixed by the reactants (CO_2 and water) and products (biomass and triglycerides), the former of which cannot be changed and the latter of which cannot be altered without significant modification of the process. The influx of solar light is dependent upon location and time of year, both of which are incorporated into the Biomass Assessment Tool (BAT) model (Webpage: NAABB Final Report). The only factor that remains is the photosynthetic efficiency, which depends on the algae strain(s) and cultivation techniques. Therefore, the only real degrees-of-freedom are the location, the algae strain, and the cultivation conditions, and only the last two can be meaningfully affected by engineering analyses – identifying the photosynthetic efficiency as the key to a cost effective algae-to-biodiesel venture.

The objective for this chapter, to develop a rigorous model for photosynthetic exergy efficiency, was initially proposed by Prof. Noam Lior of Mechanical Engineering and Applied Sciences at the University of Pennsylvania. Prof. Lior continued to support

the development of this research work until it was published in a journal article in *Chemical Engineering Science* (Silva et al., 2015). This chapter was then adapted from the completed journal article. It is designed to bridge the gap between literature studies (discussed in Section 4.2), which only consider the physical effects of photosynthesis (evaporation and carbon dioxide sequestration) (Petela, 2008; Reis and Miguel, 2006) and those that only examine the mechanism of the photosynthetic reactions (Lems et al., 2010). Exergy balances are constructed for solar light absorption, the two photosystems, ATP synthesis, the Calvin Cycle, plant metabolism, and environmental losses (transpiration and photorespiration). These, accompanied by a glossary in Appendix B, yield clearly defined exergy efficiencies that can be understood by both thermodynamicists and biologists, thus facilitating cooperation in this important area.

The exergy analysis requires the detailed description of the photosynthesis processes and reactions, which are presented in the following section.

4.1.1. Photosynthetic Organism Cell Physiology and System Description

Plant cells are composed of numerous organelles – enclosed portions of the cellular medium (or cytoplasm) with designated functions. A plant cell with the major organelles labeled is depicted in Figure 4.1a. It is beyond the scope of this chapter to explain all of the organelles. Instead, the focus is on the chloroplast, the organelle that captures sunlight, using it to convert carbon dioxide and water to organic matter (glucose herein). In terms of the analysis herein, two systems are specified and the efficiency is analyzed for each. For the first, the system boundaries are drawn around the chloroplast

organelle; whereas, the second system is the entire plant. An enlarged image of the chloroplast is shown as Figure 4.1b.

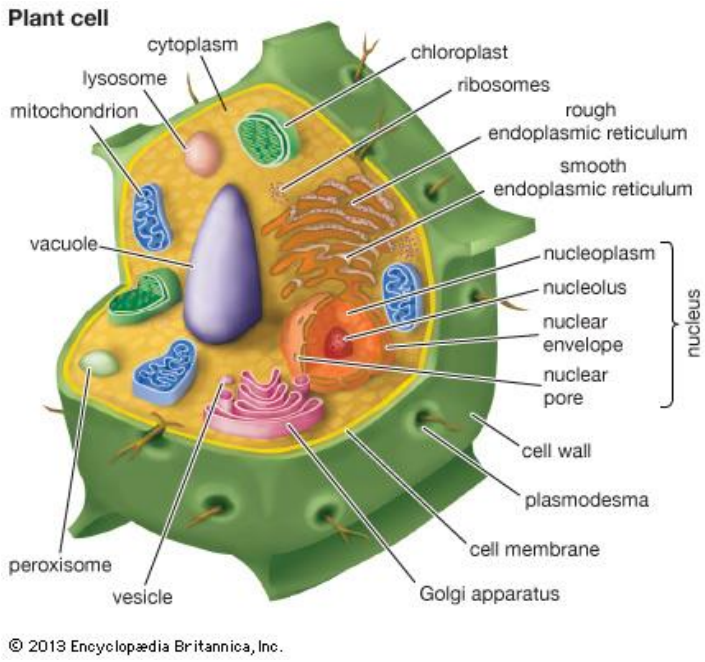

(a) Plant Cell with Organelles Labeled ((Webpage: Plant Cell Diagram), reproduced with permission). The nucleus is the information storage portion of the cell, where DNA is housed. In the rough endoplasmic reticulum (with ribosomes), proteins are manufactured using RNA (transcribed from DNA) as a template. The cell's fats and oils are manufactured in the smooth endoplasmic reticulum. Its proteins are "packaged" for transport outside the cell in the Golgi apparatus. Vesicles are the packages used for transporting species to and from the cell. Vacuoles are large vesicles used for storage within the cell. Peroxisomes are chambers used for the breakdown of fats and protein components, using peroxides. Lysosomes are chambers that contain strong enzymes that can break down virtually any organic molecules. Mitochondria are used to breakdown

organic sugars, like glucose, storing their chemical energy in intermediate ATP molecules.

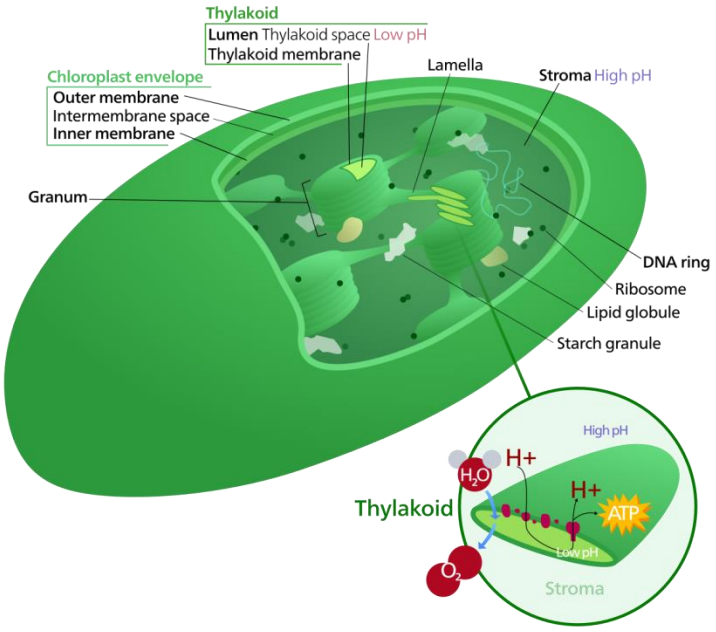

(b) Chloroplast diagram (Webpage: Chloroplast Diagram), where photosynthesis takes place (the focus of this chapter). Note that chloroplasts and mitochondria contain their own sets of DNA, which are used for the reproduction and maintenance of these organelles.

Figure 4.1. Plant cell and chloroplast diagrams.

The chloroplast is surrounded by two layers of membranes that isolate its internal solution (the stroma) from the cell's main cytoplasm. Inside the chloroplast are numerous thylakoids, compartments that contain light-absorbing pigments. These thylakoids are stacked into columns called granum. The internal space of the thylakoids (called lumen) are approximately 3.5 pH units lower than the stroma, which plant cells use to store potential exergy in the form of a proton gradient. This potential can be

converted to high-energy carrier molecules (ATP, Section 4.1.2) by a giant protein complex known as ATP synthase; this process is examined in more detail in Sections 4.3.1.3 and 4.4.1.3. An overall system diagram of the chloroplast is shown in Figure 4.2.

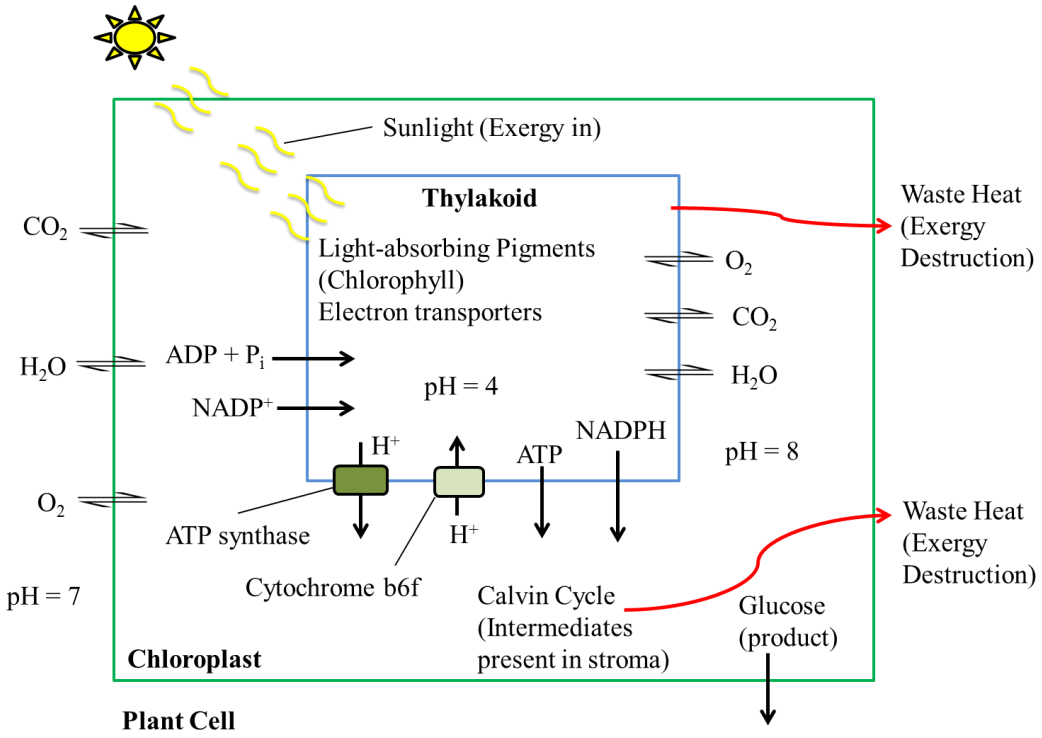

Figure 4.2. Chloroplast System Diagram.

As the double-sided arrows show, carbon dioxide, water, and oxygen are assumed to freely diffuse across the cellular boundaries while photosynthesis is occurring, and they are therefore in equilibrium in the compartments of the plant cell; the validity of this assumption is analyzed in the error analysis Section 4.5. Every chemical species discussed in this chapter – besides carbon dioxide, water, and oxygen – is present in the stroma, where the majority of the chemical reactions (in the Calvin Cycle – described in

Section 4.3.1.4) take place, with the concentrations of each species taken from the literature (Bassham and Buchanan, 1982). Exergy enters the system in the form of sunlight, which is absorbed by chlorophyll pigments. The pigments transform the sunlight's exergy into proton gradient exergy and electrical energy, which is stored in excited electrons (discussed in Section 4.1.2; see Figure 4.3). The electrical exergy and proton exergy drive the reactions that convert carbon dioxide and water to glucose and molecular oxygen (using the Calvin Cycle). All exergy not transferred into the chemical bonds of glucose is destroyed – lost to the environment as waste heat (approximately at ambient temperature).

4.1.2. Photosynthesis at a Glance

The overall reaction for photosynthesis (R4.1) and its standard Gibbs free energy change per mole of glucose, ΔG^o (Bassham and Krause, 1969; Voet et al., 2008) are:

$$6\,CO_2 + 6\,H_2O \xrightarrow[\text{light}]{} C_6H_{12}O_6 + 6\,O_2 \quad \Delta G^o = 2{,}872\ \frac{\text{kJ}}{\text{mol}} \qquad \text{(R4.1)}$$

Within the chloroplast, reaction R4.1 occurs as a series of steps decomposed into the "light" and "dark" reactions (Calvin Cycle). During the light reactions, large protein complexes (photosystem II and photosystem I) use chlorophyll pigment molecules (P680 and P700) to capture photons of light. The photons excite and displace electrons from these pigment molecules, leaving vacancies (Gust and Moore, 1985). The vacancies left by the displaced electrons are filled by splitting water, generating protons and oxygen gas, as shown in reaction R4.2 with the standard change in electrical potential, $\Delta\varepsilon^o$.

$$H_2O \rightarrow \frac{1}{2} O_2 + 2\,H^+ + 2\,e^- \quad \Delta\varepsilon^o = 0.81\,V \qquad \text{(R4.2)}$$

The excited, high-energy electrons proceed through a system of intermediate carriers (called the electron-transport chain or ETC) that pump protons against their gradient (into the lumen) and eventually reduce nicotinamide adenine dinucleotide phosphate ($NADP^+$), forming NADPH as shown in reaction R4.3. A diagram of the electron transport chain is presented as Figure 4.3, with specifics discussed in Section 4.3.2. This diagram was created with redox half-reaction potentials from the literature (Nicholls and Ferguson, 2002; Voet et al., 2008; Walz, 1997a, b, c). Two chemical reactions are described in this figure. The first involves splitting water into protons, oxygen, and electrons (which are then excited to a higher energy level, P680*). The second is the reduction of $NADP^+$ to NADPH using the high energy electrons and free protons. All other steps are the high-energy electrons passing through intermediate carriers, which are various functional groups in the protein complexes of PSII and PSI.

$$NADP^+ + H^+ + 2\,e^- \rightarrow NADPH \quad \Delta\varepsilon^o = -0.32\,V \qquad \text{(R4.3)}$$

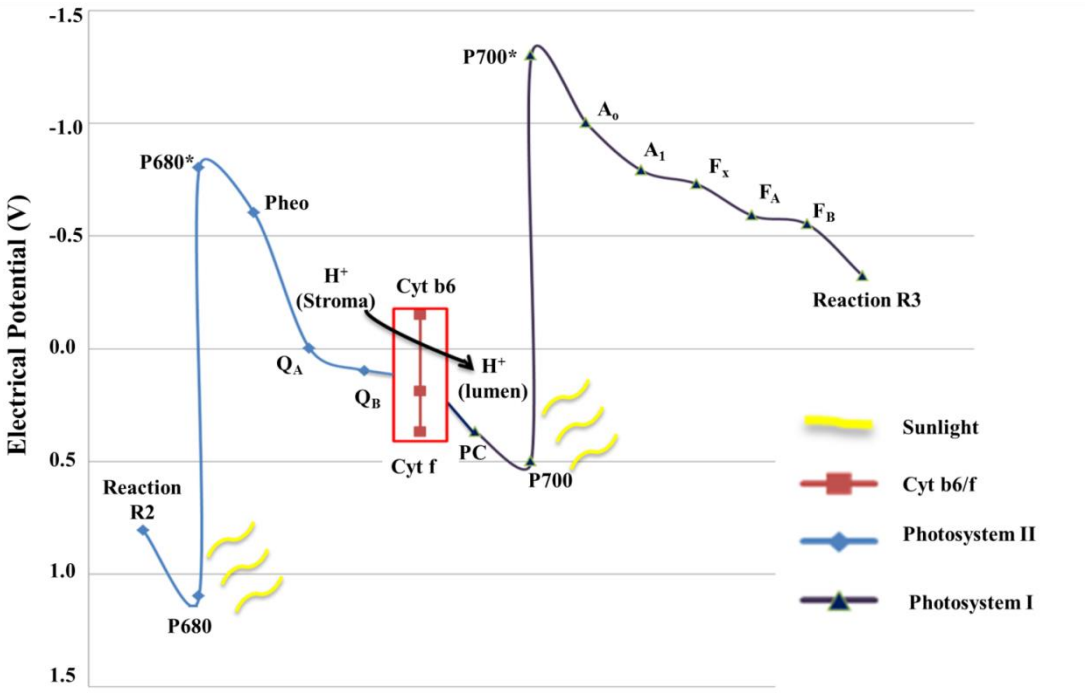

Figure 4.3. Transfer of high energy electrons through the photosystems*.

*Data taken from (Nicholls and Ferguson, 2002; Voet et al., 2008; Walz, 1997a, b, c)

The protons from water, as well as those pumped into the thylakoid membrane, flow down their concentration gradient and power ATP synthase, a proton turbine that drives the synthesis of water and adenosine triphosphate (ATP) from adenosine diphosphate (ADP) and phosphoric acid – shown as reaction R4.4. This is known as phosphorylation.

$$\mathrm{ADP} + \mathrm{P_i} \rightarrow \mathrm{ATP} + \mathrm{H_2O} \quad \Delta G^o = 32.8 \ \frac{kJ}{mol} \qquad \text{(R4.4)}$$

where P_i is phosphoric acid (H_3PO_4). Reactions R4.2, R4.3, and R4.4 make up the individual light reactions; the overall light reaction is shown in reaction R4.5 (Lehninger, 1971):

$$12\ NADP^+ + 18\ ADP + 18\ P_i + 48\ photons \rightarrow 12\ NADPH + 12\ H^+ + 18\ ATP + 6\ H_2O + 6\ O_2 \quad (R4.5)$$

During the dark reactions (or Calvin Cycle), the ATP and NADPH produced during the light reactions are consumed to convert inorganic carbon (carbon dioxide from the air) to organic carbon (glucose). Initially, three molecules of carbon dioxide are reacted with ribulose-5-phosphate to produce six molecules of 3-phosphoglycerate. The six molecules of 3-phosphoglycerate are reduced (using NADPH) and phosphorylated (using ATP), forming six molecules of glyceraldehyde-3-phosphate (GAl3P). One of these GAl3P molecules exits the cycle as the product. Meanwhile, the other five GAl3P molecules proceed through a series of isomerization and recombination reactions until the three molecules of ribulose-5-phosphate are regenerated. After two molecules of GAl3P have been produced, they are reacted to form glucose and phosphoric acid, the final products of photosynthesis. This series of reactions is described in more detail in Sections 4.3.1.4 and 4.4.1.4. The overall reaction is shown as reaction R4.6:

$$6\ CO_2 + 12\ NADPH + 12\ H^+ + 18\ ATP + 12\ H_2O \rightarrow C_6H_{12}O_6 + 12\ NADP^+ + 18\ ADP + 18\ P_i \quad (R4.6)$$

4.1.3. Definition of Exergy

Exergy (*B*) is a thermodynamic property that expresses the maximum (reversible) mechanical work necessary to produce a material (glucose, in this case) in its specified state from components common in the natural environment (carbon dioxide and water), heat being exchanged only with the environment (Szargut, 2005). Stated differently,

exergy is a measure of the quality of energy, obtained by combining the first and second laws of thermodynamics. A standard definition is shown as Eq. 4.1 (Keenan, 1951), where B is exergy, H is enthalpy, S is entropy, and T_o is the "dead-state" temperature (usually of the lowest relevant temperature of the surrounding environment).

$$B = H - T_o S \tag{4.1}$$

An exergy balance is defined based on the work of Szargut (Szargut, 2005), as shown in Eq. 4.2. Note that this formulation of the exergy balance was selected over the first principles approach (explicitly involving H and S), because this chapter focuses on a systems analysis of the chloroplast and not on thermodynamic derivations of properties.

$$B_{in} = B_{out,prod} + B_{out,waste} + \Delta B_{sys} + W_{sys} + \Sigma Q_{res}\left(1 - \frac{T_o}{T_H}\right) + \Sigma \delta B_i \tag{4.2}$$

where B_{in} is the incoming exergy of the flowing streams, $B_{out,prod}$ is the exergy leaving with the product streams, $B_{out,waste}$ is the exergy leaving with the waste streams, ΔB_{sys} is the exergy change of the system, W_{sys} is the work performed by the system, Q_{res} is the heat transferred from the system (at temperatures T_H) to a reservoir, T_o is the temperature of the "dead state", T_H is the "hot" temperature of the system, and $\Sigma \delta B_i$ is the sum of internal exergy losses (also called exergy destruction or lost work) due to irreversibilities within the system.

The "dead state" is described by the conditions (temperature, pressure, and concentration) of a system's environment at which no more useful work can be extracted from a system interacting with this environment, and it is usually closely related to the

ambient conditions surrounding a system. The dead state is defined herein as at a temperature of 298.15 K, a pressure of 1 atm, and a concentration of 1 mol/L in solution (except for carbon dioxide and oxygen, whose exergies are calculated relative to their gaseous states at this temperature and pressure, and water – whose exergy is calculated relative to saturated steam at 298.15 K). These conditions were chosen to facilitate easy comparison with previous literature studies, which have used this dead state as their reference state.

Each of the exergy terms in Eq. 4.2 can be decomposed into the physical, chemical, electrical, and solar exergy components, as shown in Eq. 4.3. The meaning of each of these terms is defined in more detail in Section 4.3.

$$B_j = B_{\text{phys},j} + B_{\text{chem},j} + B_{\text{elec},j} + B_{\text{photon},j} \tag{4.3}$$

where B_j is the exergy of a particular stream or system; $B_{\text{phys},j}$ is the physical exergy, which is due to temperature and pressure effects; $B_{\text{chem},j}$ is the chemical exergy, which is due to chemical mixing and reactions; $B_{\text{elec},j}$ is the exergy of electrical effects; and $B_{\text{photon},j}$ is the exergy of sunlight.

Typically, biological systems operate at or near ambient temperatures and pressures; therefore, physical effects are small or negligible herein. For chemical exergy, the method described by Lems et al. (Lems et al., 2007) is used. For the electrical effects, redox chemical methods are used, modified for system concentration (Lems et al., 2010; Nicholls and Ferguson, 2002). Lastly, the exergy effects of solar radiation are analyzed using the equations for photons (Lems et al., 2010; Zhu et al., 2008). The equations that describe each of these phenomena are presented in Section 4.3.

4.2. Literature Review

The mechanism of photosynthesis has been known for decades, but conflicting definitions for the exergy efficiency remain, leading to efficiencies that span orders of magnitude (41% (Lems et al., 2010) to 2.6% (Petela, 2008)). Most studies that attempt to rectify this problem present yet more definitions and more variations in efficiency. The two main types of studies consider either the physical effects (evaporation, carbon dioxide sequestration, temperature changes) and ignore the complex mechanism of the photosynthetic reactions (Petela, 2008; Reis and Miguel, 2006), or the converse (Lems et al., 2010). This chapter incorporates both biological and mechanical effects to create a more complete picture.

The exergy property has been adopted in recent analyses of photosynthesis (Bisio and Bisio, 1998; Lems et al., 2010; Petela, 2008), but many of the earlier studies used the Gibbs free energy (defined in Eq. 4.4) to calculate the "energy efficiency," (Asimov, 1968; Bassham and Buchanan, 1982; Lehninger, 1971), although enthalpy or internal energy are the appropriate variables for energy balances. Since biochemical reactions occur at approximately the ambient (or dead-state) temperature and pressure, the Gibbs free energy is essentially equal to the exergy (comparing Eq. 4.3 to Eq. 4.4). This assumption is applied in this chapter solely as a means of comparison (see Section 4.5 for more details).

$$G = H - TS \tag{4.4}$$

where G is the Gibbs free energy, H is the enthalpy, S is the entropy, and T is the temperature of the system.

Initially, the efficiency of photosynthesis was calculated by dividing the Gibbs free energy change of reaction R4.1 by the exergy contained in the photons (experimentally measured) (Asimov, 1968). It should be noted that these early studies used the energy values for photons; however, the exergy and energy values for photons differ only by approximately 5% (Section 4.3.1.1). This approach is shown as Eq. 4.5, and yielded exergy efficiencies between 32-37%.

$$\eta_{PS} = \frac{\Delta G_{rxn,R4.1}}{\Sigma B_{photon}} = \frac{2{,}976}{8{,}033} = 37\% \quad (4.5)$$

where η_{PS} is the exergy efficiency of photosynthesis, $\Delta G_{rxn,R4.1}$ is the Gibbs free energy change of reaction R4.1, and ΣB_{photon} is the summation of the exergies for the photons required to drive reaction R4.1. Later studies (Albarran-Zavala and Angulo-Brown, 2007; Bassham and Buchanan, 1982; Lehninger, 1971) separated photosynthesis into the light reactions (R4.5) and the dark reactions (R4.6). The efficiencies of the light reactions were calculated using Eq. 4.5, replacing $\Delta G_{rxn,R4.1}$ with $\Delta G_{rxn,R4.5}$. The efficiency of the dark reactions was then calculated by comparing the Gibbs free energies of synthesizing glucose (R4.1) with those of NADPH and ATP, shown in Eq. 4.6. The total efficiency for the combined reactions was given by Eq. 4.7, where η_{LR} is the exergy efficiency of the light reactions and η_{CC} is the exergy of the Calvin Cycle (dark reactions, Sections 4.3.1.4 and 4.4.1.4). Efficiencies calculated using Eq. 4.7 are equivalent to those calculated using Eq. 4.5.

$$\eta_{CC} = \frac{\Delta G_{rxn,R4.1}}{12*\Delta G_{rxn,(R4.2+R4.3)}+18*\Delta G_{rxn,R4.4}} \quad (4.6)$$

$$\eta_{PS} = \eta_{LR}\eta_{CC} \tag{4.7}$$

The next phenomenon, which was elucidated by experimental studies of chloroplast light absorption (Chain and Arnon, 1977), was that the photosystems (PSII and PSI) had limited ranges of absorption. In addition, models were constructed to represent the effects of light reaching the organism, and how the organism behaved with relation to the light-source and its environment (Albarran-Zavala and Angulo-Brown, 2007; Barber, 2009; Bisio and Bisio, 1998; Bolton and Hall, 1991; Petela, 2008). The standard range of absorption is known as the photo-active region (PAR), and is defined as the wavelength range from 400 nm to 700 nm (Bassham and Buchanan, 1982; Bolton and Hall, 1991). The relative exergy density within this region is determined using Planck's radiation distribution function (shown as Eq. 4.8) and accounting for the solar spectrum at the earth's surface (Zhu et al., 2008). Note that energy density and exergy density are the same, since they are expressed on a relative basis and for sunlight the two only differ by a factor of ($1\text{-}T_{\text{earth}}/T_{\text{sun}}$). From Eq. 4.8, the PAR region comprises roughly 43% of the total solar exergy at the earth's surface (Bassham and Buchanan, 1982; Bolton and Hall, 1991), and the revised definition of photosynthetic exergy efficiency follows (Eq. 4.9), yielding an efficiency of approximately 13% (Bolton and Hall, 1991).

$$SR(\lambda) = \frac{2*h*c^2}{\lambda^5} * \frac{1}{e^{\left(\frac{h*c}{\lambda*k_B*T_S}\right)}-1} \tag{4.8}$$

$$\eta_{PS} = \eta_{PAR}\eta_{LR}\eta_{CC} \tag{4.9}$$

From here, there is a large divergence in the literature. Many authors calculate the photosynthetic energy and exergy efficiencies by employing heuristic estimations for the efficiencies (η) (Barber, 2009; Bugbee and Monje, 1992; Thorndike, 1996) or fractions lost (σ) (Bisio and Bisio, 1998) to the various sub-processes, as shown in Eq. 4.10 and 4.11. These factors typically involve the light reactions, the Calvin Cycle, photorespiration (Bisio and Bisio, 1998; Kelly and Latzko, 2006d; Lems et al., 2010; Zhu et al., 2008) (Sections 4.3.2.3 and 4.4.2.3), photo-inhibition (Berry and Downton, 1982; Kelly and Latzko, 2006d), cellular metabolism (Bisio and Bisio, 1998; Zhu et al., 2008), and other stressors (most of these effects are defined in the glossary, Appendix B). Efficiencies derived from these equations are usually in the range of 2–13%, depending on the factors included.

$$\eta_{PS} = \prod_i \eta_i \tag{4.10}$$

$$\eta_{PS} = \prod_i (1 - \sigma_i) \tag{4.11}$$

Three in-depth exergy studies have been conducted on photosynthesis within the last decade. The first study, by Reis et al. (Reis and Miguel, 2006), presents an exergy balance with a plant as the control volume, examining solar exergy and water fluxes throughout the system. However, the complex mechanisms occurring within the organism are ignored, and thus, the majority of the exergy lost is attributed to an "internal exergy destruction" term, which does not provide insight about how to improve the efficiency. Petela (Petela, 2008) completed a similar, more complex analysis—analyzing the incoming solar radiation, the diffusive fluxes of chemical species, convective heat

transfer between the leaf and the surroundings, and radiation emissions by the leaf. His calculations yield an exergy efficiency of 2.6%. However, the most substantial exergy efficiency loss (~93 percent) is due to the vaporization of liquid water, in which the plant dissipates excess heat. Thus, it provides no information on how to improve the efficiency. Lems et al. (Lems et al., 2010) performs an exergy analysis of the light and dark reactions of photosynthesis, using photon consumption data from Voet et al. (Voet et al., 2008). They calculate exergy efficiencies for PSII, PSI, ATP synthase, two different versions of the Calvin cycle, and the overall process (41 percent). However, the effect of poor absorbance outside the PAR and other physical phenomena are not taken into account.

Finally, Melis (Melis, 2009) completes a superficial theoretical energy efficiency calculation before comparing it with experimentally measured energy efficiencies for various plants and algae. His results show that the energy efficiencies of actual organisms are 3 to 50 times smaller than the theoretical efficiencies due to saturation effects in photosystem II (Sections 4.3.1.2 and 4.4.1.2) and the Calvin Cycle (Sections 4.3.1.4 and 4.4.1.4).

4.3. Methods

The analysis in this section and Section 4.4 is separated into processes contained within the chloroplast and those performed by the plant as a whole. The reason for this distinction is that chloroplasts should, in theory, perform similarly for all C3 plants. Issues concerning the overall organism (drawing water in through the roots, dealing with photorespiration, and metabolism), however, are much more dependent upon the environment, the season and time of day, and the age of the organism. In addition, this

division provides guidance toward improving the efficiency using genetic modifications to adjust the chloroplast, as compared with improving the plant-based inefficiencies, which depend, for example, on the availability of water.

4.3.1. Chloroplast Considerations

The methods for calculating the exergy required to synthesize one mole of glucose in the light and dark reactions (within the chloroplast) are presented in this section, with calculation results in Section 4.4.1. A qualitative exergy-flow diagram involving the four major steps of the process is shown as Figure 4.4. The Color Key describes the type of exergy flows between the different biological operations, as expressed in Eq. 4.3.

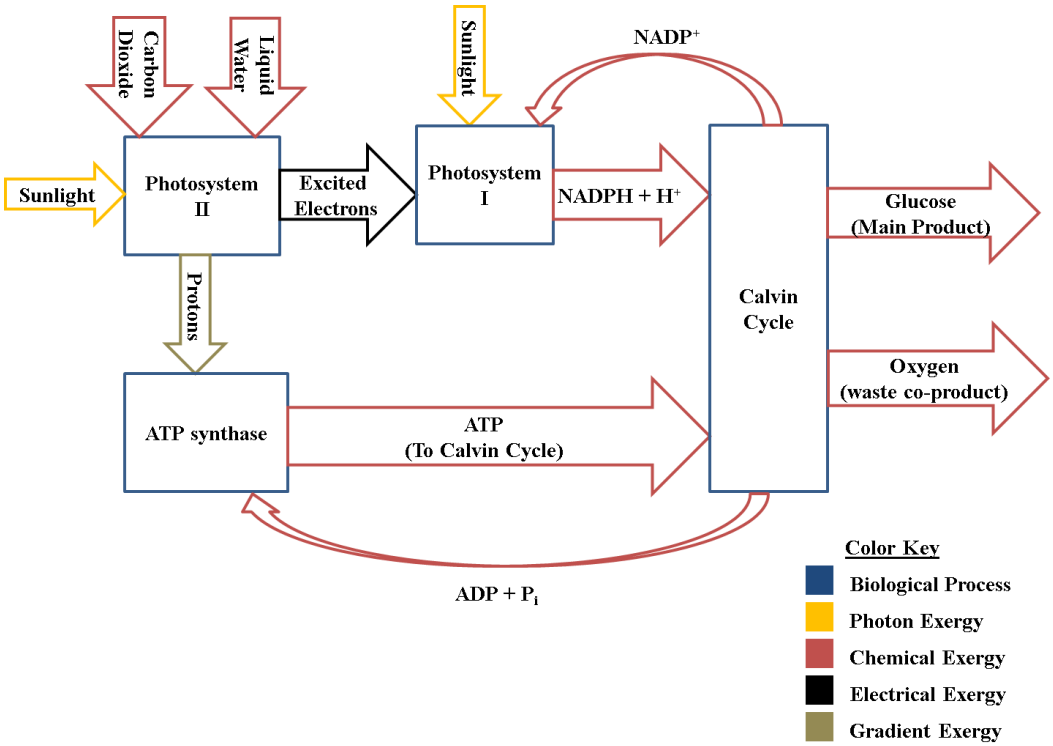

Figure 4.4. Qualitative Exergy-Flow Diagram.

The physical and biological processes are subdivided as much as possible to estimate exergy flows through the latest photosynthetic mechanisms. The exergy required to drive reaction R4.1 is the desired output, and its ratio to the total exergy input yields the exergy efficiency. To better resolve the mechanisms, several variables are analyzed, including the exergy of photons and their imperfect absorption, the electron transport chain, the proton-motive force (PMF) and ATP synthase, and the biochemical reactions of the Calvin Cycle.

Inefficiencies due to shading and indirect sunlight are not taken into account, because these effects depend upon the organism growth location, which negatively impacts any solar radiation collector. Carbon dioxide and oxygen within the chloroplast are assumed to be in equilibrium with the surrounding environment. Water is assumed to be available in excess. This assumption is dealt with in Section 4.3.2.2., as drawing water from the surrounding environment is achieved by the entire organism, not the chloroplast.

4.3.1.1. Sunlight and Absorption

Photosynthesis begins with the absorption of packets of light (photons) by light-sensitive pigments in the chloroplasts. These light-absorbing pigments are called chlorophyll, and each chlorophyll type has a different radiation absorption spectrum. All of the exergy used in photosynthesis originates from photons (except for the chemical exergy of CO_2 and water), which are collected and converted to chemical exergy during the light reactions. To determine the exergy of a mole of photons, a modified form of Planck's Law (Eq. 4.12) is applied (Lems et al., 2010; Voet et al., 2008). Note that the

only difference between Planck's Law and Eq. 4.12 is the factor $(1 - \frac{T_{\text{earth}}}{T_{\text{sun}}})$, which accounts for a 5 percent difference between the energy and exergy of photons:

$$B_{\text{photon}}(\lambda) = N_{\text{A}} \frac{hc}{\lambda} (1 - \frac{T_{\text{earth}}}{T_{\text{sun}}}) \tag{4.12}$$

where B_{photon} is the photon exergy (J/mol photons) at a given wavelength (λ), N_{A} is Avogadro's number (6.023×10^{23}), h is Planck's constant (6.626×10^{-34} J×s), c is the speed of light (3×10^{8} m/s), λ is the wavelength (m), T_{earth} is the ambient temperature of the earth (298.15 K), and T_{sun} is the temperature of the sun's surface (5,762 K) (Lems et al., 2010).

Photosynthetic pigments can absorb only certain ranges of wavelengths, and imperfectly at that. Plants primarily absorb sunlight in the photo-active region (PAR), which is defined to be from 400-700 nm (Bolton and Hall, 1991). A plot of the percentage of sunlight energy absorbed as a function of photon wavelength (Eq. 4.8) is shown as Figure 4.5 (Webpage: Introduction to Ozone). The types of solar electromagnetic radiation are shown, along with their wavelengths and the relative amount of energy they represent. The region of interest for photosynthesis is 400-700 nm, the photo-active region (PAR), which represents only 43% of the total incoming energy/exergy. Note that this is on a relative basis, so that percentages of energy and exergy absorption are the same. Factors are available for relative absorption within certain wavelength regions (Petela, 2008).

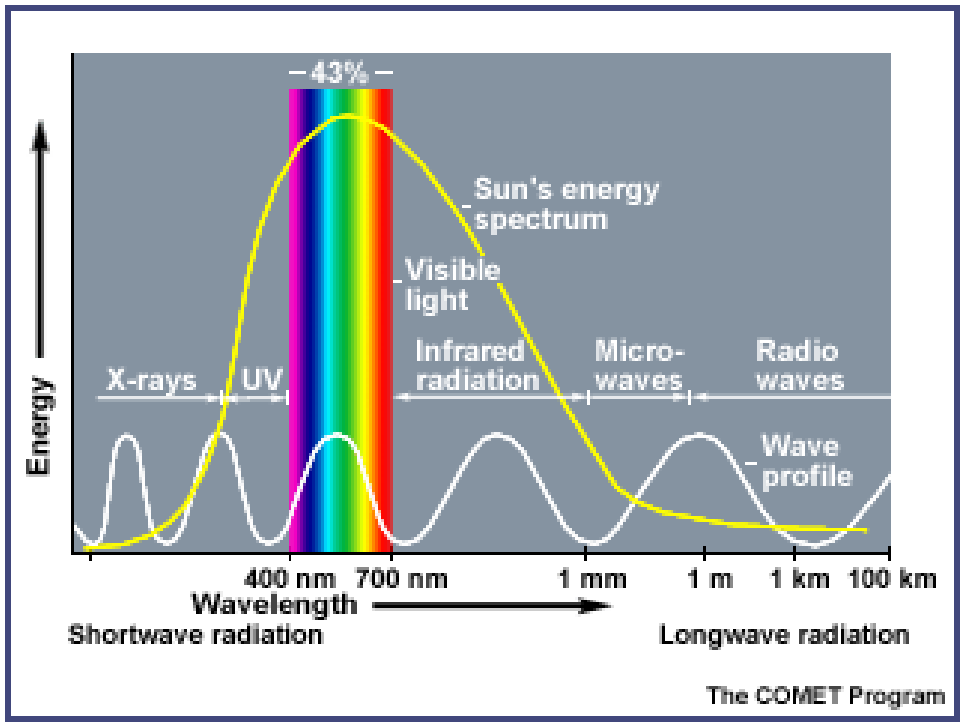

Figure 4.5. Energy absorbed as a function of wavelength of sunlight*.

*Reproduced with permission from the COMET Program (Webpage: Introduction to Ozone).

Because the calculation of photon exergy involves moles of photons, it is important to determine the average exergy for the entire mole, and to do this, the average exergy of the photon range must be taken into account. The mean-value theorem, shown as Eq. 4.13, is useful for finding the average of a continuous function over a well-defined interval (Webpage: Mean Value Theorem). More specifically, for a continuous function, $f(x)$, on a closed interval $[a, b]$, the mean-value theorem states:

$$f(c) = \frac{1}{b-a}\int_a^b f(x)dx \tag{4.13}$$

where $f(c)$ is the average value of $f(x)$ on the interval $[a, b]$. Applying the mean-value theorem to Eq. 4.12, yields:

$$B_{\text{photon,avg}} = N_{\text{A}} hc \left(1 - \frac{T_{\text{earth}}}{T_{\text{sun}}}\right) \frac{Ln(\lambda_{\text{high}}) - Ln(\lambda_{\text{low}})}{\lambda_{\text{high}} - \lambda_{\text{low}}} \qquad (4.14)$$

where $B_{\text{photon,avg}}$ is the average photon exergy (J/mol photon), N_{A} is Avogadro's number (6.023×10^{23}), h is Planck's constant (6.626×10^{-34} J×s), c is the speed of light (3×10^{8} m/s), and λ_{high} is the maximum wavelength (m), λ_{low} is the minimum wavelength (m), T_{earth} is the ambient temperature of the earth (298.15 K), and T_{sun} is the temperature of the sun's surface (5,762 K).

4.3.1.2. Electron Transport Chain

Returning to Figure 4.3, photons are absorbed by the electrons within light-absorbing pigments (P680 and P700). The electrons are excited to a higher energy state, moving farther away from the pigment's core (the nuclei of a magnesium atom within a functional group called a chlorin, which is explained in the Glossary – Appendix B). Following the principle of charge-separation (Barber, 2009; Gratzel, 2001; Gust and Moore, 1985, 1989; Gust et al., 1998, 2001; Kim et al., 2012; Luo et al., 2013), the electrons are drawn away from the pigment by a series of intermediate carriers (Q_A, Q_B, PC, A_o, A_1, F_X, F_A, and F_B) forming an electron-transport chain (ETC). It is beyond the scope of this article to focus on the intermediate carriers; see references (Nicholls and Ferguson, 2002; Walz, 1997a, b, c) for specifics. The excited forms of both the pigments and intermediate carriers exist for only several nanoseconds (Scholes et al., 2012). In terms of exergy losses, these intermediate carriers are analogous to resistors in a wire, in that the electrons pass through, dissipating some of their potential as waste heat.

In exergy balances for carrier *i* (Eq. 4.15), exergy that passes through an electron carrier is passed to the next carrier, used to do work within the chloroplast, or lost to the environment as low-grade, waste heat (exergy destruction):

$$B_{\text{carriers},i} = B_{\text{carriers},i-1} + W + \delta B \tag{4.15}$$

where $B_{\text{carrier},i}$ is the exergy of carrier *i*, *W* is the work performed by the electron transfer, and δB is the exergy destroyed. The standard reduction potential is expressed by Eq. 4.16:

$$\Delta G^o = -nF\Delta\varepsilon^o \tag{4.16}$$

where ΔG^o is the standard Gibbs free energy change, *n* is the number of moles of electrons, *F* is the Faraday constant (96,485 Coulomb/mol e^-), and $\Delta\varepsilon^o$ is the standard change in reduction potential. It can be modified to account for the effects of intracellular concentrations and used to calculate the exergy difference between electron carriers (Lems et al., 2010):

$$\Delta B_{\text{elec}} = B_{\text{carriers},i} - B_{\text{carriers},i-1} = nF\Delta\varepsilon^o + RT_o\text{Ln}(\prod[A]_i^{-\upsilon_i}) \tag{4.17}$$

where ΔB_{elec} is the exergy difference between carriers i and $i - 1$, *R* is the universal gas constant (8.3143 J/mol-K), T_o is the ambient temperature (298.15 K), $[A]_i$ is the activity of carrier *i*, and v_i is the stoichiometric coefficient of carrier *i*. The changes in exergy are presented in Tables 4.1 and 4.2 in Section 4.4.1.2. Comparing the changes of exergy throughout the system with the amount consumed by useful work reveals the sources of exergy destruction (Eq. 4.15).

4.3.1.3. ATP Synthase

ATP synthase is an assembly of hydrophobic and hydrophilic proteins that form a transmembrane protein-complex, containing a proton-translocation channel (Voet et al., 2008). As protons flow down their concentration gradient, ATP synthase acts as a turbine, using the proton-motive force (PMF) to drive its shaft. The shaft of ATP synthase forces ADP and phosphoric acid together and supplies the necessary exergy for them to react, yielding ATP and water. ATP synthase can also function in reverse, consuming ATP to pump protons against their concentration gradient. A picture of ATP synthase is shown as Figure 4.6 (Webpage: ATP synthase). The pink spheres represent protons, the violet spheres represent phosphoric acid, and the blue spheres represent adenosine. As the protons flow down their concentration gradient (from the inside of the thylakoid, into the stroma), they turn the top of ATP synthase, as depicted by the arrows. The work from turning the top is transferred down the shaft (central or thinnest part of the protein complex), powering the lower section. The lower section uses the shaft work to force ADP and phosphoric acid to react, generating ATP and water. Note that for chloroplasts, four protons must flow from the lumen to the stroma to produce one ATP molecule (Zhu et al., 2008).

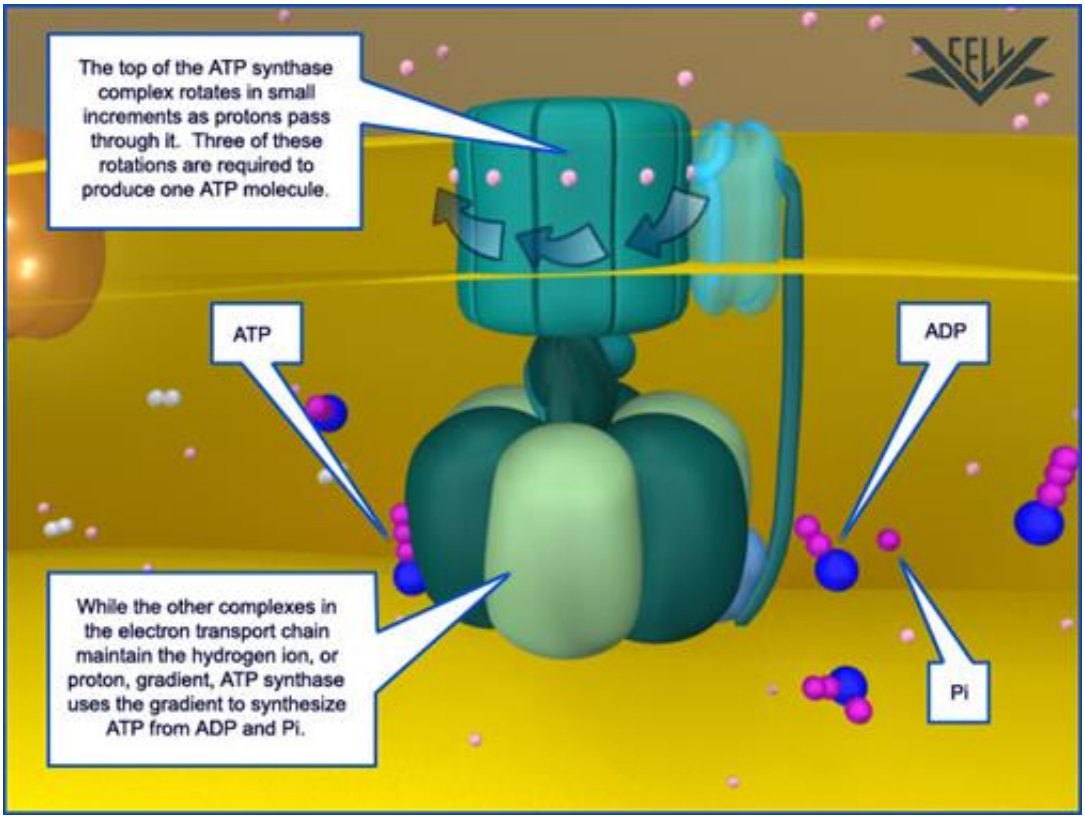

Figure 4.6. Schematic of ATP synthase*.

*Reproduced with permission from NDSU VCell Animation Project (Webpage: ATP synthase).

4.3.1.4. Dark Reactions/Calvin Cycle

The Calvin Cycle is the process by which inorganic carbon (carbon dioxide from the air or bicarbonate in solution) is reduced and converted to organic sugar molecules (glucose in this analysis). Figure 4.7 shows the chemical reaction mechanism as presented by Bassham and Buchanan (Bassham and Buchanan, 1982), modified to include the reaction numbers (used in Table 4.3), as well as to highlight the product-producing steps (red ovals). Note that the number of lines per arrow is the number of times a reaction occurs to produce one molecule of glyceraldehyde-3-phosphate (GAl3P) – the intermediate product. Two molecules of GAl3P are consumed to produce one

molecule of glucose-6-phosphate (G6P; repeating reactions C5, C6, and C7, followed by reaction C14), which is then converted to glucose by hydrolysis (not shown in Figure 4.7). Finally, reactions C1–C15 are shown in Table 4.3; whereas, the abbreviations for the species names, and thermochemical properties of the species and reactions, are given in Appendix A, Table A.1.

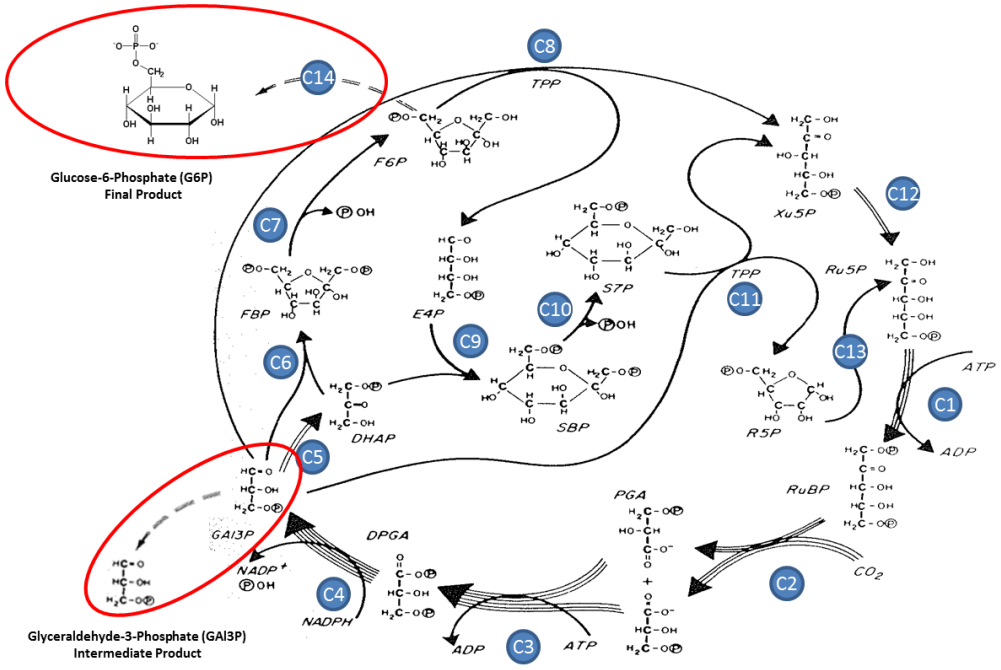

Figure 4.7. The Calvin Cycle*.

*Reproduced with permission (Bassham and Buchanan, 1982).

The dark reactions are assumed to occur isothermally and isobarically, with exergy changes due only to chemical effects. All reaction exergy losses are released as low-grade heat (the driving force). For each molecule in the reactions, its chemical exergy is estimated using the method of Lems et al. (Lems et al., 2007):

$$B_{\text{chem}} \approx \sum_k \left(\upsilon_k B_{\text{element},i}\right) + \Delta G_{\text{f}}^{o} + RT_{\text{o}}\text{Ln}[A] + RT_{\text{o}}\text{Ln}\left(1 + \sum_i \frac{\left(\prod_{l=1}^{i} K_l\right)}{[H^+]^i}\right) +$$

$$RT_{\text{o}} \sum_j \text{Ln}\left(1 + \sum_i^n \left(\prod_{l=1}^{i} K_l\right) \left[M_j\right]^i\right) \quad (4.18)$$

where B_{chem} is the chemical exergy of a species (per mole), ν_i is the number of times that atom *k* occurs in the species (stoichiometric coefficient when forming the species from reference atoms), $\Delta G_{\text{f}}^{\text{o}}$ is the standard Gibbs free energy of formation of the species, *R* is the universal gas constant, T_{o} is the dead-state temperature (298.15 K), [*A*] is the activity of the species, K_l is the chemical equilibrium constant (for either acid, base, or metal ion dissociation) for reaction *l*, $[H^+]$ is the hydrogen ion concentration, $[M_j]$ is the concentration of metal ion *j*, *k* is the atom counter, *i* and *l* are the reaction counters, and *j* is the metal ion counter.

4.3.2. Plant Considerations

Five issues are considered for the organism as a whole: chloroplast performance (Section 4.3.1), sunlight reflection by the leaves (Section 4.3.2.1), transpiration (Section 4.3.2.2), photorespiration (Section 4.3.2.3), and plant metabolism (Section 4.3.2.4). These issues were chosen because they relate directly to the organism's performance in converting sunlight, carbon dioxide, and water into biomass. Other factors, such as incident sunlight and the effects of water quality, are site dependent and thus not considered here.

4.3.2.1. Sunlight Reflection

Some of the incident light is reflected by the surfaces of the leaves or other portions of the plant cells before the light reaches the chloroplasts. This phenomenon has been mentioned by two different authors (Bisio and Bisio, 1998; Petela, 2008); however, little discussion on the specifics was presented by either source. Again, inefficiencies due to shading and indirect sunlight are not taken into account, because these effects depend upon the organism growth location, which negatively impacts any solar radiation collector.

4.3.2.2. Transpiration

While plants perform photosynthesis, their pores (stomata) remain open, permitting carbon dioxide to diffuse in and oxygen to diffuse out. Water, which enters plants through their roots, is pumped into their leaves, and emitted by transpiration through their stomata. In this way, the plant cells accumulate water, which is then used by chloroplasts in Photosystem II.

Exergy losses by transpiration are estimated using Eq. (4.19)–(4.21), used by Reis et al. (Reis and Miguel, 2006). Saturated steam at T_o is the reference state for water, with liquid water at a lower exergy. Note that the chloroplasts (and leaves) are assumed to be at the environmental temperature, and carbon dioxide and oxygen are assumed to be in equilibrium with the surrounding environment. The total exergy loss is estimated by raising the water in the plant stem to height, z, and accounting for evaporation. In addition, the effect of humidity in the air must be accounted for because, for locations remote from the sea, the concentration of water vapor in the ambient air may be the most

important factor in determining the chemical exergy of water; the last term in Eq. 4.19 accounts for this phenomena (Szargut, 2005).

$$B_w = (H - H_o) - T_o(S - S_o) + M_w g z - RT_o \mathrm{Ln}(\Phi_o) \quad (4.19)$$

$$WC = r/\phi - r \quad (4.20)$$

$$\delta B_{Gluc} = (WC)B_w \quad (4.21)$$

where B_w is the exergy of liquid water in the leaf (J/mol), T_o is the dead state temperature (298.15 K), H is the enthalpy of liquid water (J/mol), H_o is the enthalpy of saturated steam (J/mol) at T_o, S is the entropy of liquid water (J/mol-K), S_o is the entropy of saturated steam (J/mol-K) at T_o, g is the gravitational acceleration (9.81 m/s^2), M_w is the molecular weight of water (0.01802 kg/mol), Φ_o is the relative humidity, R is the universal gas constant (8.3143 J/mol-K), ϕ is the fraction of water used in photosynthesis (the remainder is lost to evaporation), r is the ratio of water to glucose in reaction R4.1, WC is the number of moles of water lost to evaporation without being used in the reaction, and δB_{Gluc} is the exergy destruction due to transpiration per mole of glucose produced.

4.3.2.3. Photorespiration

Ribulose-1,5-bisphosphate carboxylase/oxygenase (RuBisCO) is the enzyme in the Calvin Cycle that catalyzes the reaction of carbon dioxide with ribulose-1,5-bisphosphate (RuBP) in reaction C2, fixing carbon dioxide as organic carbon. About 1/3 to 1/4 of the time (Kelly and Latzko, 2006c), RuBisCO fixes oxygen (instead of carbon dioxide) to RuBP, forming one molecule of 3-phosphoglycerate (PGA) and one molecule

of 2-phosphoglycolate (Kelly and Latzko, 2006d, e), as shown in Figure 4.8 (Webpage: Photorespiration wikicommons). This is known as photorespiration (Kelly and Latzko, 2006e). The cell then initiates a series of chemical reactions, which convert the 2-phosphoglycolate to PGA and carbon dioxide (not shown in Figure 4.8); the former reenters the Calvin Cycle (Kelly and Latzko, 2006d, e). Because most of these chemical reactions occur outside the chloroplast, photorespiration has been treated as associated with the entire plant. It is noteworthy, however, that the reaction that initiates this process (RuBisCO fixing oxygen) occurs exclusively inside the chloroplast.

In Figure 4.8, the green oval represents the chloroplast, where the Calvin Cycle (CC) takes place. RuBisCO, the enzyme responsible for fixing carbon dioxide in reaction C2 (Figure 4.7), can also fix oxygen, which leads to the cycle shown here, producing 2-phosphoglycolate and 3-phosphoglycerate (molecules 3 and 2, respectively). 3-phosphoglycerate can reenter the Calvin Cycle immediately (reaction C3 in Figure 4.7), but 2-phosphoglycolate must be converted to 3-phosphoglycerate before it can be returned to the Calvin Cycle. The conversion of 2-phosphoglycolate to 3-phosphoglycerate occurs between three organelles: the chloroplast, the peroxisome (shown in pink), and the mitochondria (shown in purple).

The literature shows no concrete conclusion concerning photorespiration. In some opinions, it is considered to be an energy-dissipation mechanism to prevent photo-inhibition; that is, the oxidation of an intracellular component by excess sunlight and oxygen (Berry and Downton, 1982; Kelly and Latzko, 2006d). In other opinions, photorespiration is due to the inefficiency of RuBisCO, owing to the fact that oxygen concentrations in the air have increased drastically since RuBisCO first appeared on the

Earth (Ogren, 1982). This would explain mechanisms for mitigating photorespiration, like the "C4 cycle" and crassulacean acid metabolism (Kelly and Latzko, 2006e). In either case, photorespiration is a process, which lowers the efficiency of photosynthesis.

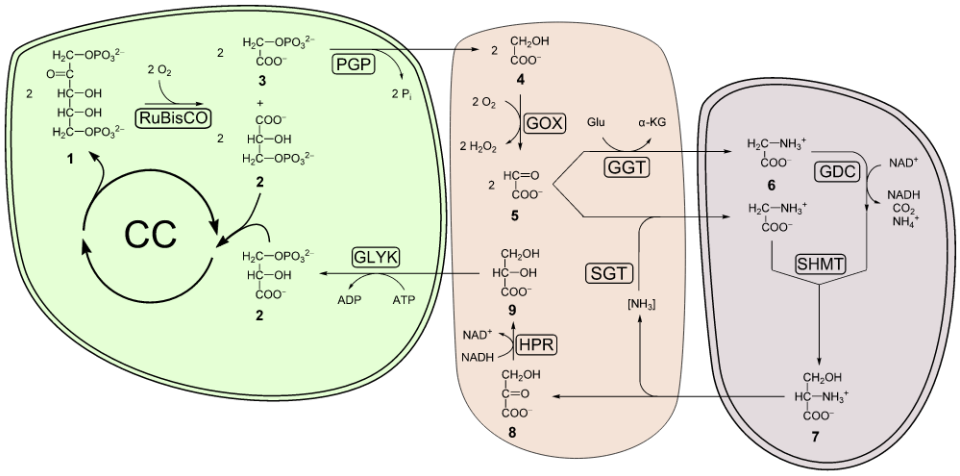

Figure 4.8. Photorespiration*.

*Reproduced with permission (Webpage: Photorespiration wikicommons).

4.3.2.4. Plant Metabolism

Metabolism includes everything from the degradation of sugars and biomass to produce high energy molecules (like ATP) to the repair, maintenance, and manufacture of the complex proteins in the photosystems and enzymes in the Calvin Cycle. Its details are too vast to be covered in a single journal article. Simplifications are therefore made herein.

The standard reaction for cellular metabolism (called respiration) is the reverse of reaction R4.1 and is shown as reaction R4.7. Its highly spontaneous nature (due to the large chemical exergy contained within glucose) is used to drive the production of high-

exergy carrier molecules, like ATP, which sustain the plant during periods of darkness. The production of ATP from glucose is shown as reaction R4.8 (Voet et al., 2008). Note that 38 ATP are produced in reaction R4.8 – the theoretical maximum. In actual practice, the number of ATP produced varies between 30 and 32, depending upon the organism that transports the molecules involved between the organelles. In addition to complete degradation, glucose can be converted to intermediates through various metabolic pathways, which build or repair organelles and other cellular components. In this way, metabolism is essentially an exergy cost for the various day-to-day intracellular operations.

$$C_6H_{12}O_6 + 6\,O_2 \rightarrow 6\,CO_2 + 6\,H_2O \qquad \Delta G^o = -2{,}872\ \frac{\text{kJ}}{\text{mol}} \qquad \text{(R4.7)}$$

$$C_6H_{12}O_6 + 6\,O_2 + 38\,\text{ADP} + 38\,H_3PO_4 \rightarrow 6\,CO_2 + 38\,\text{ATP} + 44\,H_2O \qquad \Delta G^o = -1{,}626\ \frac{\text{kJ}}{\text{mol}} \qquad \text{(R4.8)}$$

4.4. Analysis

The photosynthetic exergy efficiency of a terrestrial plant that has standard light absorption bands, shown in Figure 4.9, is calculated in this section, using the models in Section 4.3. Note that relative absorption is the amount of incident solar radiation absorbed by chloroplast pigments (P680 and P700) converted to electrical work in the form of high-energy electrons. The plant's surrounding environment is temperate, with ample water, sunlight, carbon dioxide, and a relative humidity of 40 percent (arid stress conditions are not examined herein). This yields the "maximum" efficiency of photosynthesis and the causes for each exergy loss, suggesting approaches to avoid or reduce these losses.

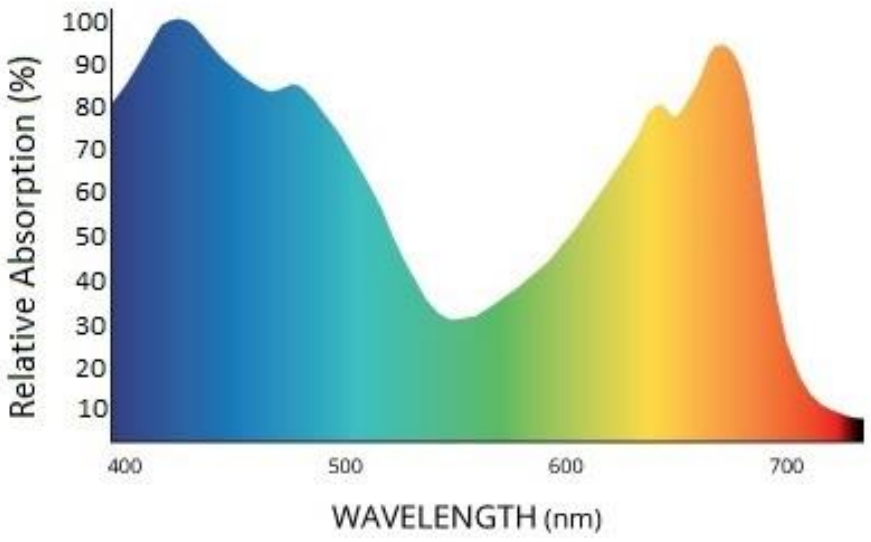

Figure 4.9. Relative light absorption in the PAR*.

*Reproduced with permission (Webpage: PAR & The Light Spectrum).

4.4.1 Chloroplast Efficiency

The exergy efficiency for a typical C3 chloroplast is calculated in this section and the accompanying subsections. It should be noted that this efficiency is based upon reversible exergy changes, and thus, does not account for kinetic and diffusive bottlenecks. It is representative of most C3 plant chloroplasts under non-stress conditions.

4.4.1.1. Sunlight and Absorbance

Only a fraction of the incident solar radiation is within the PAR (Bolton and Hall, 1991) ($\eta_{PAR} = 0.43$), the active region for chloroplast pigment absorption. It is assumed that all PAR photons that reach the chloroplast are absorbed. A small fraction of the non-PAR radiation is also absorbed, $\alpha_{non\text{-}PAR}$. Petela et al. (Petela, 2008) assigns a value of

0.05 for $\alpha_{\text{non-PAR}}$, which is used herein. Therefore, the total chloroplast exergy efficiency is:

$$\eta_{\text{solar}} = \frac{B_{\text{useful}}}{B_{\text{Total}}} = \frac{\eta_{\text{PAR}} B_{\text{sun}} + \alpha_{\text{non-PAR}}(1-\eta_{\text{PAR}}) B_{\text{sun}}}{B_{\text{sun}}} = \eta_{\text{PAR}} + \alpha_{\text{non-PAR}}(1-\eta_{\text{PAR}}) = 0.4585 \qquad (4.22)$$

where B_{sun} is the total incoming solar exergy (J). Note that the absorbed photons are split evenly between the two photosystems (24 photons to PSII and 24 photons to PSI).

Regarding the pigments P680 and P700, they absorb maximally (that is, the greatest amount of solar potential exergy absorbed and converted to electrical exergy) at 680 and 700 nm, respectively. The exergies of photons at these wavelengths are calculated using Eq. (4.12). Photons at shorter wavelengths (and, therefore, higher in exergy) are degraded to the maximal absorption wavelength (Barber, 2009). Photons at wavelenghts longer than 700 nm are instantly degraded to waste heat. When the vast majority of absorbed photons are in the PAR, it is assumed that their wavelengths are evenly distributed, with Eq. (4.14) determining the average exergy per mole of photons. According to Petela et al. (Petela, 2008) chloroplasts absorb marginally in the ultraviolet region, but since such a small fraction of that exergy is absorbed, it is excluded from the averaging.

The maximal wavelength, λ_{high}, is 700 nm and λ_{low} is 400 nm, yielding an average exergy of 212 kJ/(mol photon). Since P680 absorbs maximally at 680 nm, it absorbs roughly 167 kJ/(mol photon), yielding an absorption fraction, $\eta_{\text{PSII,abs}}$:

$$\eta_{\text{PSII,abs}} = \frac{B_{\text{useful}}}{B_{\text{Total}}} = \frac{B_{\text{PSII,maximal photon}}}{B_{\text{Average photon}}} = \frac{167}{212} = 0.789 \qquad (4.23)$$

Similarly, P700 absorbs maximally at 700 nm, yielding an average exergy of 162 kJ/(mol photon) and an absorption fraction, $\eta_{\text{PSI,abs}}$:

$$\eta_{\text{PSI,abs}} = \frac{B_{\text{useful}}}{B_{\text{Total}}} = \frac{B_{\text{PSII,maximal photon}}}{B_{\text{Average photon}}} = \frac{162}{212} = 0.766 \quad (4.24)$$

4.4.1.2. Electron Transport Chain

Reduction potentials in the electron transport chain (ETC) were taken from the literature (Nicholls and Ferguson, 2002; Voet et al., 2008; Walz, 1997a, b, c), and the change in exergy was calculated using Eq. (4.17) for 24 moles of photons (*n* in Eq. (4.17) – one photon excites one electron) entering each photosystem. Note that for all pigments and intermediate electron carriers, the excited and non-excited states are assumed to have comparable activities. Consequently, when calculating the exergy changes along the electron transport chain (Figure 4.3), the activity term in Eq. (4.17) cancels out (Bassham and Krause, 1969), and only the exergy change of the first reduction (that of P680) differs from the standard Gibbs free energy change. The validity of this assumption is examined in Section 4.5.

The results are shown in Table 4.1 for PSII and Table 4.2 for PSI. Cells in yellow represent the beginning state for each photosystem, cells in green represent electron transfers that proceed naturally, and cells in red represent the electron transfers that require an input of exergy (sunlight).

Table 4.1. Exergies and Reduction Potentials of PSII

Photosystem II				
Electron Pair Donor	**Redox Potential, ε (V)**	**Difference $\Delta\varepsilon$ (v)**	**Standard Free Energy Change ΔG^o(J) – Eq. 4.16**	**Exergy Change ΔB_{elec}(J) – Eq. 4.17**
$2H_2O \rightarrow O_2 + 4H+$	0.81	n/a	n/a	
P680	1.10	-0.29	-671,536	-819,489
P680*	-0.80	1.90	4,399,716	4,399,716
Pheo	-0.60	-0.20	-463,128	-463,128
Qa	0.00	-0.60	-1,389,384	-1,389,384
Qb	0.10	-0.10	-231,564	-231,564
Cytochrome b6f (Cytb)	0.19	-0.09	-208,408	-208,408
Plastocyanin (PC)	0.37	-0.18	-416,815	-416,815
Total Difference PSII	**0.37**	**-0.44**	**1,018,882**	**870,928**

Note: the starting point is colored yellow, all steps that proceed naturally are green, and all steps that require and input of exergy (sunlight) are red.

Table 4.2. Exergies and Reduction Potentials of PSI

Photosystem I				
Electron Pair Donor	**Redox Potential, ε (V)**	**Difference $\Delta\varepsilon$ (v)**	**Standard Free energy Change ΔG^o(J) – Eq. 16**	**Exergy Change ΔB_{elec}(J) – Eq. 17**
Plastocyanin (PC)	0.37	n/a	n/a	
P700	0.50	0.13	-301,033	-301,033
P700*	-1.30	-1.80	4,168,152	4,168,152
A0	-1.00	0.30	-694,692	-694,692
A1	-0.79	0.21	-486,284	-486,284
Fx	-0.73	0.06	-138,938	-138,938
Fa	-0.59	0.14	-324,190	-324,190
Fb	-0.55	0.04	-92,626	-92,626
Fd	-0.53	0.02	-46,313	-46,313
NADPH	-0.32	0.21	-486,284	-486,284
Total Difference PSI	**-0.32**	**-0.69**	**1,597,792**	**1,597,792**
Total Difference (NADPH - H_2O)	**-0.32**	**-1.13**	**2,616,673**	**2,468,720**

Note: the starting point is colored yellow, all steps that proceed naturally are green, and all steps that require and input of exergy (sunlight) are red.

The only two steps in PSII that perform useful work involve the transfer of electrons from water to the pigment P680 (the first reduction) and driving protons against their gradient; that is, from Q_b to plastocyanin (PC), shown red in Figure 4.3 – Q_{pool} = $\Delta B_{elec,Cytb} + \Delta B_{elec,PC} = -625{,}223$ J. In addition, exergy is delivered to PSI, shown as the "Total Difference of PSII". The work done by these processes is assumed to be 100% efficient. All exergy inputs not consumed in work-performing steps are lost as waste heat; similar to electricity flowing through a series of non-productive resistors. The incoming exergy sources to PSII are the 24 moles of photons (680 nm) and the 12 moles of water (that are split, discussed in the Section 4.4.2.2). The exergy efficiency is:

$$\eta_{\text{PSII}} = \frac{B_{\text{useful}}}{B_{\text{Total}}} = \frac{B_{\text{water split}} + B_{\text{Qpool}} + B_{\text{to PSI}}}{B_{\text{Incoming Solar}} + 12B_{\text{w}}} = \frac{819{,}489+625{,}223+870{,}928}{4{,}339{,}716+30{,}520} = 0.523 \quad (4.25)$$

Table 4.2 shows the exergy changes for the steps in PSI. The two inputs are the exergy from PSII and the solar exergy that further excites the electrons; whereas, the only useful work done is to reduce $NADP^+$ to NADPH, in the last step of the ETC (assumed to be completed with 100% efficiency). Again, this system is like a circuit. The intermediate molecules are similar to resistors that dissipate some of the electrical exergy. Taking the ratio of exergy consumed for useful work to total exergy input gives an efficiency of 49.0 percent (Eq. 4.26):

$$\eta_{\text{PSI}} = \frac{B_{\text{useful}}}{B_{\text{Total}}} = \frac{B_{\text{NADPH}}}{B_{\text{from PSII}} + B_{\text{Incoming Solar}}} = \frac{2{,}468{,}720}{870{,}928+4{,}168{,}152} = 0.490 \quad (4.26)$$

4.4.1.3. ATP Synthase

From the analysis of PSII, 1,444,712 J of exergy are stored in protons within the thylakoid membrane ($B_{\text{water split}} + B_{\text{Qpool}}$). Calculation of the exergy of reaction R4.4 (Section 4.4.1.4 and Appendix A), gives 1,043,750 J required to create 18 moles of ATP. Note that Lems et al. (Lems et al., 2010) assume that 24 ATP are produced. However, the correct number of ATP produced is 18 (Zhu et al., 2008), because in the chloroplast ATP synthase requires the relocation of four protons to produce one ATP. Therefore, the exergy efficiency is:

$$\eta_{\text{ATP synthase}} = \frac{B_{\text{useful}}}{\text{B}_{\text{Total}}} = \frac{18B_{\text{ATP}}}{B_{\text{PMF}}} = \frac{1{,}043{,}750}{1{,}444{,}712} = 0.722 \quad (4.27)$$

4.4.1.4. Calvin Cycle/Dark Reactions

The stoichiometry of the overall dark reaction was presented as reaction R4.6, with the reactions assumed to occur at T_o and atmospheric pressure, P_o. The exergies of carbon dioxide and oxygen are calculated using Eq. 2.9 in Szargut's book (Szargut, 2005). The exergy of water (2.543 kJ/mol) is discussed in Section 4.4.2.2. The exergy of NADPH is calculated in Section 4.4.1.2; $NADP^+$ is the reference state – with exergy equal to zero. The exergies of all other chemical species, shown in Table 4.A.1, are calculated using Eq. 4.18, with the exergy of the chemical elements defined in Szargut's book (Szargut, 2005), the standard free energies of formation taken from (Bassham and Krause, 1969; Krebs and Kornberg, 1957), and the activities taken from Bassham and Krause (Bassham and Krause, 1969).

Only sparse data are available to estimate the acid and ion dissociation constants; therefore, the dissociation terms are neglected in this analysis. The validity of this assumption is discussed in Section 4.5. Also, for each compound in the dark reactions, the exergy of its elements, B_{element}, the Gibbs free energy of formation, ΔG_f, its activity, $[A]$, and its exergy, B_{Total}, are given in Table 4.A.1. For each reaction, it is assumed that all exergy not transferred from the reactants to the products is lost (or destroyed) as low-grade heat, which is used to evaporate water in the cell or lost as sensible heat to the environment.

As discussed in the Introduction (Section 4.1), two passes through the Calvin Cycle produce two GAl3P molecules, which are converted to glucose using a repetition of reactions, C5, C6, and C7, as well as reactions C14 and C15. The exergy losses in each reaction are shown in Table 4.3. Note that the reaction numbers are those in Figure

4.7, and the table is color-coded, with dark red being the greatest sources of exergy destruction and dark green being the smallest. Also, "(NADPH)" and "H_3PO_4" correspond to "NADPH + H^+" and "P_i", respectively, in Reactions R4.3-R4.6.

Table 4.3. Exergy Losses in the Dark Reactions

Calvin Cycle				
Rxn. No.	**Reaction**	**δ*B*(J)**	**Reps***	**Total δ*B*(J)**
C1	(Ru5P) + (ATP) ——> (RuBP) + (ADP)	16,430	6	98,582
C2	CO_2 + (RuBP) + H_2O ——> 2*(PGA)	53,707	6	322,242
C3 + C4	(PGA) + (ATP) + (NADPH) ——> (ADP) + (GAl3P) + ($NADP^+$) + H_3PO_4	2,729	12	32,746
C5	(GAl3P) ——> (DHAP)	189	4	755
C6	(GAl3P) + (DHAP) ——> (FBP)	987	2	1,974
C7	(FBP) + H_2O ——> (F6P) + H_3PO_4	28,966	2	57,933
C8	(F6P) + (GAl3P) ——> (E4P) + (Xu5P)	3,017	2	6,035
C9	(E4P) + (DHAP) ——> (SBP)	1,011	2	2,023
C10	(SBP) + H_2O ——> (S7P) + H_3PO_4	31,249	2	62,498
C11	(S7P) + (GAl3P) ——> (R5P) + (Xu5P)	5,593	2	11,187
C12	(R5P) ——> (Ru5P)	322	4	1,289
C13	(Xu5P) ——> (Ru5P)	383	2	766
	Calvin Cycle SUM			598,030
Conversion to Glucose				
Rxn. No.	**Reaction**	**δ*B*(J)**		**Total δ*B*(J)**
C5*	(GAl3P) ——> (DHAP)	189	1	189
C6*	(DHAP) + (GAl3P) ——> (FBP)	987	1	987
C7*	(FBP) + H_2O ——> (F6P) + H_3PO_4	28,966	1	28,966
C14	(F6P) ——> (G6P)	1,298	1	1,298
C15	(G6P) + H_2O ——> (Glucose) + H_3PO_4	31,768	1	31,768
	Conversion to Glucose SUM			63,208
	Total SUM			**661,239**

* Number of Repetitions per mole of Glucose created

Note: the largest losses are shown in dark red, intermediate losses are shown as light red, then light green, and finally the smallest losses are shown as dark green.

From the light reactions, 3,509,191 J of exergy are transferred to the dark reactions in the form of 18 ATP and 12 NADPH. A total of 661,239 J are lost in the dark reactions, yielding the following exergy efficiency for the Calvin Cycle:

$$\eta_{\text{Calvin Cycle}} = \frac{B_{\text{useful}}}{B_{\text{Total}}} = \frac{18B_{\text{ATP}} + 12B_{\text{NADPH}} - \delta B_{\text{CC}}}{18B_{\text{ATP}} + 12B_{\text{NADPH}}} = \frac{3{,}509{,}191 - 661{,}239}{3{,}509{,}191} = 0.812 \quad (4.28)$$

4.4.1.5. Overall Chloroplast Efficiency

Combining the exergy efficiencies from the previous subsections, an overall chloroplast efficiency is calculated in Table 4.4 and illustrated in the exergy-flow diagram in Figure 4.10. In Table 4.4, the largest losses are shown in dark red, intermediate losses are shown as light red, then light green, and finally the smallest loss is dark green. In Figure 4.10, each rectangular region represents a bioprocess whose height is proportional to its exergy flow. Exergy enters on the left, with exergy losses in the cross-hatched regions building linearly from left-to-right. Note that half of the solar exergy is transmitted to PSI, which also receives a portion of the exergy from PSII. The remainder of the solar exergy from PSII is transmitted to ATP synthase. Then, the dark reactions (Calvin Cycle) receive the NADPH exergy and the ATP exergy. One mole of glucose, the final product of photosynthesis, is then generated by the Calvin Cycle, yielding an efficiency of 12.2 percent. Note that in Table 4.4, the inefficiencies due to photosystem absorption (due to the optimal absorption wavelengths) and the electron transfer chain are separated into different categories; whereas, in Figure 4.10 they are lumped together inside the boxes. The impact of Table 4.4's results is analyzed in Section 4.4.2.5.

Table 4.4. Overall Chloroplast Efficiency

Source of Exergy Destruction	Inlet (kJ)	Outlet (kJ)	Loss (kJ)	Efficiency η	Overall Loss (%)	PAR Loss (%)
PAR Reflection	9977	9977	0	1	0	0
Non-PAR Reflection	13,226	661	12,564	0.050	61.33	-
Photosystem II Absorption	5,319	4,193	1,126	0.788	5.50	14.45
Photosystem I Absorption	5,319	4,074	1,246	0.766	6.08	15.99
Photosystem II ETC	4,209	2,200	2,009	0.523	9.81	25.79
Photosystem I ETC	4,901	2,401	2,500	0.490	12.20	32.09
ATPsynthase	1,372	992	381	0.722	1.86	4.89
Calvin Cycle (Dark Reactions)	3,509	2,848	661	0.812	3.23	8.49
OVERALL	**23,334**	**2,848**	**20,487**	**0.122**	**100.0**	-

Note: the largest losses are shown in dark red, intermediate losses are shown as light red, then light green, and finally the smallest losses as dark green.

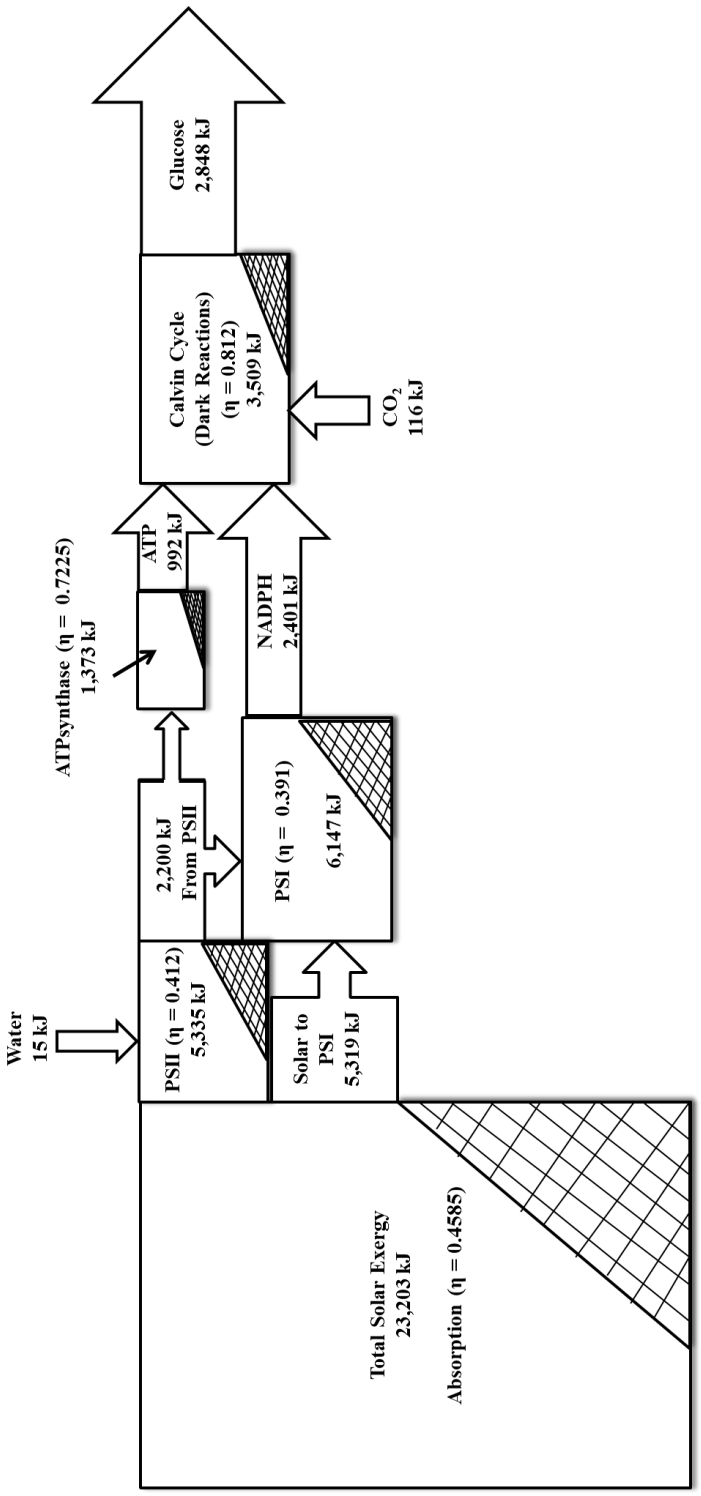

Figure 4.10. Exergy-flow diagram.

4.4.2. Plant Efficiency

In this section, the analysis is expanded to include factors that affect the plant's efficiency, but are not contained within the chloroplast. The processes that occur within the chloroplast (Section 4.4.1) have a well-defined efficiency, involving clear inputs and outputs and well-defined processes. The four phenomena discussed in Section 4.4.2 can be thought of as sinks, which drain the plant's resources without driving the production of glucose – although some of these processes are necessary (metabolic repair and maintenance of the cellular machinery, for example).

4.4.2.1. Sunlight Reflection

To ensure an accurate comparison between chloroplasts and other solar collectors, the reflectance of the incident solar exergy from the leaves must be taken into account (Webpage: PAR & The Light Spectrum). It is beyond the scope of this chapter to explore the complex mechanism of leaf radiation reflection, much of which is covered by Berry and Downton (Berry and Downton, 1982)). Instead, a reflection factor, α_{PAR}, is used herein. The literature lists values between 0.88 and 0.80 (Bassham and Buchanan, 1982; Berry and Downton, 1982; Petela, 2008). Because the reflectance portion may be a result of light degradation by chlorophyll pigments, the higher absorption factor ($\alpha_{PAR} = 0.88$) is used herein to avoid "double-counting" exergy destruction between these two phenomena.

4.4.2.2. Transpiration

Returning to Section 4.3.2.2, transpiration is essentially water leakage from the plant's leaves, a process to minimize for optimal exergy performance. Because an

efficiency does not apply, Eqs. 19-21 are used to determine the exergy loss to transpiration per mole of glucose produced.

Enthalpies and entropies are from the saturated steam tables at the reference state (saturated steam at T_o), and from the unsaturated water tables for the "high-exergy" state (water at T_o and P_o). For terrestrial plants, the height, z, is taken as 2.0 meters. The relative humidity, Φ_o, is set at 0.4 (Petela, 2008), and the water fraction within the leaf, ϕ, is set at 0.5 (Reis and Miguel, 2006).

Eq. (4.19) yields the exergy of water, B_w = 2.543 kJ/mol. The water lost by evaporation without reacting is computed using Eq. (4.20); that is, WC = 6/0.5 – 6 = 6 moles of water. Using Eq. (4.21), the exergy destruction per mole of glucose is δB_G = 15,260 J/(mol glucose synthesized).

It is important to note that, while the exergy loss is relatively insignificant for the temperate environment selected herein, exergy losses would be significant in an arid climate. For example, taking Φ_o = 0.05 and $\phi = 4.31\times 10^{-4}$ (Kluge, 1982) yields an exergy loss of 107,100 kJ/(mol glucose), making photosynthesis infeasible for C3 plants. In this case, plants having a cassulacean acid metabolism (CAM), a mechanism used to capture and store carbon dioxide during dark hours, are needed to conserve water (Webpage: Photorespiration wikicommons). More information about CAM is provided in the Glossary (Appendix B).

4.4.2.3. Photorespiration

Like transpiration, photorespiration is a process that dissipates exergy without aiding in the production of glucose. Similarly, it must be eliminated to achieve optimal

photosynthesis operation. Because an efficiency does not apply, given a mechanism for photorespiration, such as that in Figure 4.8, exergy losses in each reaction can be estimated using the equations in Section 4.3.1.4. This, however, is beyond the scope of the analysis herein.

According to Kelly et al. (Kelly and Latzko, 2006e), each "CO_2 cycle" in photorespiration uses 6 NADPH and 10 ATP, yielding 1,813 kJ exergy loss. Since RuBisCO has a carbon dioxide to oxygen affinity of 4:1 or 3:1, 453 kJ and 604 kJ, respectively, of photorespiration exergy losses per mole of glucose occur. Alternatively, photorespiration is known to degrade 1/3 to 1/4 of fixed carbon (glucose herein) (Kelly and Latzko, 2006c; Lems et al., 2010). Thus, a factor of 0.25 multiplied by the amount of fixed carbon (glucose) could be used to estimate the exergy loss, resulting in 712 kJ lost. Because the latter gives the most conservative exergy loss, it is used herein.

4.4.2.4. Plant Metabolism

When analyzing the overall plant, the metabolism is the most difficult to quantify. The exergy consumed by plant metabolism is higher for older plants which must maintain aged cellular components – during reproductive seasons as the plant diverts resources to producing seeds, and during the winter as less sunlight is available to provide exergy. The amount of exergy consumed is also highly dependent on the plant type (or other autotrophic organism) and the pressures associated with the surrounding environment (pests, poisons, photo-inhibition, etc.). For these reasons, the effects of metabolism must be measured experimentally on a case-by-case basis to meaningfully affect its exergy efficiency. However, two studies (Bassham and Buchanan, 1982; Bisio and Bisio, 1998)

estimate 1/3 of fixed carbon (glucose) as the "price" for metabolism. The more precise value of 0.375 is used herein (Bisio and Bisio, 1998), which is equivalent to 1,068 kJ exergy loss per mole of glucose generated.

4.4.2.5. Overall Plant Efficiency

The results of the previous subsections are tabulated as Table 4.5, yielding an overall plant efficiency of 3.9%, in good agreement with Petela (Petela, 2008). The vast majority of the losses (greater than 87%) occur within the chloroplast (Section 4.4.1.5), which explains the disproportionate emphasis on the internal workings of the chloroplast herein. Table 4.6 is a combination of Tables 4.4 (Section 4.4.1.5) and Table 4.5, showing the exergy losses for every step in photosynthesis. Note that "PAR Reflection" represents the leaf reflection (Section 4.4.2.1) and "Non-PAR Reflection" represents the rejection of non-PAR light by the chlorophyll pigments.

Table 4.5. Overall Plant Efficiency

Source of Exergy Destruction	Inlet (kJ)	Outlet (kJ)	Loss (kJ)	Efficiency η	Overall Loss (%)
PAR Reflection	31,102	27,370	3,732	0.880	5.36
Chloroplast	68,598	7,704	60,893	0.112	87.47
Transpiration	-	-	41	-	0.06
Photorespiration	-	-	1,926	-	2.77
Plant Metabolism	-	-	2,889	-	4.15
OVERALL	**72,461**	**2,848**	**69,614**	**0.039**	**100.0**

Table 4.6. Overall Plant Efficiency with Chloroplast Details

Source of Exergy Destruction	Inlet (kJ)	Outlet (kJ)	Loss (kJ)	Efficiency η	Overall Loss (%)	PAR Loss (%)
PAR Reflection	31,102	27,370	3,732	0.880	5.36	14.04
Non-PAR Reflection	41,228	2,061	39,167	0.050	56.26	-
Photosystem II Absorption	14,716	11,601	3,114	0.788	4.47	11.72
Photosystem I Absorption	14,716	11,270	3,446	0.766	4.95	12.96
Photosystem II ETC	11,616	6,072	5,545	0.523	7.96	20.86
Photosystem I ETC	13,553	6,640	6,913	0.490	9.93	26.01
ATPsynthase	3,788	2,737	1,051	0.722	1.51	3.95
Calvin Cycle (Dark Reactions)	9,493	7,704	1,789	0.812	2.57	6.73
Transpiration	-	-	41	-	0.06	0.16
Photorespiration	-	-	1,926	-	2.77	7.25
Metabolism	-	-	2,889	-	4.15	10.87
OVERALL	**72,461**	**2,848**	**69,614**	**0.039**	**100.0**	-

Clearly, the largest loss is due to the reflectance of non-PAR radiation. The second largest PAR loss (third largest loss total) is due to the degradation of photons relating to the maximal absorption wavelength of each chlorophyll pigment (P700 and P680). To improve the efficiency of photon absorption, one option is to tune the chlorophyll light-gathering antennas (Webpage: "Tuning" microalgae for high photosynthesis efficiency; Barber, 2009; Gust and Moore, 1985; Gust et al., 2001; Kelly and Latzko, 2006d; Perrine et al., 2012), which are usually composed of carotenoids that absorb light in regions of the solar spectrum where chlorophyll is ineffective. In one approach, genetic modification of the antennas are sought to harness more light to be transferred to the chlorophyll pigment, where it enters the electron transport chain (Gust and Moore, 1985). Note that genetic modifications have been reported that boost the size and effectiveness of algae antennas (Webpage: "Tuning" microalgae for high

photosynthesis efficiency; Perrine et al., 2012). However, the beneficial effects of increasing the antenna size have been contested (Melis, 2009). Another approach involves creating a photo-ecosystem (Bisio and Bisio, 1998), with various photosynthetic organisms having different maximal absorption wavelengths, giving maximal absorption ranges that span the entire visible spectrum (Barber, 2009). Such photo-ecosystems often have substantially higher efficiencies, as demonstrated by forests and jungles having higher biomass densities than crop fields.

Most PAR exergy losses are due to inefficiencies in PSII and PSI, during the electron transfers between carriers. Over the past 30 years, this has motivated studies (Barber, 2009; Gust and Moore, 1985) and attempts to replicate the biological electron-transport chain (ETC) (Gust and Moore, 1989; Gust et al., 1998, 2001; Kim et al., 2012). Thus far, artificial ETCs have been unstable (Barber, 2009; Kim et al., 2012). Some charge-separation is necessary to draw electrons away from the pigment molecules (Gust and Moore, 1985), and the greater the charge-separation, the more favorable the process. However, greater charge-separation yields increased exergy losses. Therefore, a method for improving photosynthetic efficiency can be found by formulating a numerical model for charge-separation, and then performing optimization (assuming that nature has not already done this) to determine the charge-separation distance for maximum efficiency. Another approach (possibly more feasible in synthetic replications) is to have the intermediate electron carriers perform work, like the Q_{pool} complex in PSII. Note also that plastiquinol diffusion within the thylakoid membrane is the rate-limiting step of the ETC (Kelly and Latzko, 2006d; Melis, 2009), which consequently is the rate-limiting step in carbon dioxide saturated photosynthesis (Kelly and Latzko, 2006a).

The next most substantial loss of PAR exergy, besides those of the photosystems, is due to the plant's metabolism, with photorespiration being of a similar order of magnitude. Some level of metabolism is essential for the plant's reproduction and maintenance of its biological machinery, and therefore the majority of these losses are likely unavoidable. In terms of photorespiration, thus far, attempts to remove it genetically have been unsuccessful (Kelly and Latzko, 2006b). But, a lower oxygen content in the local environment is most effective in decreasing losses to photorespiration. Note that aquatic organisms, such as algae, typically have almost negligible rates of photorespiration – as oxygen has a low solubility in water. In addition, algae concentrate dissolved carbon dioxide (as bicarbonate) inside their cells using pumps (Kelly and Latzko, 2006a; Ogren, 1982). This pumping is against a concentration gradient, and thus, consumes exergy, but it is a small cost compared to photorespiration.

The Calvin Cycle and ATP synthase have relatively small exergy losses, and some degree of exergy loss is required to drive the process forward at a reasonable rate. In the limit of negligible exergy loss, these processes would take an infinite amount of time, which is infeasible. Note that although not limiting in a thermodynamic sense, the Calvin Cycle can cause substantial decreases in exergy efficiency by slowing down photosynthesis (Webpage: "Tuning" microalgae for high photosynthesis efficiency; Melis, 2009). This justifies the search for genetic modifications of key enzymes (particularly SBPase (Kelly and Latzko, 2006b) and RuBisCO (Melis, 2009)) to increase the actual efficiency of photosynthesis.

Transpiration in non-arid environments causes small losses of exergy that are not worthy of further analysis. Managing transpiration in arid environments would depend largely upon irrigation techniques, which are beyond the scope of this chapter.

Overall, the exergy efficiency calculated herein (3.9%) is higher than that typically observed for terrestrial-plant photosynthesis (about 1%), although it is reasonable for algae (3-4%) (Bassham and Buchanan, 1982). The higher value for efficiency is because mass-transfer limitations and kinetic hold-ups were not taken into account, because only reversible transfer of exergy is modeled. As such, the efficiency computed herein is an upper bound for terrestrial plants that have not been genetically modified.

4.5. Error Analysis and Validation

All data used herein were taken from previous literature sources. It is assumed that these data are accurate. No standard deviations were reported; thus, it was impossible to analyze the errors originating from measurement inaccuracies. The comparisons discussed in this section are calculated using Eq. 4.29 and tabulated in Table 4.7.

$$Maximum\ Percent\ Difference = \frac{|LV - SV|}{|LV|} \tag{4.29}$$

where *SV* is the "standard value" (used herein) and LV is the literature value that is the largest deviation from *SV*.

Table 4.7. Error Analysis Table

Point of Comparison	**Source of Comparison**	**Maximum Percent Difference**
PAR Reflection	(Bisio and Bisio, 1998)	18.6
PAR Reflection	(Bassham and Buchanan, 1982)	5.4
Average Photon Exergy	(Zhu et al., 2008)	8.9
Loss to Reflection and Re-transmittance	(Bisio and Bisio, 1998)	2.9
Excitation of P680	(Nicholls and Ferguson, 2002; Walz, 1997a, b, c)	9.0
Excitation of P700	(Nicholls and Ferguson, 2002; Walz, 1997a, b, c)	7.0
Redox Potential of ETC (per step)	(Lems et al., 2010)	1.0
Exergy of NADPH	(Lems et al., 2010)	3.0
PMF Exergy	(Lems et al., 2010)	4.4
ATP hydrolysis	(Lems et al., 2010)	12.0
Overall Light Reaction Efficiency	(Bassham and Buchanan, 1982)	0.0
Overall Light Reaction Efficiency	(Lems et al., 2010)	32.0[a]
ATP synthase Efficiency	(Lems et al., 2010)	17.1
Calvin Cycle Efficiency	(Bassham and Buchanan, 1982; Lems et al., 2010)	2.4
Calvin Cycle Efficiency	(Lems et al., 2010)	4.7
Transpiration	(Reis and Miguel, 2006)	900.0[b]
Photorespiration	(Bolton and Hall, 1991)	50.0
Photorespiration	(Lems et al., 2010)	25.0
Photorespiration	(Kelly and Latzko, 2006e)	57.2
Overall Photosynthetic Efficiency	(Bisio and Bisio, 1998)	30.0
Overall Photosynthetic Efficiency	(Bassham and Buchanan, 1982)	95.0

a – Reference (Lems et al., 2010) neglected reflectance and imperfect light absorption. Adjusting for this herein yields a difference of 4.3%.

b – Transpiration was calculated differently in the two studies, and thus, even though the values were dissimilar, in both studies, transpiration had a marginal effect on the overall efficiency.

Different PAR radiation percentages are reported (Bassham and Buchanan, 1982; Bisio and Bisio, 1998). The true value depends on location, time of day, time of year, and weather conditions. However, all sources report absorption fractions between 0.40-0.50; many agreeing on roughly 0.43.

With regard to the assumption that the excited and ground-state compounds are present in roughly equal concentrations, the appendix in Lems et al. (Lems et al., 2010) provides a thorough calculation of the ratio of [P700]/[$P700^+$], which equals 11. This yields an exergy change proportional to ln([P700]/[$P700^+$]) = 2.4. Because the exergies of the other carriers (e.g., NADPH) are on the order of 200 kJ, differences of only one percent are anticipated. However, the redox potentials in Tables 4.1 and 4.2 (Nicholls and Ferguson, 2002; Voet et al., 2008; Walz, 1997a, b, c), when compared with the incoming exergy of the photons using Eq. (4.12), differ by approximately nine percent for PSII and seven percent for PSI. When the factor, $(1 - T_{earth}/T_{sun})$, is neglected, these differences are reduced to 4.2 and 1.6 percent. These differences are attributed to the crude calculation of activities in Eq. 4.17. More accurate concentration information would improve these estimates.

Comparing the exergy value of NADPH computed in Table 4.2 (2,468 kJ) with that of Lems et al. (Lems et al., 2010) (2,541 kJ), yields approximately a 3% difference. Similarly, for the exergy transferred to the PMF from PSII, the values are 1,508 kJ and 1,444 kJ, yielding a 4.4% difference. In this chapter, the exergy change of ATP hydrolysis (R4.4) is 58 kJ, in contrast with the commonly accepted 50-51 kJ (13.7 percent difference). The 58 kJ value is in good agreement with Lems et al. (Lems et al., 2007) (the source of Eq. 4.18), despite neglecting the acidic and ionic dissociation

effects. Clearly, the exergy calculation method needs further attention. Note that this causes a decrease in Calvin Cycle efficiency (81 percent compared with 85 percent in Lems et al. (Lems et al., 2010), and 83 percent in Bassham et al. (Bassham and Buchanan, 1982)). The ATP synthase efficiency is lower here when compared with Lems et al. (Lems et al., 2010) (72 percent compared with 82 percent in Lems et al. (Lems et al., 2010)), because they assume that an ATP molecule is generated for every three protons moved from the lumen to the stroma; however, most sources report that it takes four protons to generate an ATP molecule in the chloroplast (Voet et al., 2008; Zhu et al., 2008).

The overall efficiency of the light reactions, 32 percent herein, is in exact agreement with Bassham et al. (Bassham and Buchanan, 1982). Lems et al. (Lems et al., 2010) predict 47 percent, but they do not account for the imperfect absorption of the average photon. When the photon absorption efficiencies of both PSII and PSI are set to unity, the efficiency herein rises to 41 percent (again, their assumption of 3 protons per ATP leads to an artificially inflated efficiency).

Exergy loss due to water evaporation (transpiration) is not examined in most studies, although the equations are fairly standard (Szargut, 2005). The results of Reis et al. (Reis and Miguel, 2006) are most relevant, although their model is based upon fluxes throughout a 24-hour cycle. Their result is an order of magnitude smaller than 21 kJ reported herein. However, both are negligible compared to the losses in the other bioprocesses analyzed. Regarding photo-respiration, no rigorous modeling has been done. The estimates of exergy destruction are based upon two other studies (Bolton and Hall, 1991; Lems et al., 2010).

Finally, the overall exergy efficiency is comparable to flux-based studies (Petela, 2008; Reis and Miguel, 2006), even though it does not account for irreversible processes and fluxes (like carbon dioxide diffusion and ETC bottlenecks), which would need to be analyzed using irreversible thermodynamics (Kjelstrup et al., 2010; Sliepcevich and Finn, 1963). This implies that diffusive fluxes have a small impact on the overall thermodynamic efficiency (even though they may have a substantial impact on the real/observed efficiency). Non-flux based studies report higher efficiencies (Bassham and Buchanan, 1982; Bolton and Hall, 1991; Bugbee and Monje, 1992), because they do not account for photo-degradation, incomplete PAR absorption (Petela, 2008), photorespiration, or transpiration. However, when the PAR absorption factor and absorption efficiency factors are set to unity, and losses due to transpiration and photorespiration are eliminated, the overall efficiency rises to 14 percent, in nearly perfect agreement with Bugbee et al (Chain and Arnon, 1977) and Bolton et al. (Bolton and Hall, 1991).

4.6. Conclusions

Photosynthesis produces 100 billion tons of dry biomass annually, which is equivalent to a hundred times the weight of the human population (Barber, 2009). The biomass created on earth every second contains 37 TJ of chemical exergy (Szargut, 2005). In contrast, humans use only 13 TJ per second, which means that biomass theoretically has the potential to satisfy all human needs. To be realizable, however, the photosynthetic efficiency would need to be increased substantially. Therefore, it is crucial that the mechanism and efficiencies of photosynthesis are well understood.

A literature search over the last 53 years was performed, uncovering a broad array of approaches, definitions, and efficiencies. Overall, the theoretical efficiency decreased with increasing knowledge of the process, from 37 percent (Asimov, 1968) to 2.61 percent (Petela, 2008). The major factors in the comprehensive analysis herein present a more thorough picture of the process and its inefficiencies.

In this chapter, photosynthesis is decomposed into processes that occur within the chloroplast (PAR Reflection, Non-PAR reflection, PSII Absorption, PSI Absorption, PSII ETC, PSI ETC, ATP synthase, and Calvin Cycle) and those that affect the organism as a whole (Leaf PAR Reflection, Transpiration, Photorespiration, and Plant Metabolism). The exergy changes associated with each sub-step are calculated and summed to determine the exergy efficiency of each step. These steps, in turn, are combined to yield an overall photosynthetic efficiency of 12.2% for the chloroplast and 3.9 percent for the organism as a whole, which agrees with the photosynthetic efficiency presented in Chapter 2.

Using a controlled environment boosts the efficiency of photosynthesis by increasing access to nutrients (water, carbon dioxide) and decreasing access to oxygen, which causes photorespiration. This is a key reason algae are promising (Sukenik et al., 1991) and have higher efficiencies (in addition to their bicarbonate pumps).

Note that the photosynthetic analysis developed here focused upon glucose so that comparisons could be made with previous studies. However, judging by the high efficiency of the Calvin Cycle, the same carbon could have been converted to triglycerides with comparable efficiency. The lipid synthesis pathways are not entirely understood for algae (Webpage: Algae Lipid Synthesis), but if the Kennedy pathway (for

plants) can accurately be applied to algae (Webpage: Glyceraldehyde Dehydration; Webpage: Kennedy Pathway; Webpage: Lipid Biosynthesis), it can be assumed that the efficiency for synthesizing triglycerides will be close to that of the Calvin Cycle. In addition, algae do not suffer from photorespiration because of their CO_2 concentration mechanism; therefore, the maximum efficiency without genetic modification should be roughly 3% higher, giving a maximum efficiency of 7% without genetic modification or improvements in cultivation techniques.

Overall, the major exergy losses during photosynthesis are due to light absorption by the photosystems and the transfer of this exergy as high-energy electrons through the intermediate carriers. Methods that could be implemented to boost the photosynthetic efficiency will be discussed in detail in Chapter 6, in the discussion of future work.

4.7. Nomenclature

Term	Acronym
Adenosine DiPhosphate	ADP
Adenosine TriPhosphate	ATP
Calvin Cycle	CC
Cytochrome b6f	Ctyb
Electron-Transport Chain	ETC
Glyceraldehyde-3-Phosphate	GAl3P
Glucose-6-Phosphate	G6P
Nicotinamide Adenine Dinucleotide Phosphate (oxidized)	$NADP^+$

Nicotinamide Adenine Dinucleotide Phosphate (reduced)	NADPH
National Alliance for Biofuels and Bioproducts	NAABB
Photo-Active Region	PAR
3-Phosphoglycerate	PGA
Photosystem I	PSI
Photosystem II	PSII
Phosphoric acid	P_i
Plastocyanin	PC
Photosynthetic Organism	PO
Proton-Motive Force	PMF
Ribulose-1,5-Bisphosphate	RuBP
Ribulose-1,5-Bisphosphate	RuBisCO

Variable	**Quantity**	**Units**
B	Exergy	J
W	Work	J
Q	Heat	J
T	Temperature	K
N_A	Avagadro's Number	molecules/mole
h	Planck's Constant	J*s
c	Speed of Light	m/s
λ	Wavelength	nm

a	Lower Bounding Constant	dimensionless
b	Upper Bounding Constant	dimensionless
$f(x)$	A Function	dimensionless
$f(c)$	Average Value of Function f(x)	dimensionless
G	Gibbs Free Energy	J
F	Faraday's Constant	C/mol
n	Number of Moles	moles
ε	Redox Potential	V
$[A]$	Chemical Activity	dimensionless
v	Stoichiometric Coefficient	moles
R	Ideal Gas Constant	J/mol-K
K	Equilibrium Constant	varies
$[H^+]$	Concentration of Protons	moles/L
$[M]$	Concentration of a Metal Ion	moles/L
H	Enthalpy	J/mol
S	Entropy	J/mol-K
M_w	Molecular Weight	g/mole
g	Gravity Constant	m/s^2
z	Height	m
Φ	Relative Humidity	dimensionless
WC	Water Lost to Evaporation	moles of water
r	Ratio of Water to Glucose in R1	dimensionless
ϕ	Fraction of Water Used in Photosynthesis	dimensionless

η	Efficiency	dimensionless

Subscript	**Meaning**
out	Leaving the system
in	Entering the system
prod	Products
waste	Waste
sys	Internal to the System
res	Reservoir (Environment)
o	Ambient/Dead-State
H	High
phys	Physical (Temperature and Pressure)
chem	Chemical (Mixing and Reactions
elec	Electrical
photon	Photon (Sunlight)
earth	Of the Earth
sun	Of the Sun
low	Lower Bound
high	Upper Bound
carriers	Refering to carriers in the ETC
element	Refers to Chemical Elements
f	Of Formation

i	Series Counter
j	Series Counter
k	Series Counter
l	Series Counter
Gluc	Glucose
w	Water
solar	Relating to Incoming Solar Exergy
useful	Exergy Used to Do Work or Transferred to the next Process
Total	Total Incoming Exergy
PAR	Photo-Active Region
non-PAR	Outside of the Photo-Active Region
PSII	Photosystem II
PSI	Photosystem I
abs	Absorption
water split	Involving the Split of Water in the Light Reactions into Protons and Molecular Oxygen
Qpool	Relating to the PSII Complex that Pumps Protons Against Their Gradient
to PSI	Sent to Photosystem I
Incoming Solar	Exergy Entering the System from the Sun
NADPH	NADPH formation reaction (R4.2 + R4.3)
from PSII	Coming from Photosystem II

ATP	Relating to the ATP Hydrolysis Reaction
PMF	Proton-Motive Force
CC	Calvin Cycle

Greek letter	**Meaning**
Δ	Change
δ	Destruction

Superscript	**Meaning**
o	Standard and dead state for exergy

CHAPTER 5

Phase Equilibria of Algae-oil to Biodiesel Reactor Systems

5.1. Introduction

In Chapter 3, the extraction step was found to be energy intensive and have widely variable economic estimates (Silva et al., 2014). An alternative, using high-pressure CO2, has been demonstrated experimentally (Soh and Zimmerman, 2011) and found to highly-effective and also selective at extracting algae-oil. Similarly, several studies have shown the potential of supercritical CO2 as a co-solvent in the transesterification reactions (Glisic and Orlovic, 2014; Macaira et al., 2014; Soh et al., 2013; Soh and Zimmerman, 2011, 2015), allowing high conversions at relatively low temperatures. It is thus possible that these two steps could be combined, although this has not been demonstrated yet. However, performing the oil-extraction and conversion in the same step or at least the same process should yield considerable cost savings by eliminating pre-processing and purification steps that are currently required.

This chapter focuses on the conversion of triglyceride to biodiesel using supercritical CO_2 — with the kinetic mechanism shown in Figure 5.1, rather than the extraction of oil from algae. In Figure 5.1, TG is triglyceride, MEOH is methanol, DG is diglyceride, FAME is fatty-acid methyl-ester (biodiesel), MG is monoglyceride, GLY is glycerol, and critical CO_2 is carbon dioxide in or near the critical region. Because the oils are derived from algae, water is assumed to be present.

Due to lack of data, diglycerides and monoglycerides are excluded from the calculations herein. Also, triolein and methyl-oleate are the only triglyceride and FAME

molecules having sufficient data to be included — making triolein an initial-pass approximation for algae-oil in this chapter. Therefore, this analysis involves just six chemical species: triolein, methyl-oleate, methanol, glycerol, water, and carbon dioxide.

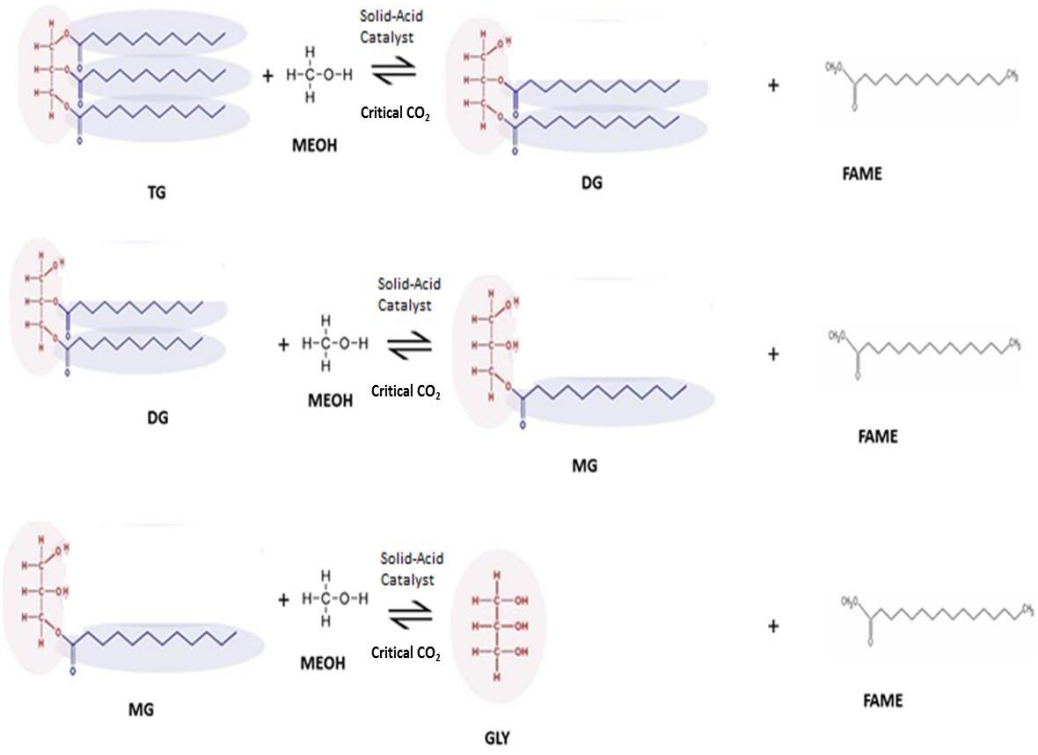

Figure 5.1. Triolein to biodiesel conversion mechanism.

Kinetic pre-exponential factors and activation energies for the conversion of algae-oils to biofuels are available (Changi et al., 2011; Patil et al., 2012; Soh and Zimmerman, 2013). However, previous studies that modeled the phase behavior for the algae-oil transesterification used crude models (like Redlich-Kwong in ASPEN PLUS (Anikeev et al., 2012; Glisic and Orlovic, 2014; Macaira et al., 2014), which are not suitable in the critical region or with large, asymmetric molecules. The most advanced

equation-of-state (EoS) used for supercritical systems has been the Cubic Plus Association (CPA) EoS, which was used to study supercritical alcohols (Andreatta et al., 2008; Andreatta et al., 2010; Velez et al., 2010).

The objective of this chapter is to use the SAFT EoS to model the phase behavior of a biodiesel reactor [up to three phases (vapor, polar liquid, nonpolar liquid) or as few as one supercritical phase (Hegel et al., 2007)]. The miscibility between the phases has drastic effects on the concentrations (and reaction rates).

It will be shown that a reliable phase equilibria model is needed to describe the reactor conversions. But, predictions with commercially-available SAFT phase-equilibria models are not yet sufficiently accurate in the critical region for triolein, methanol and CO_2. This chapter presents experimental data and shows the reason for the inadequacy of their predictions. Suggestions to improve their predictive capability in future studies are presented in Chapter 6.

In the sections that follow, cubic and SAFT equations-of-state are reviewed, the latter designed for use with long-chain hydrocarbons. Then, pure-species, binary, and ternary data are used to compare two SAFT variants [PC-SAFT in ASPEN PLUS (Gross and Sadowski, 2001, 2002) and SAFT-γ Mie in gPROMS (gSAFT) (Lymperiadis et al., 2007; Papaioannou et al., 2014)] and RK-ASPEN. Finally, a multiphase-reactor model, using approximate RK-ASPEN to model VLLE, is formulated and evaluated with experimental data.

5.2. Theory

This section provides a brief review for readers not actively involved in PVT calculations for phase equilibria.

5.2.1. Cubic Equations-of-State

Cubic equations-of-state (EoS) were first developed to describe simple vapor-liquid equilibria (VLE). They relate the changes in pressure (P) to those in molar volume (V) and temperature (T), based on two pure-species parameters. The cubic EoSs are named as such because they contain a cubed molar volume term. These equations are relatively easy to solve, as the three molar volume roots can be determined analytically.

The Van der Waals equation is the simplest cubic EoS. It is a modification of the ideal gas law to account for a fluid's particle volume and attractive forces:

$$P = \frac{RT}{V-b} - \frac{a}{V^2} \tag{5.1}$$

where R is the gas constant (8.314 J/mol-K), a is an empirical parameter that accounts for the attractive or repulsive forces between molecules in the fluid, and b is an empirical parameter that accounts for the volume of the molecules in the fluid (Smith et al., 2002). The values for a and b are approximated using the critical temperature (T_C) and the critical pressure (P_C):

$$a = \frac{27R^2T_C^2}{64P_C} \tag{5.2}$$

$$b = \frac{RT_C}{8P_C} \tag{5.3}$$

This equation offers great improvement over the ideal gas equation because it can predict phase equilibria. However, it has limited accuracy because, as Soave, Redlich, and

Kwong (Soave, 1972) and Peng and Robinson (Peng and Robinson, 1976) show, *a* should be a function of temperature.

The Soave-Redlich-Kwong equation is available in ASPEN PLUS as the RK-ASPEN property method. It adds temperature dependence to the attractive term, *a*, and accounts for binary interactions. RK-ASPEN is described by Eqs. 5.4-5.10:

$$P = \frac{RT}{V-b} - \frac{a}{V(V+b)} \tag{5.4}$$

$$a = \sum_i \sum_j x_i\, x_j (a_i a_j)^{0.5} (1 - K_{a,ij}) \tag{5.5}$$

$$b = \sum_i \sum_j x_i\, x_j \left(\frac{b_i + b_j}{2}\right) (1 - K_{b,ij}) \tag{5.6}$$

The parameters a_i and b_i are calculated using Eqs. 5.7-5.10. The attractive parameter, a_i, depends on the reduced temperature ($T_{ri} = T/T_{ci}$), the critical temperature (T_{ci}) and critical pressure (P_{ci}), the accentric factor (ω_i), and an extra polar parameter (η_i). The size parameter, b_i, depends only on the critical temperature and critical pressure. γ_i is a parameter that accounts for accentricity of the molecule.

$$a_i = 0.42747 \propto_i \frac{R^2 T_{Ci}^2}{P_{Ci}} \tag{5.7}$$

$$\propto_i = \left[1 + \gamma_i\left(1 - T_{ri}^{0.5}\right) - \eta_i (1 - T_{ri})(0.7 - T_{ri})\right]^2 \tag{5.8}$$

$$\gamma_i = 0.48508 + 1.5517\omega_i - 0.15613\omega_i^2 \tag{5.9}$$

$$b_i = 0.08664 \frac{RT_{Ci}}{P_{Ci}} \tag{5.10}$$

The binary interaction parameters, $K_{a,ij}$ and $K_{b,ij}$, are determined from Eqs. 5.11 and 5.12, in which $K_{a,ij}^{\ 0}$, $K_{a,ij}^{\ 1}$, $K_{b,ij}^{\ 0}$, and $K_{b,ij}^{\ 1}$ are all parameters regressed using binary VLE or liquid-liquid equilibrium (LLE) data (ASPEN Physical Property System.)

$$K_{a,ij} = K_{a,ij}^0 + K_{a,ij}^1 \frac{T}{1000} \tag{5.11}$$

$$K_{b,ij} = K^0_{b,ij} + K^1_{b,ij}\frac{T}{1000} \tag{5.12}$$

The Soave-Redlich-Kwong equation more accurately predicts the VLE and saturation conditions of mixtures (Soave, 1972). Peng and Robinson also modified the Van der Waals equation empirically to better fit phase equilibrium data and thermodynamic properties (Peng and Robinson, 1976). The standard Peng-Robinson model is:

$$P = \frac{RT}{V-b} - \frac{a}{V(V+b)+b(V-b)} \tag{5.13}$$

In this model, the attractive parameter, *a*, and the volume parameter, *b*, are:

$$a = \sum_i \sum_j x_i\, x_j (a_i a_j)^{0.5}(1 - K_{ij}) \tag{5.14}$$

$$b = \sum_i x_i b_i \tag{5.15}$$

To obtain *a* and *b*:

$$a_i = 0.45724 \propto_i \frac{R^2 T_{Ci}^2}{P_{Ci}} \tag{5.16}$$

$$\propto_i = \left[1 + \gamma_i\left(1 - T_{ri}^{0.5}\right)\right]^2 \tag{5.17}$$

$$\gamma_i = 0.37464 + 1.54226\omega_i - 0.26992\omega_i^2 \tag{5.18}$$

$$b_i = 0.07780\frac{RT_{Ci}}{P_{Ci}} \tag{5.19}$$

$$K_{ij} = K_{ij}^{(1)} + K_{ij}^{(2)}T + \frac{K_{ij}^{(3)}}{T} \tag{5.20}$$

The binary parameter, K_{ij}, is symmetric in the Peng-Robinson EoS ($K_{ij} = K_{ji}$) (ASPEN Physical Property System.) The Peng-Robinson EoS often gives better liquid density predictions without sacrificing the accuracy of other properties such as vapor pressures. However, it also fails to predict thermodynamic properties and phase

equilibria accurately near the critical region (Peng and Robinson, 1976). To obtain more accurate estimates, a non-cubic EoS should be used.

5.2.2. PC-SAFT

More recently, new EoSs were derived using statistical mechanics to represent complex fluid mixtures. The statistical associating fluid theory (SAFT), which treats molecules as freely-jointed spherical segments (Chapman et al., 1990), is prominent among them. Gross and Sadowski modified the original SAFT formulation by: (1) adding a dispersion expression for chain molecules based on perturbation theory (Wertheim, 1984a,b, 1986a,b), (2) readjusting the other pure-species parameters to improve accuracy (Gross and Sadowski, 2001), and (3) adding an association term (Gross and Sadowski, 2002). Their EoS is referred to as the perturbed chain-SAFT, or PC-SAFT.

In PC-SAFT, molecules are modeled as chains of spherical segments. The pair-potential of a segment is described by Eq. 5.21, which uses a modified square-well potential, in which $u_{ij}(r)$ is the pair-potential, r is the radial distance between segments, σ_{ij} is the segment diameter, ε_{ij} is the energy of the square-well interaction, and λ_{ij} is the attractive range of the interaction (Gross and Sadowski, 2001). In this case, $S_{ij} = 0.12\sigma_{ij}$. Note that the variable, λ_{ij}, is not actually used in the final version of the equation since it is regressed out, but is included here for completeness.

$$u_{ij}(r) = \begin{cases} \infty, & r < (\sigma_{ij} - S_{ij}) \\ 3\varepsilon_{ij}, & (\sigma_{ij} - S_{ij}) \le r < \sigma_{ij} \\ -\varepsilon_{ij}, & \sigma_{ij} < r \le \lambda_{ij}\sigma_{ij} \\ 0, & r > \lambda_{ij}\sigma_{ij} \end{cases} \tag{5.21}$$

The EoS is formulated in terms of the Helmholtz free energy, as shown in Eq. 5.22. Four terms account for four phenomena: an ideal-gas contribution (ig); a hard-chain contribution (hc), which accounts for repulsive forces between chains (individual species in this chapter); a dispersion (disp) contribution, which accounts for attractive forces between species; and an association contribution (assoc) for species that can hydrogen bond or those with electron lone pairs. For Eq. 5.22, A is the Helmholtz free energy, N is the number of molecules, k_B is the Boltzmann constant, and T is the absolute temperature.

$$\frac{A}{Nk_BT} = \frac{A^{ig}}{Nk_BT} + \frac{A^{hc}}{Nk_BT} + \frac{A^{disp}}{Nk_BT} + \frac{A^{assoc}}{Nk_BT} \tag{5.22}$$

For non-associating molecules, the equation is described by three pure-species parameters: the segment diameter, σ_{ij}, the energy of the square-well potential ε_{ij}, and the number of segments per chain, m_i. The like (ε_{ii}, σ_{ii}, and m_i) parameters are regressed from pure-species densities and liquid vapor pressures. The unlike parameters (ε_{ij} and σ_{ij}) are calculated using:

$$\varepsilon_{ij} = \sqrt{\varepsilon_{ii}\varepsilon_{jj}}(1 - K_{ij}) \tag{5.23}$$

$$\sigma_{ij} = \frac{1}{2}(\sigma_{ii} + \sigma_{jj}) \tag{5.24}$$

where K_{ij} represents the binary interaction parameter for molecules *i* and *j*, which is regressed using experimental binary data and calculated using Eq. 5.20.

The hard-chain contribution is dependent on reduced densities:

$$\zeta_n = \frac{\pi}{6}\rho \sum_i x_i m_i {D_{ii}}^n \qquad n \in (0, 1, 2, 3) \tag{5.25}$$

where ζ_n is the reduced density, ρ is the number density (molecules/m^3), x_i is the mole fraction of chemical species *i*, m_i is the number of segments in species *i*, and D_{ii} is a temperature-dependent collision diameter of *i* (in meters), which is defined in Eq. 5.26. Note that for a value of $n = 3$, ζ_3 is a dimensionless density, more commonly referred to as the packing fraction.

$$D_{ii} = \int_0^{\sigma_{ii}} \left[1 - \exp\left(-\frac{u_{ii}(r)}{k_B T}\right)\right] dr, \qquad n \in (0, 1, 2, 3) \tag{5.26}$$

The dispersion contribution is characterized as the sum of the first- and second-order Helmholtz perturbation expansions:

$$\frac{A^{disp}}{Nk_BT} = \frac{A_1}{Nk_BT} + \frac{A_2}{Nk_BT} \tag{5.27}$$

where the first- and second-order Helmholtz functions depend on the interacting segments' radial distributions, hard-chain Helmholtz energies, reduced radial distance, and reduced potential function (Gross and Sadowski, 2001). The universal model constants (not described in this chapter) used to calculate the two Helmholtz terms were adjusted using pure-species data from the n-alkane series. These adjustments eliminate

the parameter, λ_{ij}. For further discussion of this topic, see the original PC-SAFT paper (Gross and Sadowski, 2001).

Finally, the association term is:

$$\frac{A^{assc}}{Nk_BT} = \sum_i x_i \left[\sum_A [\mathrm{Ln}(X_{A_i}) - \frac{X_{A_i}}{2}] + \frac{1}{2}M_i\right] \tag{5.28}$$

where M_i is the number of association sites on each molecule and X_{Ai} is the mole fraction of molecules i not bonded at an individual site, A. The summation is performed over all associating sites for each molecule. X^{Ai} is dependent on a bonding volume term, κ^{AiBjA}, and a dimensionless association energy term, ε^{AiBj}/k_BT, which are the other pure-species parameters required for an associating molecule. For cross-associating mixtures, these terms are described by simple combining rules:

$$\varepsilon^{\mathrm{A}_i\mathrm{B}_j} = \frac{1}{2}(\varepsilon^{\mathrm{A}_i\mathrm{B}_i} + \varepsilon^{\mathrm{A}_j\mathrm{B}_j}) \tag{5.29}$$

$$\kappa^{\mathrm{A}_i\mathrm{B}_j\mathrm{A}} = \sqrt{\kappa^{\mathrm{A}_i\mathrm{B}_i}\kappa^{\mathrm{A}_j\mathrm{B}_j}}\left(\frac{\sqrt{\sigma_{ii}\sigma_{jj}}}{0.5(\sigma_{ii}+\sigma_{jj})}\right)^3 \tag{5.30}$$

There is also a dipole-dipole component of the equation that depends on the dipole-moment and dipole-fraction parameters. The polar Helmholtz term depends on the second- and third-order terms in a Helmholtz perturbation expansion:

$$A^{\mathrm{polar}} = \frac{A_2}{1-\frac{A_3}{A_2}} \tag{5.31}$$

where the second- and third-order perturbation expansions depend on the summation of the dipole-moment and dipole-fraction parameters over all species (ASPEN Physical Property System.; Ominik et al., 2005). Because the dipole-dipole portion of the

equation led to numerical instability when performing phase equilibria calculations, it was not used herein. Consequently, three pure-species parameters are required for non-hydrogen bonding systems (ε_{ii}, σ_{ii}, and m_i), five pure-species parameters are required for hydrogen bonding systems (ε_{ii}, σ_{ii}, and m_i, κ^{AiBjA}, ε^{AiBj}), and up to 3*NC* binary parameters are required, where *NC* is the number of species. The factor of 3 takes into account all binary parameters in Eq. 5.20.

5.2.3. SAFT-γ Mie

An alternative to modeling molecules as chains of spherical segments is to model them as combinations of different functional groups. This approach has been used previously for both pure-species parameters (i.e., Joback or Marrero and Gani methods) (Poling et al., 2001) activity coefficient models (like UNIFAC) (Fredenslund et al., 1975), and cubic EoS (Espinosa et al., 2002). The advantages of this approach are that the assumption of perfectly spherical segments can be relaxed by introducing a shape factor, and parameters do not need to be regressed for every molecule in the system. As long as all of the functional groups in a molecule are known, the molecule's thermodynamic properties and behavior in mixtures can be predicted. This is useful for systems where large numbers of similar molecules are present, as is often seen in biological systems. When working with the biodiesel system, the group methodology is helpful to represent the large ranges of fatty-acid methyl-esters (FAMEs) and triglycerides.

The most recent implementation of the group-contribution methodology within the SAFT framework is in the SAFT-γ Mie EoS (Papaioannou et al., 2014). Like PC-

SAFT, SAFT-γ Mie is formulated in terms of the Helmholtz free energy. However, the formulation is different as it involves terms for the monomeric functional-group interactions. The SAFT-γ Mie equation is:

$$\frac{A}{Nk_{\mathrm{B}}T} = \frac{A^{\mathrm{ig}}}{Nk_{\mathrm{B}}T} + \frac{A^{\mathrm{mono}}}{Nk_{\mathrm{B}}T} + \frac{A^{\mathrm{chain}}}{Nk_{\mathrm{B}}T} + \frac{A^{\mathrm{assoc}}}{Nk_{\mathrm{B}}T} \tag{5.32}$$

where A is the Helmholtz free energy, N is the number of molecules, k_{B} is Boltzmann's constant, T is the absolute temperature, A^{ig} is the ideal gas contribution, A^{mono} is the contribution of the individual functional groups, A^{chain} is the contribution of the full molecules, and A^{assoc} is the association contribution. Unlike PC-SAFT, there is no term to account for the dipole-dipole interactions that occur in molecules having lone electron pairs. However, since this term was set to zero in PC-SAFT, it allows a more symmetric comparison of the models.

Another major difference between the two SAFT EoSs, is that SAFT-γ Mie replaces the square-well potential energy function with the Mie function (a generalized form of the Lennard-Jones equation). The Mie potential energy function is displayed in:

$$U_{kl}(r) = \Omega_{kl}^{\mathrm{Mie}} \varepsilon_{kl} \left[\left(\frac{\sigma_{kl}}{r} \right)^{\lambda_{R,kl}} - \left(\frac{\sigma_{kl}}{r} \right)^{\lambda_{at,kl}} \right] \tag{5.33}$$

$$\Omega_{kl}^{\mathrm{Mie}} = \frac{\lambda_{R,kl}}{\lambda_{R,kl} - \lambda_{at,kl}} \left(\frac{\lambda_{R,kl}}{\lambda_{at,kl}} \right)^{\left(\frac{\lambda_{at,kl}}{\lambda_{R,kl} - \lambda_{at,kl}} \right)} \tag{5.34}$$

where σ_{kl} is the group segment diameter, ε_{kl} is the depth of the potential well between groups, $\lambda_{R,kl}$ and $\lambda_{at,kl}$ are the repulsive and attractive exponents of the intergroup interactions, respectively, and Ω_{kl} is a function of $\lambda_{R,kl}$ and $\lambda_{at,kl}$, which ensures that the minimum interaction energy is ε_{kl}.

The hard-sphere diameter is calculated using Eq. 5.26, with the Mie potential replacing the square well potential used in PC-SAFT. However, unlike with the case of the square-well potential, Eq. 5.26 cannot be solved analytically for the Mie potential, and a Gauss-Legendre procedure has been applied (Paricaud, 2006) to allow incorporation into the code. As before, the hard-sphere diameter is used to calculate the reduced densities (Eq. 5.25), which are used in both the monomeric and chain contribution terms.

The monomer contribution in Eq. 5.32 is analogous to the hard-sphere and dispersion contributions from Eq. 5.22, but for functional groups instead of molecules. The dispersion contribution is also calculated using a perturbation expansion, but SAFT-γ Mie uses a third-order perturbation expansion, compared with the second-order expansion in Eq. 5.27. The chain contribution is determined by calculating molecule-averaged quantities for σ_{kl}, ε_{kl}, $\lambda_{R,kl}$, $\lambda_{at,kl}$, D_k, and ζ_n. These averaged molecule parameters are used to calculate a pair potential function that is summed over the number of species to yield the chain contribution of the Helmholtz free energy. The association term is similar to Eq. 5.28, only its formulation is in terms of the associating sites per functional group, which is summed over the various molecules in the solution:

$$\frac{A^{\text{assoc}}}{Nk_{\text{B}}T} = \sum_{i=1}^{NC} x_i \sum_{k=1}^{NG_i} ng_{k,i} \sum_{A=1}^{N_{ST,k}} nsg_{k,A} \left(LnX_{i,k,A} + \frac{1-X_{i,k,A}}{2} \right) \qquad (5.35)$$

where NC is the number of chemical species, NG_i is the number of groups for species i, $ng_{k,i}$ is the number of groups of type k in molecule i, $N_{ST,k}$ is the total number of site types on a given group k, and $nsg_{k,a}$ is the number of sites of type A on group k. $X_{i,k,A}$ represents the fraction of molecules of species i that are not bonded at a site of type A on group k. $X_{i,k,A}$ is a complex function of $\varepsilon^{\text{HB}}_{kl,AB}$ (the interaction energy between two bonding sites)

and $r^c_{kl,AB}$ (the interaction range between two bonding sites) for associating sites *A* and *B* on groups *k* and *l* respectively. The potential energy function which characterizes the association energy is described by the square-well potential energy function:

$$u^{HB}_{kl,AB}(r_{kl,AB}) = \begin{cases} -\varepsilon^{HB}_{kl,AB}, & r_{kl,AB} \le r^c_{kl,AB} \\ 0, & r_{kl,AB} > r^c_{kl,AB} \end{cases} \tag{5.36}$$

Overall, for each group, four like parameters need to be regressed for a non-associating system (σ_{kk}, ε_{kk}, $\lambda_{R,kk}$, $\lambda_{at,kk}$) and six like parameters need to be regressed for an associating system (σ_{kk}, ε_{kk}, $\lambda_{R,kk}$, $\lambda_{at,kk}$, $\varepsilon^{\mathrm{HB}}_{kl,AB}$, $r^{\mathrm{c}}_{kl,AB}$). The unlike parameters can either be regressed from data or calculated using the following equations:

$$\sigma_{kl} = \frac{1}{2}(\sigma_{kk} + \sigma_{ll}) \tag{5.37}$$

$$\varepsilon_{kl} = \frac{\sqrt{\sigma^3_{kk}\sigma^3_{ll}}}{\sigma^3_{kl}}\sqrt{\varepsilon_{kk}\varepsilon_{ll}} \tag{5.38}$$

$$\lambda_{R,kl} = 3 + \sqrt{(\lambda_{R,kk} - 3)(\lambda_{R,ll} - 3)} \tag{5.39}$$

$$\lambda_{at,kl} = 3 + \sqrt{(\lambda_{at,kk} - 3)(\lambda_{at,ll} - 3)} \tag{5.40}$$

$$D_{kl} = \frac{1}{2}(D_{kk} + D_{ll}) \tag{5.41}$$

$$\varepsilon^{HB}_{kl,AB} = \sqrt{\varepsilon^{HB}_{kk,AA}\varepsilon^{HB}_{ll,BB}} \tag{5.42}$$

$$r^{HB}_{kl,AB} = \frac{1}{2}(r^c_{kk,AA} + r^c_{ll,BB}) \tag{5.43}$$

Note that instead of Eq. 5.41, Eq. 5.26 could be used to calculate the unlike hard-sphere diameter. However, Eq. 5.41 is used to decrease the numerical complexity. It is also important to realize that while it appears that SAFT-γ Mie requires many more parameters than PC-SAFT (4 compared to 3 for non-associating systems, or 6 compared to 5 for associating systems), the SAFT-γ Mie parameters are for groups, which can be used for multiple molecules. SAFT-γ Mie also does not require separate binary parameters (K_{ij}), which further decreases the number of regressed parameters required for complex systems.

5.2.4. Tangent-Plane-Distance Criterion

The equations-of-state are used to calculate thermodynamic parameters, such as fugacity coefficients and liquid molar volumes. However, determining the phase distribution and compositions in a multiphase mixture requires that the Gibbs free energy be minimized subject to mass-balance constraints (Gautam and Seider, 1979; Iglesias-Silva et al., 2003; McDonald and Floudas, 1995a; Ne´ron et al., 2012; White and Seider, 1981). For this purpose, the *Gibbs flash method* in ASPEN PLUS was used (Gautam and Seider, 1979; White and Seider, 1981). Note that two flash convergence algorithms are available in ASPEN PLUS: "Inside-Out" and direct minimization of Gibbs free energy (Gautam and Seider, 1979). The former is implemented in the FLASH2 and FLASH3 blocks and the latter in the RGIBBS block. To the author's knowledge, the latter uses an approximate phase-splitting algorithm as the free energy is minimized.

While, with good initial guesses, it is possible to find the correct phase distribution through direct minimization of the Gibbs free energy (Nichita et al., 2002), it

is preferable to check the stability of the resulting phases by using the Gibbs free energy of mixing to estimate the tangent-plane-distance function (McDonald and Floudas, 1995b; Michelsen and Mollerup, 2007; Sun and Seider, 1995). The tangent-plane-distance function compares the total Gibbs free energy after creating a new, infinitesimal phase with the Gibbs free energy of the initial phase, shown as Eq. 5.44, where ΔG is the total Gibbs free energy of the phase, $\bar{Z}$ is the vector of moles in the initial phase, and $\overline{Y}$ is the vector of moles in the infinitesimal phase. This expression can be reformulated in terms of the Gibbs free energies of mixing as Eq. 5.45 (Sun and Seider, 1995), where $\bar{y}$ is the vector of mole fractions in the infinitesimal phase, $\overline{z}$ is the vector of mole fractions in the initial phase, $\Delta G_{\mathrm{m}}(\bar{y})$ is the Gibbs free energy mixing surface, $\Delta G_{\mathrm{m}}^{\mathrm{T}}(\overline{z})$ is the tangent plane, and $F(\bar{y})$ is the tangent-plane-distance function (the difference between the tangent plane and the Gibbs free energy of mixing surface). If $F(\bar{y})$ is greater than zero for all values of $\bar{y}$, the initial phase is stable. Otherwise, the initial phase is unstable, guesses for another phase are estimated, and the Gibbs free energy is re-minimized.

A more common formulation of the tangent-plane-distance function is shown as Eq. 5.46, where μ_i is the chemical potential of species *i* in the phase (Sun and Seider, 1995). Finally, the tangent-plane-distance function is reformulated using Eq. 5.47 and 5.48 to give Eq. 5.49, where $\mu_{i,ref}$ is the chemical potential of species *i* in the pure ideal gas evaluated at *T*, *R* is the gas constant, *T* is the absolute temperature, f_{i} is the fugacity of species *i* in the phase, *P* is the pressure of the system, ϕ_i is the fugacity coefficient of species *i* in the phase, x_i is the mole fraction of species *i* in the phase, and $\phi_{o,i}$ is the fugacity coefficient of species *i* in the original phase.

Eq. 5.49 is used herein in a FORTRAN algorithm written by Prof. Romain Privat (Webpage: Prof. Romain Privat's Homepage), which examines the stability of every phase separately. The code uses the objective function, Φ, defined by Michelsen (Michelsen and Mollerup, 2007), in Eq. 5.50, where W_i is the non-normalized concentration for the infinitesimal phase. Since the minimum of the objective function satisfies the necessary constraint (Michelsen and Mollerup, 2007), Eq. 5.51 – the minimum can be found by minimizing the sum of the squares, shown in Eq. 5.52. The objective function, Γ, is minimized using a custom-written NLP solver with numerous initial guesses. If the minimum of Eq. 5.49 is found to be negative, the initial phase(s) is unstable. Otherwise, the phase(s) is assumed to be stable. This code was incorporated within ASPEN PLUS by the authors, permitting ϕ_i and $\phi_{o,i}$ to be calculated using the ASPEN PLUS physical property system.

$$\Delta G\left(\overline{Y}\right) = \Delta G\left(\overline{Z} - \overline{Y}\right) + \Delta G\left(\overline{Y}\right) - \Delta G(\bar{Z}) \geq 0, \forall\, \overline{Y} \tag{5.44}$$

$$F(\overline{y}) = \Delta G_m(\bar{y}) - \Delta G_m^T(\bar{z}) \geq 0, \forall\, \overline{y} \tag{5.45}$$

$$F(\overline{y}) = \sum_{i=1}^{NC} y_i \left(\mu_i(\overline{y}) - \mu_i(\bar{z})\right) \geq 0, \forall\, \overline{y} \tag{5.46}$$

$$\mu_i = \mu_{i,ref} + RTLn(f_i) \tag{5.47}$$

$$f_i = P\phi_i x_i \tag{5.48}$$

$$F(\overline{y}) = RT \sum_{i=1}^{NC} y_i (Ln(y_i) + Ln(\phi_i) - Ln(z_i) - Ln\left(\phi_{o,i}\right)) \tag{5.49}$$

$$\Phi(T, P, z, W) = 1 + \sum_{i=1}^{NC} W_i * (Ln(W_i) + \mathrm{Ln}(\phi_i) - Ln(z_i\phi_{o,i}) - 1) \tag{5.50}$$

$$Ln(W_i) + \mathrm{Ln}(\phi_i) - Ln\left(z_i\phi_{o,i}\right) = 0, \ \forall i \tag{5.51}$$

$$\Gamma(T, P, z, W) = \sum_{i=1}^{NC} (Ln(W_i) + \mathrm{Ln}(\phi_i) - Ln\left(z_i\phi_{o,i}\right))^2 \tag{5.52}$$

5.3. Experimental

5.3.1. Vapor-Liquid Equilibria

Methyl-oleate and methanol equilibrium data were measured using a 500 mL bulb connected to a condenser and setup for total or partial reflux. The bulb was heated with an electric heating jacket, and the cooling water was circulated at 7°C. The well-insulated apparatus was mixed by a magnetic stir bar in the liquid phase and heated to obtain a low boil. The system was then operated at total reflux for 1-hour to attain equilibrium. A small sample of the condensed vapor was collected using a 3-way valve. The liquid was sampled from a stopcock at the bottom of the bulb. Following sampling, methanol was added through the condenser to obtain data at a higher methanol composition.

5.3.2. Liquid-Liquid Equilibria

Each species was added at equal mass loadings to a 10 mL separatory funnel that was used for equilibration and sampling. The apparatus was affixed to a rotisserie-style rotor inside a preheated oven and rotated for at least 3 hours to provide adequate contact between the two liquids. The samples were then left to equilibrate for at least 5 hours. The top phase was sampled using a pipette and the bottom phase was sampled through the funnel's stopcock. During sampling, the first few drops of sample were discarded to insure a representative sample was taken. All experiments were run at least in duplicate.

5.3.3. Sample Preparation

To obtain the methyl-oleate concentration, samples were diluted in heptane containing 0.05 g/L of methyl-laurate as an internal standard. For the analysis of triolein, samples were diluted in 1:1 chloroform:methanol containing 0.1 g/L tripalmitin as an internal standard. They were then transesterified using 14% boron trifluoride in methanol. The sample headspace was sparged with nitrogen, and the reaction took place at 100°C for 1-hour. The reacted samples were diluted with heptane containing 0.05 g/L of methyl-laurate as an internal standard. For analysis of glycerol, samples were silylated using ASTM Standard test method D6584 – 13 (ASTM, 2013).

5.3.4. Analysis

The sample analysis was performed using a Perkin-Elmer AutoSystem XL Gas Chromatograph and Gold Mass Spectrometer (GC-MS). The GC was fitted with a 15m × 0.25mm × 0.25μm 5% phenyl polydimethylsiloxane column (Agilent, DB-5ht) and joined with a 5m × 0.53mm deactivated, Hi-Temp guard column using a press fit union. All analytical samples were run on the GC-MS using ASTM Standard test method D6584 – 13 (ASTM, 2013). Methyl-oleate and silylated glycerol were analyzed at a mass-to-charge ratio (*m/z*) of 264 and 205 with retention times of 11.00 and 5.87 minutes, respectively. The results of the analysis are shown as Appendix C.

5.4. Regression Methodology

This section discusses the techniques used to regress the pure-species and binary-interaction parameters necessary for PC-SAFT in ASPEN PLUS and SAFT-γ Mie in gPROMS. The same pure-species and binary data sets were used to regress parameters in

both PC-SAFT and SAFT-γ Mie. The Britt-Luecke method (Britt and Luecke, 1973) in ASPEN PLUS was used to regress the parameters for PC-SAFT. The Levenberg-Marquardt algorithm (Marquardt, 1963) was used in gPROMS for SAFT-γ Mie.

5.4.1. Pure Species

The majority of the pure-species data were obtained from the NIST database within ASPEN PLUS (NIST Data Bank, ASPEN Plus). For methyl-oleate (Bonhorst et al., 1948; Ott et al., 2008; Pratas et al., 2010; Yuan et al., 2005), glycerol (Association, 1963; Cammenga et al., 1977), CO_2 (Duschek et al., 1990), and triolein (Perry et al., 1949; Santander et al., 2011), sufficient data were not present in the NIST databanks. Supplementary data were obtained from the literature (Perry and Green, 2007; Saleh and Wendland, 2005; Stull, 1947). For all species except carbon dioxide, liquid density and liquid vapor-pressure data were used to regress the pure-species parameters. Liquid density data were weighted more heavily (roughly 200 times) than vapor-pressure data, leading to more accurate predictions of liquid phase behavior, and in particular liquid-liquid equilibria. The liquid phase predictions must be accurate, because in a biodiesel production reactor, the reactions occur exclusively in the liquid phases due to the nonvolatile triglycerides. It is also essential to capture the liquid-liquid behavior of the aqueous (methanol) phase and the nonpolar (oil) phase to obtain an accurate prediction of the reaction rates.

With regard to carbon dioxide, the pure-species parameters were regressed entirely from densities for the three phases (vapor, liquid, and supercritical). Because ASPEN PLUS accepts data input as either a vapor or a liquid phase, the supercritical

region needed to be partitioned into these two categories. Densities greater than the critical density (467.6 kg/m^3) (Webpage: Carbon dioxide thermophysical properties) were classified as liquid, while all others were classified as vapor. Plots of the density as a function of temperature were also generated to visualize the phase distribution, as shown in Figure 5.2. From these, good agreement between the data points and the PC-SAFT method is observed.

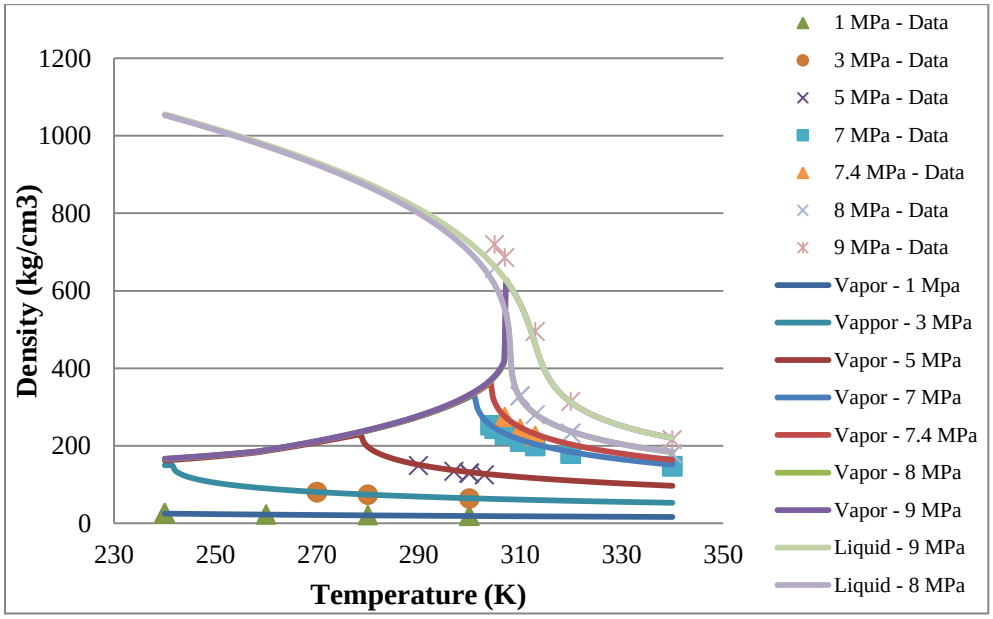

Figure 5.2. CO_2 density as a function of temperature using the PC-SAFT EoS.

5.4.2. Binary

Binary data were obtained from the NIST interface in ASPEN PLUS (NIST Data Bank, ASPEN Plus), the literature (Koohyar et al., 2013; Korgitzsch, 1993; Soujanya et al., 2010), as well as the experiments in Section 5.3. The regressed binary interaction parameters for PC-SAFT are shown below. Only $b_{i,j}$ and $c_{i,j}$ were regressed, with the others set to zero. For SAFT-γ Mie, the cross-interaction energies for unlike groups, ε_{ij},

were regressed using binary data. In some cases, unlike well-distance parameters, λ_{ij}, were added to improve the fit.

$$\varepsilon_{ij} = (1 - K_{i,j})\sqrt{\varepsilon_i \varepsilon_j} \tag{5.53}$$

$$K_{i,j} = a_{i,j} + \frac{b_{i,j}}{T_r} + c_{i,j} Ln(T_\mathrm{r}) + d_{i,j} T_\mathrm{r} + e_{i,j} T_\mathrm{r}^2 \tag{5.54}$$

$$T_\mathrm{r} = \frac{T}{T_\mathrm{ref}} \tag{5.55}$$

where $\varepsilon_{i,j}$ is the square-well potential energy constant for two unlike molecules *i* and *j*, ε_i and ε_j are the square-well potential energy constants for pure species *i* and *j*, respectively, $K_{i,j}$ is the binary interaction parameter for molecules *i* and *j*, $a_{i,j}$, $b_{i,j}$, $c_{i,j}$, $d_{i,j}$, and $e_{i,j}$ are empirical constants that are fit to binary data for molecules *i* and *j*, T_r is the reduced temperature, *T* is the system temperature, and T_ref is the chosen reference temperature (298.15 K).

5.5. Results

5.5.1. Parameter Results

The pure-species PC-SAFT parameters are shown in Table 5.1. A similar set of parameters were regressed for SAFT-γ Mie (the gSAFT package in gPROMS); however, at this time, those parameters cannot be released for intellectual property reasons. The groups that were used by SAFT-γ Mie are shown in Table 5.2. Where "R" represents a set of cross interacting parameters that were regressed from data and "X" indicates no parameters were regressed, because the necessary data does not exist.

In Table 5.1, PCSFTM is m_i in Eq. 5.25, representing the length of the molecule. Note that fits are empirical and while they follow a logical trend, the parameters are not meant to agree with theoretical molecular properties. PCSFTU is the interaction energy,

ε_i. PCSFTV is the characteristic diameter, σ_i. PCSFAU is the association site interaction energy (for hydrogen bonding molecules), $\varepsilon^{A_iB_i}$. PCSFAV is the association site interaction volume (for hydrogen-bonding molecules), $\kappa^{A_iB_i}$. PCSFMU and PCSFXP are the characteristic dipole-moment and the characteristic dipole-fraction parameters, respectively. The latter two parameters are not used herein because they led to numerical instability for regressions and simulations. The effect of lone pairs was not accounted for in SAFT-γ Mie for similar reasons.

Table 5.1. Pure-Species Parameters for PC-SAFT

PURE COMPONENT							
Param.	Unit	spec	spec	spec	spec	spec	spec
		Methyl-oleate	Triolein	Glycerol	Methanol	Water	Carbon dioxide
m_i	-	9.039	16.184	2.1512	0.55347	0.33444	1.8102
ε_i	K	248.47	282.84	472.16	120.97	139.5	179.83
σ_i	-	3.7465	4.4475	3.7517	4.6043	4.5938	2.9107
ε^{AiBi}	K	0	0	3832.4	3602.3	3965.5	0
κ^{AiBi}	-	0	0	0.00189	0.01171	0.00634	0
μ	-	0	0	0	0	0	0
X_p	-	0	0	0	0	0	0

Table 5.2. SAFT-γ Mie groups

Group	CH_3	CH_2	CH=	COO	$C_9H_{11}O_6$	$C_3H_8O_3$	CO_2	CH_3OH	H_2O
CH_3	-	R	R	R	R	R	R	R	R
CH_2	R	-	R	R	R	R	R	R	R
CH=	R	R	-	R	R	R	R	R	R
COO	R	R	R	-	X	R	R	R	R
$C_9H_{11}O_6$	R	R	R	X	-	R	R	R	R
$C_3H_8O_3$	R	R	R	R	R	-	X	R	R
CO_2	R	R	R	R	R	X	-	R	R
CH_3OH	R	R	R	R	R		R	-	R
H_2O	R	R	R	R	R	R	R	R	-

The binary interaction parameters regressed from vapor-liquid and liquid-liquid equilibria data are shown in Tables 5.3 and 5.4. Only b_{ij} and c_{ij} (in Eq. 5.54) were regressed to avoid over-regressing parameters.

Table 5.3. Binary-Species Parameters for PC-SAFT (from VLE data)

Species *i*	Methanol	Glycerol	Glycerol	Water
Species *j*	Carbon Dioxide	Methanol	Water	Methanol
Temp. units	°C	°C	°C	°C
$a_{i,j}$	0	0	0	0
$b_{i,j}$	-0.1317	-0.3297	0.21467	-0.5846
$c_{i,j}$	0.3591	-0.1476	-1.6503	2.726
$d_{i,j}$	0	0	0	0
$e_{i,j}$	0	0	0	0
T_{ref}	25	25	25	25
Species *i*	Carbon Dioxide	Methanol	CO_2	CO_2
Species *j*	Water	Methyl-oleate	FAME	TG
Temp. units	°C	°C	°C	°C
$a_{i,j}$	0	0	0	0
$b_{i,j}$	-0.4504	-0.1658	-0.0429	0.13616
$c_{i,j}$	-0.0191	-1.463	1.0185	0.29994
$d_{i,j}$	0	0	0	0
$e_{i,j}$	0	0	0	0
T_{ref}	25	25	25	25

Table 5.4. Binary-Species Parameters for PC-SAFT (from LLE data)

Species i	Triolein	Methyl-oleate	Methyl-oleate	Triolein	Triolein
Species j	Methanol	Water	Glycerol	Glycerol	Water
Temp. units	°C	°C	°C	°C	°C
$a_{i,j}$	0	0	0	0	0
$b_{i,j}$	-0.0682	-0.31655	-0.03783	-0.10413	-0.17356
$c_{i,j}$	0.01725	-0.12144	0.01543	-0.01823	0.20112
$d_{i,j}$	0	0	0	0	0
$e_{i,j}$	0	0	0	0	0
T_{ref}	25	25	25	25	25

The pure-species parameters for RK-ASPEN are in Table 5.5. They were taken from the NIST databank, with the exception of triolein, which decomposes before reaching its critical point. Consequently, its critical properties were generated using group-contribution methods (Anikeev et al., 2012; Glisic and Orlovic, 2014; Macaira et al., 2014). The binary interaction parameters (in Eqs. 5.11 and 5.12) are in Table 5.6. They were regressed using the same data and algorithm as for those in PC-SAFT.

Table 5.5. Pure-Species Parameters for RK-ASPEN

Param.	Units	spec.	spec.	spec.	spec.	spec.	spec.
		Methyl oleate	Water	Methanol	Triolein	Glycerol	CO_2
ω	-	0.96055	0.34407	0.5585	1.6862	0.55381	0.22567
V_C	m^3/kmol	1.2339	0.0587	0.118	3.007	0.2447	0.09431
P_C	Pa	1.17E+06	2.21E+07	8.01E+06	4.68E+05	7.50E+06	7.38E+06
T_C	K	768	647.11	512.7	947.1	850	304.16

Table 5.6. Binary Interaction Parameters for RK-ASPEN (using VLE or LLE data)

$K^1_{a,ij}$	Glycerol	Water	0.0815	$K^1_{a,ij}$	Glycerol	MEOH	0.0049
$K^1_{b,ij}$	Glycerol	Water	0.1925	$K^1_{b,ij}$	Glycerol	MEOH	0.038
$K^1_{a,ij}$	Methyl-oleate	Water	-4.8307	$K^1_{a,ij}$	Methyl-oleate	MEOH	-1.3533
$K^1_{b,ij}$	Methyl-oleate	Water	-1.6375	$K^1_{b,ij}$	Methyl-oleate	MEOH	-0.6083
$K^1_{a,ij}$	Water	Methanol	0.1295	$K^1_{a,ij}$	Water	CO_2	-1.9801
$K^1_{b,ij}$	Water	Methanol	0.3595	$K^1_{b,ij}$	Water	CO_2	-0.9809
$K^1_{a,ij}$	Methanol	CO_2	0.2373	$K^1_{a,ij}$	CO_2	FAME	0.1983
$K^1_{b,ij}$	Methanol	CO_2	0.0316	$K^1_{b,ij}$	CO_2	FAME	-0.2123
$K^1_{a,ij}$	CO_2	Triolein	0.2086	$K^1_{a,ij}$	Methanol	T-OLE	-1.7758
$K^1_{b,ij}$	CO_2	Triolein	0.1955	$K^1_{b,ij}$	Methanol	T-OLE	-0.7823
$K^1_{a,ij}$	Methyl-oleate	Glycerol	-11.177	$K^1_{a,ij}$	Glycerol	T-OLE	-1.127
$K^1_{b,ij}$	Methyl-oleate	Glycerol	-8.2022	$K^1_{b,ij}$	Glycerol	T-OLE	-0.7685
$K^1_{a,ij}$	Triolein	Water	97.529				
$K^1_{b,ij}$	Triolein	Water	-11.754				

5.5.2. Pure Species

Figures 5.3-5.7 below show the plots of pure-species liquid densities and vapor pressures for the five noncritical compounds contained within the system (water, methanol, glycerol, triolein, and methyl-oleate). Predictions over the range of temperatures and pressures were generated for each species using PC-SAFT, SAFT-γ Mie (gSAFT), and RK-ASPEN. All three EoSs provide excellent predictions of vapor pressures, with the exception of triolein; however, the cubic EoS (RK-ASPEN), yields poor predictions of liquid densities. This underestimation of liquid density by RK-ASPEN would lead to drastic underestimations of process-vessel sizes.

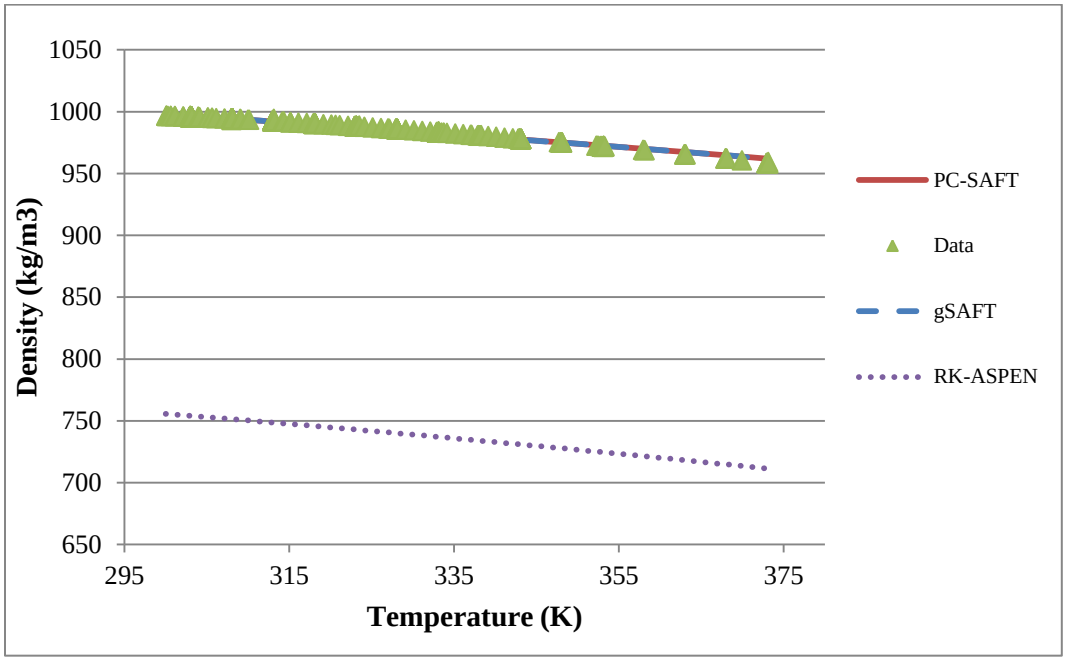

(a) Liquid density

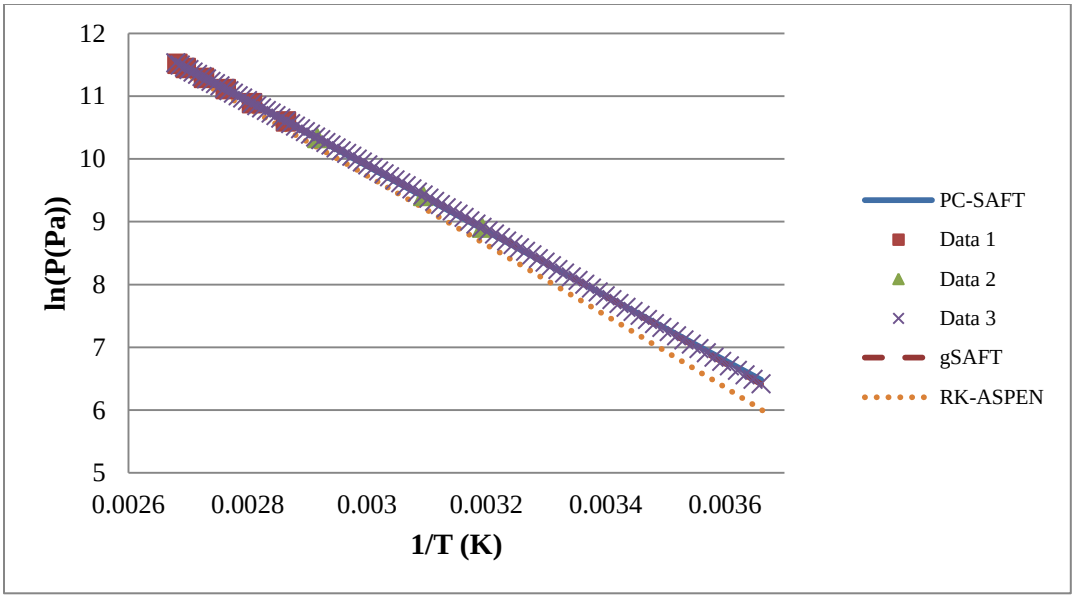

(b) Liquid vapor pressure

Figure 5.3. Water properties.

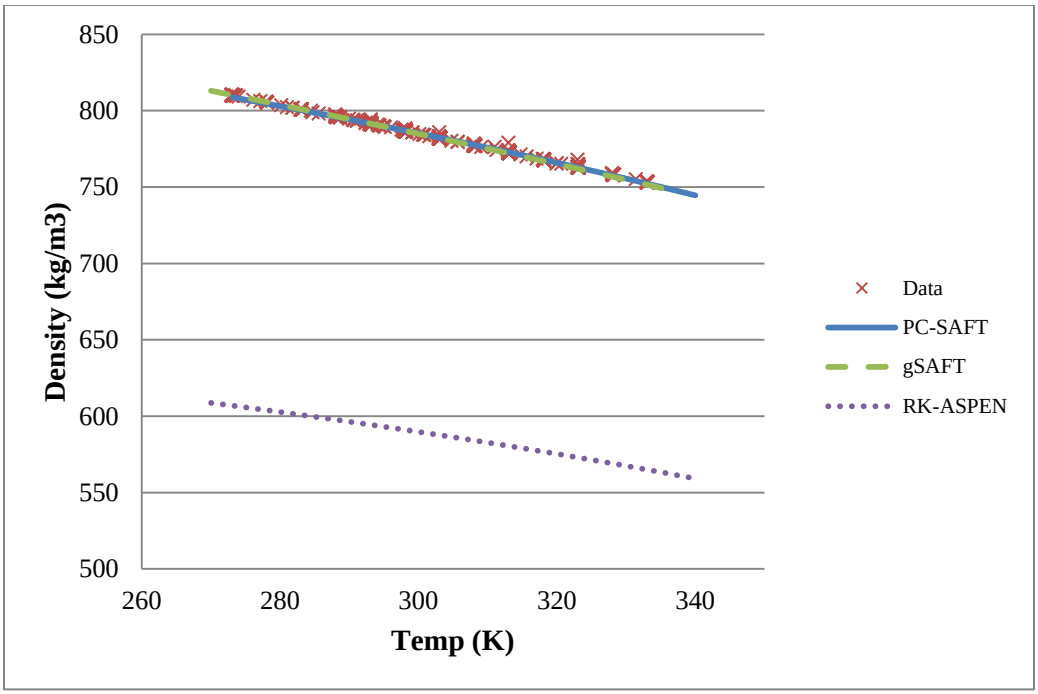

(a) Liquid density

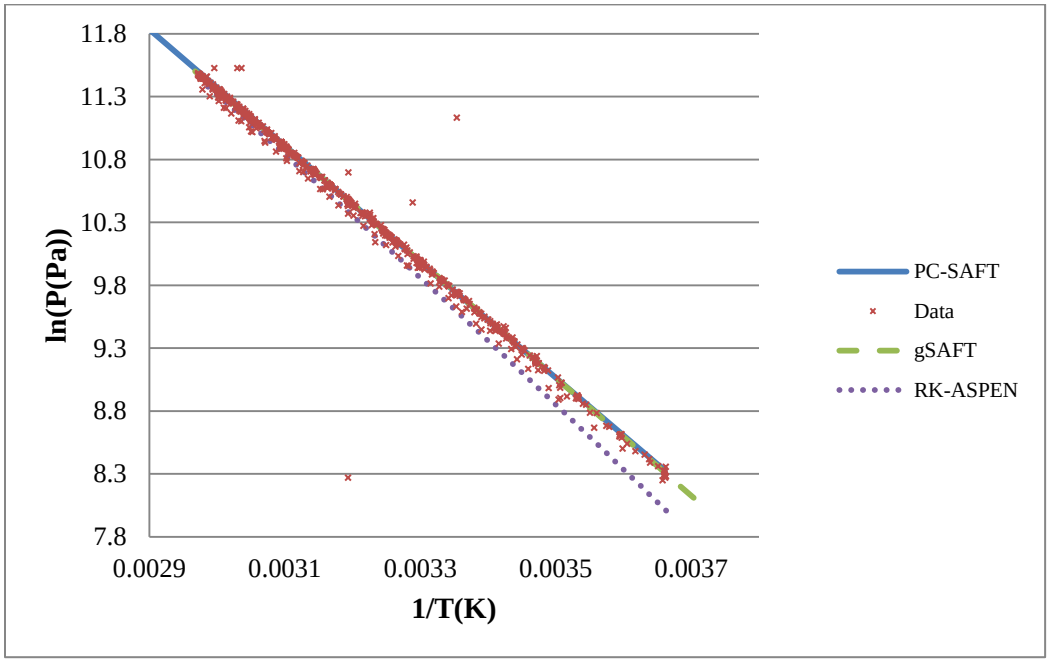

(b) Liquid vapor pressure

Figure 5.4. Methanol properties.

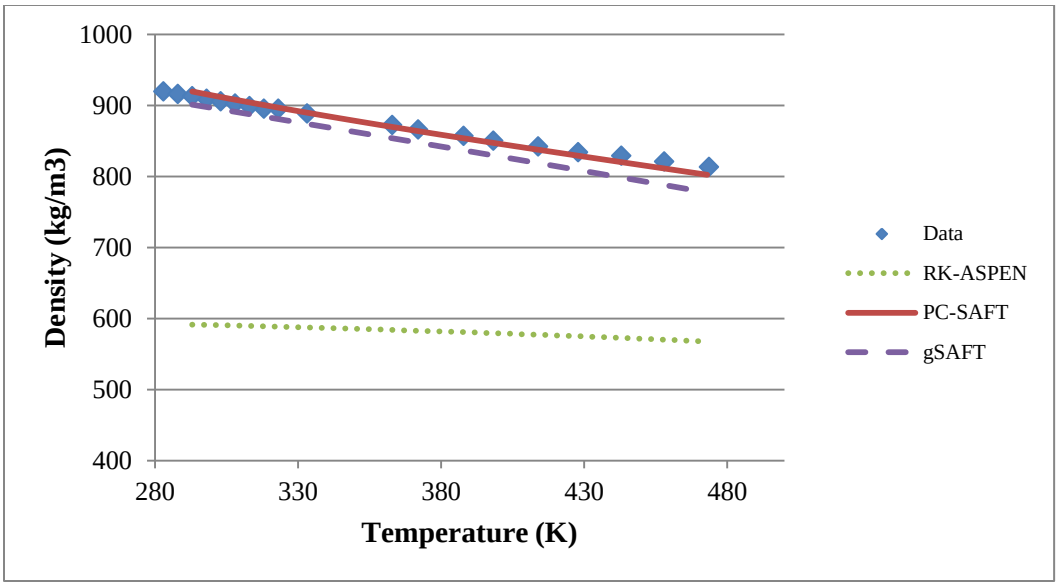

(a) Liquid density

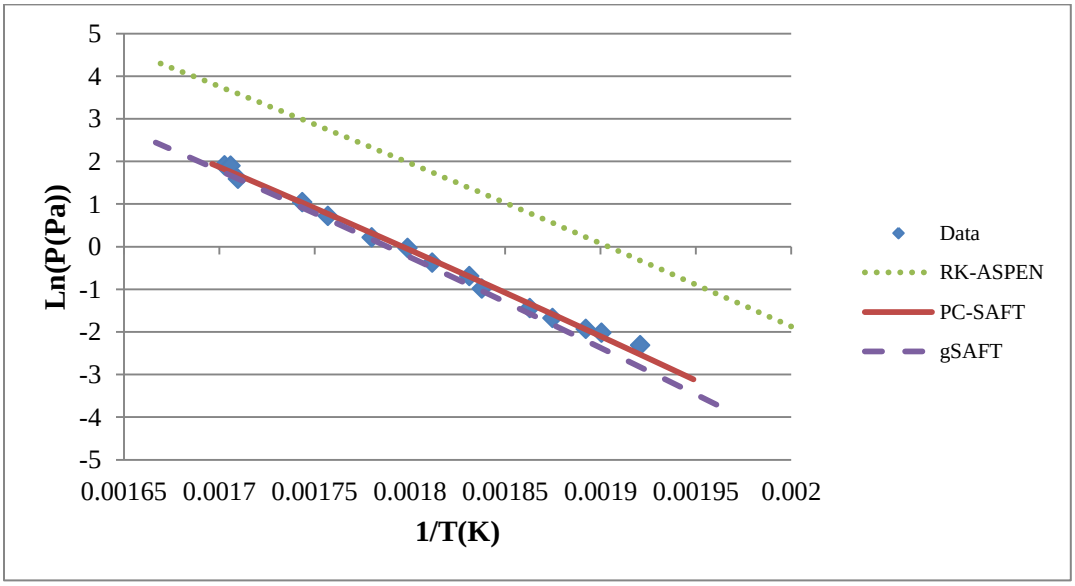

(b) Liquid vapor pressure

Figure 5.5. Triolein properties.

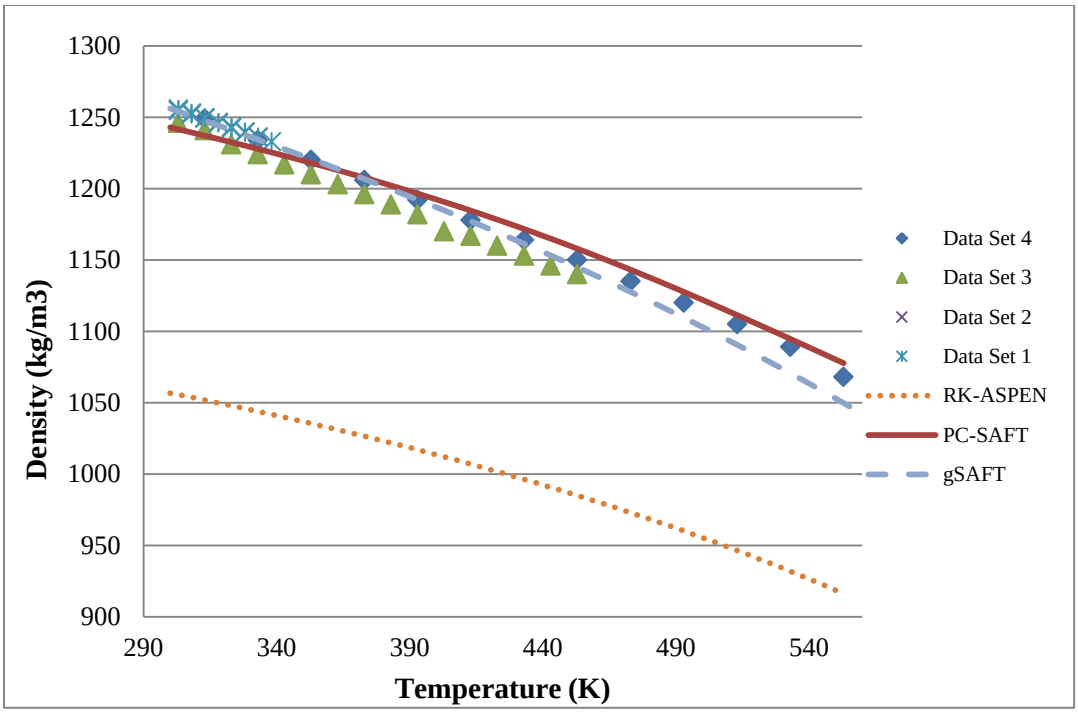

(a) Liquid density

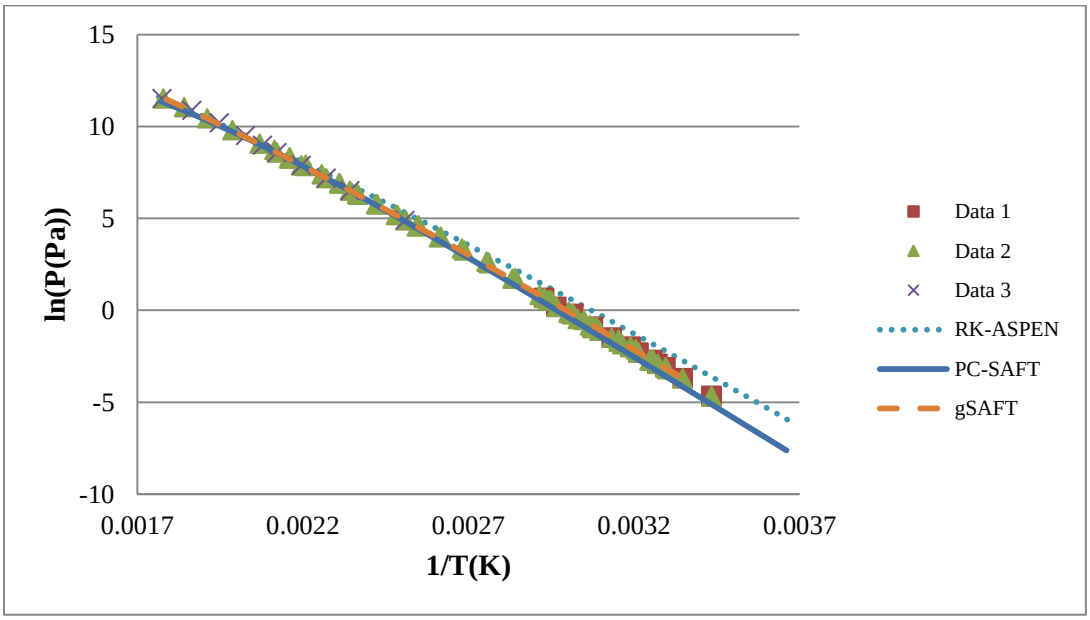

(b) Liquid vapor pressure

Figure 5.6. Glycerol properties.

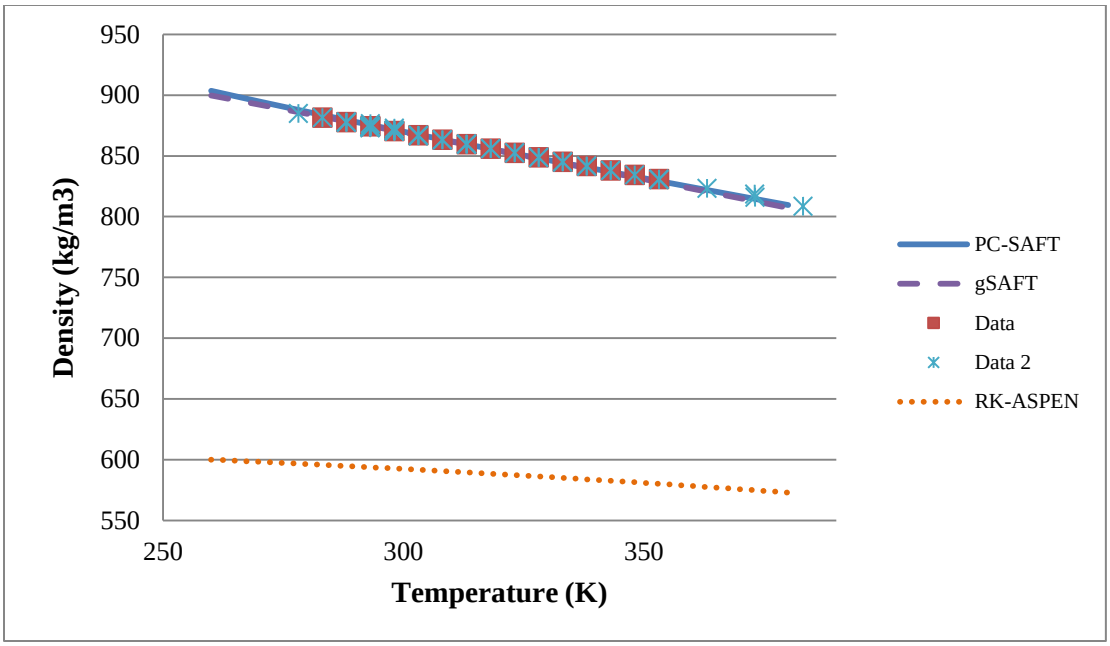

(a) Liquid density

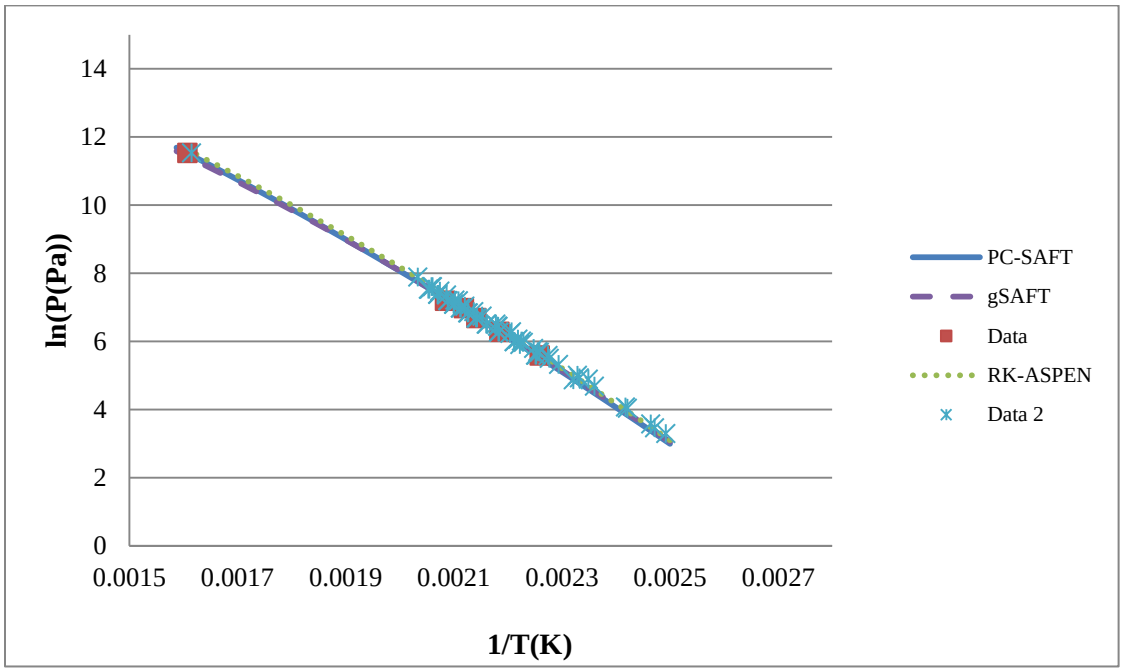

(b) Liquid vapor pressure

Figure 5.7. Methyl-oleate properties.

In Figure 5.8, liquid, vapor, and supercritical phase densities of CO_2 are plotted as a function of pressure at various temperatures. Both versions of the SAFT EoS show excellent agreement with the data in all three regimes (vapor, liquid, and supercritical). By contrast, RK-ASPEN is accurate in the vapor regimes and at temperatures far above the critical region, which limits its ability to predict gas-expanded liquid (GXL) (Ye et al., 2012) systems.

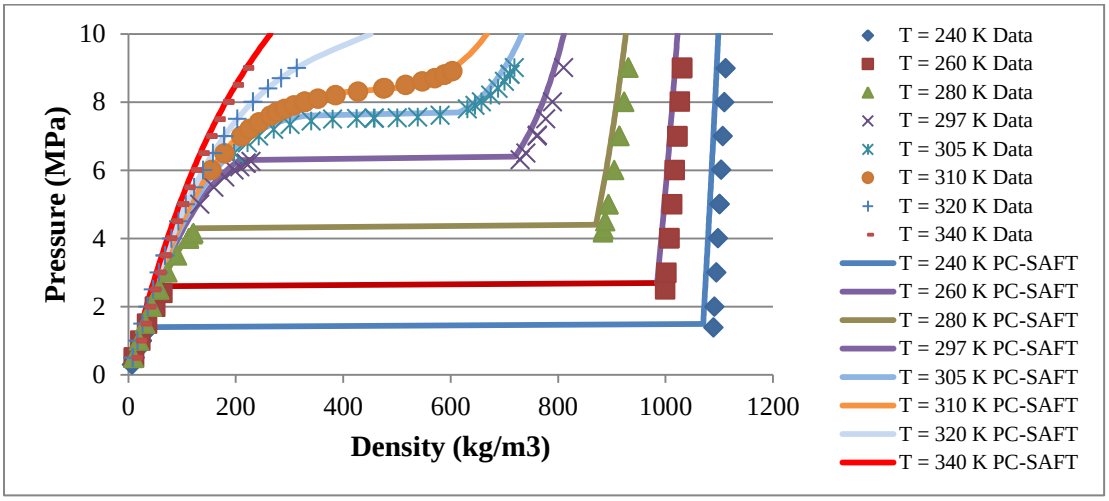

(a) PC-SAFT predictions

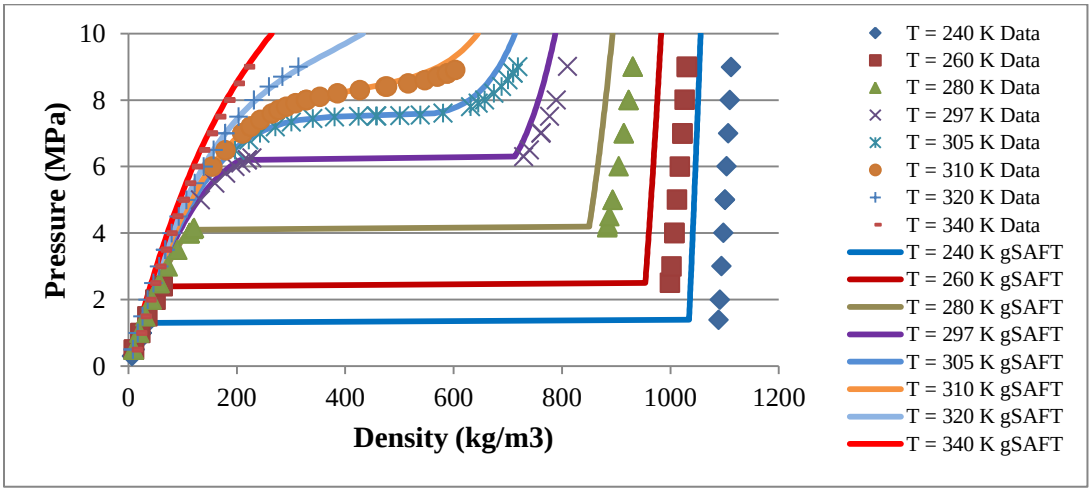

(b) gSAFT Mie predictions

Figure 5.8. CO_2 densities.

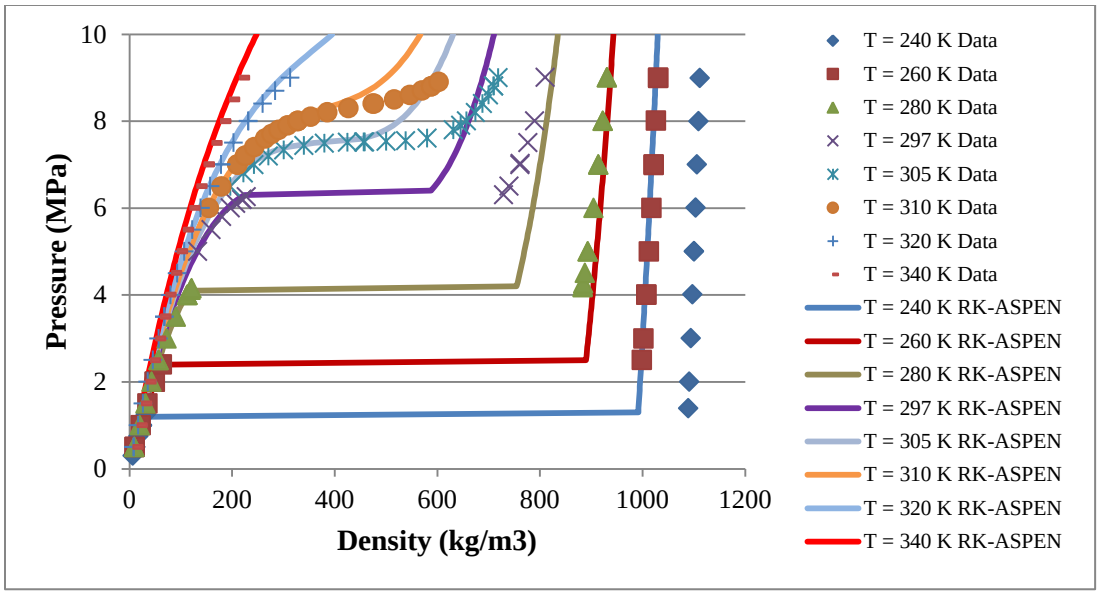

(c) RK-ASPEN predictions

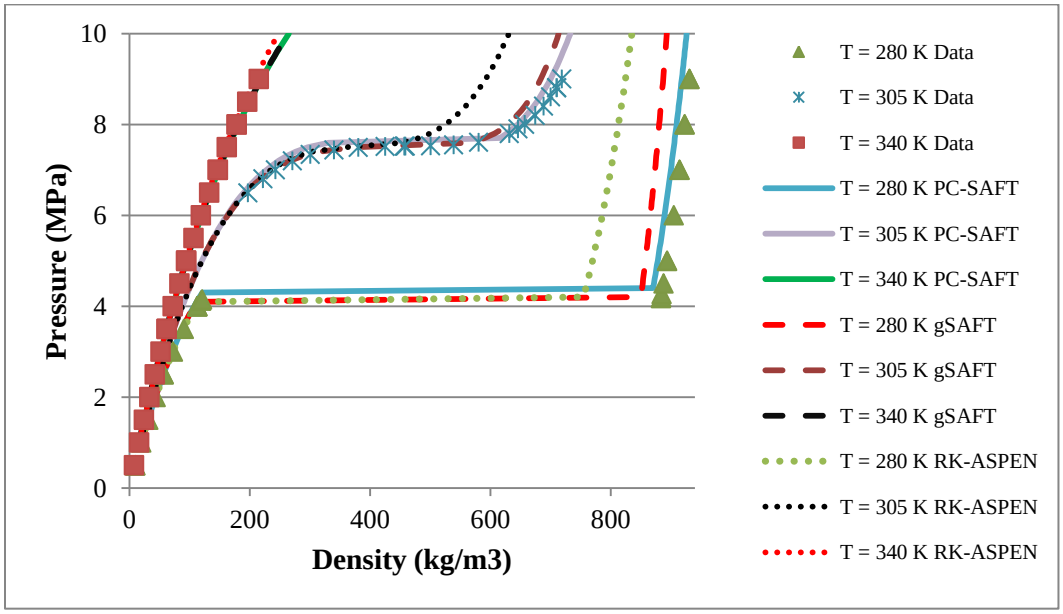

(d) Comparison of three EoSs

Figure 5.8. CO_2 densities (Cont'd.)

5.5.3. Binary VLE Mixtures

Figures 5.9-5.16 show bubble- and dew-point curves for binary mixtures involving the six species in the biodiesel system considered herein. Figures 5.9-5.12 do not involve CO_2, and consequently, the data are in excellent agreement with all three equations-of-state. Of these binary pairs, methanol and water (Figure 5.12) agreement is the most difficult to achieve because of the strong associating groups on both species. SAFT-γ Mie performs the best, due to the regression of cross-association parameters; whereas, PC-SAFT's binary parameters only affect the segment interaction energy, ε, and the cross association is calculated using combining rules.

Introducing CO_2 drives the mixtures toward their critical points, which are in a significantly more difficult region to predict. RK-ASPEN performs well for CO_2 and methanol (Figure 5.13) because the molecules are small and do not associate. Association becomes more important for water and CO_2, as they combine to form carbonic acid, (Figure 5.14) and consequently, RK-ASPEN becomes less effective. PC-SAFT also does not perform that well in this system, mainly because of the heavy weighting of liquid phase behavior (discussed in section 5.4.1.). While the same weighting factors were used for SAFT-γ Mie for the groups regressed herein, it was less sensitive to the effects of weighting because certain groups (like CH_3 and CH_2) had already been regressed previously and were not weighted.

The biggest advantage of a SAFT EoS relative to a cubic EoS arises for the long-chain species (triolein and methyl-oleate) in Figures 5.15 and 5.16. RK-ASPEN fails to predict accurately the behavior of long-chain molecules as seen in Figures 5.15a, c, and 5.16 (but, not 5.15b). It should be noted that alpha factors were not used herein to

improve RK-ASPEN's behavior, because it was meant to be a benchmark against previous work (Anikeev et al., 2012; Glisic and Orlovic, 2014; Macaira et al., 2014).

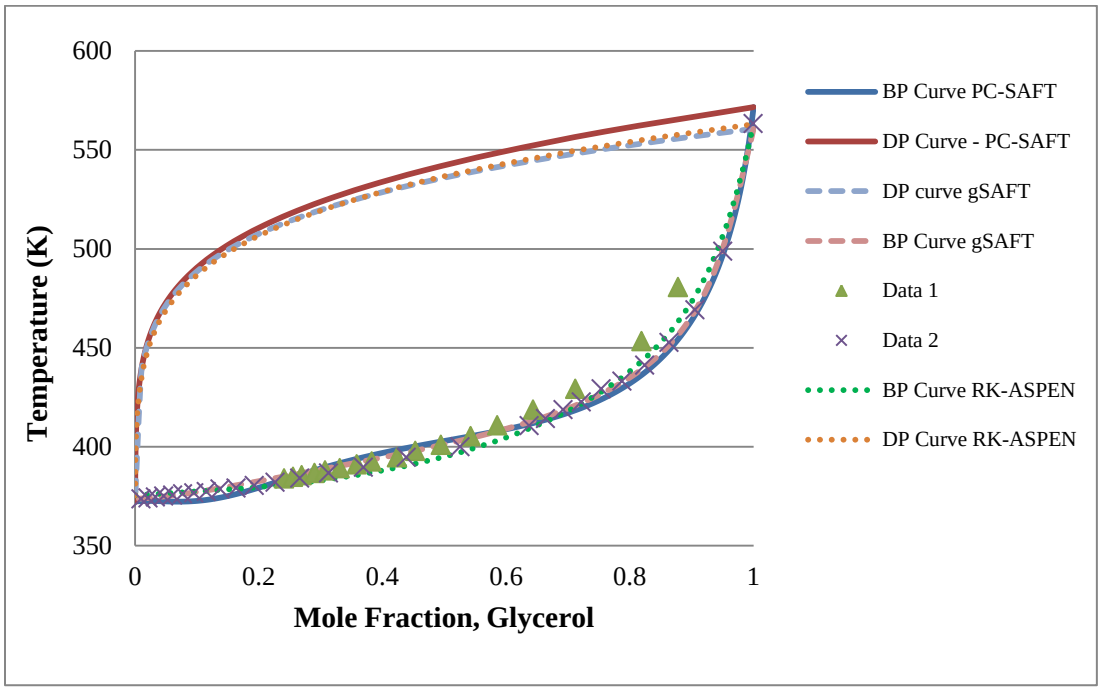

Figure 5.9. Glycerol and water VLE at 1 atm.

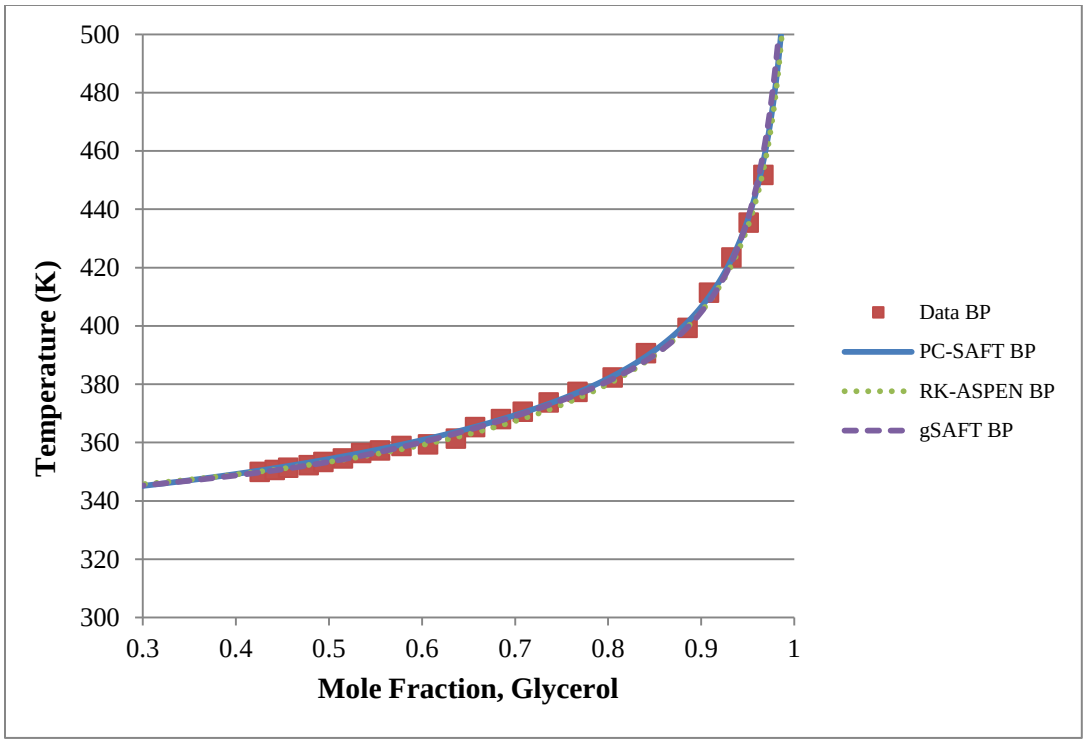

(a) T-x bubble-point curve.

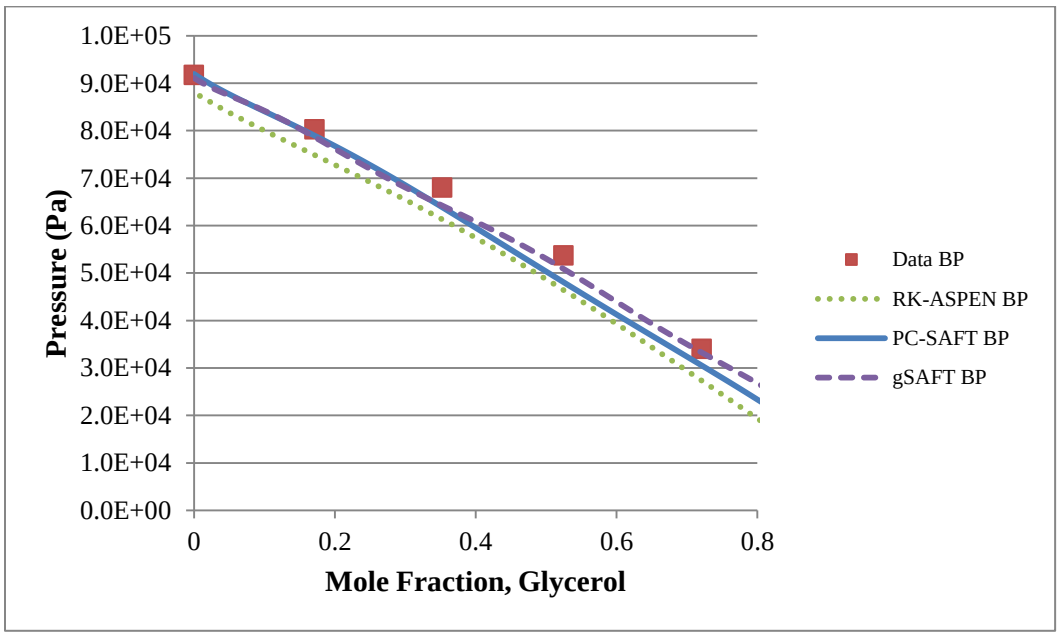

(b) P-x bubble-point curve.

Figure 5.10. Methanol and glycerol VLE at 1 atm.

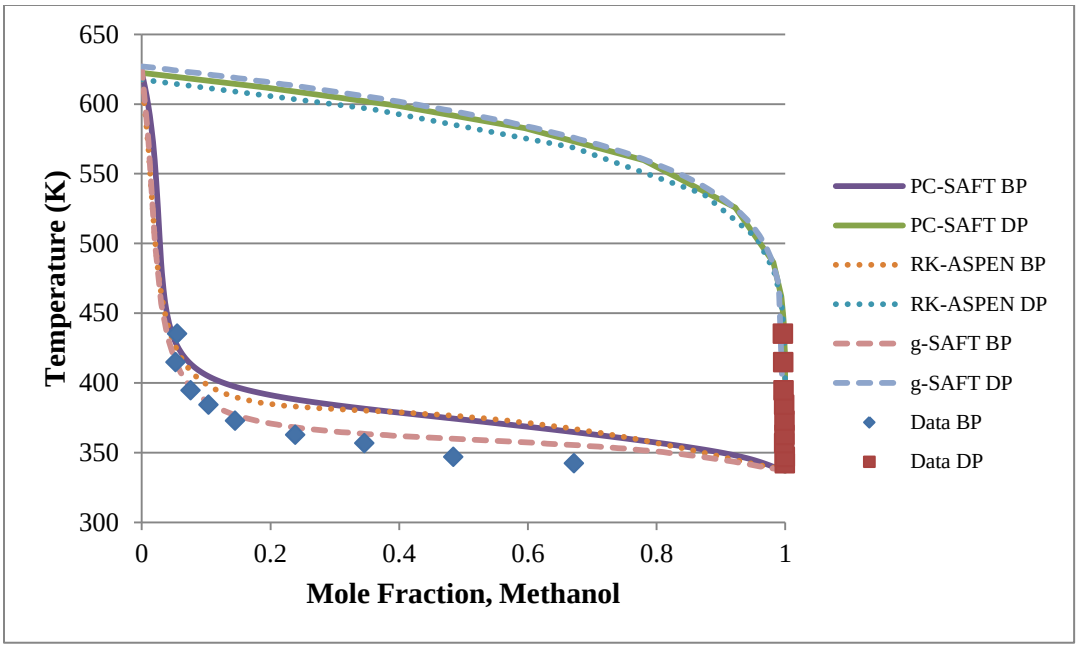

(a) Full-scale.

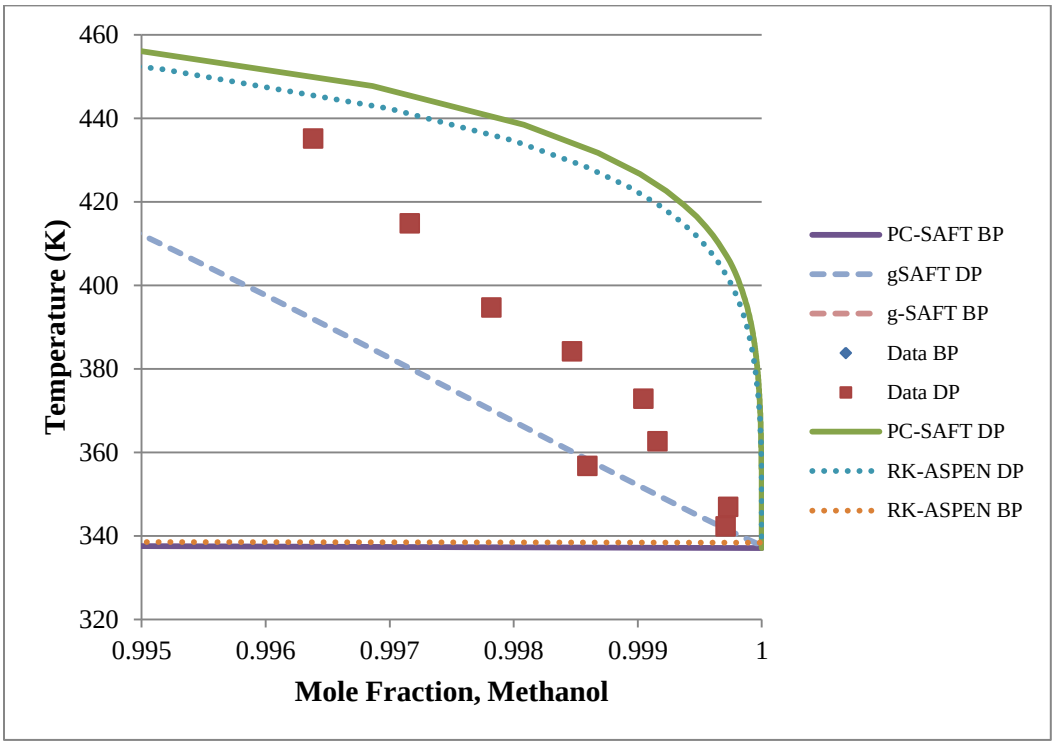

(b) Expanded vapor region.

Figure 5.11. Methanol and methyl-oleate VLE at 1 atm.

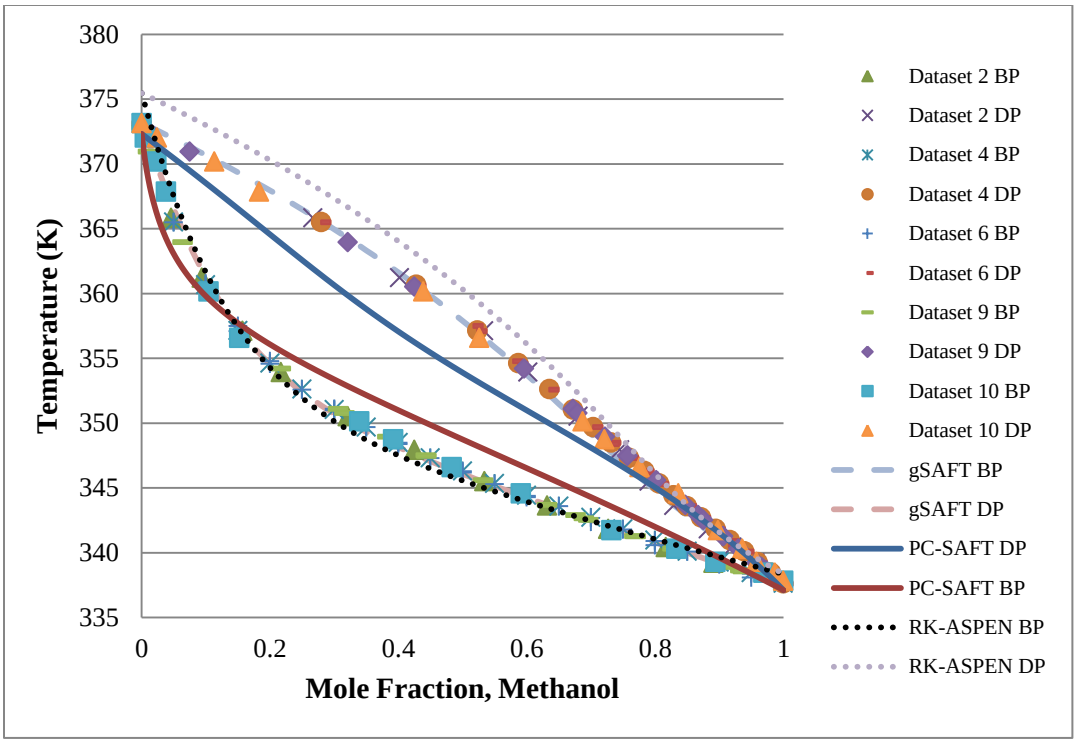

Figure 5.12. Methanol and water VLE at 1 atm.

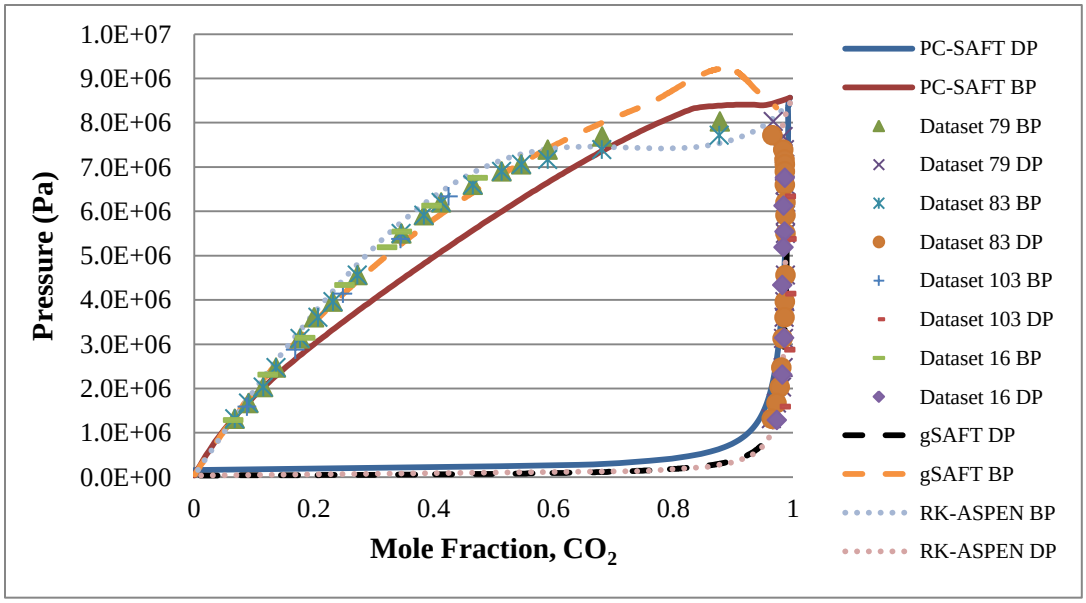

(a) At 313.14 K (full-scale)

Figure 5.13. Methanol and CO_2 VLE.

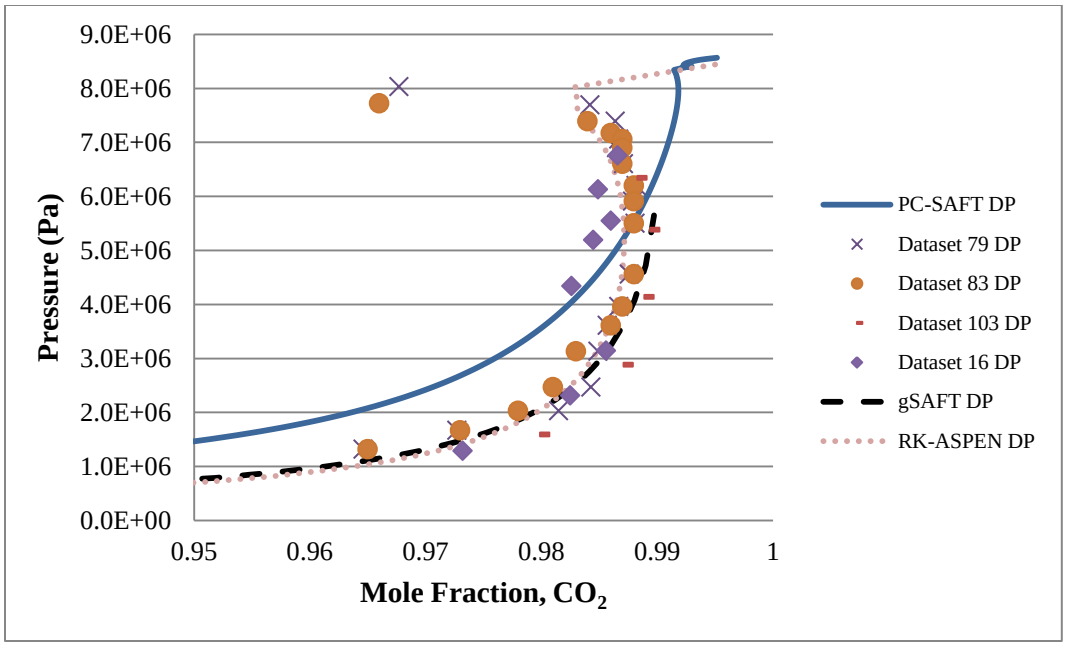

(b) At 313.14 K (expanded vapor region)

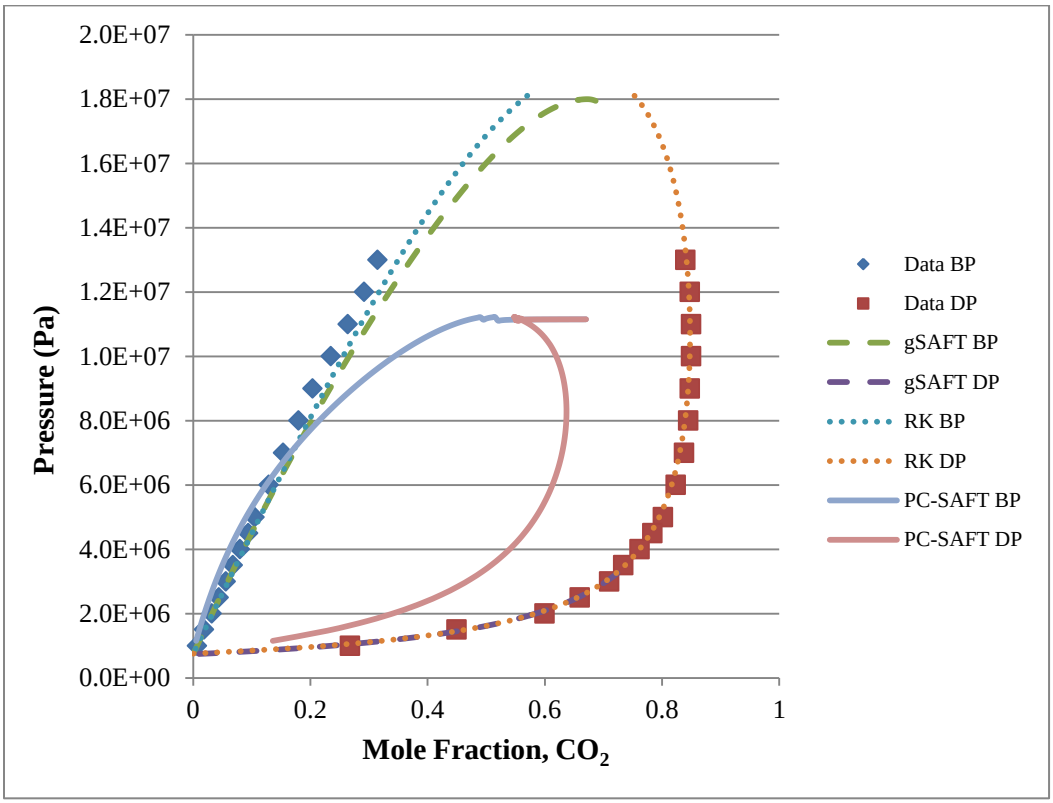

(c) At 398.06 K

Figure 5.13. Methanol and CO_2 VLE (Cont'd)

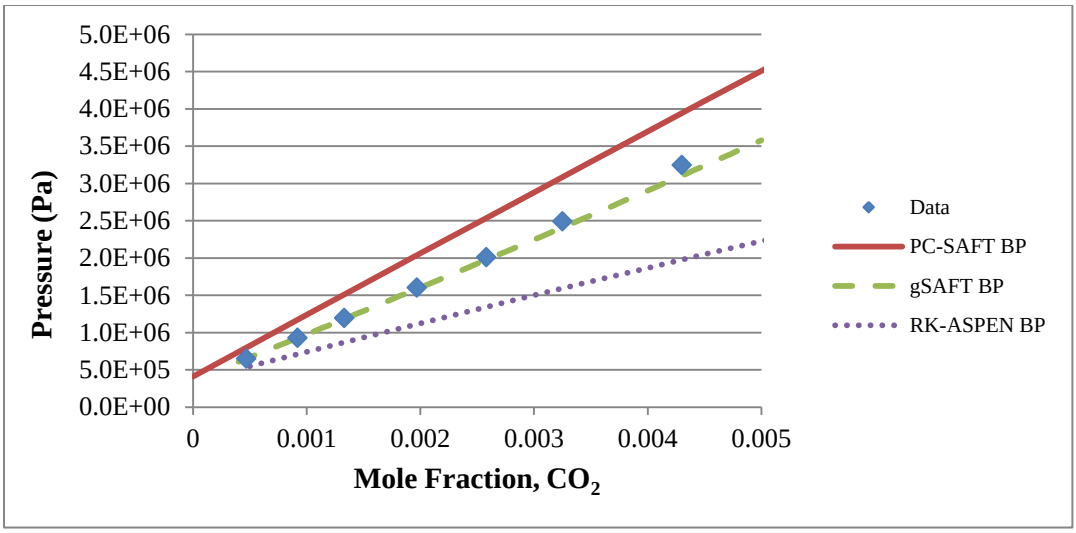

(a) At 413.12 K (bubble-point curve).

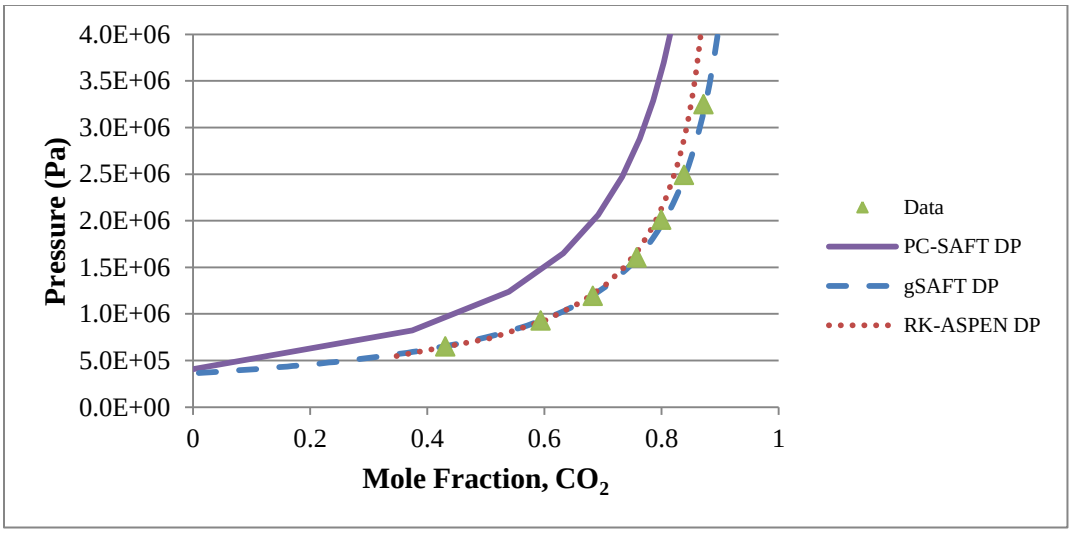

(b) At 413.12 K (dew-point curve).

Figure 5.14. Water and CO_2 VLE.

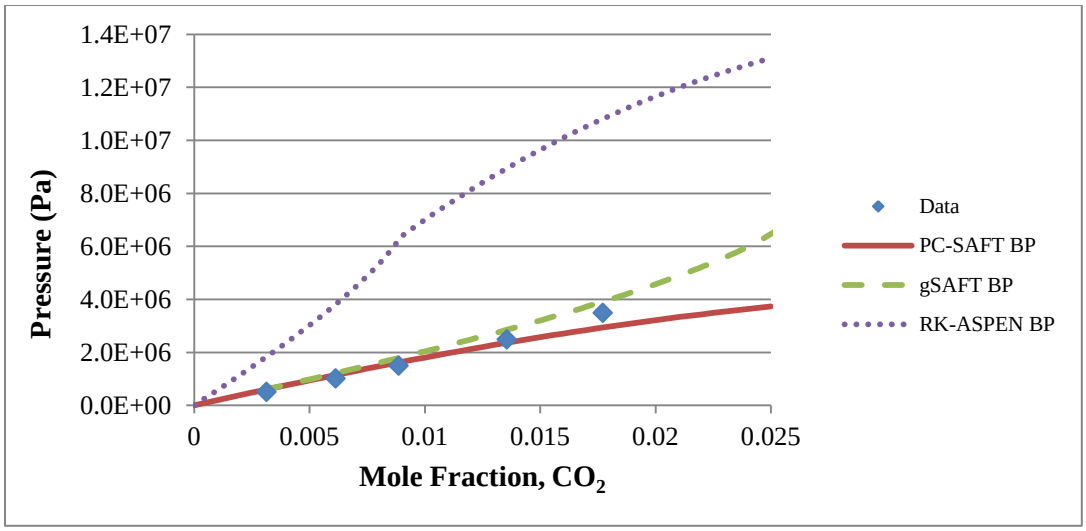

(c) At 298.28 K (bubble-point curve).

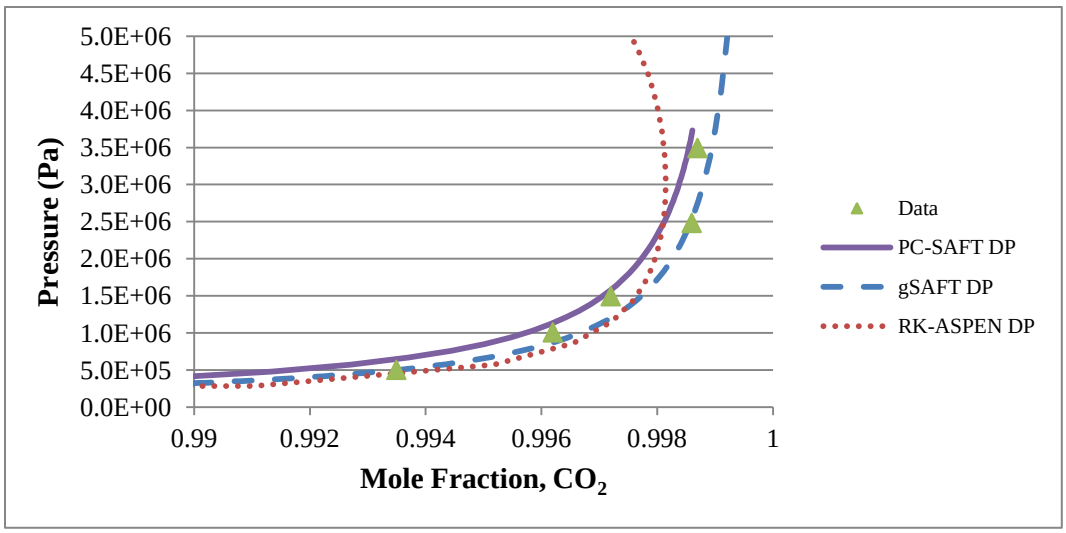

(d) At 298.28 K (dew-point curve).

Figure 5.14. Water and CO_2 VLE (Cont'd.)

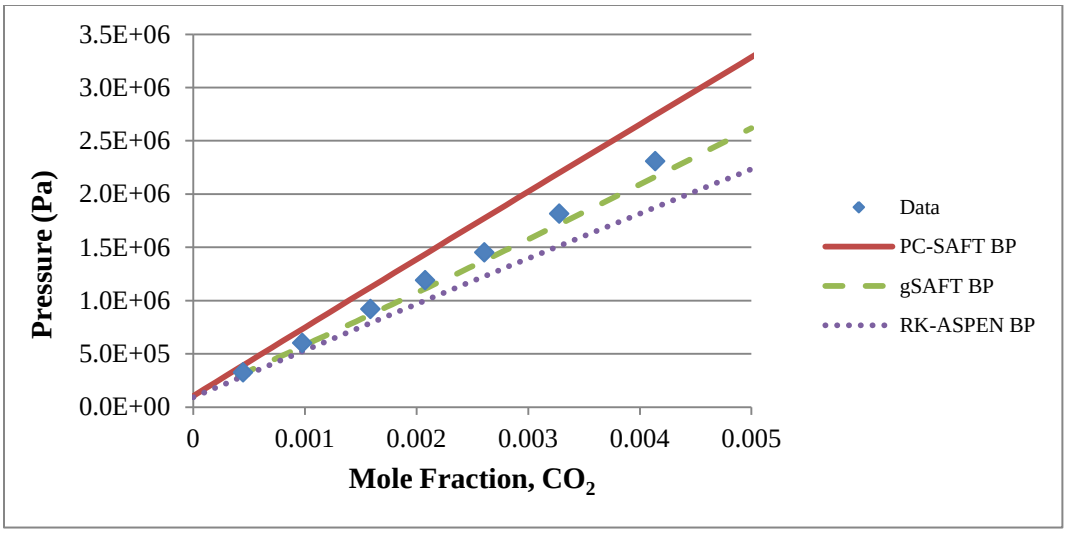

(e) At 373.12 K (bubble-point curve).

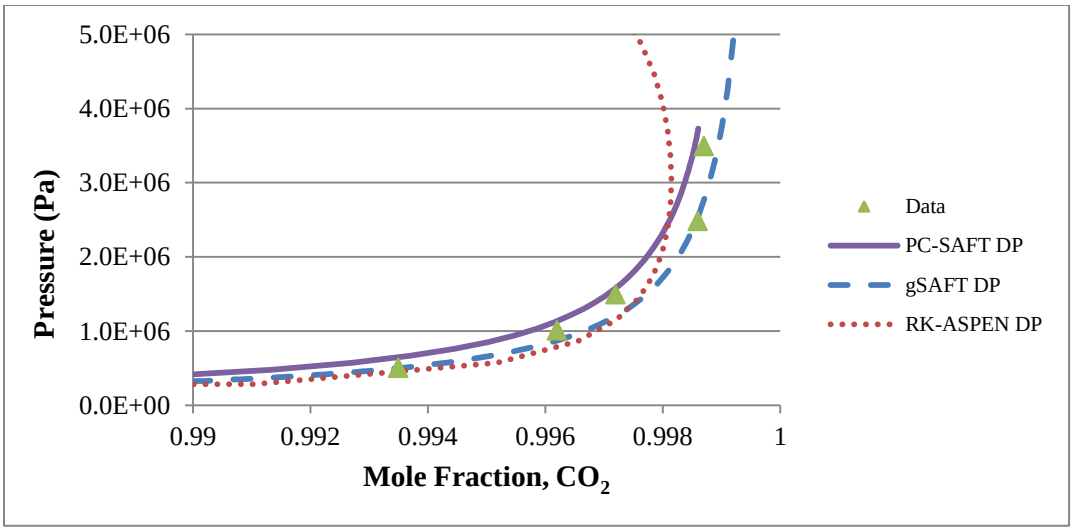

(f) At 373.12K (dew-point curve).

Figure 5.14. Water and CO_2 VLE (Cont'd.)

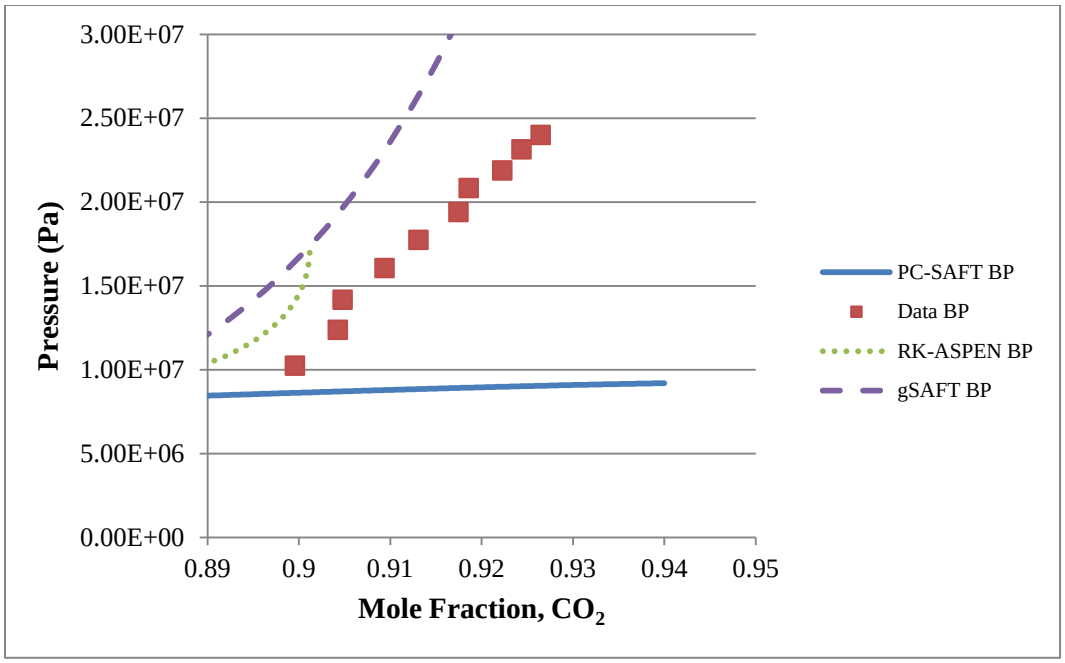

(a) At 313 K (bubble-point curve)

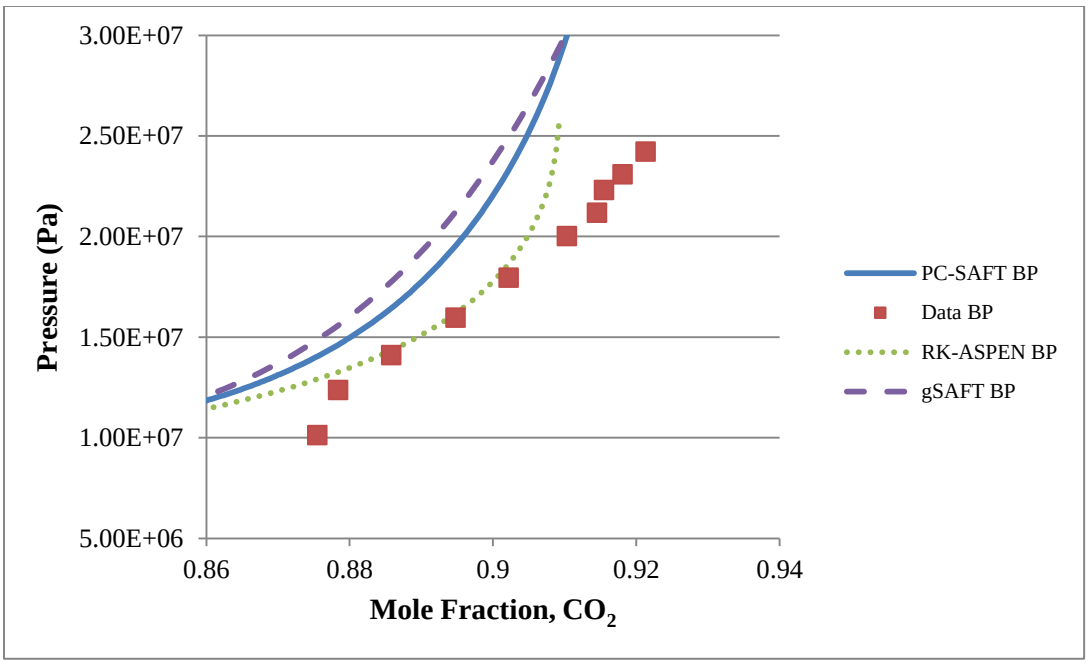

(b) At 333 K (bubble-point curve)

Figure 5.15. Triolein and CO_2 VLE.

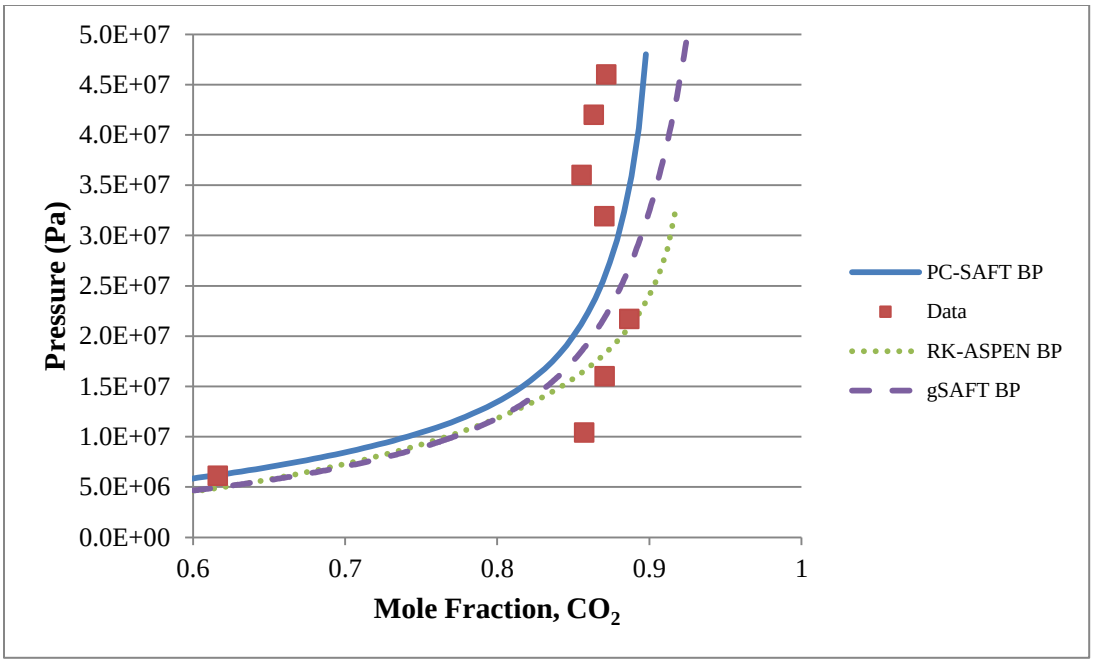

(c) At 363 K (bubble-point curve)

Figure 5.15. Triolein and CO_2 VLE (Cont'd.)

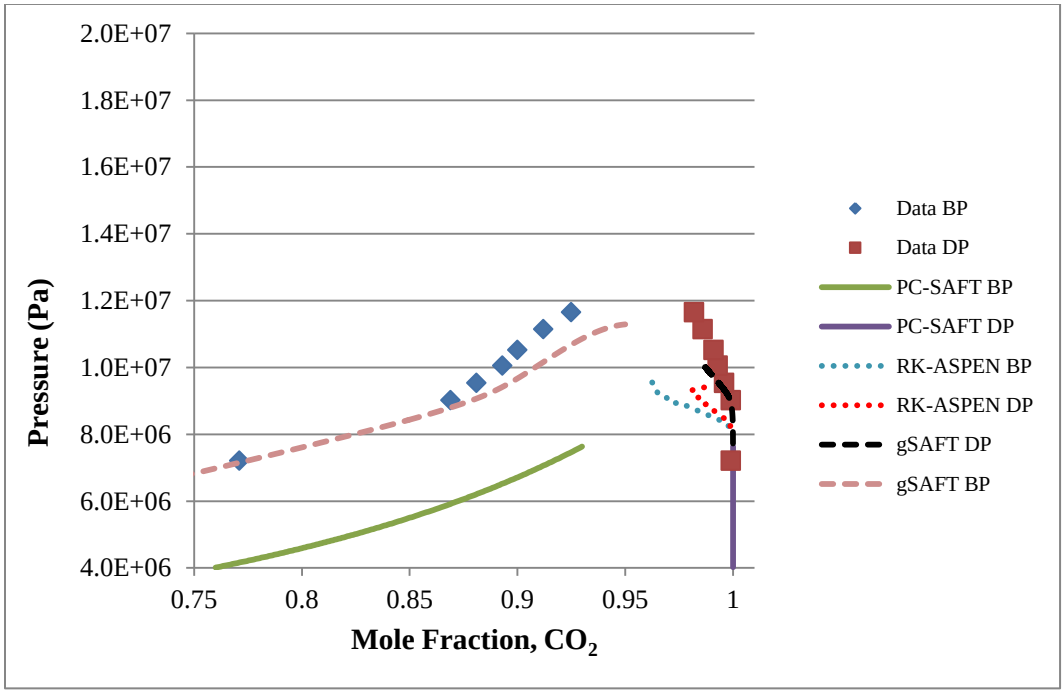

(a) At 313 K

Figure 5.16. Methyl-oleate and CO_2 VLE.

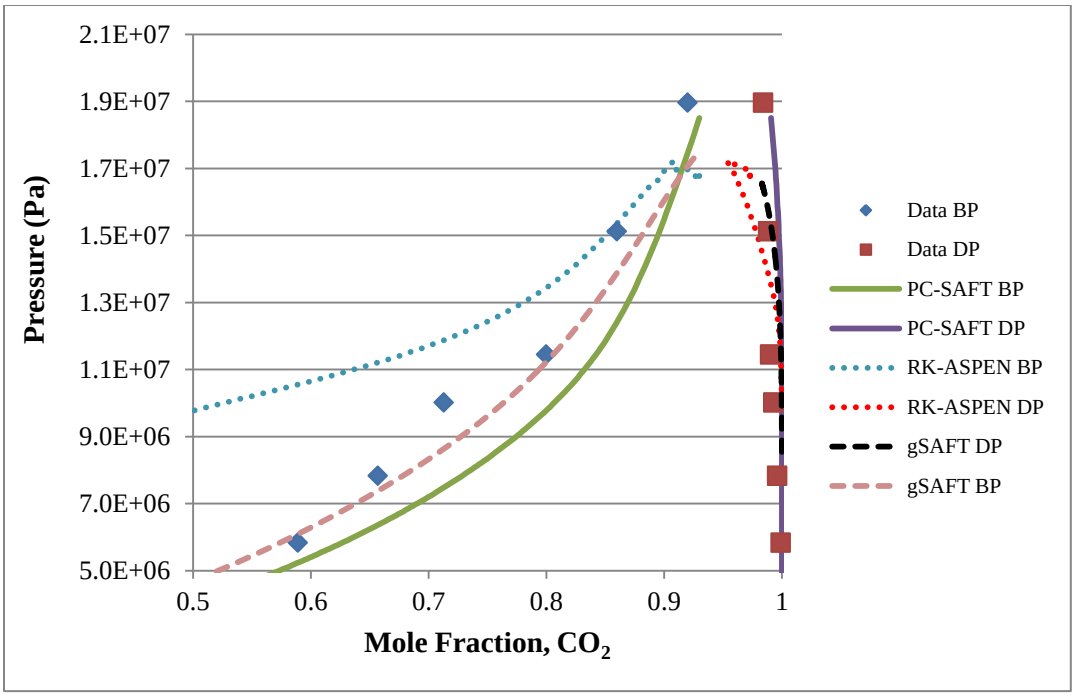

(b) At 333 K

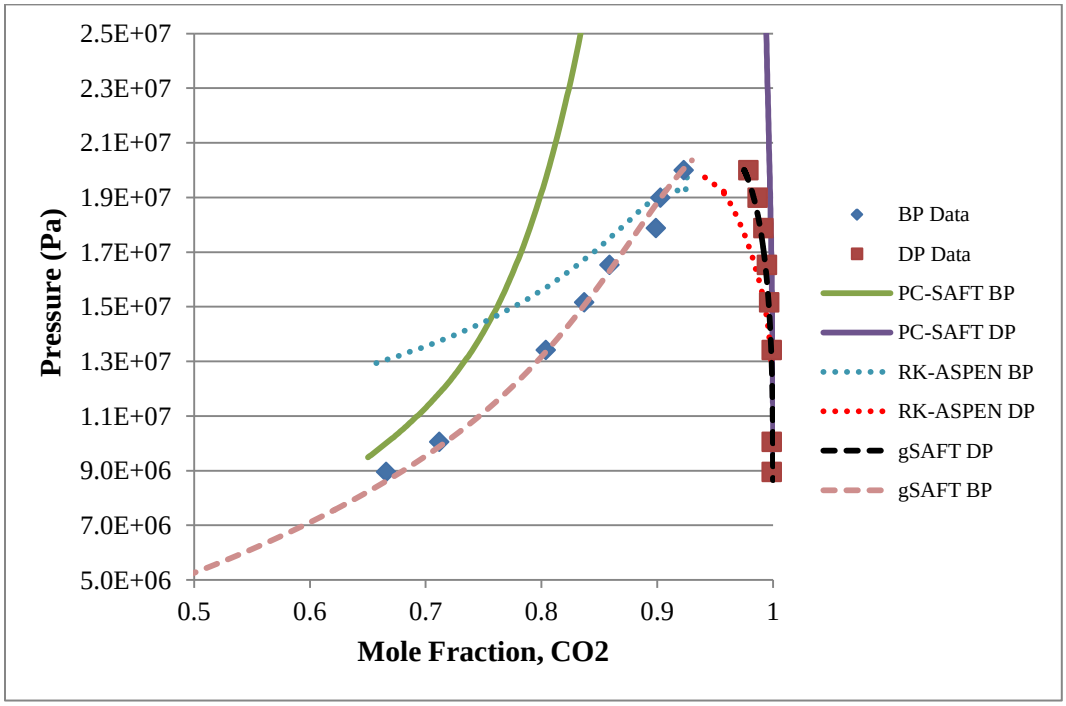

(c) At 343 K

Figure 5.16. Methyl-oleate and CO_2 VLE (Cont'd.)

5.5.4. Binary LLE Mixtures

Figures 5.17-5.21 display liquid-liquid equilibria for the six species in the biodiesel system. In the previous section, all of the data, except for methanol and methyl-oleate, were obtained from the NIST databank or the literature, with numerous datasets for each binary pair. All of the LLE data, except for methyl-oleate and water, were measured by the authors (see Appendix C). While a dataset for triolein and methanol existed, it was of questionable accuracy (Tang et al., 2006). Overall, as anticipated, the EoSs were less effective in predicting LLE than VLE data.

For methyl-oleate and water (Figure 5.21), the two available datasets differed by an order of magnitude (Lee et al., 2010b; Oliveira et al., 2008). The former is displayed because all three EOSs provided reasonable agreement. However, there were only three datapoints and the EoSs estimates did not fully agree with data. Thus, these data should be investigated more thoroughly in future studies.

Reasonable agreement with the triolein and water LLE data (Figure 5.18) were obtained by both SAFT equations. RK-ASPEN failed to yield LLE predictions at these conditions. Similarly, in Figure 5.17, both SAFT equations provide much better agreement with the triolein-methanol LLE data.

The datasets involving glycerol (Figures 5.19 and 5.20) had the most questionable quality of those measured by the authors. PC-SAFT predicts the data most effectively (as with the other LLE data), but surprisingly, all three EoSs, without binary interaction parameters, better trace the glycerol data. For the other systems, as expected, the binary interaction parameters improved agreement with the data.

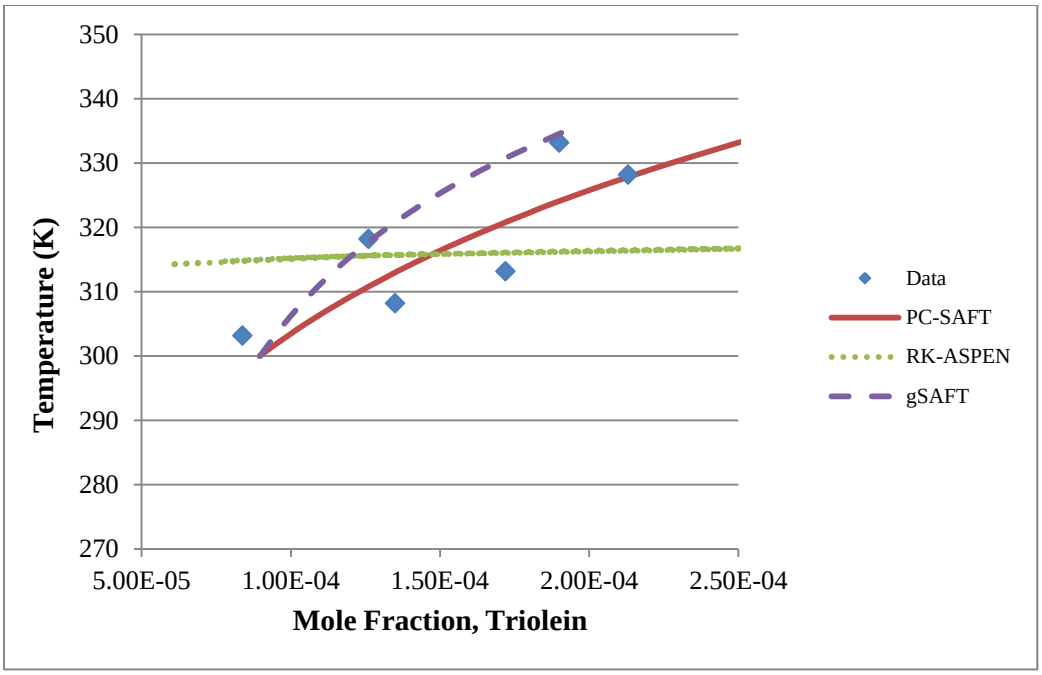

Figure 5.17. Triolein in the methanol phase (LLE at 1 atm).

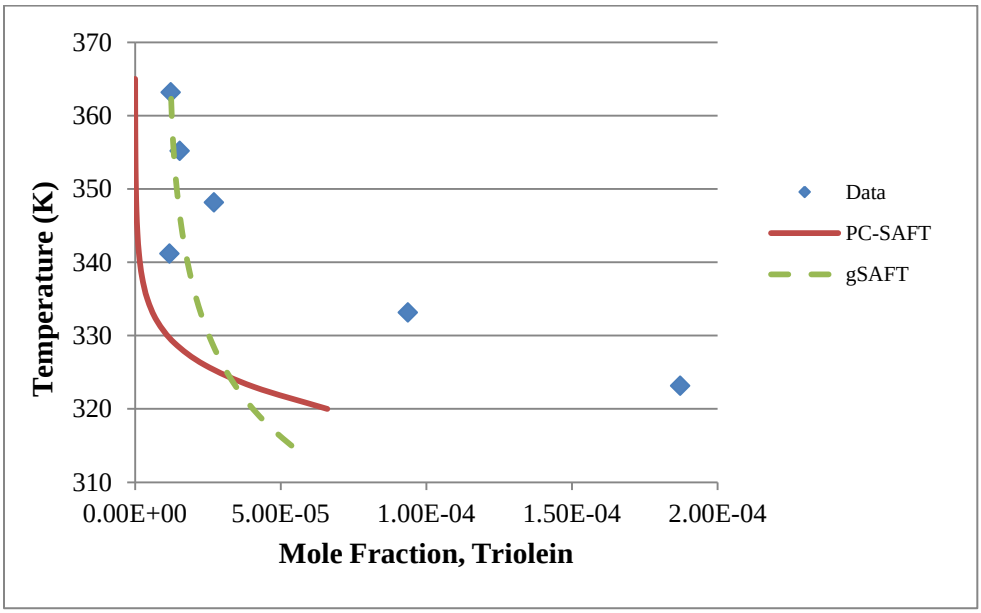

Figure 5.18. Triolein in the water phase (LLE at 1 atm).

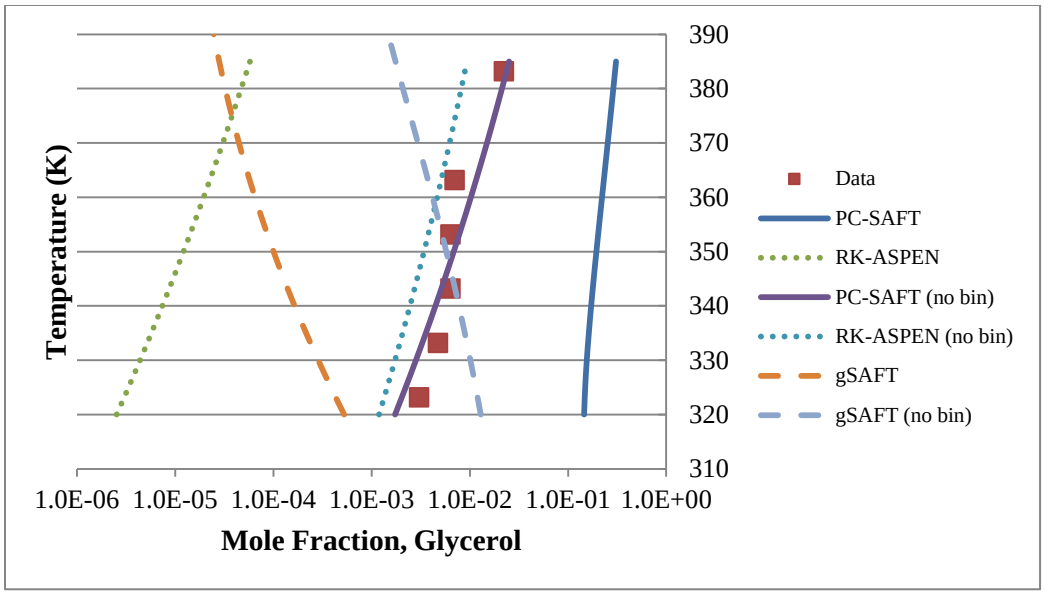

(a) Glycerol in the triolein phase

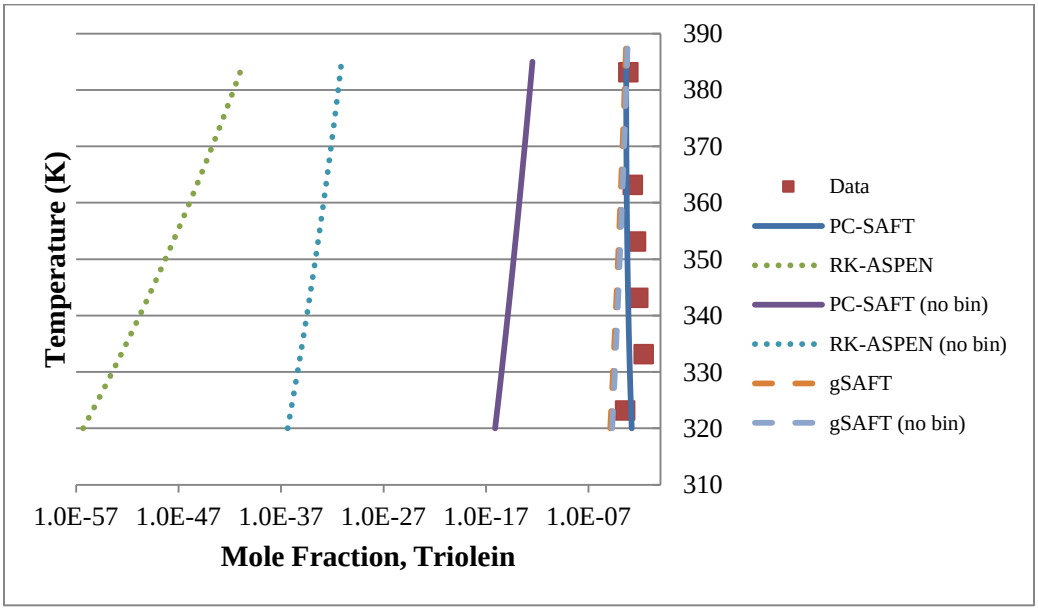

(b) Triolein in the glycerol phase*

*note that the two gSAFT curves overlap, and it is difficult to distinguish them

Figure 5.19. Glycerol and triolein LLE at 1 atm.

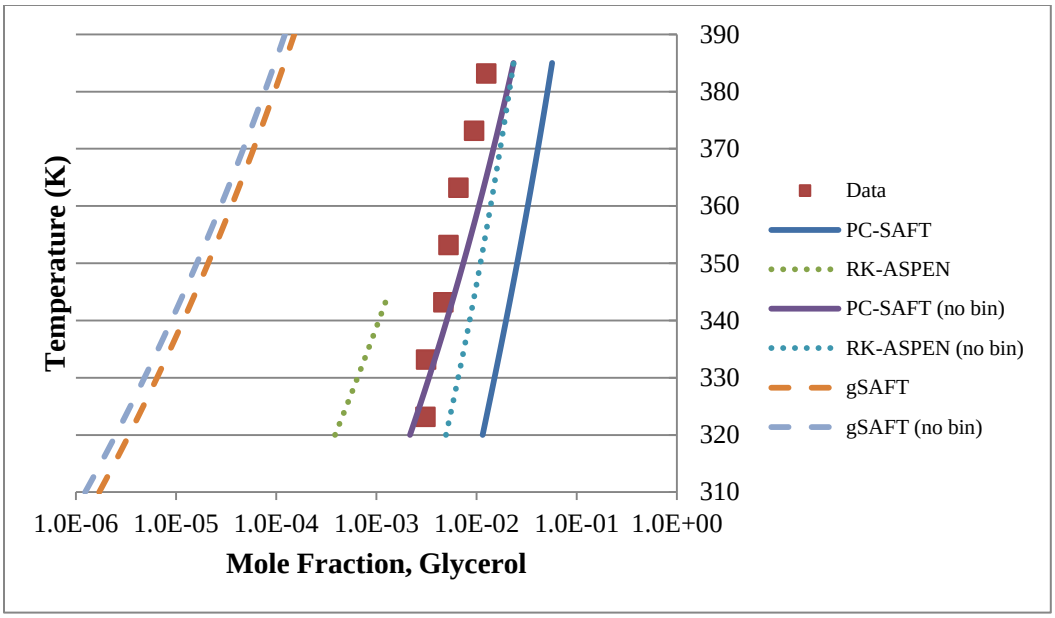

(a) Glycerol in the methyl-oleate phase

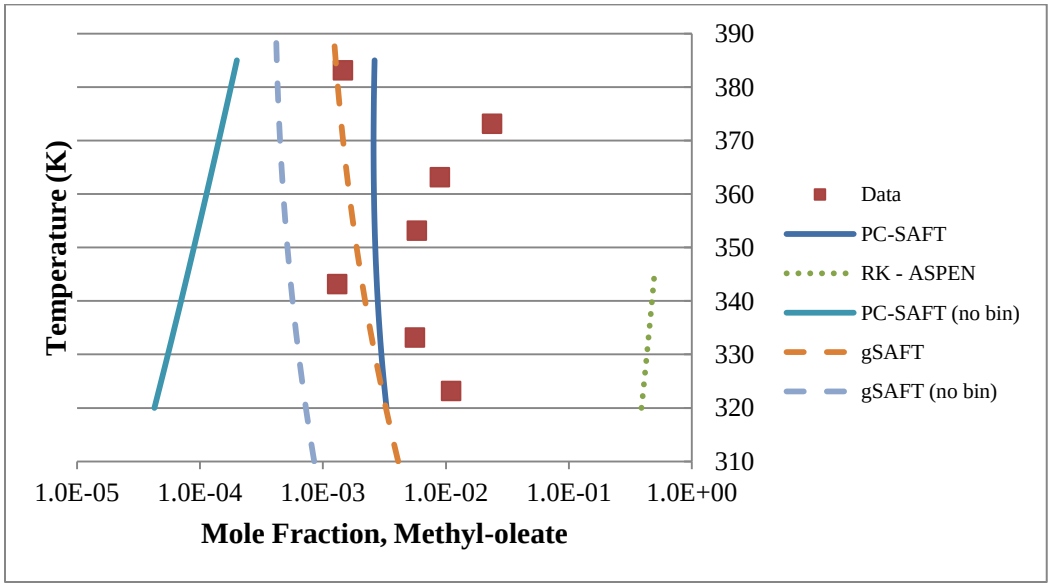

(b) Methyl-oleate in the glycerol phase

Figure 5.20. Glycerol and methyl-oleate LLE at 1 atm.

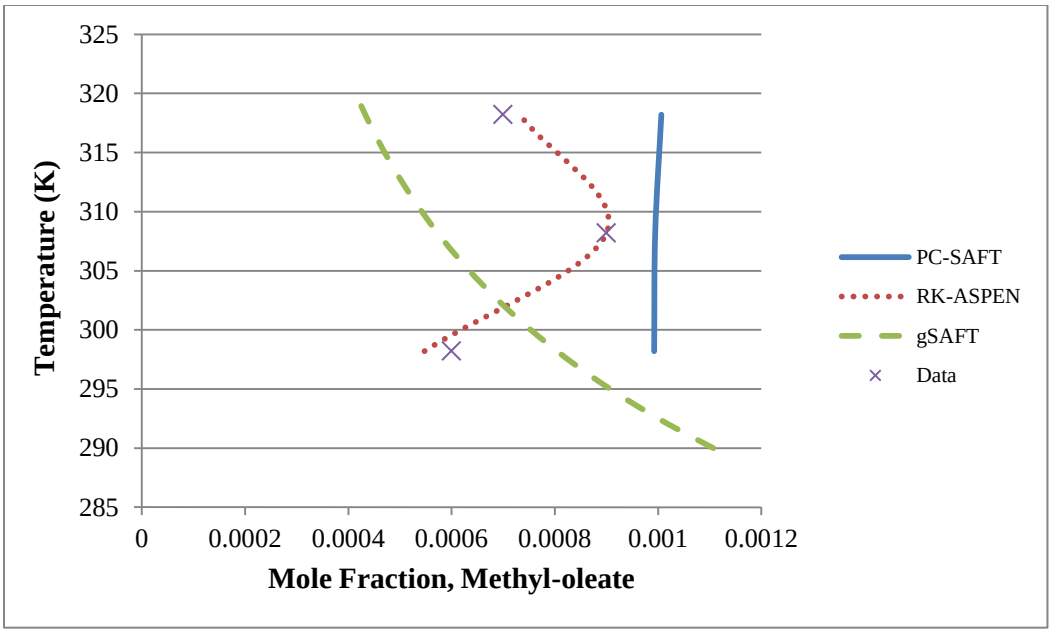

(a) Methyl-oleate in the water phase

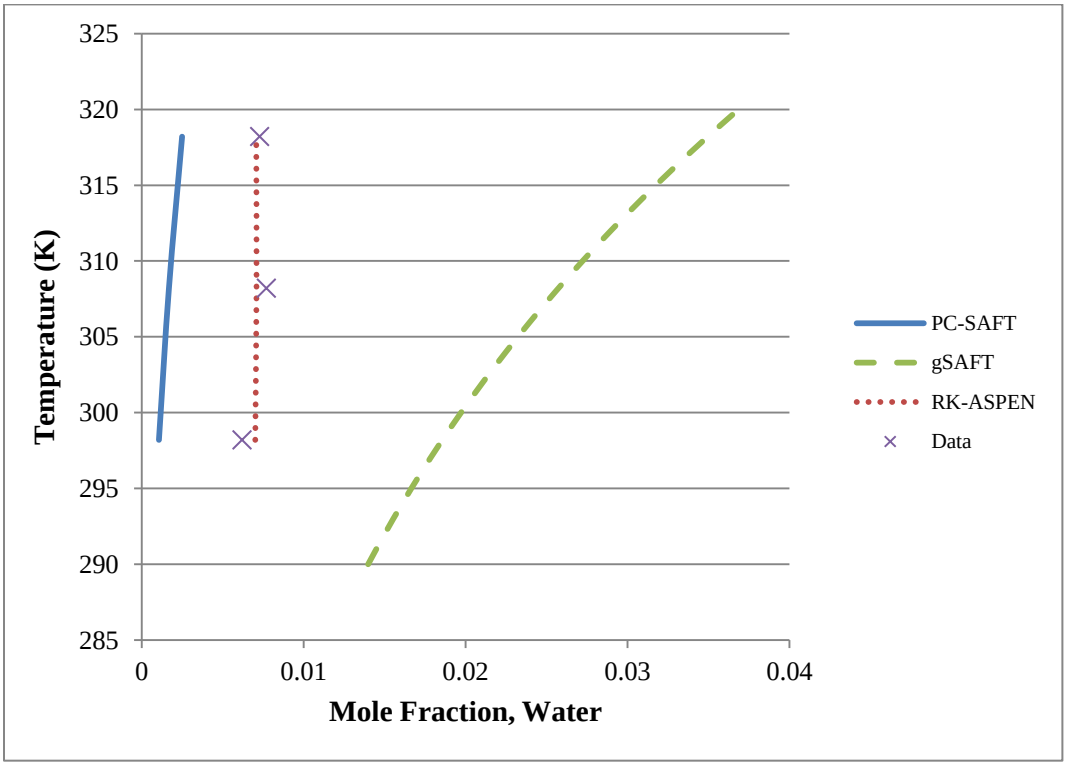

(b) Methyl-oleate in the water phase

Figure 5.21. Methyl-oleate and water LLE at 1 atm.

5.5.5. Ternary LLE Mixtures

LLE data and model predictions for water, methanol, and methyl-oleate at 318.2 K and 1 atm are shown in Figure 5.22. For RK-ASPEN, significant deviations occur at high water concentrations in the aqueous phase, because RK-ASPEN doesn't accurately represent strongly associating mixtures. Good agreement is obtained by both SAFT EoSs, especially for regions of high water concentrations. PC-SAFT slightly under-predicts the solubility of methanol and methyl-oleate at high concentrations of both, while gSAFT over-predicts their solubility. However, the latter does a much better job of predicting the shape of the phase boundary curve.

For glycerol, methanol, and methyl-oleate at 333 K and 1 atm (Figure 5.23) poor agreement is achieved with RK-ASPEN, again because of its difficulty in representing associating systems. Good agreement is achieved with PC-SAFT, but not with gSAFT. The poor predictions shown for gSAFT could be due to either over-regression of parameters, because glycerol has two different associating sites (primary and secondary alcohol groups), for which separate parameters were regressed — as opposed to PC-SAFT, where the two standard associating parameters were regressed for the entire molecule. The inaccuracy shown for gSAFT could also result from the fact that methyl-oleate was represented using an assembly of groups, instead of unique parameters for the complete molecule, as was done for PC-SAFT. Between these two explanations, the first is more likely, as it explains the disparity in performance by gSAFT between Figures 5.22 and 5.23 — suggesting future attempts should use fewer parameters. Note that the PC-SAFT binary interaction parameters for glycerol and methyl-oleate were not used

because they detract from the model performance when the glycerol, methyl-oleate, and methanol are present (Korgitzsch, 1993; Lee et al., 2010b).

These two ternary mixtures are typical of the effluent streams from the biodiesel reactor. Clearly, PC-SAFT should yield the best predictions for liquid-liquid phase distributions in the reactor effluent and product separation and purification units of a biodiesel process. Although, in further investigations, the regression of group parameters in gSAFT needs to be examined more closely.

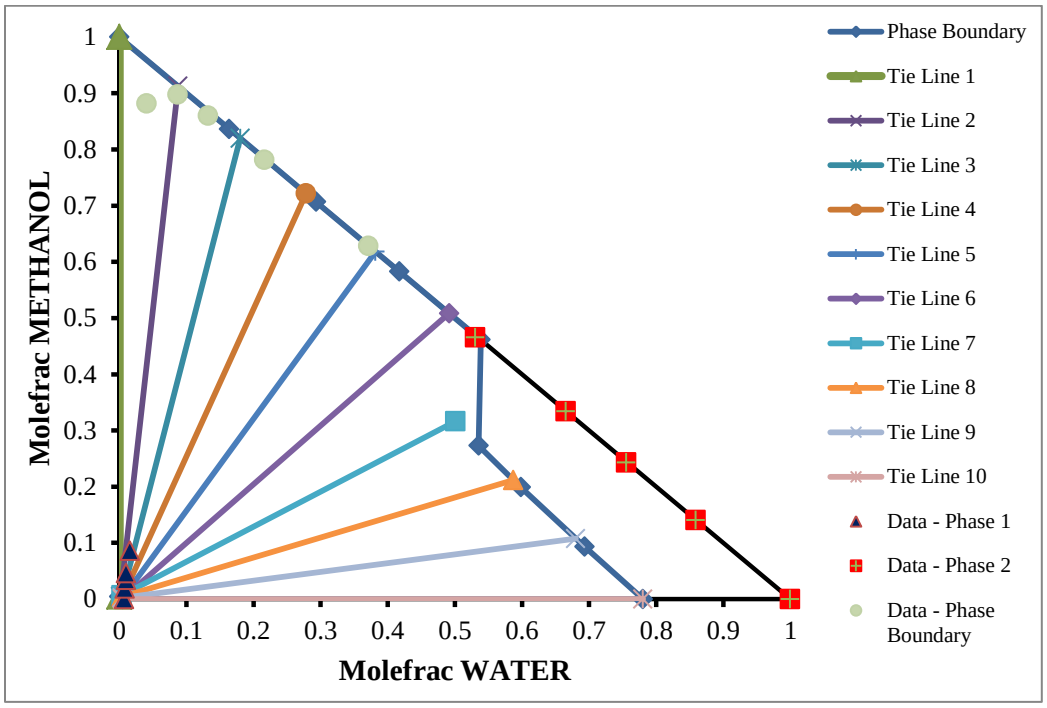

(a) Predicted with RK-ASPEN

Figure 5.22. LLE for water, methanol, and methyl-oleate at 318.2 K and 1 atm.

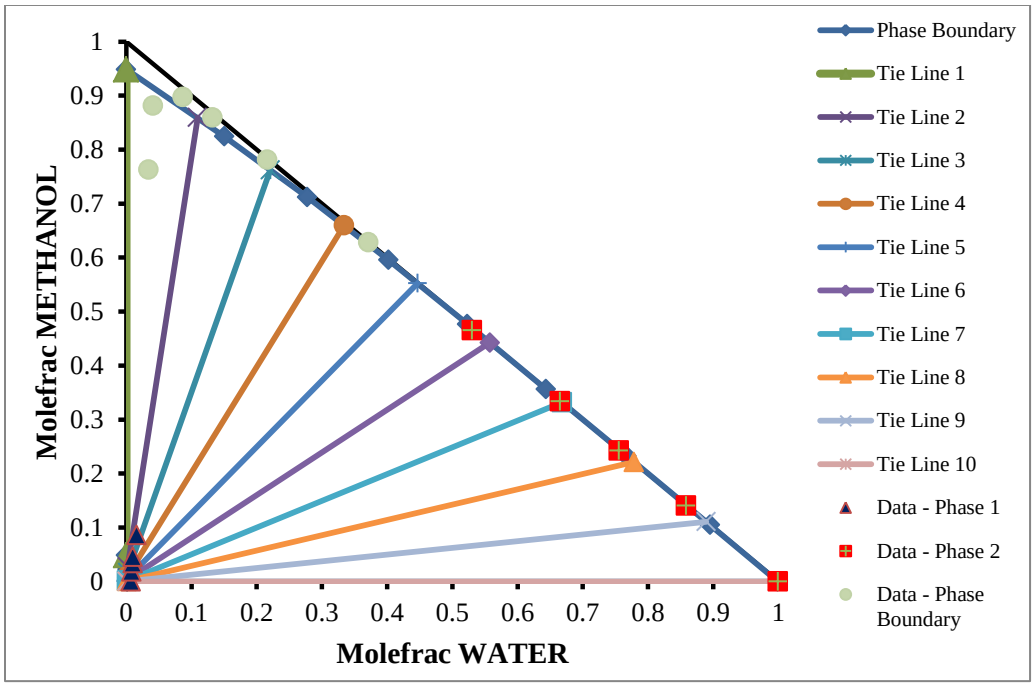

(b) Predicted with PC-SAFT

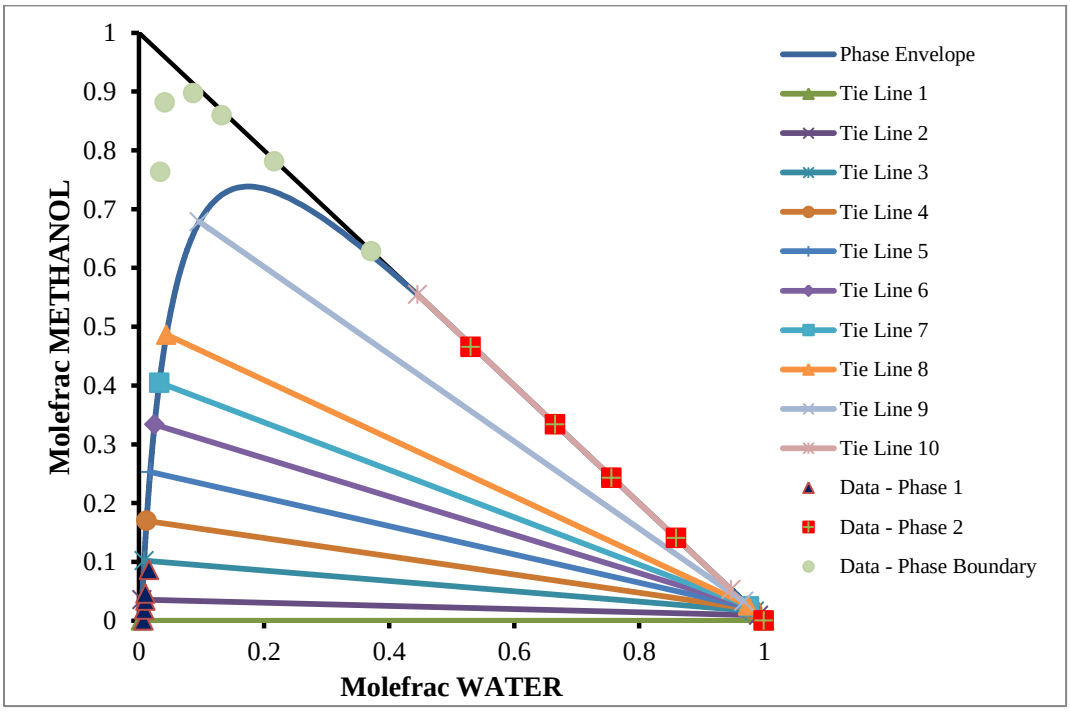

(c) Predicted with SAFT-γ Mie (gSAFT)

Figure 5.22. LLE for water, methanol, and methyl-oleate at 318.2 K and 1 atm (Cont'd.)

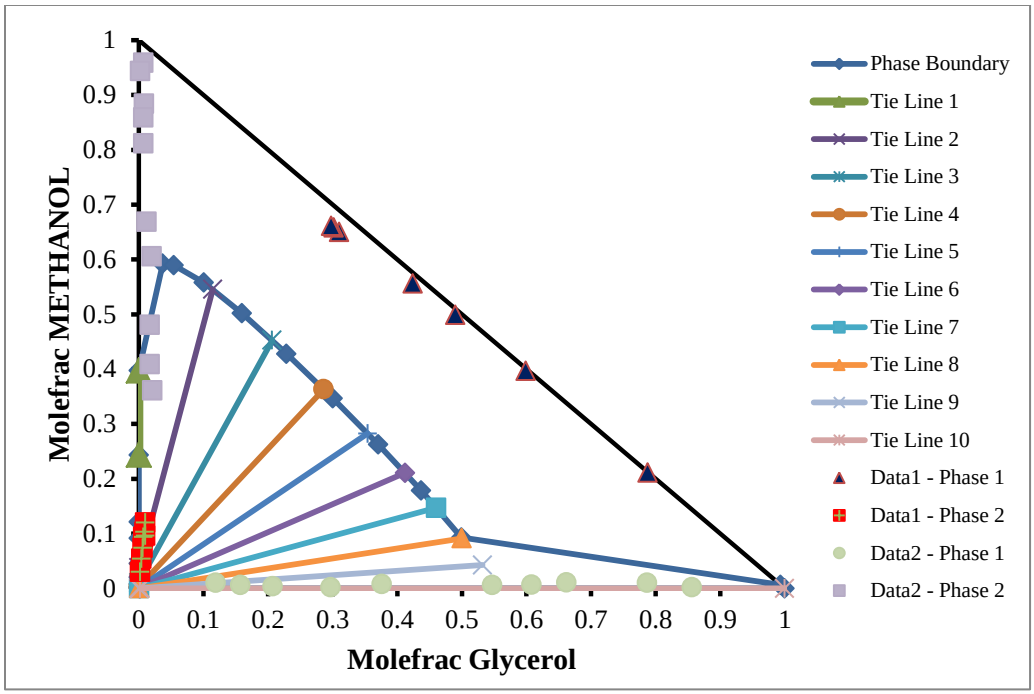

(a) Predicted with RK-ASPEN

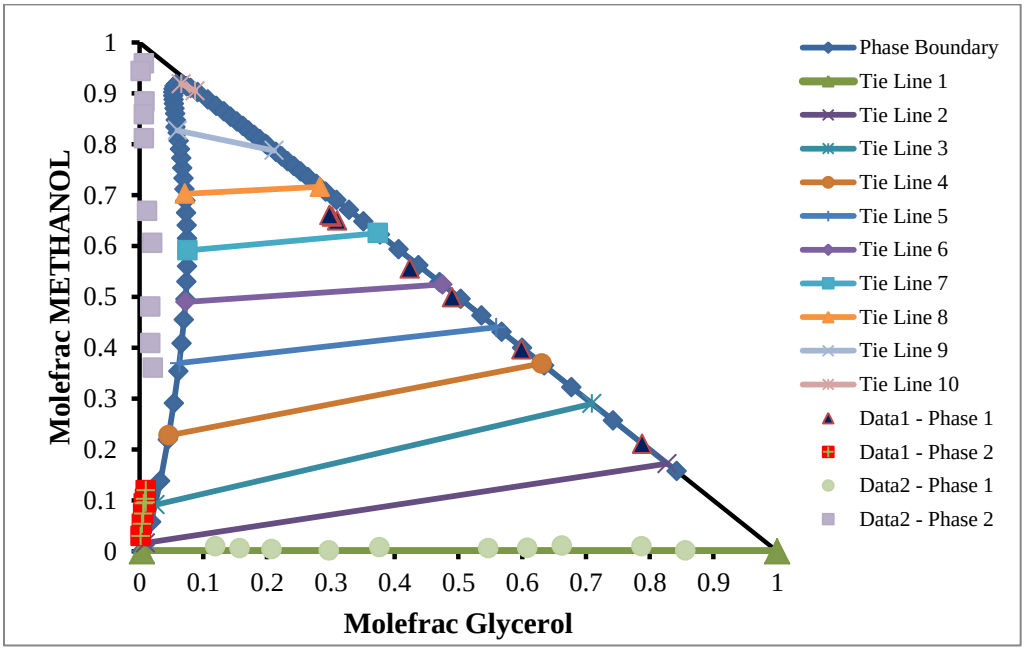

(b) Predicted with PC-SAFT

Figure 5.23. LLE for glycerol, methanol, and methyl-oleate at 333 K and 1 atm.

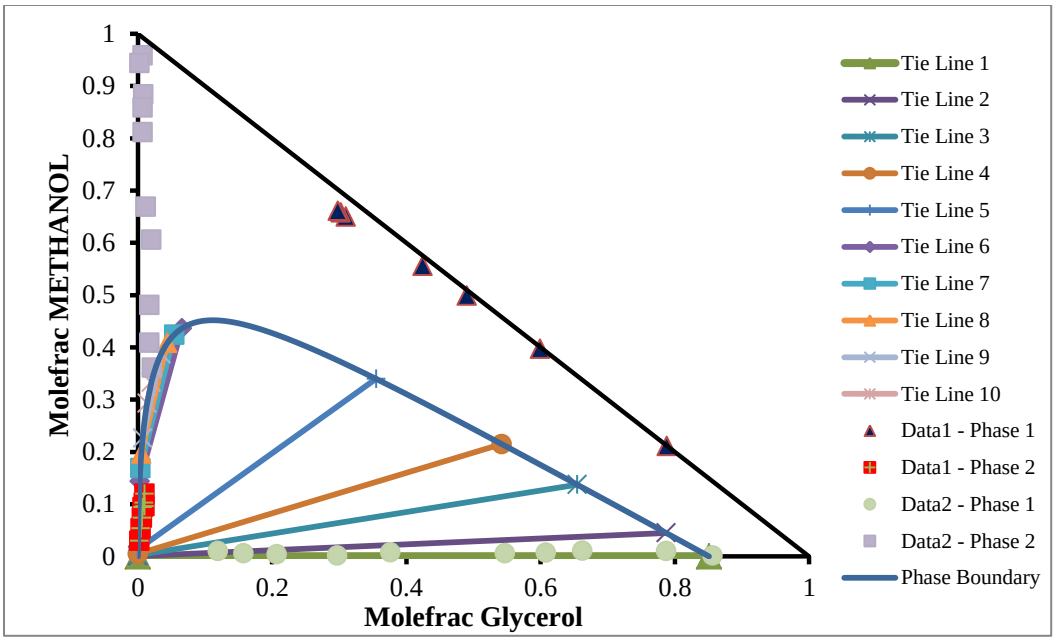

(c) Predicted with SAFT-γ Mie (gSAFT)

Figure 5.23. LLE for glycerol, methanol, and methyl-oleate at 333 K and 1 atm (Cont'd.)

5.5.6. Ternary Inlet Mixtures

Figure 5.24 examines the phase distributions of triolein, methanol, and CO_2 mixtures at various pressures and compositions typical of the inlet conditions for a biodiesel reactor using CO_2 to increase conversion rates (Soh et al., 2013; Soh and Zimmerman, 2015). Only the triolein mole fraction is shown. The mole fractions of methanol and CO_2 are based on the triolein mole fraction with the triolein:methanol molar ratio fixed at 1:4,032. As shown in the legend, each symbol represents a different phase distribution at equilibrium, where dashes (V) represent a vapor (or supercritical) phase, triangles (L) a liquid (or supercritical) phase, stars (VLE) vapor and liquid phases at equilibrium, diamonds (LLE) two liquid phases at equilibrium, and circles (VLLE) vapor-liquid-liquid equilibria. Open spaces arise when the *Gibbs flash method* in ASPEN PLUS algorithm did not converge. Note that a supercritical phase can be classified as

either a vapor or liquid by the equilibrium algorithm, and therefore, for example, the transition from vapor to liquid at elevated pressures in Figure 5.24 (c and d) is not physically realistic.

The lines, which represent approximate phase boundaries, connect experimental phase transition data (Soh et al., 2013); that is, orange circles (showing a transition from supercritical phase to VLE) and purple crosses (showing a transition from VLE to VLLE). Unfortunately, as can be seen in the five sub-figures, none of the EoSs accurately predict all three of these regions.

RK-ASPEN with no binary interaction parameters (Figure 5.24(a)) is most effective in predicting the VLLE region, but the *Gibbs flash method* fails to converge in much of the VLE or supercritical regions. RK-ASPEN with binary interaction parameters (Figure 5.24(b)) is more robust in terms of convergence, and correctly represents most of the supercritical region and the VLE region, but fails to predict any VLLE behavior.

gSAFT (Figure 5.24(e)) predicts the supercritical region and the VLE region, as well as their transition, almost perfectly. However, like RK-ASPEN with binary interaction parameters, it fails to predict any VLLE behavior, because it does not predict a liquid-liquid split between methanol and triolein at these conditions (as opposed to those in Figure 5.17). The poor predictions in the VLLE region are likely due to two factors: (1) the weighting factors for the liquid density [200] and vapor pressure [1] used during the regressions herein (Section 5.4) were not applied to groups that had been regressed in prior studies (CH_3 and CH_2, which are crucial for triolein and methyl-oleate property estimation); (2) the group contribution method is not as accurate as regressing

parameters for individual molecules. Thus future studies should regress "groups" that are equivalent to triolein and methyl-oleate, and ranges of weighting factors should be adjusted to compare the estimates of PC-SAFT and gSAFT. If gSAFT were shown to be more accurate using "molecular" groups, which is likely given the binary systems diagrams in Sections 5.5.2 and 5.5.3, the molecules could be dissected into various groups, with the objective of increasing flexibility without significantly decreasing accuracy.

PC-SAFT with no binary interaction parameters (Figure 5.24(c)) accurately predicts the supercritical region and much of the VLLE region, but fails to predict any part of the VLE region. PC-SAFT with binary interaction parameters clearly improves predictions in the VLE region, but only at low triolein mole fractions, as shown in Figure 5.24(d). The supercritical region is predicted as a liquid phase, and the transition from VLE to VLLE is predicted properly – but VLE is predicted in a significant portion of the VLLE region. After adjusting convergence tolerances and flash algorithms, but obtaining the same incorrect phase distributions, phase stability checks were implemented for PC-SAFT with binary interaction parameters.

To check phase stability, the tangent-plane-distance criteria (Michelsen and Mollerup, 2007; Sun and Seider, 1995), as discussed in Section 5.2, was implemented, using the FORTRAN code provided by Prof. Romain Privat (Webpage: Prof. Romain Privat's Homepage). When using PC-SAFT with binary interaction parameters (Figure 5.24(d)), the Privat code showed that the liquid phase in the VLE predictions (in the intermediate portion of the VLLE region) is unstable, as shown in the lower enclosed region of Figure 5.25. Similarly, it showed that the liquid phases predicted for high

triolein concentrations in the VLE region are unstable. Note, however, that negative tangent-plane distances were observed at higher triolein mole fractions in the supercritical region, indicating that a second phase at equilibrium is incorrectly predicted by PC-SAFT with interaction parameters.

Additional code was not written to reinitialize the flash calculations with improved guesses for the phases at equilibrium – primarily because the effect of the phase distribution on the rate of the transesterification reaction(s) is examined next in Section 5.6. However, improvements in the ASPEN PLUS flash algorithms (RGIBBS and FLASH3) in the critical region would allow higher fidelity thermodynamic models (like PC-SAFT) to be used more effectively for these mixtures – thus yielding more accurate predictions for reactor conversions.

Note that phase stability was not examined for gSAFT – as Process Systems Enterprise (PSE), creator of gSAFT, performs tangent-plane distance phase-stability checks.

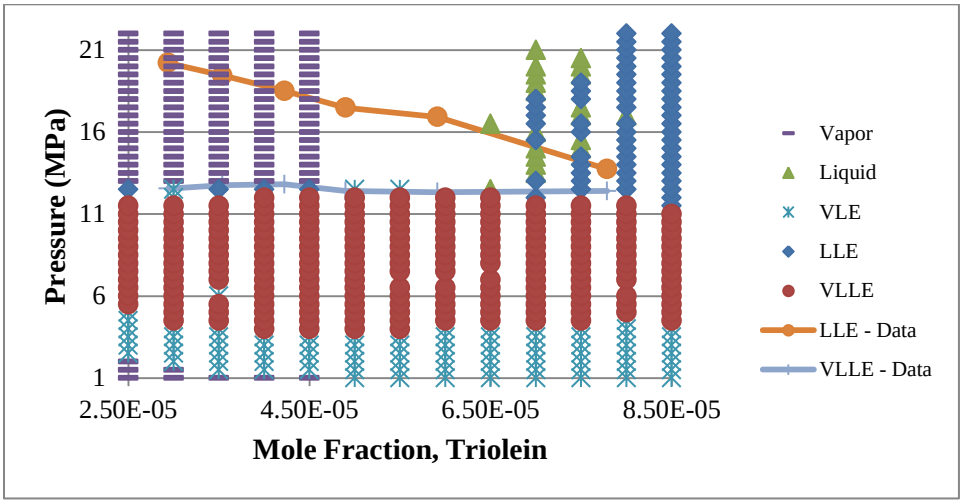

(a) Predicted with RK-ASPEN (no binary interaction parameters)

Figure 5.24. Triolein, methanol, and CO_2 phase equilibria at 353.15 K.

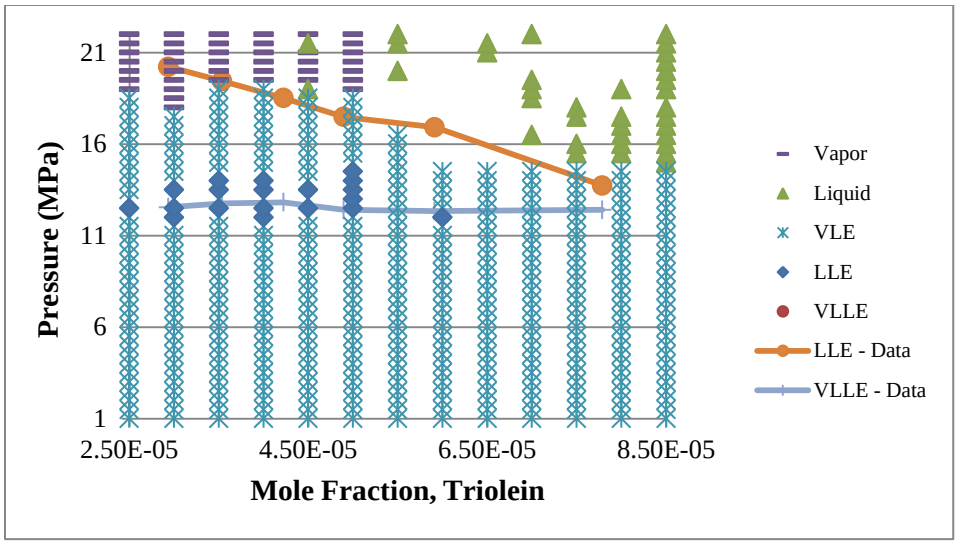

(b) Predicted with RK-ASPEN (with binary interaction parameters)

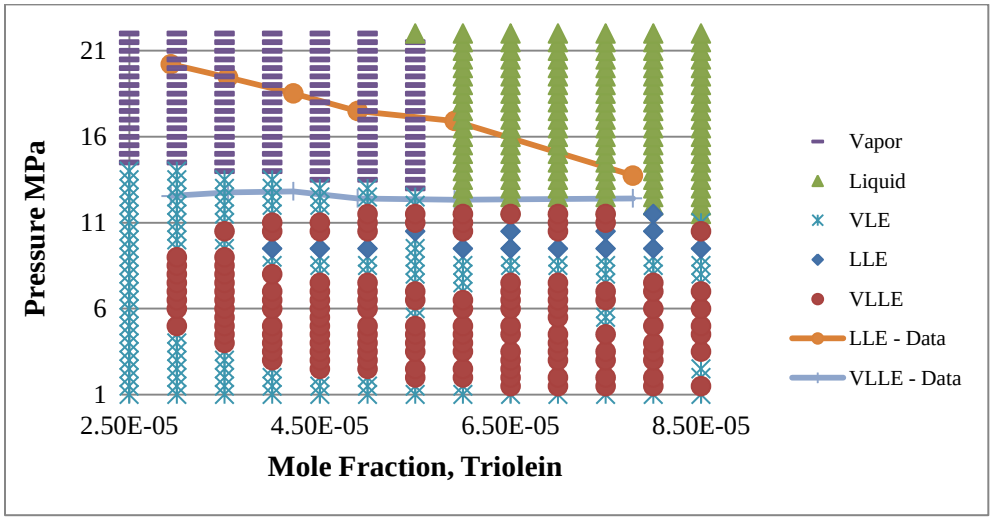

(c) Predicted with PC-SAFT (no binary interaction parameters)

Figure 5.24. Triolein, methanol, and CO_2 phase equilibria at 353.15 K (Cont'd.)

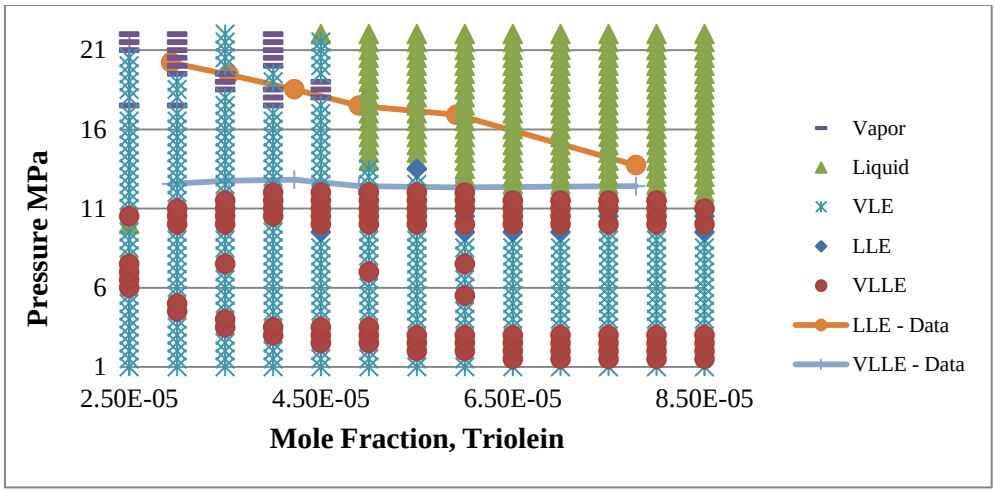

(d) Predicted with PC-SAFT (with binary interaction parameters)

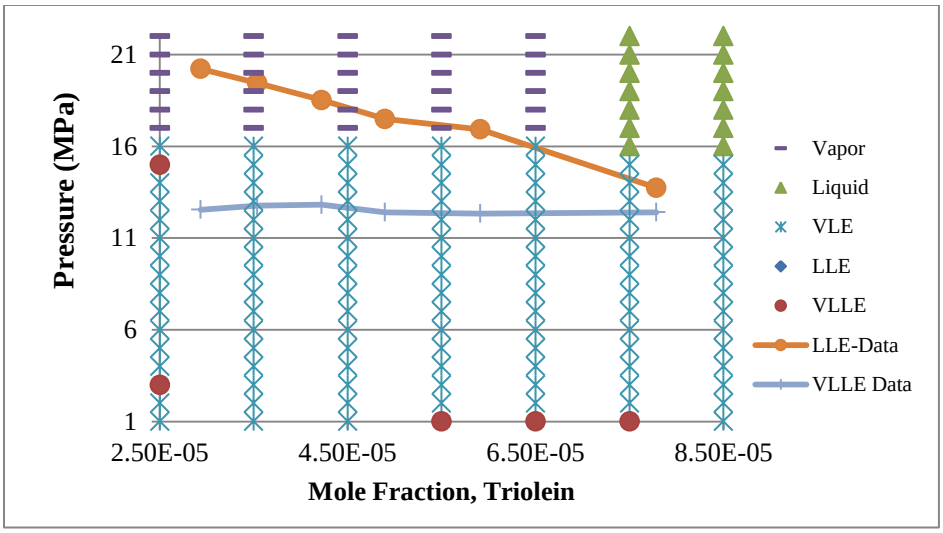

(e) SAFT-γ Mie (gSAFT)

Figure 5.24. Triolein, methanol, and CO_2 phase equilibria at 353.15 K (Cont'd.)

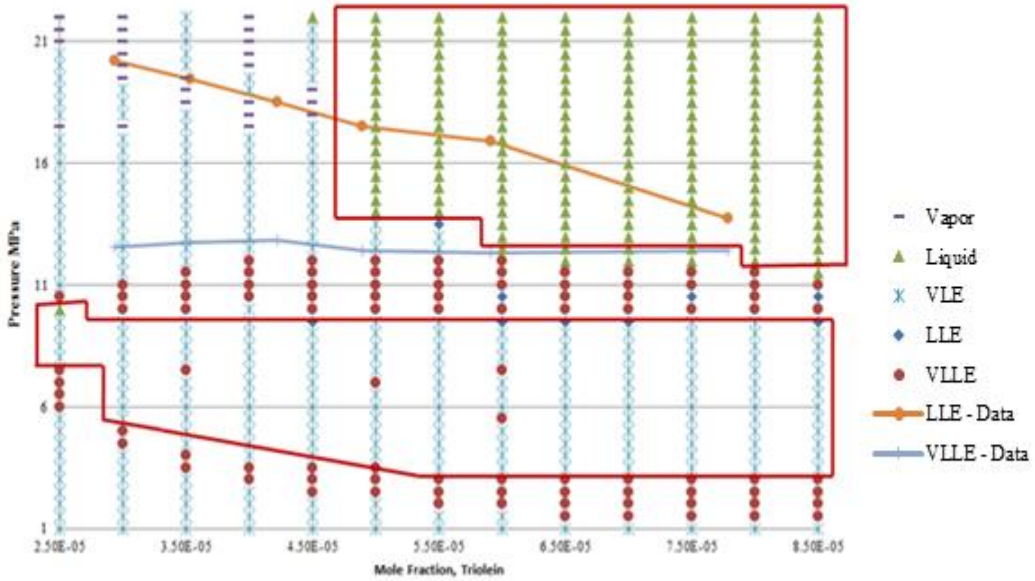

Figure 5.25. Tangent-plane-distance regions of stability and instability*

*(PC-SAFT with binary parameters at 353.15 K). The unstable regions are enclosed in two polygons.

5.6. Kinetics and Reactor Design

For the transesterification reaction involving triolein, methanol, and CO_2, overall composition data were measured in time at various catalyst loadings, using a Nafion solid-acid catalyst in both bead and powder form at 95°C and 9.65 MPa (Soh and Zimmerman, 2015). These data include triolein, diolein, monoolein, and methyl-oleate concentrations. Glycerol, methanol, and CO_2 concentrations at each time were calculated using initial substrate loadings and mole balances. Because phase equilibrium data involving diolein and monoolein were unavailable, the simplified reaction:

$$TG_{branch} + methanol \underset{carbon\ dioxide}{\overset{solid-acid\ catalyst}{\Longleftrightarrow}} methyl\ oleate\ + \frac{1}{3} glycerol \quad \text{(R5.1)}$$

was used in place of the kinetic mechanism in Figure 5.1. The mechanism is formulated in terms of the triglyceride-branch species, TG_{branch}, where three moles of TG_{branch} are equivalent to a mole of triolein, two moles of TG_{branch} and one-third of a mole of glycerol is equivalent to a mole of diolein, and one mole of TG_{branch} and two-thirds of a mole of glycerol is equivalent to a mole of monoolein.

This reaction mechanism was translated into the intrinsic reaction-rate:

$$rxn = k_f[cat]^{n_f}[TG_{branch}][methanol] - k_r[cat]^{n_{rev}}[FAME][glycerol]^{\frac{1}{3}} \quad (5.56)$$

with the ODE mass balances:

$$\frac{d[C_i]}{dt} = \nu_{R5.1,i} * rxn \quad (5.57)$$

where k_f is the forward rate constant, k_r is the reverse rate constant, [cat] is the catalyst concentration, n_f is the exponent of the catalyst concentration in the forward direction, n_{rev} is the exponent of the catalyst concentration in the reverse direction, $[C_i]$ is the concentration of species i, and $\nu_{R5.1,i}$ is the stoichiometric coefficient of species i in reaction R5.1.

Initially, k_f, k_r, n_f, and n_{rev} were regressed using the bulk concentrations in the experimental 50 mL, agitated reactor vessel (Soh and Zimmerman, 2015). An explicit Euler integration was used in MS Excel with a time-step of 18 seconds. The sum-of-the-square differences between the concentration data and the integrated concentrations for triolein, methanol, and methyl-oleate (for the entire stirred tank) were incorporated into a relative, weighted least-squares objective function, which weighted the concentration differences more heavily as reaction time increased (Silva et al., 2014). Note that triolein, methanol, and methyl-oleate concentrations were weighted equally. Also, glycerol concentrations were not included in the objective function because the calculated

moles of glycerol were substantially larger than experimental values – with each mole of diolein replaced by two moles TG_{branch} and two-thirds mol glycerol and each mole of monoolein replaced by one mole TG_{branch} and one-third mol glycerol.

The minimization of the objective function yielded the kinetic constants in column 2 of Table 5.7. These constants served as initial guesses in a custom-written FORTRAN subroutine in ASPEN PLUS that incorporates the effect of the phase behavior on the reaction kinetics using the algorithm in Figure 5.26.

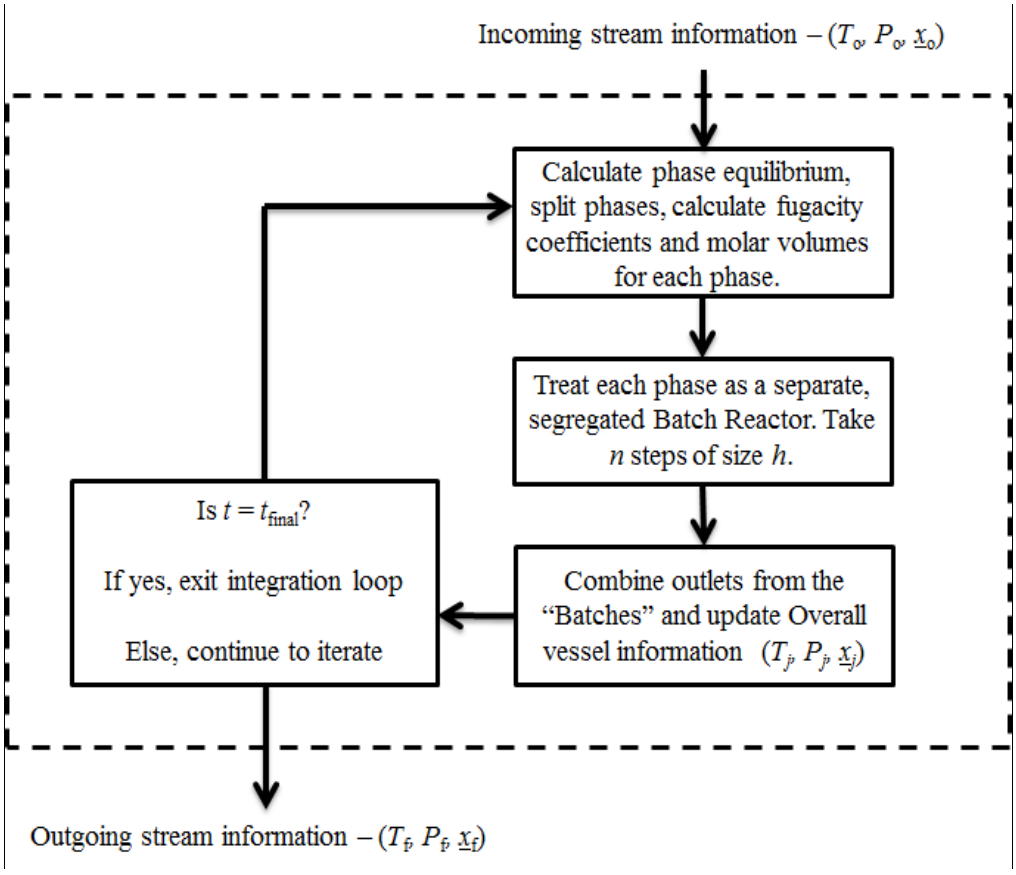

Figure 5.26. Multiphase-kinetic reactor algorithm created for ASPEN PLUS.

As with the MS Excel model, experimental data for eight loadings, over a 4-hour reaction time, were used. The reaction temperature was maintained at 95°C. The total vessel volume was the sum of the three "phase" batch reactors, and was calculated every

10 time-steps (18 seconds per time-step) along with the phase equilibria. The phase volumes remained nearly constant during the 4-hour reaction, with the vapor phase (methanol and CO_2) taking about two-thirds of the vessel volume. The aqueous liquid (methanol and glycerol) accounted for most of the remaining third, with the apolar liquid (triolein, methyl oleate, with some methanol) never exceeding 0.25% of the total volume. The change in vessel volume throughout the reaction was less than 1%, with no volume adjustments implemented.

Because RK-ASPEN with no binary interaction parameters (Figure 5.24a) is the only thermodynamics package to predict VLLE at the reactor conditions (95^{o}C and 9.65 MPa), it was used to determine the four kinetic constants in column 3 of Table 5.7 – again using a relative, weighted least-squares regression. The concentration profiles for triolein, methanol, and methyl-oleate are shown in Figure 5.27, and the reaction rate profiles are shown in Figure 5.28. Note that the CO_2 concentration profiles in each phase do not change appreciably. CO_2 accounts for roughly 92.5 mol% in the vapor phase, 61.7 mol% in the apolar liquid phase, and 43.7 mol% in the aqueous liquid phase. Overall, 63.3% of the total CO_2 moles are in the vapor phase, 0.57% in the apolar liquid phase, and 36.11% in the aqueous liquid phase.

Table 5.7. Kinetic Parameters

Constant	MS Excel	ASPEN PLUS	Units
k_f	0.063	0.104	$(m^3)^2/(kmol^2 s)$
k_r	0.006	0.114	$(m^3)^2/(kmol^2 s)$
n_f	1.253	1.269	-
n_{rev}	0.700	0.700	-

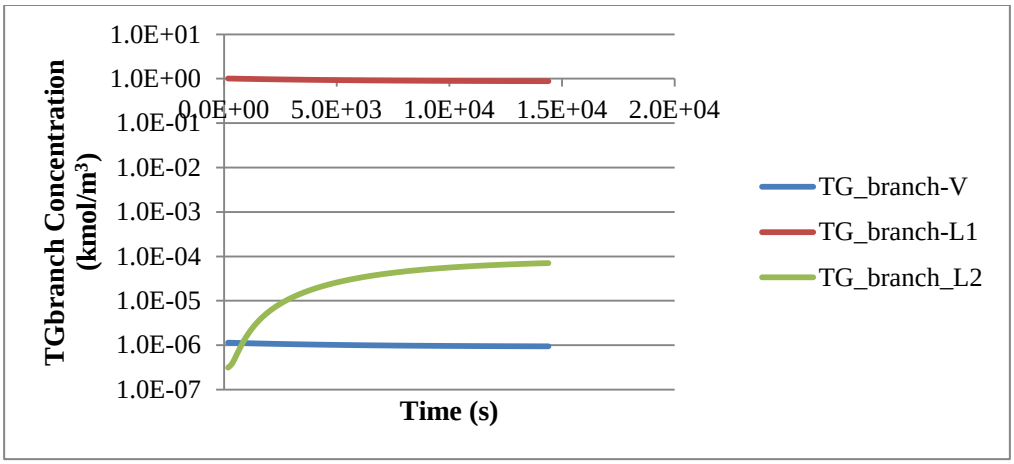

(a) TG_{branch} concentration profiles

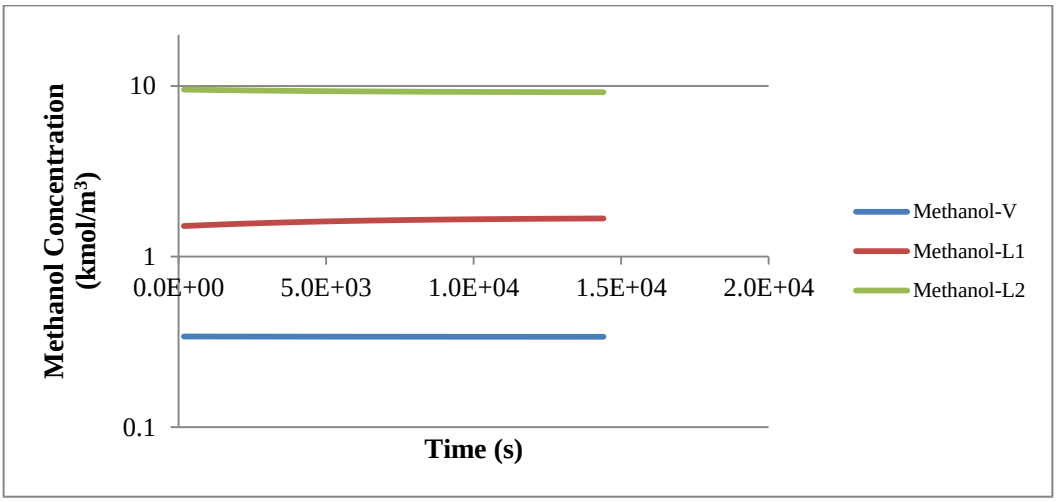

(b) Methanol concentration profiles

Figure 5.27. Concentrations with time.

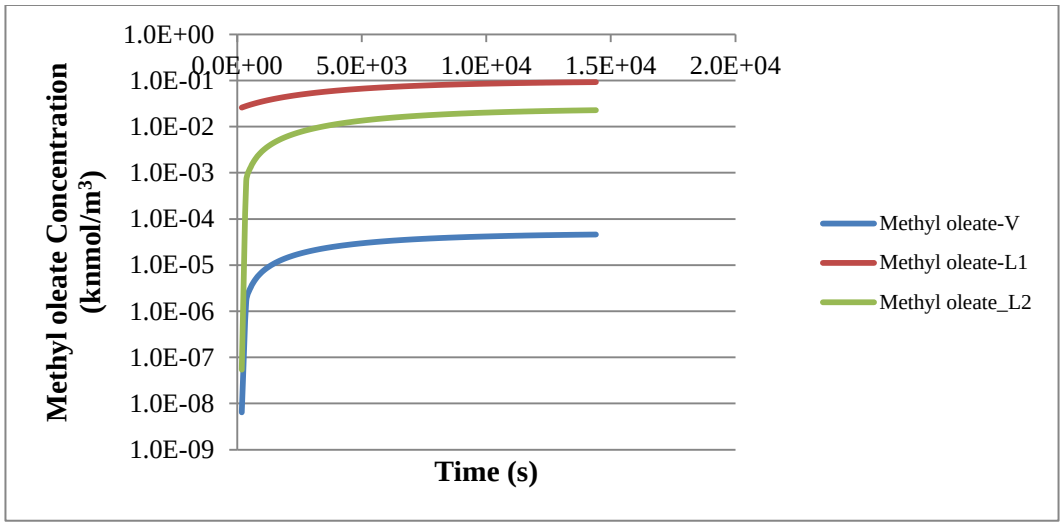

(c) Methyl-oleate concentration profiles

Figure 5.27. Concentrations with time (Cont'd.)

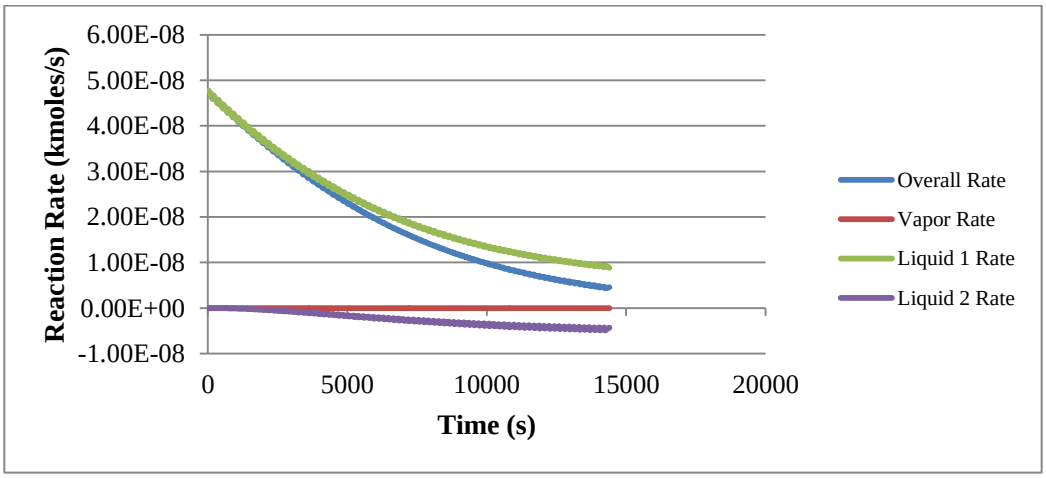

Figure 5.28. Reaction rates.

Liquid 1 is the triolein (apolar liquid) phase and liquid 2 is the aqueous phase. Note that methanol distributes between the two phases, due to CO_2 increasing its solubility in the apolar phase. The forward reaction occurs almost exclusively in the apolar liquid phase. The vapor phase has a negligible reaction rate because of triolein's

low vapor pressure. The reverse reaction occurs in the second liquid, because essentially all produced glycerol moves to the aqueous phase and there is negligible triolein present to drive the forward reaction. Note that the system is predicted to remain in the 3-phase region throughout the course of the reaction.

Although conversions are comparable when using the same kinetic constants, the reaction proceeds slower in this 3-phase model than in the 1-phase model in MS Excel, with 77.3% of triolein converted compared to 81.6%), which does not agree with the experimental data (Soh et al., 2013). This is likely because RK-ASPEN under-predicts the solubility of methanol in the triolein phase. The high solubility also explains why the *Gibbs flash method* predicts only one liquid phase, because it has difficulty distinguishing between two phases with high mutual solubility. Clearly, more robust phase equilibria algorithms, which check the phase stability, are needed to analyze this system.

5.7. Conclusions

Biodiesel production, using supercritical fluids, has become a topic of growing concern in the last several years (Changi et al., 2011; Patil et al., 2012; Soh et al., 2013). Numerous attempts have been made to model this system (Andreatta et al., 2010; Anikeev et al., 2012; Glisic and Orlovic, 2014; Macaira et al., 2014), but all previous studies used traditional, cubic equations-of-state. This chapter compares PC-SAFT in ASPEN PLUS and SAFT-γ Mie in gPROMS to RK-ASPEN in ASPEN PLUS for pure-species, binary, and ternary systems.

A simplified biodiesel system using six species (triolein, methanol, carbon dioxide, methyl-oleate, glycerol, and water) has been studied. For the pure species, all

three equations matched the liquid vapor-pressure data, but only the SAFT EoSs correctly predicted the liquid densities. PC-SAFT's VLE predictions were poorer on average than those of gSAFT and RK-ASPEN, but it provided the best agreement with LLE data. PC-SAFT gave good predictions for the ternary LLE systems, and for portions of the triolein, methanol, carbon dioxide mixture phase map, but ultimately none of the EoSs studied herein gave accurate predictions for the triolein, methanol, and CO2 mixtures. For PC-SAFT, this shortcoming was attributed to phase instability. Whereas, for gSAFT, the poor predictions in the VLLE region are likely to be a combination of improper weighting factors in regression of parameters from experimental data and the lower accuracy of using a group-contribution methodology. However, the SAFT EoSs are clearly more robust than RK-ASPEN, and given Figure 5.24(d) and the unstable phase distributions in the two polygons in Figure 5.25, it is likely that PC-SAFT can correctly representing the phase distribution for this system. In future work, a single-group molecule approach should be used in gSAFT to determine the full extent of its predictive capabilities, as it incorporates a more robust phase equilibria algorithm than ASPEN PLUS; that is, gSAFT checks the phase stability after convergence of flash calculations.

RK-ASPEN (with no binary parameters) gave reasonable agreement with experimental results in the VLLE region, and thus, was used in the multiphase-reactor model. The model showed comparable conversions in the VLLE and supercritical regions. This is economically promising, permitting the much lower pressure VLLE systems to achieve high conversions. As newer flash algorithms are introduced in ASPEN PLUS and the parameter databank in gSAFT becomes more refined, it will become possible to model these reactions and the accompanying separations with greater

accuracy, eventually allowing an extraction-transesterification process to be synthesized, optimized, and economically evaluated. The implications for future work are examined in more detail in Chapter 6.

5.8. Nomenclature

Quantity	Meaning	Units
$[C]$	Concentration	$kmol/m^3$
$[cat]$	Catalyst concentration	$kmol/m^3$
$[glycerol]$	Concentration of glycerol	$kmol/m^3$
$[methanol]$	Concentration of methnaol	$kmol/m^3$
$[methyl\text{-}oleate]$	Concentration of methyl-oleate	$kmol/m^3$
$[TG_{branch}]$	Concentration of TG_{branch}	$kmol/m^3$
a	EoS Parameter	-
A	Helmholtz free energy	J
b	EoS Parameter	-
c	EoS Parameter	-
d	EoS Parameter	-
D	Collision diameter	m
e	EoS Parameter	-
F	tangent plane distance function	J
f	Fugacity	Pa
G	Gibbs free energy	J

K	Binary interaction parameter	-
k	Rate constant	$(m^3)^2/(kmol^2\text{-}s)$
k_B	Boltzmann's constant	J/molecule-K
m	Segment length	-
M	number of association sites on each molecule	-
N	Number of molecules	molecules
n	Exponent	-
NC	Number of species	-
NG	Number of groups	-
ng	number of groups in a molecule	-
nsg	Number of sites on a group	-
NST	Number of Sites	-
P	Pressure	Pa
R	Gas Constant	J/mol-K
r	Radial distance between segments	m
rxn	Intrinsic reaction rate	$kmol/m^3\text{-}s$
S	Empirical Square-well parameter	m
s	Shape parameter	-
T	Temperature	K
t	Time	s
u	Square-well potential energy	J
V	Volume	m^3

W	Non-normalized mole fraction	-
x	Mole fraction	-
X	Association mole fraction	-
y	Mole fraction	-
Y	Moles	mol
z	Mole fraction	-
Z	Moles	mol

Quantity	**Meaning**	**Units**
α	Temperature fitting parameter	-
γ	Accentricity fitting parameter	-
Γ	Objective function	-
ε	Energy of the square-well interaction	J
ζ	Reduced density	-
η	Extra polar parameter	-
κ	Association bonding volume	m^3
λ	Range of the interaction	m
μ	Chemical potential	J/mol
ν	Stochiometric coefficient	-
ρ	Number density	Molecules/m^3
σ	Segment diameter	m
φ	Fugacity coefficient	-
Φ	Objective function	-

ω	Accentric factor	-
Ω	Minimum interaction parameter	-

Subscript	**Meaning**
1	Order of perturbation term
2	Order of perturbation term
a	Relating to parameter *a*
A	Association
at	Attractive
b	Relating to parameter *b*
B	Association
c	Critical
f	Forward
m	Mixing
n	Power of the collision diameter
r	Reduced
R	Repulsive
R5.1	Relating to reaction R5.1
ref	Reference
rev	Reverse

Superscript	**Meaning**
0	Binary interaction coefficient order

1	Binary interaction coefficient order
A	Associating group
assoc	Association contribution
B	Associating group
chain	Chain contribution
disp	Dispersion contribution
HB	Associating
hc	Hard-chain contribution
ig	Ideal-gas contribution
mono	Monomer contribution
polar	Polar contribution
T	Tangent

CHAPTER 6

Conclusions and Future Work

This thesis explores biofuel production from algae using a systems-based approach. It employs numerous software packages, including ASPEN PLUS and gPROMS to perform thermophysical property and phase-equilibria calculations, as well as calculations for chemical process synthesis. AIMMS, GAMS, and MS Excel are used to optimize parameters for ASPEN PLUS and gPROMS models. Mass, energy, and exergy balances constructed in MS Excel, ASPEN PLUS, and gPROMS are used in various chapters to determine the limiting factors in processing systems and to discover ways to improve, eliminate, or bypass them. The models created herein should yield better process designs and more accurate economic analyses.

6.1. Conclusions

Chapter 2 presented a novel method to approach the algae-to-biodiesel process venture, employing a systems-based approach. An *energy-limited*, thermodynamic model for algae cultivation was developed in ASPEN PLUS and combined with approximate models for the other three processing steps (harvesting, extraction, and lipid-upgrading) to obtain upper-bounding cost-estimates for algae-to-biofuel production. The key results of this analysis were: (1) high land-area requirements for cultivation are required due to the low photosynthetic efficiency, and (2) the recycling of water, nutrients, and waste products (glycerol, cell debris) is needed to drastically improve the process economics.

The thermodynamic cultivation model in Chapter 2 was combined with cost estimates for the NAABB harvesting and extraction technologies, as well as a rigorously modeled glycerolysis/transesterification process in Chapter 3. An overall process superstructure was synthesized, with outputs being fed into a techno-economic model. A sensitivity analysis was developed, which identified key research areas for an algae-to-biodiesel venture.

The cost of algae pond construction represented 90% of the total capital expense (CAPEX) because massive fields (farms) are required to grow algae at a sufficient rate — due to low photosynthetic efficiency. This was the key factor investigated in Chapter 4, where exergy balances were examined using data and methodology developed over the past six decades to yield a thorough analysis of the photosynthetic exergy efficiency. Even though Chapter 4 assumed equilibrium conditions, the estimates are accurate for an algae system because cultivated algae are grown with excess CO_2; thus, their RuBisCO enzymes are saturated, eliminating the most important mass-diffusion limitations experienced by terrestrial plants (Kelly and Latzko, 2006a). Therefore, the efficiency estimate (4%) in Chapters 2 and 3 was found to be approximately accurate (with 3.9% calculated in Chapter 4). Chapter 4 also confirmed the "light limited" growth hypothesis upon which Chapter 2 is based. Overall, the largest impact on efficiency (and therefore CAPEX cost) was shown to be the algae-cell's poor absorption of diffuse sunlight.

The operating expenses (OPEX) were somewhat-evenly distributed between cultivation, harvesting, and lipid-upgrading — with extraction representing a negligible contribution in the base case. Harvesting had the largest OPEX, because of high electricity consumption. However, the methods used to harvest algae are repurposed

waste-water treatment methods, used for many decades, and thus, just small improvements are likely. The best chance to decrease electricity costs for the entire venture is to optimize the cultivation pond depth for high biomass concentrations — as will be explored in Section 6.2.1.

Although the extraction cost was minimal in the base-case techno-economic analysis of Chapter 3, the sensitivity analysis showed that it had the greatest economic variability. This is to be expected because algae-oil extraction is the only new processing step in an algae-to-biodiesel venture. Algae growth has been studied since World War II (Morimura et al., 1955; Tamiya, 1957; Tamiya et al., 1953), harvesting techniques have been used in waste-water treatment for decades, and transesterification methods have been used to produce biodiesel from vegetable oils for roughly twenty years. Therefore, research into algae-oil extraction techniques should yield substantial benefits because they comprise an under-explored area.

A novel method to perform both the extraction and transesterification was explored in Chapter 5. Supercritical CO_2 lyses the algae cells, leaches the oil from the spent biomass, and enhances the reaction rate between the triglycerides and methanol by increasing their mutual solubility. Chapter 5 identified two underutilized equations-of-state (PC-SAFT and SAFT-γ Mie) and used them to construct a preliminary analysis of a supercritical extraction/transesterification process by examining the phase equilibria of key mixtures. The performance of these two equations-of-state (EoSs) was analyzed and compared to the RK-ASPEN EoS, which was used in previous studies (Glisic and Orlovic, 2014; Macaira et al., 2014). Overall, performance for most systems by the two SAFT variants was superior to that of RK-ASPEN. However, more work is needed

before these EoSs can be fully utilized to perform the cost analyses and optimizations that will lead to improvements in an overall algae-to-biodiesel venture.

6.2. Future Work

Areas for future research include: (1) algae cultivation, (2) measurements of thermophysical property data for algae and related biochemical compounds, (3) alternative algae-to-biofuels production methods, (4) improved light absorption during photosynthesis and co-cultivation, (5) superior phase-equilibrium algorithms, (6) improved algae-oil extraction, and (7) experimental studies of supercritical CO_2 biodiesel production. These are discussed next.

6.2.1. Algae Cultivation

The large volumes of the algae cultivation ponds in Chapters 2 and 3 were shown to be the major costs for algae-to-biodiesel ventures. The area of the ponds, which was calculated using the methods described in Chapter 2, determines the land cost and evaporation rate. The pond depth was only briefly discussed, although it significantly impacts the pond installation cost per unit area, as well as the concentration of the algae slurry transferred to the harvesting step, and consequently, the equipment sizes and power costs for harvesting. Thus, the best chance to reduce the harvesting cost is optimization of the pond depth to ensure that the highest concentration of algae enters the harvesting process (Dunlop et al., 2013). Reducing this large volume of water is clearly a future objective – and is currently being examined by Dunlop at Pan Pacific Technologies.

Similarly, the effect of recycling glycerol, debris, and water has been shown to be economically advantageous. While the effects of algae consuming glycerol have been studied at a lab-scale (Boussiba et al., 1987; Tornabene et al., 1983), and the effect of salinity is understood (Rao et al., 2007; Taylor et al., 2005), no attention has been given to algae consumption of spent biomass (Dunlop et al., 2013). The performance of algae, when grown using their own spent debris, can have substantial economic impacts and should be explored experimentally.

6.2.2. Thermophysical Property Data

In Chapters 2-5, significant limitations were experienced due to limited thermophysical property and phase equilibria data. Chapter 2 used enthalpies and entropies of formation for yeast cells because data were unavailable for algae cells. In addition, in Chapters 2 and 3, a simplified set of algae-derived triglycerides were used because of data limitations. In Chapter 3, crude assumptions were required for many species (diglycerides and monoglycerides) for which data did not exist or were insufficient (for many triglycerides and FAMEs). The Joback group contribution method (Poling et al., 2001) was used to determine the pure-species properties (molar volumes and heat capacities), and UNIFAC was used for mixtures involving these species.

In Chapter 4, the expressions for chemical exergy were simplified (assuming unit species activities) due to lack of data. In addition, rigorous estimates for the exergy losses in alternative biochemical pathways (besides those of the Calvin Cycle) were not computed because free energies of formation and concentrations within the cells were unknown.

Finally, the kinetic mechanism in Chapter 5 was simplified to exclude diglycerides and monoglycerides because pure-species (liquid-densities and liquid-vapor pressures) and binary (VLE or LLE) data were unavailable. Similarly, triolein and methyl-oleate were used to represent triglyceride and fatty-acid methyl-ester (FAME) molecules because insufficient data were available for other species.

In summary, to improve cost and profitability estimates and to seek more optimal designs, thermodynamic data for a broader array of algae-related species are needed. These data will facilitate more innovative algae-to-biofuel ventures.

6.2.3. Alternative Algae-to-Biofuel Production Methods

While Chapter 3 explored a wide array of options for the algae-to-biofuel venture (Silva et al., 2014), it was not feasible to explore them all. In particular, photo-bioreactors and alternative lipid-upgrading processes were not examined (Dunlop et al., 2013; Silva et al., 2014), the former due to high cost estimates (Davis et al., 2011; Richardson et al., 2012; Sun et al., 2011), and the latter due to scarcity of kinetics data (Duan and Savage, 2010; Jones et al., 2014; Zhu et al., 2014). In addition, algae harvesting and extraction methods were only given a cursory examination. Here, rigorous modeling could lead to significant improvements in the economic outlook. As newer methods are developed and more data become available, new options (or improved methods) can provide advantages over older methods for the four major processing steps (cultivation, harvesting, extraction, and upgrading).

6.2.4. Light Absorption during Photosynthesis and Co-Cultivation

For the photosynthetic efficiency, the loss of most non-photo-active-region (PAR) radiation and the reflectance of PAR radiation account for the majority of the exergy lost (64.4 percent). Thus, research to tune the photosynthetic antennas (Webpage: "Tuning" microalgae for high photosynthesis efficiency; Melis, 2009; Perrine et al., 2012) is particularly important. Perhaps coupling photosynthetic and photovoltaic systems will be beneficial, especially with the latter absorbing the non-PAR radiation (without the PAR radiation). Similarly, using different photosynthetic organisms (each of which absorbs different wavelengths) and building a photo-ecosystem (Barber, 2009; Bisio and Bisio, 1998; Scholes et al., 2012) could significantly decrease photo-degradation. Perhaps chemical engineers can design controllers for these complex systems.

Because electron-transport chain (ETC) losses are substantial, and attempts to improve the efficiency of this process have been mostly unsuccessful, future studies are justified. Note that exergy losses to ATP synthase and the Calvin Cycle are relatively low and likely to be unavoidable. Therefore, future efforts to improve photosynthesis are likely to focus upon absorbance and the ETC.

Lastly, kinetic and diffusional bottlenecks in this system arise because of slow electron transfer in the electron-transport chain (Webpage: "Tuning" microalgae for high photosynthesis efficiency; Melis, 2009). Note that although carbon dioxide sequestration by RuBisCO is typically the rate-limiting step, this concern is eliminated for algae because of excess CO_2 in cultivation. This study did not explore the effect of kinetic bottlenecks because it only addresses reversible exergy transfer, providing an upper bound. However, while this assumption yields a reasonable estimate for the actual

efficiency herein, analysis of the irreversible effects will likely become important in future works — as improvements to the theoretical efficiency are realized and new bottlenecks emerge.

6.2.5. Superior Phase Equilibrium Algorithms and EoS Parameters

The RK-ASPEN EoS without binary interaction parameters, although it should have yielded the poorest agreement with the VLLE data, was the only EoS that correctly predicted the VLLE region for triolein, methanol, and CO_2. Consequently, while approximate, it was used for the multiphase-reactor code. But, VLE solutions obtained by the PC-SAFT EoS with binary parameters were found to be unstable for the triolein, methanol, and CO_2 system in the VLLE region — which was likely due to the high mutual solubility between the apolar and aqueous liquid phases.

Therefore, the *Gibbs flash method*, which was used to perform the phase-equilibrium calculations in Chapter 5, is not suitable for complex gas-expanded liquid (GXL) systems (Ye et al., 2012), where these high mutual-solubility conditions occur. An improved phase-equilibrium algorithm is needed to minimize the Gibbs free energy, check for phase stability, and then re-minimize the Gibbs free energy, repeating this cycle until the correct phase distribution is obtained at equilibrium (at the global minimum of the Gibbs free energy). Such an algorithm has been developed for specific EoSs (McDonald and Floudas, 1995a, b). Similar techniques are needed in ASPEN PLUS.

In gPROMS, the phase algorithm incorporates phase-stability checking, but due to time constraints, the parameter database could not be fully optimized for the GXL system in Chapter 5. Parameters for certain groups (CH_3 and CH_2) were taken from previous

works, which did not use proper weighting factor, and over-regression was likely a problem for other groups (particularly glycerol). In future works, to fully gauge the effectiveness of the gSAFT package, single-group molecule approach should be used and the parameter database should be optimized for this system.

6.2.6. Algae-Oil Extraction

Chapter 3 identified algae-oil extraction as the most variable step in the economics of biodiesel production. The use of supercritical fluids (methanol or CO_2) for extraction was a key reason for examining the phase equilibria in Chapter 5 (Soh and Zimmerman, 2011). The SAFT-γ Mie EoS was selected because of its ability to estimate group parameters using sparse data for species types (for example, triglycerides or fatty-acid methyl-esters (FAME)) to calculate the necessary group parameters (Papaioannou et al., 2014). Then, predictions for the thermophysical properties and phase equilibria involving a wide range of these species could be estimated.

The extraction calculations were not carried out in this work due to time constraints, although the gSAFT package in gPROMS is capable of performing such calculations. Alternatively, with phase-equilibria data for additional triglyceride and FAME species, the PC-SAFT EoS could be used to model the extraction.

6.2.7. Experimental Exploration of Supercritical CO_2 Biodiesel Production

In Chapter 5, phase-equilibria data were difficult to obtain for many systems, particularly LLE systems, because most studies seeking to analyze the supercritical

conversion of bio-oils to biofuels focus only on the kinetics (Changi et al., 2011; Levine et al., 2010; Macaira et al., 2014), neglecting the complex thermodynamic behavior.

Data were generated for use in Chapter 5, but numerous LLE datasets were either of questionable quality (triolein and glycerol, FAME and glycerol) or were incomplete (triolein and methanol, triolein and water). In addition, there were few data concerning phase equilibria of the range of GXL systems that comprise the reactor inlet (Figure 5.24). Only several cloud point and dew point measurements were taken, with no information regarding the compositions of the phases (Soh et al., 2013). Finally, no information was available about the phase behavior as the reactions progressed, and the reactions were only carried out at one temperature and pressure (Soh and Zimmerman, 2015).

As discussed in Section 6.2.2, more experimental data would assist in validating new and existing EoSs. LLE data should be taken to validate and improve upon the measurements reported in Chapter 5 and Appendix C. The reacting triolein, methanol, CO_2 mixture should be studied visually to examine the phase changes while the reactions proceed and confirm theoretical predictions (Hegel et al., 2007). The reactions should be carried out at several temperatures and pressures, given the optimal catalyst loadings (Soh and Zimmerman, 2015), to validate and optimize the models.

6.3. Broader Impact

The high-fidelity modeling approaches in this research will permit more rigorous techno-economic models to be formulated and optimized for biofuels systems. As a result, the advantages and disadvantages of using algae to produce biodiesel will be

clearer, which will help guide future researchers towards areas where the greatest impacts can be made and away from areas that are unpromising. However, substantial work remains before the models become truly representative of commercial-scale processes.

The results presented herein represent several stepping stones on the pathway to developing sustainable bio-fuel production that can compete with petroleum-based fuels. Numerous novel techniques have been developed in all five areas explored by the NAABB. However, feasibility and future development requires process engineers to: (1) assemble the necessary thermodynamic and kinetic data, (2) develop complex process and systems models, and (3) synthesize techno-economic analyses for commercial-scale ventures that are competitive with pre-existing fuel-production processes.

Many of the techniques developed herein could be applied to other biochemical systems (Chapters 2 and 4), large-scale processing systems (Chapter 3), and supercritical and GXL systems (Chapter 5). This research is multi-disciplinary, involving aspects of economics, biology, bio-processing, exergy analyses, and chemical engineering.

6.4. Nomenclature

Acronyms	Term
CAPEX	Capital Expense
EoS	Equation of State
FAME	Fatty-acid Methyl-Ester
GXL	Gas-expanded Liquid
NAABB	National Alliance for the Advance of Biofuels and Bioproducts
OPEX	Operating Expense
PAR	Photo-active Region

Appendix A. Biochemical Reference Data

In this Appendix, the thermophysical properties required to estimate the exergies of the species in the Calvin Cycle reactions (Sections 4.3.1.4 and 4.4.1.4) are discussed and tabulated in Table 4.A.1. The species are numbered in order of appearance in the Calvin Cycle reactions. Also, each molecule is abbreviated using the notation in Table 4.3. Note the chemical formula is that used herein; it may not represent the actual chemical formula; e.g., for NADPH/$NADP^+$ and ATP/ADP. For these pairs, an "equivalent" formula is used (Lems et al., 2007) because the excluded atoms are shared between the pairs (NADPH/$NADP^+$ and ATP/ADP) and every reaction containing ATP has ADP on the other side, and similarly with NADPH/$NADP^+$.

Table A.1. Calvin Cycle – Detailed Values

Number	Molecule	Name	Formula	$B_{elements}$ (kJ/mol)	ΔG_f (kJ/mol)	$[A]$	$R*T_0*\mathrm{Ln}([A])$ (kJ/mol)	B_{total} (kJ/mol)
1	Ru5P	Ribulose 5-Phosphate	$C_5H_{11}O_8P$	4227.1	-1651.1	0.000012	-28.08753085	2547.85
2	ATP	Adenosine Triphosphate	$P_3O_9H_4$	3074.2	-2672.1	0.0018432	-15.6078331	386.54
3	RuBP	Ribulose 1,5-Bisphosphate	$C_5H_{12}O_{11}P_2$	5212.5	-2551.5	0.00204	-15.35635622	2645.62
4	ADP	Adenosine Diphosphate	$P_2O_6H_3$	2088.8	-1794.5	0.00013924	-22.01100114	272.33
5	CO_2	Carbon Dioxide	CO_2	414.2	-394.4	-	-	19.40
6	H_2O	Water (liquid)	H_2O	238.1	-237.2	-	-	2.54
7	PGA	3-Phosphoglycerate	$C_3H_7O_7P$	2932.4	-1609.2	0.0014	-16.28960969	1306.93
8	NADPH	Nicotinamide Adenine Dinucleotide Phosphate (reduced)	$H^- + H^+$	236.1	-17.1	0.001	-17.12369359	206.01
9	GAl3P	Glyceraldehyde 3-Phosphate	$C_3H_7O_6P$	2930.4	-1339.1	0.000032	-25.65614483	1565.66
10	$NADP^+$	Nicotinamide Adenine Dinucleotide Phosphate (oxidized)	-	-	0,0	0.001	-17.12369359	0.00
11	H_3PO_4	Phosphoric Acid	H_3PO_4	1223.5	-1147.6	0.001	-17.12369359	58.76
12	DHAP	Dihydroxyacetone Phosphate	$C_3H_7O_6P$	2930.4	-1346.7	0.00064	-18.2299985	1565.47
13	FBP	Fructose 1,6-Bisphosphate	$C_6H_{14}O_{12}P_2$	5860.8	-2707.8	0.000097	-22.90709704	3130.14
14	F6P	Fructose 6-Phosphate	$C_6H_{13}O_9P$	4875.4	-1811.8	0.00053	-18.69749876	3044.95
15	E4P	Erythrose 4-Phosphate	$C_4H_9O_7P$	3578.7	-1492.6	0.00002	-26.82124084	2059.36
16	Xu5P	Xylulose 5-Phosphate	$C_5H_{11}O_8P$	4227.1	-1652.1	0.000021	-26.70029449	2548.24
17	SBP	Sedoheptulose 1,7-Bisphosphate	$C_7H_{16}O_{13}P_2$	6509.1	-2862.8	0.000114	-22.50678437	3623.81
18	S7P	Sedoheptulose 7-Phosphate	$C_7H_{15}O_{10}P$	5523.7	-1966.8	0.000248	-20.58010154	3536.35
19	R5P	Ribose 5-Phosphate	$C_5H_{11}O_8P$	4227.1	-1653.4	0.000034	-25.50586194	2548.17
20	G6P	Glucose 6-Phosphate	$C_6H_{13}O_9P$	4875.4	-1813.9	0.00073	-17.90383274	3043.66
21	Glucose	Glucose	$C_6H_{12}O_6$	3890.0	-917.2	0.001	-17.12369359	2955.67
*	Oxygen	Oxygen	O_2	3.97	0	-	-	3.97
*	Hydrogen	Hydrogen	H_2	-	-	-	-	236.09

$B_{element}$ is the exergy of the elements, as defined by Szargut (Szargut, 2005) and described more thoroughly in Table 4.A.2; ΔG_f is the standard Gibbs free energy of formation for each compound, as described in the literature (Bassham and Krause, 1969; Krebs and Kornberg, 1957); it should be noted that the value for phosphoric acid (which was missing from Bassham and Krause (Bassham and Krause, 1969)) is taken from Lems et al. (Lems et al., 2007); [*A*] is the activity of the species, taken from the literature (Bassham and Krause, 1969); *RT*Ln([*A*]) is the exergy change due to mixing; and B_{total} is the exergy of the molecule, calculated using Eq. 4.18. The exergy changes and standard Gibbs free energy changes for important reactions (not in the Calvin Cycle) are shown in Table 4.A.3.

Table A.2. Elemental Exergies

Element	Ref Species	Standard Chemical Exergy (species) kJ	Standard Chemical Exergy (element) kJ/mol
C (s,gr)	CO_2(g)	19.87	410.26
H (H_2(g))	H_2O (g)	9.49	236.09
O (O_2(g))	O_2(g)	3.97	3.97
P (s,w)	HPO_4^{-2}	-	861.4

Note that in Table 4.A.1, NADPH and $NADP^+$ are assumed to be present in the concentration ratio, 1:1. Also, $NADP^+$ is assumed to be the ground state, and therefore, its exergy is zero. The values for the concentrations of ATP and ADP presented by Lems et al. (Lems et al., 2007) do not agree with those presented by Bassham and Krause (Bassham and Krause, 1969). The former are more recent and

are used herein. Different concentration values are tabulated for both glucose and glucose-6-phosphate, all of which are within an order of magnitude, resulting in differences of less than 1% in the overall Calvin Cycle calculations. Finally, as mentioned in Section 4.4.1.4, the exergies for CO_2 and O_2 are calculated using Eq. 2.9 in Szargut's book (Szargut, 2005).

Table A.3. Exergy and Standard Gibbs Free Energy Changes

Rxn1:	$(NADPH) + 1/2*O_2 \rightarrow (NADP^+) + H_2O$			
$\Delta G°$	=	-220.05	kJ/mol	
ΔB	=	205.45	kJ/mol	
Rxn2:	$(ATP) + H_2O \rightarrow (ADP) + H_3PO_4$			
$\Delta G°$	=	-32.8	kJ/mol	
ΔB	=	58.0	kJ/mol	
Rxn3	$C_6H_{12}O_6 + 6*O_2 \rightarrow 6*H_2O + 6*CO_2$			
$\Delta G°$	=	-2872.23	kJ/mol	
ΔB	=	2847.83	kJ/mol	

Appendix B. Photosynthesis Glossary

1. ATP synthase – a giant protein complex that uses the exergy stored in proton gradients to drive ATP synthesis, as seen in reaction R4.4.

2. Autotroph – an organism that uses radiant or inorganic sources of exergy to produce cellular components, sugars, and high exergy carrier molecules (like ATP). Plants and algae are two examples of autotrophs.

3. C4 Cycle – a carbon fixation pathway, which lowers RuBisCO's tendency to fix oxygen and begin photorespiration. It is named for the 4-carbon molecule (oxaloacetate) which results from the first step of carbon fixation, in contrast to the 3-carbon molecule (3-phosphoglycerate) that is produced by C3 (normal) plants.

4. Chlorin – a large aromatic ring composed of carbon, nitrogen, and hydrogen. It is the central group of a chlorophyll molecule, having a magnesium atom at its center. The aromatic behavior allows for easy excitation of the shared electrons by sunlight.

5. Chlorophyll – pigment molecules present within chloroplasts that are responsible for capturing sunlight and converting it to electrical energy (high-energy electrons).

6. Chloroplast – the organelle that captures sunlight, using it to convert carbon dioxide and water to organic matter (biomass) – see Figure 4.1b.

7. Crassulacean Acid Metabolism (CAM) – a carbon fixation pathway that reduces water loss in arid conditions. CAM plants keep their pores open at night to collect CO_2 – which is fixed into malate (a 4-carbon molecule) – and closed during the day (the opposite of normal, or C3, plants) to reduce transpiration. The malate is concentrated around the enzyme RuBisCO in the cells, essentially eliminating photorespiration.

8. Cyclic-photophosphorylation – the process by which electrons are excited by PSI and passed backward to the cytochrome b6f complex (top red node in Figure 4.3), driving protons against their gradient. The electrons are then returned to PSI by plastoquinol, and the protons are used by ATP synthase to produce ATP by reaction R4.4.

9. Electron transport chain (ETC) – a series of functional groups that capture solar exergy, as high energy electrons, and channel these electrons through a series of carriers that increase their charge separation from the original nucleus, thus making them available for other purposes.

10. Metabolism – the physical and chemical processes in an organism that produce and maintain its components as well as those processes that absorb radiant exergy or degrade substances to provide exergy.

11. Organelle – enclosed portion of the cellular medium (cytoplasm) with a designated function – see Figure 4.1.

12. P680 – a chlorophyll pigment molecule, most commonly associated with Photosystem II, that has maximal absorption of sunlight with a wavelength of 680 nm.

13. P700 – a chlorophyll pigment molecule, most commonly associated with Photosystem I, that has maximal absorption of sunlight with a wavelength of 700 nm.

14. Photo-inhibition – the overexposure of chlorophyll to sunlight, which damages these pigments through oxidation.

15. Photon – a quantum of electromagnetic radiation that has zero mass and charge, and a spin of one.

16. Photosystem I (PSI) – a protein complex that captures sunlight, using it to excite electrons to a higher energy state and eventually produce NADPH from $NADP^+$,

H^+, and two excited electrons. It is composed of a chlorophyll pigment molecule (typically P700) and electron transporter molecules, which are shown in Figure 4.3.

17. Photosystem II (PSII) – a protein complex that captures sunlight, using it to drive protons against their gradient and split water – releasing protons, molecular oxygen, and electrons (which are excited to a higher energy state). It is composed of a chlorophyll pigment molecule (typically P680) and electron transporter molecules, which are shown in Figure 4.3.

18. Plastiquinol (PQ) – the reduced form of plastoquinone. It is the last carrier molecule in the Photosystem II electron-transport chain, bringing the electrons from Photosystem II to Photosystem I.

19. Proton-motive force – the exergy stored in the proton gradient between the inside of the thylakoid (high concentration) and the chloroplast fluid (low concentration).

20. Redox Potential, ε(V) – a measure of the affinity for a chemical species to acquire electrons, thereby becoming reduced. Moving from a smaller redox potential to a larger redox potential is a process that occurs naturally, requiring no input of exergy.

21. Relative Absorption – the amount of solar exergy (photons) that can be absorbed and converted to chemical or electrical exergy by chlorophyll pigments.

22. Respiration – the process by which cells decompose glucose to energy-carrier molecules like ATP, or necessary intermediates used to produce cellular components.

23. RuBisCO – official name: ribulose-1,5-bisphosphate carboxylase/oxygenase, is an enzyme which catalyzes carbon (CO_2) fixation in the Calvin Cycle. It can also catalyze the reaction of oxygen with 1,5-bisphosphate, which is the first step in photorespiration.

24. Transpiration – the loss of the plant's water reserves through pores in the leaves (known as stomata).

Appendix C. Experimental Phase Equilibria Data

The data measured according to the methods described in section 5.3 are listed in Tables C.1-C.5. Table C.1 is the only vapor-liquid equilibrium dataset. All others are liquid-liquid equilibria. For the LLE datasets, each temperature was measured twice; however, some experiments resulted in physically impossible concentrations. A dash is used to denote this in the tables. Finally, for the methanol and triolein (Table C.2) and water and triolein (Table C.5) LLE datasets, only one of the liquid phases could be sampled. The data in all tables is accurate to three significant figures.

Table C.1. Methanol and Methyl-oleate VLE (mole fractions)

T(K)	*x*, Methanol	*x*, Methyl-oleate	*y*, Methanol	*y*, Methyl-oleate
342.25	0.672	0.328	1.000	0.000291
346.95	0.484	0.516	1.000	0.000271
356.75	0.346	0.654	0.999	0.00141
362.65	0.239	0.761	0.999	0.000840
372.85	0.145	0.855	0.999	0.000955
384.15	0.104	0.896	0.998	0.00153
394.65	0.0759	0.924	0.998	0.00218
414.85	0.0528	0.947	0.997	0.00284
435.15	0.0552	0.945	0.996	0.00362

Table C.2. Methanol and Triolein LLE (mole fractions)

T(K)	x_1, Methanol	x_1, Triolein
303.15	1.000	0.0000758
303.15	1.000	0.0000877
303.15	1.000	0.0000879
308.15	1.000	0.000110
308.15	1.000	0.000147
308.15	1.000	0.000148
313.15	1.000	0.000082
313.15	1.000	0.000128
318.15	1.000	0.000118
318.15	1.000	0.000120
318.15	1.000	0.000140
313.15	1.000	0.000305
328.15	1.000	0.000168
328.15	1.000	0.000259
333.15	1.000	0.000173
333.15	1.000	0.000207

Table C.3. Glycerol and Methyl-oleate LLE (mole fractions)

Temperature (K)	x_1, Glycerol	x_1, Methyl-oleate	x_2, Glycerol	x_2, Methyl-oleate
323.15	0.00231	0.998	-	-
323.15	0.00389	0.996	0.989	0.0111
333.15	0.00317	0.997	0.992	0.00811
333.15	0.00309	0.997	0.997	0.00318
343.15	0.00513	0.995	0.999	0.00140
343.15	0.00419	0.996	0.999	0.00122
353.15	0.00510	0.995	0.996	0.00376
353.15	0.00542	0.995	0.992	0.00792
363.15	0.00627	0.994	0.998	0.00207
363.15	0.00690	0.993	0.984	0.0161
373.15	0.00993	0.990	0.995	0.00470
373.15	0.00906	0.991	0.956	0.0445
383.15	0.0121	0.988	1.000	0.000208
383.15	0.0128	0.987	0.997	0.00272

Table C.4. Glycerol and Triolein LLE (mole fractions)

Temperature (K)	x_1, Triolein	x_1, Glycerol	x_2, Triolein	x_2, Glycerol
323.15	0.000371	1.000	-	-
323.15	0.000421	1.000	0.997	0.00306
333.15	0.0252	0.975	0.995	0.00499
333.15	-	-	0.995	0.00453
343.15	0.00255	0.997	0.993	0.00716
343.15	0.0134	0.987	0.994	0.00559
353.15	0.00459	0.995	0.993	0.00713
353.15	-	-	0.994	0.00562
363.15	0.00224	0.998	0.993	0.00719
363.15	-	-	0.993	0.00688
383.15	0.000820	0.999	0.981	0.0191
383.15	0.000767	0.999	0.975	0.0254

Table C.5. Water and Triolein LLE (mole fractions)

Temperature (K)	x_1, Triolein	x_1, Water
323.15	1.87E-04	1.000
333.15	3.96E-05	1.000
333.15	8.99E-06	1.000
333.15	2.33E-04	1.000
341.15	1.83E-05	1.000
341.15	6.17E-06	1.000
341.15	1.10E-05	1.000
348.15	2.00E-05	1.000
348.15	5.78E-05	1.000
348.15	3.48E-06	1.000
355.15	1.85E-05	1.000
355.15	7.50E-06	1.000
355.15	2.01E-05	1.000
363.15	1.76E-05	1.000
363.15	7.00E-06	1.000

REFERENCES

Algae Biofuels: An Introduction, <http://www.jatrophabiodiesel.org/algae/about-algae.php>, [Accessed 11/25/2013].

Algae Industry Magazine – NAABB Chooses Harvesting and Extraction Technologies, <http://www.algaeindustrymagazine.com/naabb-chooses-ultrasonic-harvester-technology/>, [Accessed 12/10/2012].

Algae Industry Magazine – Natural Vs. Synthetic Flocculents, <http://www.algaeindustrymagazine.com/natural-vs-synthetic-flocculents/>, [Accessed 12/10/2012].

Algae Lipid Synthesis, <http://lipidlibrary.aocs.org/plantbio/tag_algae/index.htm>, [Accessed 05/08/2015].

Aspentech. Aspen Physical Property System. Burlington, Ma: Aspen Technology, Nov. 2013. Pdf.

Atmospheric CO_2 Concentrations over Thousands of Years, <https://upload.wikimedia.org/wikipedia/commons/1/1c/Carbon_Dioxide_400kyr.png>, [Accessed 05/07/2015].

Atmospheric Concentration of CO_2 with Time, <http://www.physicalgeography.net/fundamentals/7aCO2.html >, [Accessed 05/07/2015].

ATP Synthase. <http://vcell.ndsu.nodak.edu/animations/etc/atpsynthase.htm>, [Accessed 01/27/2014].

Biodiesel Magazine – Standard-for Good Reason, <http://www.biodieselmagazine.com/articles/715/standard-for-good-reason>, [Accessed 11/07/2012].

Carbon Dioxide Thermophysical Properties <http://webbook.nist.gov/cgi/cbook.cgi?ID=C124389&Mask=4>, [Accessed 04/30/2014].

Chloroplast Diagram. <https://commons.wikimedia.org/wiki/Category:Chloroplasts#/media/File:Chloroplast_(borderless_version)-en.svg>, [Accessed 07/28/2014].

Climate Change 2007: Synthesis Report, <https://www.ipcc.ch/pdf/assessment-report/ar4/syr/ar4_syr.pdf>, [Accessed 05/07/2015].

Consumer Price Index, <http://www.usinflationcalculator.com/inflation/consumer-price-index-and-annual-percent-changes-from-1913-to-2008/>, [Accessed 6/24/2013].

CRC Handbook of Chemistry and Physics, Section 3, <http://www.hbcpnetbase.com/>, [Accessed 06/03/2012].

Degumming – Introduction, <http://lipidlibrary.aocs.org/processing/degum-intro/index.htm>, [Accessed 12/10/2012].

Eia: Real Prices Viewer, <http://www.eia.gov/forecasts/steo/realprices/>, [Accessed 05/07/2015].

Fat Content and Fatty-Acid Composition of Seed Oils, <http://curezone.com/foods/fatspercent.asp>,

Flocculants Info, <http://www.flocculants.info/>, [Accessed 12/10/2012].

Glyceraldehyde Dehydration, <https://en.wikipedia.org/wiki/Glycerol-3-phosphate_dehydrogenase>, [Accessed 05/08/2015].

Green Car Congress – NAABB Selects Los Alamos Ultrasonic Algae Harvester for Phase Ii Development, <http://www.greencarcongress.com/2012/05/niaabb-selects-los-alamos-ultrasonic-algae-harvester-for-phase-ii-development.html>, [Accessed 12/10/2012].

How Much Petroleum Is Imported?, <http://www.eia.gov/tools/faqs/faq.cfm?id=727&t=6>, [Accessed 05/07/2015].

Introduction to Ozone. <http://www.ucar.edu/learn/1_5_1.htm>, [Accessed 01/27/2014].

Kennedy Pathway, <http://lipidlibrary.aocs.org/Lipids/tag2/index.htm>, [Accessed 05/08/2015].

Learn About Biodiesel, <http://www.epa.gov/region09/waste/biodiesel/questions.html#whyuse>, [Accessed 11/25/2013].

Lipid Biosynthesis, <http://lipidlibrary.aocs.org/plantbio/fa_biosynth/index.htm>, [Accessed 05/08/2015].

Mean Value Theorem. <https://en.wikipedia.org/wiki/Mean_value_theorem>, [Accessed 01/27/2014].

Methanex – Us Methanol Price, <http://www.methanex.com/products/methanolprice.html>, [Accessed 06/03/2012].

NAABB Final Report, <http://www.energy.gov/eere/bioenergy/downloads/national-alliance-advanced-biofuels-and-bioproducts-synopsis-naabb-final>, [Accessed 04/29/2015].

National Research Council, 2012. Sustainable Development of Algal Biofuels in the United States. National Academies Press, Washington DC.

Nist Data Bank. Aspen Plus.

Origin Oil Single-Step Extraction, <http://www.originoil.com/technology/single-step-extraction.html>, [Accessed 12/10/2012].

PAR & the Light Spectrum. <http://www.fondriest.com/environmental-measurements/wp-content/uploads/2014/03/384x304xpar_photosynthesis-wavelength.jpg.pagespeed.ic.BGjGExN3Pl.jpg>,

Photorespiration Wikicommons. <https://commons.wikimedia.org/wiki/File:Photorespiration_de.svg>, [Accessed 01/29/2014].

Plant Cell Diagram. <http://media-1.web.britannica.com/eb-media/04/114904-004-29F75B95.jpg>, [Accessed 07/28/2014].

Price of Industrial-Grade Chitosan <http://www.alibaba.com/product-gs/525308760/High_Qulaity_chitosan_industrial_grade.html?s=p>, [Accessed 11/25/2013].

Prof. Romain Privat's Homepage, <http://lrgp.univ-lorraine.fr/axes-de-recherche/reactions-et-reacteurs/thermodynamique-et-energie-therme/permanents/fiche/?tx_wecstaffdirectory_pi1%5Bcurstaff%5D=130>, [Accessed 05/06/2015].

Sodium Methoxide MSDS, <http://www.sciencelab.com/msds.php?msdsId=9927332>, [Accessed 12/07/2012].

Soystats – Biodiesel Consumption, <http://www.soystats.com/2012/Default-frames.htm>, [Accessed 12/03/2012].

SRS Energy, Algae Fractionation, <http://www.solutionrecovery.com/algae/>, [Accessed 12/10/2012].

SRS Energy, Solvent Extraction, <http://www.srsbiodiesel.com/SolventExtraction.aspx>, [Accessed 12/10/2012].

Sustainable Development of Algal Biofuels in the United States, <http://www.nap.edu/catalog/13437/sustainable-development-of-algal-biofuels-in-the-united-states>, [Accessed 05/11/2015].

Triglyceride Synthesis, <http://lipidlibrary.aocs.org/plantbio/tag_algae/index.htm>, [Accessed 05/08/2015].

"Tuning" Microalgae for High Photosynthesis Efficiency. <http://www.lanl.gov/newsroom/news-stories/2013/March/microalgae-for-high-photosynthesis-efficiency.ph>, [Accessed 02/06/2014].

U.S. Department of Energy, Office of Energy Efficiency and Renewable Energy, Biomass Program, 2010. National Algal Biofuels Technology Roadmap. <http://www.eere.energy.gov/biomass/pdfs/algal_biofuels_roadmap.pdf>, [Accessed December 12, 2012].

U.S. Energy Information Administration, How Much Oil Does the United States Consume Per Year?, <http://www.eia.gov/tools/faqs/faq.cfm?id=33&t=6>, [Accessed 05/07/2015].

U.S. Retail Diesel Price, <http://ycharts.com/indicators/us_diesel_price>, [Accessed 12/03/2012].

Albarran-Zavala, E., Angulo-Brown, F., 2007. A Simple Thermodynamic Analysis of Photosynthesis. *Entropy* 9, p. 152-168.

Andreatta, A.E., Casas, L.M., Hegel, P., Bottini, S.B., Brignole, E.A., 2008. Phase Equilibria in Ternary Mixtures of Methyl Oleate, Glycerol, and Methanol. *Ind. Eng. Chem. Res.* 47, p. 5157-5164.

Andreatta, A.E., Lugo, R., Hemptinne, J.C.d., Brignole, E.A., Bottini, S.B., 2010. Phase Equilibria Modeling of Biodiesel Related Mixtures Using the Gca-Eos Model. *Fluid Phase Equil.* 296.

Anikeev, V., Stepanov, D., Yermakova, A., 2012. Thermodynamics of Phase and Chemical Equilibrium in the Processes of Biodiesel Fuel Synthesis in Subcritical and Supercritical Methanol. *Ind. Eng. Chem. Res.* 51, p. 4783-4796.

Anitescu, G., Bruno, T.J., 2012. Liquid Biofuels: Fluid Properties to Optimize Feedstock Selection, Processing, Refining/Blending, Storage/Transportation, and Combustion. *Energy & Fuels* 26, p. 324-348.

Asimov, I., 1968. Photosynthesis. Basic Books Inc., London.

Association, G.P., 1963. Physical Properties of Glycerine and Its Solutions, New York.

ASTM, 2013. Standard Test Method for Determination of Total Monoglycerides, Total Diglycerides, Total Triglycerides, and Free and Total Glycerin in B-100 Biodiesel Methyl Esters by Gas Chromatography, West Conshohocken, PA, 2013.

Barber, J., 2009. Photosynthetic Energy Conversion: Natural and Artificial. *Chem. Soc. Rev.* 38, p. 185-196.

Barclay, B., Weaver, C., Metz, J., 2005. Development of a Docosahexaenoic Acid Production Technology Using Schizochytrium: A Historical Perspective. In: Cohen, Z., Ratledge, C. *Single Cell Oils*. *AOCS Press*, Champaign, IL. p. 36-52.

Bassham, J.A., Buchanan, B.B., 1982. Photosynthesis. Vol. 2 *Acad. Press*. p. 147.

Bassham, J.A., Krause, G.H., 1969. Free Energy Changes and Metabolic Regulation in Steady-State Photosynthetic Carbon Reduction. *Biochim. Biophys. Acta* 189, p. 207-221.

Benneman, J., Oswald, W., 1996. Final Report to the Department of Energy, Pittsburgh Energy Technology Center. Systems and Economic Analysis of Microalgae Ponds for Conversion of CO_2 to Biomass. <http://www.osti.gov/bridge/servlets/purl/493389-FXQyZ2/webviewable/493389.pdf>, [Accessed December 12, 2012].

Berry, J.A., Downton, W.J.S., 1982. Photosynthesis. Vol. 2 *Acad. Press*. p. 263.

Bhattacharya, A., Motard, R.L., Dunlop, E.H., 1986. Bioaspen: System for Technology Development. NASA Contractor Report. NASA CR-181086.

Bilanovic, D., Shelef, G., 1988. Flocculation of Microalgae with Cationic Polymers – Effects of Medium Salinity. *Biomass* 17, p. 65-76.

Bisio, G., Bisio, A., 1998. Some Thermodynamic Remarks on Photosynthetic Energy Conver. *Energy Conver. Manage.* 39, p. 741-748.

Blackburn, S., Parker, N., 2005. Microalgal Life Cycles: Encystment and Excystment. In: Anderson, R.A. *Algal Culturing Techniques*. Elsevier, Burlington, MA. p. 399-417.

Bolton, J.R., Hall, D.O., 1991. The Maximum Efficiency of Photosynthesis. *Photochem. and Photobiol* 53, p. 545-548.

Bonhorst, C.W., Althouse, P.M., Triebold, H.O., 1948. Esters of Naturally Occurring Fatty Acids-Physical Properties of Methyl, Propyl, and Isopropyl Esters of C6 to C18 Saturated Fatty Acids. *Ind. Eng. Chem.* 40, p. 2379-2384.

Boussiba, S., Vonshak, A., Cohen, Z., Avissar, Y., Richmond, A., 1987. Lipid and Biomass Production by Halotolerant Microalga Nannochloropsis Salina. *Biomass* 12, p. 37-47.

Bretner, L.B., Eckelman, M.J., Zimmerman, J.B., 2011. Combinatorial Life Cycle Assessment to Inform Process Design of Industrial Production of Algal Biodiesel. *Envir. Sci. Tech.* 45, p. 7060-7067.

Britt, H.I., Luecke, R.H., 1973. The Estimation of Parameters in Nonlinear, Implicit Models. *Technometrics* 15, p. 233-247.

Bugbee, B., Monje, O., 1992. The Limits of Crop Productivity: Theory and Validation. *BioSci.* 42, p. 494-502.

Burlew, J.S., 1953. Algal Culture. From Laboratory to Pilot Plant. Carnegie Institution of Washington Publication 600, Washington DC. p. 204-235.

Cammenga, H.K., Schulze, F.W., Theuerl, W., 1977. Vapor Pressure and Evaporation Coefficient of Glycerol. *J. Chem. Eng. Data* 22, p. 131-134.

Chain, R.K., Arnon, D.I., 1977. Quantum Efficiency of Photosynthetic Energy Conversion. *Proc Natl Acad Sci U S A* 74, p. 3377-3381.

Chang, A., Liu, Y.A., 2009. Integrated Process Modeling and Product Design of Biodiesel Manufacturing. *Ind. Eng. Chem. Res.* 49, p. 1197-1213.

Changi, S., Pinnarat, T., Savage, P.E., 2011. Mechanistic Modeling of Hydrolysis and Esterification for Biofuel Processes. *Ind. Eng. Chem. Res.* 50, p. 12471-12478.

Chapman, W.G., Gubbins, K.E., Jackson, G., Radosz, M., 1990. New Reference Equation of State for Associating Liquids. *Ind. Eng. Chem. Res.* 29, p. 1709-1721.

Cheng, K.C., Ogden, K.L., 2011. Algal Biofuels: The Research. *Chem. Eng. Prog.* 107, p. 42-47.

Cornet, J.F., Dussap, C.G., Gros, J.B., 1998. Kinetics and Energetics of Photosynthetic Micro-Organisms in Photobioreactors. *Adv. Biochem. Eng./Biotech.* 59, p. 153-224.

Czartoski, T.J., Perkins, R., Villaneuva, J.L., Richards, G., 2011. Algae Biomass Fractionation. Patent Number US2011/0086386A1.

Davis, J.M., 2002. Basic Cell Culture. 2 ed; Oxford University Press, Oxford.

Davis, R., Aden, A., Pienkos, P.T., 2011. Techno-Economic Analysis of Autotrophic Microalgae for Fuel Production. *Appl. Energy* 88, p. 3524-3531.

Demirbas, A., Demirbas, M.F., 2011. Importance of Algae Oil as a Source of Biodiesel. *Energy Conv. Manage.* 52, p. 163-170.

Döker, O., Salgin, U., Yildiz, N., Aydog˘mus, M., Çalimli, V., 2009. Extraction of Sesame Seed Oil Using Supercritical CO_2 and Mathematical Modeling. *J.Food Eng.* 97, p. 360-366.

Duan, P., Savage, P.E., 2010. Hydrothermal Liquefaction of a Microalga with Heterogeneous Catalysts. *Ind. Eng. Chem. Res.* 50, p. 52-61.

Dunlop, E.H., Coaldrake, A.K., Silva, C.S., Seider, W.D., 2013. An Energy-Limited Model of Algal Biofuel Production: Towards the Next Generation of Advanced Biofuels. *AIChE J.* 59, p. 4641-4654.

Duschek, W., Kleinrahm, R., Wagner, W., 1990. Measurement and Correlation of the (Pressure, Density, Temperature) Relation of Carbon Dioxide I. The Homogeneous Gas and Liquid Regions in the Temperature Range from 217 K to 340 K at Pressures up to 9 Mpa. *J. Chem. Thermo.* 22, p. 827-840.

Eckelberry, N.D., Green, M.P., Fraser, S.A., 2010. Systems, Apparatus and Methods for Obtaining Intracellular Products and Cellular Mass and Debris from Algae and Derivative Products and Process of Use Thereof. ORIGINOIL INC. Int'l. Patent Number WO 2010/123903.

Erasmus, U., 1993. Fats That Heal, Fats That Kill: The Complete Guide to Fats, Oils, Cholesterol and Human Health. Alive Books.

Espinosa, S., Fornari, T., Bottini, S.B., Brignole, E.A., 2002. Phase Equilibria in Mixtures of Fatty Oils and Derivatives with near Critical Fluids Using the Gc-Eos Model. *J. Supercrit. Fluids* 23, p. 91-102.

Evans, L.B., 1988. Bioprocess Simulation: A New Tool for Process Development. *Nature Biotech.* 6, p. 200-203.

Fredenslund, A., Jones, R.L., Prausnitz, J.M., 1975. Group-Contribution Estimation of Activity Coefficients in Nonideal Liquid Mixtures. *AIChE J.* 21, p. 1086-1099.

Galbe, M., Zacchi, G., 1992. Simulation of Ethanol Production Processes Based on Enzymatic Hydrolysis of Lignocellulosic Materials Using Aspen Plus. *Appl. Biochem Biotech.* 34-35, p. 93-104.

Gautam, R., Seider, W.D., 1979. Calculation of Phase and Chemical Equilibria, Parts I-III. *AIChE J.* 25, p. 991-1015.

Gebreslassie, B.H., Waymire, R., You, F., 2013. Sustainable Design and Synthesis of Algae-Based Biorefinery for Simultaneous Hydrocarbon Biofuel Production and Carbon Sequestration. *AIChE J.* 59, p. 1599-1621.

Geciova, J., Bury, D., Jelen, P., 2002. Methods for the Disruption of Microbial Cells for Potential Use in the Dairy Industry–a Review. *Int'l. Dairy J.*12.

Glisic, S.B., Orlovic, A.M., 2014. Review of Biodiesel Synthesis from Waste Oil under Elevated Pressure and Temperature: Phase Equilibrium, Reaction Kinetics, Process Design, and Techno-Economic Study. *Renew. Sustain. Energy Revs.* 31, p. 708-725.

Goodrum, J.W., Geller, D.P., 2002. Rapid Thermogravimetric Measurements of Boiling Points and Vapor Pressure of Saturated Medium- and Long-Chain Triglycerides. *Bioresource Tech.* 84, p. 75-80.

Gratzel, M., 2001. Molecular Photovoltaics That Mimic Photosynthesis. *Pure Appl. Chem.* 73, p. 459-467.

Gross, J., Sadowski, G., 2001. Perturbed-Chain Saft: An Equation of State Based on a Perturbation Theory for Chain Molecules. *Ind. Eng. Chem. Res.* 40, p. 1244-1260.

Gross, J., Sadowski, G., 2002. Application of the Perturbed-Chain Saft Equation of State to Associating Systems. *Ind. Eng. Chem. Res.* 41, p. 5510-5515.

Gust, D., Moore, T.A., 1985. A Synthetic System Mimicking the Energy Transfer and Charge Separation of Natural Photosynthesis. *J. Photochem.* 29, p. 173-184.

Gust, D., Moore, T.A., 1989. Mimicking Photosynthesis. *Science* 244, p. 35-41.

Gust, D., Moore, T.A., Moore, A.L., 1998. Mimicking Bacterial Photosynthesis. *Pure & Appl. Chem* 70, p. 2189-2200.

Gust, D., Moore, T.A., Moore, A.L., 2001. Mimicking Photosynthetic Solar Energy Transduction. *Acc. Chem. Res.* 34.

Handler, R.M., Canter, C.E., Kalnes, T.N., Lupton, F.S., Kholiquov, O., Shonard, D.R., Blowers, P., 2012. Evaluation of Environmental Impacts from Microalgae Cultivation in Open-Air Raceway Ponds: Analysis of the Prior Literature and Investigation of Wide Variance in Predicted Impacts. *Algal Res.* 1, p. 83-92.

Harith, Z.T., Yusoff, F.M., Mohamed, M.S., Din, M.S.M., Ariff, A.B., 2009. Effect of Different Flocculants on the Flocculation Performance of Microalgae, Chaetoceros Calcitrans, Cells. *African J. Biotech.* 8, p. 5971-5978.

Hegel, P., Mabe, G., Pereda, S., Brignole, E.A., 2007. Phase Transitions in a Biodiesel Reactor Using Supercritical Methanol. *Ind. Eng. Chem. Res.* 46, p. 6360-6365.

Heredia-Arroyo, T., Wei, W., Hu, B., 2010. Oil Accumulation Via Heterotrophic/ Mixotrophic Chlorella Protothecoides. *Appl. Biochem. Biotech.* 162, p. 1978-1995.

Iglesias-Silva, G.A., Bonilla-Petriciolet, A., Eubank, P.T., Holste, J.C., Hall, K.R., 2003. An Algebraic Method That Includes Gibbs Minimization for Performing Phase Equilibrium Calculations for Any Number of Components or Phases. *Fluid Phase Equil.* 210, p. 229-245.

Iqbal, J., Theegala, C., 2013. Microwave Assisted Lipid Extraction from Microalgae Using Biodiesel as a Co-Solvent. *Algal Res.* 2, p. 34-42.

Jones, S., Zhu, Y., Anderson, D., Hallen, R., Elliott, D., Schmidt, A., Albrecht, K., Hart, T., Butcher, M., Drennan, C., Snowden-Swan, L., Davis, R., Kinchin, C., 2014. Process Design and Economics for the Conversion of Algal Biomass to Hydrocarbons: Whole Algae Hydrothermal Liquefaction and Upgrading. Pacific Northwest National Laboratory.

Keenan, J.H., 1951. Availability and Irreversibility in Thermodynamics. *Brit. J. Appl. Phys.* 2, p. 183-192.

Kelly, G.J., Latzko, E., 2006a. Carbon Metabolism: On Land and at Sea. *Thirty Years of Photosynthesis, 1974-2004*. Springer, Berlin.

Kelly, G.J., Latzko, E., 2006b. Carbon Metabolism: Quantification and Manipulation. *Thirty Years of Photosynthesis, 1974-2004*. Springer, Berlin.

Kelly, G.J., Latzko, E., 2006c. Carbon Metabolism: The Calvin Cycle's Golden Jubilee. *Thirty Years of Photosynthesis, 1974-2004*. Springer, Berlin.

Kelly, G.J., Latzko, E., 2006d. Carbon Metabolism: The Chloroplast's Sesquicentenary, and Some Thoughts on the Limits to Plant Productivity. *Thirty Years of Photosynthesis, 1974-2004*. Springer, Berlin.

Kelly, G.J., Latzko, E., 2006e. Control of Carbon Metabolism through Enzyme Regulation and Membrane-Mediated Metabolite Transport. *Thirty Years of Photosynthesis, 1974-2004*. Springer, Berlin.

Kemp, R.B., 1999. From Macromolecules to Man. Vol. 4 *Handbook of Thermal Anal. and Calorimetry*. Elsevier, Amsterdam.

Kim, J.H., Lee, M., Lee, J.S., Park, C.B., 2012. Self-Assembled Light-Harvesting Peptide Nanotubes for Mimicking Natural Photosynthesis. *Angew. Chem. Int. Ed.* 51, p. 517-520.

Kjelstrup, S., Bedeaux, D., Johannessen, E., Gross, J., 2010. Non-Equilibrium Thermodynamics for Engineers. World Scientific, Hackensack, NJ, USA.

Kluge, M., 1982. Photosynthesis. Vol. 2 Acad. Press. p. 231.

Knothe, G., Gerpen, J.V., 2010. The Biodiesel Handbook. 2nd ed; AOCS Publishing, Illinois.

Koohyar, F., Rostami, A.A., Chaichi, M.J., Kiani, F., 2013. Study on Thermodynamic Properties for Binary Systems of Water + L-Cysteine Hydrochloride Monohydrate, Glycerol, and D-Sorbitol at Various Temperatures. *J.Chem.Phys.* 2013, p. 1-10.

Korgitzsch, F.M., 1993. Study of Phase Equilibria as a Fundament for the Refinement of Vegetable and Animal Fats and Oils. Technical University of Berlin.

Krebs, H.A., Kornberg, H.L., 1957. Energy Transformations in Living Matter, a Survey. Springer-Verlag, Berlin, Gottingen, Heidelberg.

Kumoro, A.C., Soedarto, H., 2012. Experimental and Modeling Studies of the Reaction Kinetics of Alkaline–Catalyzed Used Frying Oil Glycerolysis Using Isopropyl Alcohol as a Reaction Solvent. *J.Appl. Sci., Engi. Tech.* 4, p. 869-876.

Lee, J.Y., Yoo, C., Jun, S.Y., Ahn, C.Y., Oh, H.M., 2010a. Comparison of Several Methods for Effective Lipid Extraction from Microalgae. *Biores. Tech.*101, p. S75-S77.

Lee, M.J., Lo, Y.C., Lin, H.M., 2010b. Liquid–Liquid Equilibria for Mixtures Containing Water, Methanol, Fatty Acid Methyl Esters, and Glycerol. *Fluid Phase Equil.* 299, p. 180-190.

Lehninger, A.L., 1971. Bioenergetics. 2nd ed; W. A. Benjamin Inc., Menlo Park, California.

Lems, S., van der Kooi, H.J., de Swaan Arons, J., 2007. Thermodynamic Analysis of the Living Cell: Design of an Exergy-Based Method. *Int. J. Exergy* 4, p. 339-356.

Lems, S., van der Kooi, H.J., de Swaan Arons, J., 2010. Exergy Analyses of the Biochemical Processes of Photosynthesis. *Int. J. Exergy* 7, p. 333-351.

Levine, R.B., Pinnarat, T., Savage, P.E., 2010a. Biodiesel Production from Wet Algal Biomass through in Situ Lipid Hydrolysis and Supercritical Transesterification. *Energy Fuels* 24, p. 5235−5243.

Li, Y., Horsman, M., Wu, N., Lan, C.Q., Dubois-Calero, N., 2008. Biofuels from Microalgae. *Biotech. Prog.* 24, p. 815-820.

Luo, Y., Lee, J.K., Zhao, H., 2013. Challenges and Opportunities in Synthetic Biology for Chemical Engineers. *Chem. Eng. Sci.* 103, p. 115-119.

Lymperiadis, A., Adjiman, C.S., Galindo, A., Jackson, G., 2007. A Group Contribution Method for Associating Chain Molecules Based on the Statistical Associating Fluid Theory (Saft–Γ). *J. Chem. Phys.* 127, p. 234903-234901 – 234903-234922.

Macaira, J., Santana, A., Costa, A., Ramirez, E., Larroyoz, M.A., 2014. Process Intensification Using CO_2 as a Cosolvents under Supercritical Conditions Applied to Design of Biodiesel Production. *Ind. Eng. Chem. Res.* 53, p. 3985-3995.

Marquardt, D.W., 1963. An Algorithm for Least-Squares Estimation of Nonlinear Parameters. *J. Soc. Indust. Appl. Math.* 11, p. 431-441.

Martin, M., Grossmann, I.E., 2012. Simultaneous Optimization and Heat Integration for Biodiesel Production from Cooking Oil and Algae. *Ind. Eng. Chem. Res*. 51, p. 7998-8014.

McDonald, C.M., Floudas, C.A., 1995a. Global Optimization for the Phase and Chemical Equilibrium Problem: Application to the Nrtl Equation. *Comput. Chem.Eng.* 19, p. 1111-1141.

McDonald, C.M., Floudas, C.A., 1995b. Global Optimization for the Phase Stability Problem. *AIChE J.* 41, p. 1798-1814.

Melis, A., 2009. Solar Energy Conversion Efficiencies in Photosynthesis: Minimizing the Chlorophyll Antennae to Maximize Efficiency. *Plant Sci.* 177, p. 272-280.

Michelsen, M.L., Mollerup, J., 2007. Thermodynamic Models: Fundamentals and Computational Aspects. 2 ed; Tie-Line Publications.

Moquin, P.H.L., Temelli, F., King, J.W., Palcic, M.M., 2005. Kinetic Modeling of the Glycerolysis Reaction for Soybean Oils in Supercritical Carbon Dioxide Media. *J. Amer. Oil Chem. Soc.* 82, p. 613-617.

Morimura, Y., Nihei, T., Sasa, T., 1955. Outdoor Bubbling Culture of Some Unicellular Algae. *J. Gen. Appl. Microbiol.* 1, p. 173-179.

Muneer, T., 2004. Solar Radiation and Daylight Models 2 ed; Elsevier, Amsterdam.

Ne´ron, A., Lantagne, G., Marcos, B., 2012. Computation of Complex and Constrained Equilibria by Minimization of the Gibbs Free Energy. *Chem. Eng. Sci.* 82, p. 260-271.

Nichita, D.V., Gomez, S., Luna, E., 2002. Multiphase Equilibria Calculation by Direct Minimization of Gibbs Free Energy with a Global Optimization Method. *Comput. Chem. Eng.* 26, p. 1703-1724.

Nicholls, D.G., Ferguson, S.J., 2002. Bioenergetics 3. *Acad. Press*, San Diego, CA.

O'Grady, J.P., Morgan, J.A., 2011. Heterotrophic Growth and Lipid Production of Chlorella Protothecoides on Glycerol. *Bioprocess and Biosys. Eng.* 34, p. 121-125.

Ogren, W.L., 1982. Photosynthesis. Vol. 2 *Acad. Press*. p. 191.

Oliveira, M.B., Varanda, F.R., Marrucho, I.M., Queimada, A.J., Coutinho, J.A.P., 2008. Prediction of Water Solubility in Biodiesel with the Cpa Equation of State. *Ind. Eng. Chem. Res.* 47, p. 4278-4285.

Ominik, A., Chapman, W.G., Kleiner, M., Sadowski, G., 2005. Modeling of Polar Systems with the Perturbed-Chain Saft Equation of State. Investigation of the Performance of Two Polar Terms. *Ind. Eng. Chem. Res.* 44, p. 6928-6938.

Ott, L.S., Huber, M.L., Bruno, T.J., 2008. Density and Speed of Sound Measurements on Five Fatty Acid Methyl Esters at 83 Kpa and Temperatures from (278.15 to 338.15) K. *J. Chem. Eng. Data* 53, p. 2412-2416.

Papaioannou, V., Lafitte, T., Avendaño, C., Adjiman, C.S., Jackson, G., Müller, E.A., Galindo, A., 2014. Group Contribution Methodology Based on the Statistical Associating Fluid Theory for Heteronuclear Molecules Formed from Mie Segments. *J Chem. Phys.* 140, p. 054107.

Paricaud, P., 2006. A General Perturbation Approach for Equation of State Development: Applications to Simple Fluids, Ab Initio Potentials, and Fullerenes. *J. Chem. Phys.* 124, p. 154505-154501 - 154505-154517.

Patil, P.D., Grude, V.D., A. Mannarswamy, Deng, S., Cooke, P., Munson-McGee, S., Rhodes, I., Lammers, P., Nirmalakandan, N., 2012. Optimization of Direct Conversion of Wet Algae-to-Biodiesel under Supercritical Methanol Conditions. *Biores.. Tech.* 102, p. 118-122.

Peng, D.Y., Robinson, D.B., 1976. A New Two-Constant Equation of State. *Ind. Eng. Chem. Fund.* 15, p. 59-64.

Perrine, Z., Negi, S., Sayre, R.T., 2012. Optimization of Photosynthetic Light Energy Utilization by Microalgae. *Algal Res.* 1, p. 134-142.

Perry, E.S., Weber, W.H., Daubert, B.F., 1949. Vapor Pressures of Phlegmatic Liquids. I. Simple and Mixed Triglycerides. *J. Am. Chem. Soc.* 71, p. 3720-3726.

Perry, R.H., Green, D.W., 1999. Physical and Chemical Data, Chapter 2. *Perry's Chemical Engineer's Handbook.* 7th ed; *McGraw-Hill,* New York, New York.

Perry, R.H., Green, D.W., 2007. Perry's Handbook of Chemical Engineering. Vol. 8 *McGraw-Hill Prof.*

Petela, R., 2008. An Approach to the Exergy Analysis of Photosynthesis. *Solar Energy* 82, p. 311-328.

Phillips, J.C., Mattamal, G.J., 1978. Effect of Number of Carboxyl Groups on Liquid Density of Esters of Alkylcarboxylic Acids. *J. Chem. Eng. Data.* 23, p. 1-6.

Pokoo-Aikins, G., Nadim, A., El-Halwagi, M.M., Mahalec, V., 2010. Design and Analysis of Biodiesel Production from Algae Grown through Carbon Sequestration. *Clean Tech. Environ. Pol.* 12, p. 239-254.

Poling, B.E., Prausnitz, J.M., O'Connell, J.P., 2001. Pure Component Constants, Chapter 2. *The Properties of Gases and Liquids*. 5th ed; *McGraw-Hill*, New York, New York.

Pratas, M.J., Freitas, S., Oliveira, M.B., Monteiro, S.C., Lima, A.S., Coutinho, J.A.P., 2010. Densities and Viscosities of Fatty Acid Methyl and Ethyl Esters. *J. Chem. Eng. Data* 55, p. 3983-3990.

Rao, A.R., Dayananda, C., Sarada, R., Shamala, T.R., Ravishankar, G.A., 2007. Effect of Salinity on Growth of Green Alga Botryococcus Braunii and Its Constituents. *Biores. Tech.* 98, p. 560-564.

Reis, H.A., Miguel, A.F., 2006. Analysis of the Exergy Balance of Green Leaves. *Int. J. Exergy* 3, p. 231-237.

Richardson, J.W., Johnson, M.D., Outlaw, J.L., 2012. Economic Comparison of Open Pond Raceways to Photo Bio-Reactors for Profitable Production of Algae for Transportation Fuels in the Southwest. *Algal Res.* 1, p. 93-100.

Saleh, B., Wendland, M., 2005. Measurement of Vapor Pressures and Saturated Liquid Densities of Pure Fluids with a New Apparatus. *J. Chem. Eng. Data* 50, p. 429-437.

Sánchez, E., Ojeda, K., El-Halwagi, M., Kafarov, V., 2011. Biodiesel from Microalgae Oil Production in Two Sequential Esterification/Transesterification Reactors: Pinch Analysis of Heat Integration. *Chem. Eng. Jour.* 176-177, p. 211-216.

Santander, C.M.G., Rueda, S.M.G., Silva, N.d.L.d., Camargo, C.L.d., Kieckbusch, T.G., Maciel, M.R.W., 2011. Measurements of Normal Boiling Points of Fatty Acid Ethyl Esters and Triacylglycerols by Thermogravimetric Analysis. *Fuel* 92, p. 158-161.

Scholes, G.D., Mirkovic, T., Turner, D.B., Fassioli, F., Buchleitner, A., 2012. Solar Light Harvesting by Energy Transfer: From Ecology to Coherence. *Energy Env.. Sci.* 5, p. 9374-9393.

Seider, W.D., Seader, J.D., Lewin, D.R., 2004. Product and Process Design Principles: Synthesis, Analysis and Evaluation. 2nd ed; *Wiley*, Hoboken, NJ. p. 301-366.

Seider, W.D., Seader, J.D., Lewin, D.R., Widagdo, S., 2009a. Design of Heat Exchangers, Chapter 18. *Product and Process Design Principles: Synthesis, Analysis, and Design*. 3rd ed; *Wiley*, New Jersey.

Seider, W.D., Seader, J.D., Lewin, D.R., Widagdo, S., 2009b. Heat Exchanger Networks, Chapter 9. *Product and Process Design Principles: Synthesis, Analysis, and Design*. 3rd ed; *Wiley*, New Jersey.

Seider, W.D., Seader, J.D., Lewin, D.R., Widagdo, S., 2009c. Manufacturing Cost and Profitability Analysis, Chapter 23. *Product and Process Design Principles: Synthesis, Analysis, and Design*. 3rd ed; *Wiley*, New Jersey.

Sheehan, J., Dunahay, T., Benemann, J., Roessler, P., 1998. A Look Back at the Us Department of Energy's Aquatic Species Program: Biodiesel from Algae, Close-out Report. National Renewable Energy Laboratory, <http://www.nrel.gov/biomass/pdfs/24190.pdf>, [Accessed December 12, 2012].

Shelef, G., Sukenik, A., Green, M., 1984. Microalgae Harvesting and Processing: A Literature Review. Technion Research and Development, Foundation Ltd. SERI/STR–231–2396, UC Category: 61a, DE84013036.

Silva, C.S., Seider, W.D., Lior, N., 2015. Exergy Efficiency of Plant Photosynthesis. *Chem. Eng. Sci.* In Press.

Silva, C.S., Soliman, E., Cameron, G., Fabiano, L.A., Seider, W.D., Dunlop, E.H., Coaldrake, A.K., 2014. Commercial-Scale Biodiesel Production from Algae. *Ind. Eng. Chem. Res.* 53, p. 5311-5324.

Sliepcevich, C.M., Finn, D., 1963. A Macroscopic Approach to Irreversible Thermodynamics. *Ind. Eng. Chem. Fund.* 2, p. 249.

Smith, B.T., Davis, R.H., 2012. Sedimentation of Algae Flocculated Using Naturally-Available Magnesium-Based Flocculants. *Algal Res.*1, p. 32-39.

Smith, M., Ness, H.C.V., Abbott, M.M., 2002. Introduction to Chemical Engineering Thermodynamics. 6 ed; *McGraw-Hill*.

Soave, G., 1972. Equilibrium Constants from a Modified Redlich-Kwong Equation of State. *Chem. Eng. Sci.* 27, p. 1197-1203.

Soh, L., Curry, J., Beckman, E.J., Zimmerman, J.B., 2013. Effect of System Conditions for Biodiesel Production Via Transesterification Using Carbon Dioxide–Methanol Mixtures in the Presence of a Heterogeneous Catalyst. *ACS Sustain. Chem. Eng.* 2, p. 387-395.

Soh, L., Zimmerman, J., 2011. Biodiesel Production: The Potential of Algal Lipids Extracted with Supercritical Carbon Dioxide. *Green Chem.* 13, p. 1422−1429.

Soh, L., Chen, C.C., Kwan, T.A., Zimmerman, J., 2015. Role of CO2 in mass transfer, reaction kinetics, and inter-phase partitioning for the transesterification of triolein in an expanded methanol system with heterogeneous acid catalyst. Submitted to *Sustainable Chemistry and Engineering.*

Soujanya, J., Satyavathi, B., Prasad, T.E.V., 2010. Experimental (Vapour+ Liquid) Equilibrium Data of (Methanol+Water), (Water+Glycerol) and (Methanol+Glycerol) Systems at Atmospheric and Sub-Atmospheric Pressures. *J. Chem. Thermo.* 42, p. 621-624.

Stull, D.R., 1947. Vapor Pressure of Pure Substances. Organic and Inorganic Compounds. *Ind. Eng. Chem. Res.* 39, p. 517-540.

Su, Y., Liu, Y.A., Tovar, C.A.D., Gani, R., 2011. Selection of Prediction Methods for Thermophysical Properties for Process Modeling and Product Design of Biodiesel Manufacturing. *Ind. Eng. Chem. Res.* 50, p. 6809-6836.

Sukenik, A., Levy, R.S., Levy, Y., Falkowski, P.G., Dubinksy, Z., 1991. Optimizing Algal Biomass Production in an Outdoor Pond: A Simulation Model. *J. Appl. Phycology* 3, p. 191-201.

Sum, A.K., Biddy, M.J., Pablo, J.J., Tupy, M.J., 2003. Predictive Molecular Model for the Thermo and Transport Properties of Triacylglycerols. *J. Phys. Chem. B.* 107, p. 14443–14451.

Sun, A., Davis, R., Starbuck, M., Ben-Amotz, A., Pate, R., Pienkos, P.T., 2011. Comparative Cost Analysis of Algal Oil Production for Biofuels. *Energy* 36, p. 5169-5179.

Sun, A.C., Seider, W.D., 1995. Homotopy-Continuation Method for Stability Analysis in the Global Minimization of the Gibbs Free Energy. *Fluid Phase Equil.* 103, p. 213-249.

Sussman, M.V., 1980. Availability (Exergy) Analysis. Mulliken House, Lexington, MA.

Szargut, J., 2005. Exergy Method, Technical and Ecological Applications. *WIT Press*, Billerica, MA.

Tamiya, H., 1957. Mass Culture of Algae. *Annu. Rev. Plant Physio.* 8, p. 309-334.

Tamiya, H., Hase, E., Shabita, K., Mituya, A., Iwamura, T., Nihei, T., Sasa, T., 1953. Kinetics of Growth of Chlorella, with Special Reference to Its Dependence on Quality of Available Light and on Temperature. In: Burlew, J.S. *Algal Culture. From Laboratory to Pilot Plant.* Carnegie Institution of Washington Publication 600, Washington DC. p. 204-235.

Tang, Z., Du, Z., Min, E., Gao, L., Jiang, T., Han, B., 2006. Phase Equilibria of Methanol-Triolein System at Elevated Temperature and Pressure. *Fluid Phase Equil.* 239, p. 8-11.

Taylor, R., Fletcher, R.L., Raven, J.A., 2005. Preliminary Studies on the Growth of Selected 'Green Tide' Algae in Laboratory Culture: Effects of Irradiance, Temperature, Salinity and Nutrients on Growth Rate. *Botanica Marina* 44, p. 327-336.

Tenney, M.W., Jr., W.F.E., Schuessler, R.G., Pavoni, J.L., 1969. Algal Flocculation with Synthetic Organic Polyelectrolytes. *Appl.Microbio.* 18, p. 965-971.

Terigar, B.G., Balasubramanian, C.M., Lima, M., Boldor, D., 2011. Soybean and Rice Bran Oil Extraction in a Continuous Microwave System: From Laboratory to Pilot-Scale. *J. Food Eng.* 104, p. 208-217.

Thorndike, E.H., 1996. Energy and the Environment. Pub *Addison-Wesley*, Reading, Mass, USA.

Tornabene, T.G., Holzer, G., Lien, S., Burris, N., 1983. Lipid Composition of the Nitrogen Starved Green Alga Neochloris Oleoabundans. *Enzyme Microbial Tech.* 5, p. 435-440.

Velez, A., Hegel, P., Mabe, G., Brignole, E.A., 2010. Density and Conversion in Biodiesel Production with Supercritical Methanol. *Ind. Eng. Chem. Res.* 49, p. 7666-7670.

Voet, D., Voet, J.G., Pratt, C.W., 2008. Fundamentals of Biochemistry. 3rd ed; *Wiley*.

Vyas, A.P., Verma, J.L., Subrahmanyam, N., 2009. A Review on Fame Production Processes. *Fuel* 89, p. 1-9.

Walz, D., 1997a. Chapter 5, "Chloroplasts". Vol. 4 *Bioenergetics*. *Basel*; Boston; Berlin : Birkhauser.

Walz, D., 1997b. Chapter 7, "Photosystem Ii and Water Oxidation in Cyanobacteria, Algae, and Higher Plants". Vol. 4 *Bioenergetics*. *Basel*; Boston; Berlin : Birkhauser.

Walz, D., 1997c. Chapter 8, "the Photosystem I Reaction Center in Oxygenic Photosynthesis". Vol. 4 *Bioenergetics*. *Basel*; Boston; Berlin : Birkhauser.

Weissman, J.C., Goebel, R.P., 1987. Design and Analysis of Microalgal Open Pond Systems for the Purpose of Producing Fuels. S.E.R. Institute <http://www.nrel.gov/docs/legosti/old/2840.pdf>, [Accessed 08/26/2013].

Wertheim, M.S., 1984a. Fluids with Highly Directional Attractive Forces: I. Statistical Thermodynamics. *J. Stat. Phys.* 35, p. 19.

Wertheim, M.S., 1984b. Fluids with Highly Directional Attractive Forces: II. Thermodynamic Perturbation Theory and Integral Equations. *J. Stat. Phys.* 35, p. 35-47.

Wertheim, M.S., 1986a. Fluids with Highly Directional Attractive Forces: III. Multiple Attraction Sites. *J. Stat. Phys.* 42, p. 459-476.

Wertheim, M.S., 1986b. Fluids with Highly Directional Attractive Forces: IV. Equilibrium Polymerization. *J. Stat. Phys.* 42, p. 477-492.

White, C.W., III, Seider, W.D., 1981. Computation of Phase and Chemical Equilibrium. *AIChE J.* 27, p. 466-471.

Witsch, H.v., Harder, R., 1953. Stoffproduktion Durch Grünalgen Und Diatomeen in Massenkultur. In: Burlew, J.S. *Algal Culture. From Laboratory to Pilot Plant*. Carnegie Institution of Washington Publication 600, Washington DC. p. 154-165.

Wooley, R., Ruth, M., Glassner, D., Sheehan, J., 2008. Process Design and Costing of Bioethanol Technology: A Tool for Determining the Status and Direction of Research and Development. *Biotech. Prog.* 15, p. 794-803.

Wooley, R.J., Putsche, V., 1996. Development of an Aspen Plus Physical Property Database for Biofuels Components. NREL/MP, Golden, CO.

Ye, K., Freund, H., Xie, Z., Subramaniam, B., Sundmacher, K., 2012. Prediction of Multicomponent Phase Behavior of CO_2-Expanded Liquids Using Ceos Models and Comparison with Experimental Data. *J. Supercrit. Fluids* 67, p. 41-52.

Yuan, W., Hansen, A.C., Zhang, Q., 2005. Vapor Pressure and Normal Boiling Point Predictions for Pure Methyl Esters and Biodiesel Fuels. *Fuel* 84, p. 943-950.

Zarinabadi, S., Kharrat, R., Yazdi, A.V., 2010. Extraction of Oil from Canola Seeds with Supercritical Carbon Dioxide: Experimental and Modeling. Proceedings of the World Congress on Engineering and Computer Science. WCES, San Francisco, California.

Zhang, X., Hu, Q., Sommerfield, M., Puruhito, E., Chen, Y., 2010. Harvesting Algal Biomass for Biofuels Using Ultrafiltration Membranes. *Biores. Tech.* 101, p. 5297-5304.

Zhang, Y., Dub, M.A., McLean, D.D., Kates, M., 2003a. Biodiesel Production from Waste Cooking Oil: 1. Process Design and Technological Assessment. *Biores.Tech* 89, p. 1-16.

Zhang, Y., Dub, M.A., McLean, D.D., Kates, M., 2003b. Biodiesel Production from Waste Cooking Oil: 2. Economic Assessment and Sensitivity Analysis. *Biores. Tech.* 90, p. 229-240.

Zhu, X., Long, S.P., Ort, D.R., 2008. What Is the Maximum Efficiency with Which Photosynthesis Can Convert Solar Energy to Biomass? *Current Opin. Biotech.* 19, p. 153-159.

Zhu, Y., Biddy, M.J., Jones, S.B., Elliott, D.C., Schmidt, A., 2014. Techno-Economic Analysis of Liquid Fuel Production from Woody Biomass Via Hydrothermal Liquefaction (Htl) and Upgrading. *J. Appl. Energy* 129, p. 384-394.